Synthesis, Characterization and Performance Analysis of Reduced Graphene Oxide (RGO) based Photocatalysts for Hydrogen Generation from Water

Thesis submitted by

Arundhati Sarkar

Doctor of Philosophy (Engineering)

Chemical Engineering Department
Faculty Council of Engineering & Technology
Jadavpur University
Kolkata, India
2023

JADAVPUR UNIVERSITY

KOLKATA – 700032, INDIA

INDEX NO. 299/16/E

I. Title of the Thesis: Synthesis, Characterization and Performance Analysis of Reduced Graphene Oxide (RGO) based Photocatalysts for Hydrogen Generation from Water

II. Name, Designation and Institution of Supervisor(s):

1. Dr. Kajari Kargupta, Professor, Chemical Engineering Department, Jadavpur University, Kolkata – 700032, India

2. Dr. Saibal Ganguly, Ex-Professor & H.O.D, Chemical Engineering Department, BITS PILANI, Goa Campus, India

III. List of publications

1. **Arundhati Sarkar**, Sourav Chaule, Sayantanu Mandal, Suparna Saha, Saibal Ganguly, Dipali Banerjee, Kajari Kargupta *Enhanced photocatalytic hydrogen generation by splitting water using Sodium Alginate decorated rGO-CdS hybrid photo-catalyst*, Materials Today: Proceedings (Elsevier). (2023). Citescore: 3.2 Number of citations: 1

2. Soumyajit Maitra, **Arundhati Sarkar**, Toulik Maitra, Somoprova Halder, Kajari Kargupta, Subhasis Roy, *Solvothermal phase change induced morphology transformation in* $CdS/CoFe_2O_4@Fe_2O_3$*hierarchical nanosphere arrays as ternary heterojunction photoanodes for solar water splitting*, New Journal of Chemistry (Royal Society of Chemistry). 45 (2021) 12721–12737. Impact Factor: 3.3 Number of citations: 16

3. Soumyajit Maitra, **Arundhati Sarkar**, Toulik Maitra, Somoprova Halder, Subhasis Roy, Kajari Kargupta, *Cadmium Sulphide sensitized crystal facet tailored nanostructured Nickel Ferrite @ hematite core-shell ternary heterojunction photoanode for photoelectrochemical water splitting*, MRS Advances (Springer). 5 (2020) 2585–2593. Impact Factor: 0.8 Number of citations: 1

IV. List of patents: Nil

V. List of presentation (International Conference):

1. **Arundhati Sarkar,** Anjik Chowdhury, Debargha Chakravorty, Saibal Ganguly and Kajari Kargupta “Synthesis of inexpensive, recyclable reduced graphene oxide (rGO) based ferritic photocatalyst for hydrogen generation from water by visible irradiation” International Conference on Nanotechnology: Ideas, Innovations and Initiatives-2017 (ICN:31-2017), IIT Roorkee, Roorkee, India, December 6-8, 2017

2.**Arundhati Sarkar,** Anjik Chowdhury , Kajari Kargupta “Synthesis of cost-effective graphene based ferritic photocatalyst for hydrogen generation from water” 70th Chemical Engineering Congress India 2017, CHEMCON-2017, Haldia Institute of Technology, Haldia, India, December 27-30, 2017

3. **Arundhati Sarkar,** Sourav Chaule, Suparna Saha, Dipali Banerjee, Saibal Ganguly and Kajari Kargupta “rGO-CdS-Sodium-Alginate hybrid visible light active photo-catalyst for enhanced generation of hydrogen by splitting of water” Current Trends in Material Science and Engineering (CTMSE)-2019, S.N. Bose National Centre for Basic Sciences, Kolkata, India, July 18-20, 2019

4. **Arundhati Sarkar,** Milan Kumar Mandal, Suparna Saha, Dipali Banerjee, Kajari Kargupta, “Reduced graphene oxide/transition metal based nanohybrid: solid state Z- scheme photocatalytic system for enhanced hydrogen generation by water splitting” 2nd International Conference on Advances in Bioprocess Engineering and Technology (ICABET)-2020, Heritage Institute of Technology, Kolkata, India, January 20-22, 2020

5. **Arundhati Sarkar,** Sourav Chaule, Sayantanu Mandal, Suparna Saha, Saibal Ganguly, Dipali Banerjee, Kajari Kargupta “Enhanced Vapor Phase Photocatalytic Water Splitting using Sodium Alginate decorated rGO-CdS Hybrid Photo-catalyst” Platinum Jubilee Celebration of Indian Institute of Chemical Engineers, International Conference on Advances in Chemical and Material Sciences (ACMS)-2022, Heritage Institute of Technology, Kolkata, India, April 14-16, 2022

6. **Arundhati Sarkar,** Anjik Chowdhury, Rashmi Ghosh, Saibal Ganguly , Dipali Banerjee and Kajari Kargupta “Synthesis of reduced graphene oxide based visible light active spinel ferrite photocatalyst (rGO-$SnFe_2O_4$) for hydrogen generation from water” International

Conference on Chemical Engineering Innovations and Sustainability (ICEIS)-2023 Chemical Engineering Department, Jadavpur University, Kolkata, 26-27 February, 2023

VI. List of presentation (National Conferences):

1. **Arundhati Sarkar,** Milan Kumar Mandal, Suparna Saha and Kajari Kargupta "Rapid generation of hydrogen from water and sunlight: Development of efficient visible light active solid state nano-hybrid photocatalytic system", Indian International Science Festival 2019, Biswa Bangla Convention Centre, Kolkata, India, November 5-8, 2019

VII. Awards

Awarded First Prize as Young Scientist Award-Nanomaterials and Nanotechnology (YSA-NN) for presenting paper entitled "Reduced graphene oxide/transition metal based nanohybrid: solid state Z- scheme photocatalytic system for enhanced hydrogen generation by water splitting" in the 2nd International Conference on Advances in Bioprocess Engineering and Technology (ICABET)-2020, Heritage Institute of Technology, Kolkata, India, January 20-22, 2020

“Statement of Originality”

I **Arundhati Sarkar** registered on **17/08/2016** do hereby declare that this thesis entitled” **“Synthesis, Characterization and Performance Analysis of Reduced Graphene Oxide (RGO) based Photocatalysts for Hydrogen Generation from Water”** contains literature survey and original research work done by the undersigned candidate as part of Doctoral studies.

All information in this thesis have been obtained and presented in accordance with existing academic rules and ethical conduct. I declare that, as required by these rules and conduct, I have fully cited and referred all materials and results that are not original to this work.

I also declare that I have checked this thesis as per the “Policy on Anti Plagiarism, Jadavpur University, 2019”, and the level of similarity as checked by iThenticate software is 9%

Arundhati Sarkar

Signature of Candidate:

Date: 16.08.2023

Kajari Kargupta 16/08/2023

Certified by Supervisor(s)

(Signature with date, seal)

Professor
CHEMICAL ENGINEERING DEPARTMENT
JADAVPUR UNIVERSITY
Kolkata-700 032

Ganguly 16/8/2023

Certified by Supervisor(s)

(Signature with date, seal)

Prof. Saibal Ganguly (Retired)
Consultant
Ex Head and Chairman GRC, BITS Goa
Ex Professor, Ch[illegible] Engg., UTP Malaysia
Ex Advisor, DR[illegible]try of Defense
Ex faculty, Che[illegible]gg., IIT Kharagpur
Email: ganguly[illegible]11@gmail.com

Certificate from the Supervisors

This is to certify that the thesis entitled **"Synthesis, Characterization and Performance Analysis of Reduced Graphene Oxide (RGO) based Photocatalysts for Hydrogen Generation from Water"** submitted by **Arundhati Sarkar** who got her name registered on 17/08/2016 for the award of Ph. D. (Engg.) degree of Jadavpur University, is absolutely based upon his own work under the supervision of **Prof. Kajari Kargupta** and **Prof. Saibal Ganguly**, that neither her thesis nor any part of the thesis has been submitted for any degree or any other academic award anywhere before.

Kajari Kargupta 16/08/23

Signature of the supervisor

Professor
CHEMICAL ENGINEERING DEPARTMENT
JADAVPUR UNIVERSITY
Kolkata-700 032

Ganguly 16/8/2023

Signature of the supervisor

Prof. Saibal Ganguly (Retired)
Consultant
Ex Head and Chairman GRC, BITS Goa
Ex Professor, Chemical Engg., UTP Malaysia
Ex Advisor, DRDO, Ministry of Defense
Ex faculty, Chemical Engg., IIT Kharagpur
Email: gangulysaibal2011@gmail.com

To the Divinity

Acknowledgement

I thank God Almighty for all the blessings.

I am highly obliged and grateful to my Research Supervisor **Prof. Kajari Kargupta** and Co-Supervisor **Prof. Saibal Ganguly** for their excellent guidance, endless encouragement and cooperation extended to me, right from the time of onset of this task till its successful completion.

I am very grateful to **Prof. Rajat Chakraborty**, Head of the Department, Chemical Engineering Department for all the necessary help I got during my research work.

I am also indebted to **Jadavpur University, particularly, Dept. of Chemical Engineering** for supporting me and giving me the opportunity to use the equipments and the utilities to do my research.

I would like to convey my sincere gratitude to **Mr. Sayantanu Mandal, Mr. Arindam Mandal, Ms. Swagata Das,** without whose tremendous support and effort, I wouldn't be able to forge ahead to perform my research work. I am thankful to my seniors **Late Ms. Shubhanwita Saha, Ms. Priyanka Ghosh**, **Ms. Suparna Saha** and **Mrs. Paramita Das** who have taught me various aspects of technical research and have guided me. I would like to thank **Mr. Anirban Mukherjee** for his endless support, during my research work. My sincere appreciation also extends to **Mr. Sourav Chaule, Mr. Milan Kumar Mandal, Mr. Raushan Kumar, Mr. Suman Das,** the post graduate research students, who have worked in this laboratory and have advanced the course of the research work, which has been immensely helpful. I am thankful to all the undergraduate research students, especially **Ms. Rashmi Ghosh, Mr. Anjik Chowdhury, Mr. Debargha Chakraborty, Mr. Digonto Chakraborty, Mr. Sneham Das, Mr. Sourav Karmakar, Ms. Pratyusha Mukherjee**, who have played key roles in advancing the research work. My heartfelt gratitude extends to all the M.E. students, **Chandan Da, Palash Da, Aditi, Vivekananda da, Annesha, Chinmoy, Sarthak, Biswajit, Annesha, Divya, Sourodip, Tithi, Ayantan, Pawan, Arijit** and B.E. students, especially **Sayani, Pritam, Lyangom** who have been a part of this lab. I would like to thank my M.E. Batchmates from the lab: **Amrita, Ananta, Biswajit Da, Vaswar, Debasis Da, Subhadip, Sumalya** for always encouraging me.

I would also like to extend my thanks to **Mr. Ajay Kumar Prodhan (Ajay Da)** who has been a pivotal part of my research work and has helped me all throughout my work.

I am thankful to **Mr. Soumyajit Maitra,** undergraduate research student, Chemical Engineering Department, Rajabazar Science College, Calcutta University, Kolkata, West Bengal, India for his constant support and valuable inputs. I also thank **Mr. Prasenjit Chakraborty,** Department of Physics, I.I.E.S.T, Shibpur, Howrah, West Bengal, India for his kind cooperation.

I am thankful to **Mr. Argha Dey** and **Mr. Atanu Kumar Paul,** who have supported me thoroughly, throughout these years.

I would like to express gratitude to all my fellow researchers working at the Department, especially **Ms. Aishwarya Das, Mr. Sourav Barman, Mr. Saswata Chakraborty, Ms. Sumona Das, Ms. Poulami Karan and Mr. Kaustav Nath** for lending their support, whenever needed. I would like to thank all the research scholars, my seniors, and my juniors for their immense support.

I sincerely thank **Ms. Moumita Sharma, Ms. Dolanchapa Sikdar, Ms. Antara Ganguli, and Mr. Shiladitya Ghosh** for their invariable support.

My sincere gratitude is forwarded to **Ms. G Sneha Raju** and **Mr. Biswarup Mondal** for their invaluable inputs.

I am thankful to **Shweta, Tirtha, Gitanjali, Purushottam** and **Sathomoy** for their supportive stance.

I want to thank my fellow researchers, **Mr. Pratik Das** and **Mr. Anadi Biswas** for their positive inputs.

Sayantani, Sumana, Supriya, thank you for your patience, right from school and **Naireeta, Anushree,** from college. **Saheli** and **Abhishek**, thank you for your advices.

I express joy in thanking **Diya** and **Samrat** for their constant dose of encouragement.

I extend my thanks to **Dipankar, Rinki, Soumya** and **Ratna** for their enthusiasm in supporting me.

My deepest gratitude is forwarded to **Ms. Anindita Shil, Ms. Ayantika Sarkar, Mr. Arijit Sarkar, Ms. Puja Das, Mr. Amrik Sarkar, Mr. Biplab Dey, Mr. Tanmoy Dey, Mrs. Puspali Sen, Mrs. Papri Biswas, Mr. Partha Guha Neogi** and **Mr. Amit Guha Neogi.**

My heartfelt respect and gratitude is given to my source of inspiration my Pishi, **Late Ms. Arati Sarkar**. My deepest respect to my Boro Jethu **Late Mr. Bholanath Sarkar**, my maternal grandparents **Late Mr. Pijush Kanti Dey** and **Late Mrs. Tripti Rani Dey**, my paternal grandparents **Late Shri Annada Charan Sarkar** and **Late Smt. Sati Rani Sarkar**, without whose blessings I wouldn't be able to carry on the research work.

Thanks to all of you, those whom I have named and whom I couldn't, due to lack of space, for helping, guiding and supporting me.

I am grateful to my parents, my Maa, **Mrs. Sukla Sarkar** and Bapi, **Mr. Anil Kumar Sarkar** and all of my family members, who have encouraged and supported me all through and helped me in all respect.

Arundhati Sarkar
16.06.2023

Arundhati Sarkar

There is a crack in everything, that's how the light goes in.

-Leonard Cohen

Preface

The present thesis, entitled "Synthesis, Characterization and Performance Analysis of Reduced Graphene Oxide Based Photocatalyst for Hydrogen Generation from Water'' deals with efficient solar green hydrogen generation from photocatalytic water splitting using reduced Graphene Oxide (rGO) and transition metal-based powder like photocatalyst and organic alginate hydrogel encapsulated three-dimensional spherical bead like photocatalyst. The major barriers in the process of photocatalytic water splitting towards its commercialization are slow reaction kinetics, rapid recombination of photogenerated electrons and holes, low yield of hydrogen, photo-corrosion of semi-conductors, metal aggregation, and metal loss, low water retention capacity of the photocatalysts. In order to address these challenges different strategies are adopted here to (a) Use of reduced graphene oxide rGO as an excellent electron transporter with a work function 4.42 eV, and an electron mobility of 200000 cm ^{2} $V^{-1}s^{-1}$) along with transition metal (having half- filled d orbital) based nanohybrid photo-catalyst namely rGO-CdS, rGO-ZnO (b) exploration of rGO- ZnO(1:3)-WO_3 Type II heterojunction (c) exploration of Z scheme photo-catalytic system CdS-rGO-WO_3 comprising of hydrogen evolution photocatalyst CdS (HEP) and oxygen evolution photocatalyst WO_3 (OEP), having solid state mediator (rGO) involving two step photoexcitation. These strategies allow tuning of the band gap for better absorptivity in visible spectrum, lowering of recombination of photogenerated electron-hole pairs, utilization of higher redox potential (in Z scheme), minimize photo-corrosion, the aggregation of photocatalyst and enhance the photocatalytic activity and apparent quantum efficiency of the synthesized powder like nano-hybrid photocatalyst with respect to pristine photocatalyst. Incorporation of rGO enhances the activity (mmol g^{-1} h^{-1}) of pristine ZnO from 2.5 to 10.4 (at an optimized ratio of 1:3)) and of pristine CdS from 4.9 to 6.9. Incorporation of WO_3 with rGO- ZnO(1:3) formation of heterojunction further enhances the activity to 13.2 mmol g^{-1} h^{-1} and utilization of Z scheme further improve the activity of CdS-rGO-WO_3 to 11.6 mmol g^{-1} h^{-1}. Further to enhance the water retention capacity and hydrophilicity of the photo-catalysts, a new strategy of encapsulation of powder photocatalyst inside the nano-cage of organic alginate hydrogel (resulting in 3D spherical bead like catalysts) is adopted. Alginate engulfed CdS-rGO-WO_3 and rGO-ZnO(1:3)-WO_3, synthesized successfully are hydrated (pre-adsorbed with water) for 6 hours before using for hydrogen generation while dynamic adsorption of water continues. The encapsulation allows higher retention capacity of water, enhanced adsorption (physical/chemical) of confined-water (instead of bulk water) improves the hydrophilicity of the core photocatalyst; hydrated

materials stabilizes the photo-induced holes and electron and slower down the process of recombination and remarkably enhances the photocatalytic activity (up to 81.8 mmol g^{-1} h^{-1} (CdS-rGO-WO_3-alginate) and 90.6 mmol g^{-1} h^{-1} (ZnO-rGO-WO_3-alginate)) as well as apparent quantum efficiency. Further, inlet flow rate invariant sustainable continuous hydrogen generation is achieved using encapsulated bead like photocatalyst which implies that each bead of photocatalyst acts as a miniaturized photoreactor. The metal organic frame work used eliminates the toxicity of the pristine powder like photocatalyst. Therefore, the thesis proposes environ friendly, recyclable, low cost (based on cost analysis), highly efficient alginate encapsulated rGO based heterojunction photocatalyst for enhanced continuous hydrogen generation which can be further utilized for commercialization of photocatalytic water splitting.

List of Abbreviations

GO	Graphene oxide
VB	Valence Band
CB	Conduction Band
VB	Valence Band
PEC	Photo Electro Catalytic
WE	Working Electrode
CE	Counter Electrode
RE	Reference Electrode
XRD	X-ray diffraction
FTIR	Fourier transform Infrared Spectroscopy
EDX	Energy Dispersive X-Ray analysis
SEM	Scanning electron microscopy
FESEM	Field emission scanning electron microscopy
TEM	Transmission electron microscopy

CONTENTS

Page Number

Chapter 1

Introduction

Chapter 2

Synthesis, characterization and photocatalytic performance study of rGO-ZnO/WO_3 heterojunction photocatalyst for solar green hydrogen generation

Chapter 3

Synthesis, characterization and photocatalytic performance study of solid-state mediator rGO based CdS-rGO-WO_3 Z scheme photocatalytic system for solar green hydrogen generation

Chapter 4

Organic alginate encapsulated rGO-WO_3 based photocatalyst for continuous solar green hydrogen generation

Chapter 5

Summary and Future Scope

Supporting work: Annexure

Chapter 6

Synthesis, characterization and photocatalytic performance study of rGO-$SnFe_2O_4$ photocatalyst for solar hydrogen generation

Chapter 1

Introduction

Highlights:

- Introduction
- Preface of Hydrogen Energy
- Photocatalytic water splitting: Present state of the Art
- Two-step photoexcitation: Z scheme photocatalytic systems
- Preface of Graphene: Role of Graphene in Photocatalytic water splitting
- Immobilized photocatalytic system: Hydrogel encapsulated photocatalyst into three-dimensional (3D) network microstructures
- Process Bottlenecks of photocatalytic water splitting
- Research Aims and Objectives
- Overview of the Thesis
- Choice of material
- Methodology
- Brief description of research work

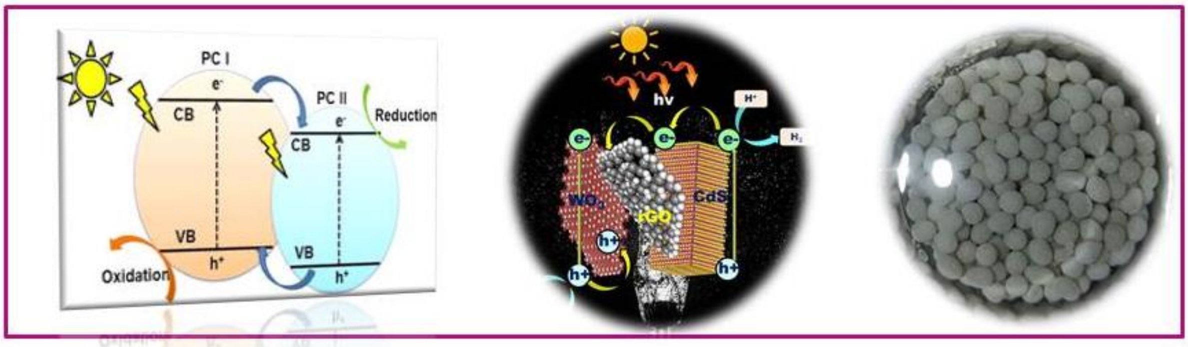

Introduction

The dawn of human civilization begun with the invention of fire, when sparks flew from two stones rubbed together, by the ancestors of human kind. Energy is needed for the sustenance of human beings on the Earth. It is one of the prime components in determining the economic growth of a nation [1]. Fossil fuels like coal, oil and natural gas are traditional energy sources. Energy generated by the combustion of fossil fuels, is utilized for the generation of electricity, as sources of heat and energy in power plants, in industries and in transportation [2].

Fossil fuel reserves are being gradually depleted by the overconsumption of the natural resources. The pace of consumption of energy became more rapid during the last five decades, as the global population increased from 3.7 billion to 7.2 billion, with a rise in the global energy consumption to 548 exajoules (EJ) [3]. The issue of global energy security is significant in this context as the geopolitical dynamics of the nations also shifts along with the climate change and the exhaustion of fossil fuel reserves. Majority of the oil and gas reserves are owned by nations torn by conflicts and political turmoil [4]. So the necessity to be freed from foreign energy sources for the reason of energy security is quite understandable. Moreover, the combustion of fossil fuels causes emission of greenhouse gases that has resulted in global warming. A long term effect of the rise in temperature due to global warming is a slow change in climate and weather, causing gradual melting of glaciers in the polar regions and rise in the global sea water level, posing a threat to nature. The nations took a pledge by signing the historic Paris climate agreement at the 21st Conference of Parties (COP21) of the United Nations Framework Convention on Climate Change (UNFCCC) to keep the temperature rise under check, ideally by 1.5°C [5]. China and the United States are the largest emitters of greenhouse gases followed by India [6].

The development of alternative forms of fuels is therefore necessary in replacing traditional fuels to address the current distressing situation of the planet. The advent of alternative forms of energy sources like wind energy, solar energy, geothermal energy, tidal energy has been observed in the recent years. China is the frontrunner in generating renewable energy, as reported in the Renewables 2022 Global Status Report [7], contributing to about 43% of the total global energy, followed by USA (42.9 GW) and India(15.4 GW) (**Figure1.1 a)**. There has been a gradual development in the potential of renewable energy generation in India.

According to the Energy Statistics Report-2022 (**Figure 1.1 b**), India, major portions of the renewable energy sector, in terms of possibility of production, is dominated by solar power potential 748.99 GW (50.24%) and wind power potential of 695.50 GW (46.66%) followed by small hydro power potential at 21.13 MW (1.42%) [8].

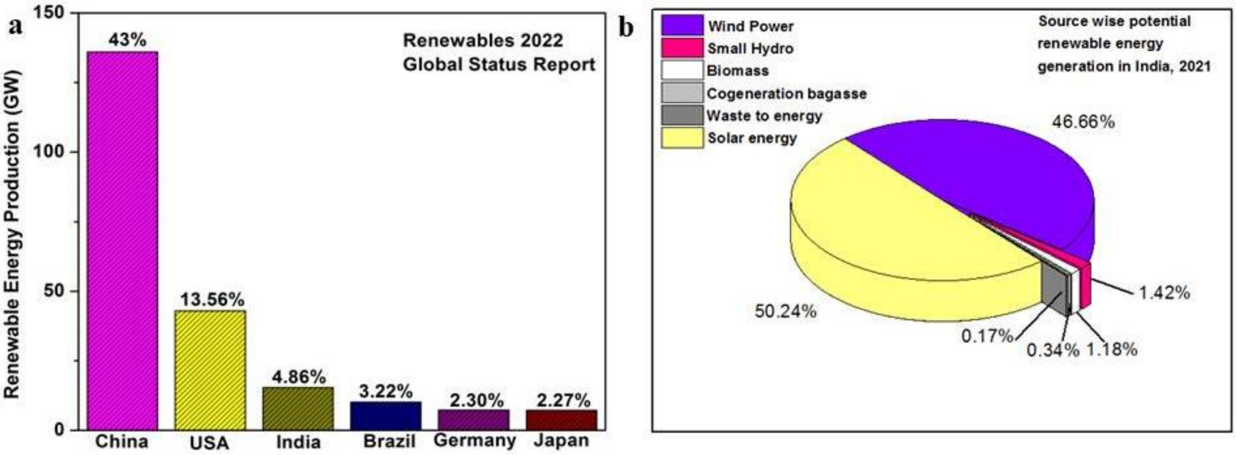

Figure 1.1a) Country wise generation of renewable energy b) Source wise potential renewable energy production in India

1.1 Preface of Hydrogen Energy

Hydrogen Energy: A fuel of the future

Hydrogen is primarily a carrier of energy, rather than a primary source of energy. Hydrogen can be an alternative secondary source of energy in the near future and a hydrogen based economy can be a replacement of the fossil fuel based economy. This is because hydrogen has the largest energy capacity per unit mass [140MJ kg^{-1}] amongst all the other fuels [9].

1.1.1 Advantages of Hydrogen:

i. Hydrogen is a clean fuel because during combustion of hydrogen, only water is produced and there is no emission of greenhouse gases.

ii. Hydrogen can be used as a fuel to be used in fuel cell for production of electricity. This will be beneficial for the development of decentralized electricity distribution (off grid) in remote areas.

iii. Due to the abundance of hydrogen, it is much cheaper compared to other renewable energy sources.

Hydrogen can be derived from clean and renewable sources, however only 5% of commercial hydrogen is obtained in that way. 95% of the hydrogen produced is procured from non-renewable sources like fossil fuels by steam reforming [10]. These processes are costly, releases harmful carbon dioxide, causing pollution in the atmosphere. Hydrogen can be labeled according to the sources and the method of production used [11]:

- **Grey Hydrogen:** When hydrogen is derived from fossil fuel sources like natural gas or coal, then it is labeled as Grey Hydrogen. Presently, hydrogen is produced commercially from fossil fuel sources either by steam methane reforming or by coal gasification. These processes cause emissions of harmful greenhouse gases like Carbon dioxide (CO_2).

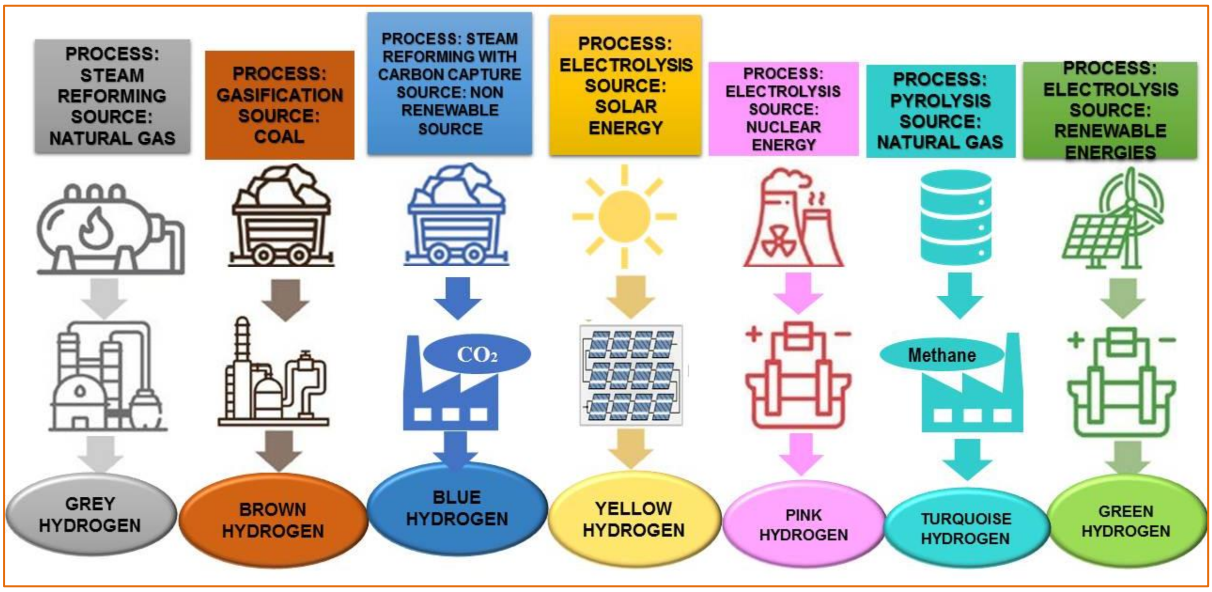

Figure 1.2 Classification of hydrogen according to the sources and pathways of production

- **Brown Hydrogen:** Lignite coal or brown coal is used to produce hydrogen by coal gasification process. Hydrogen generated by this process is termed as Brown Hydrogen.
- **Blue Hydrogen:** The process of grey hydrogen production and Blue hydrogen production are almost similar. When major portion of the CO_2 emission is sequestered during production of hydrogen, by carbon capture and storage (CCS), then thus obtained hydrogen is coined as Blue hydrogen [12]. Hydrogen derived this way is also known as “low carbon” hydrogen.

- **Yellow Hydrogen:** Hydrogen generated by electrolysis of water using solar energy. The source of the electricity utilized for electrolysis is from renewable energy like solar energy.
- **Pink Hydrogen:** The hydrogen produced by electrolysis utilizing nuclear energy, is referred to as Pink hydrogen. There is no emission of CO_2 during this process of production and can be denoted as a sub-category of Green Hydrogen.
- **Turquise Hydrogen:** The hydrogen produced by the methane pyrolysis reaction, is referred to as Turquoise Hydrogen. There is no emission of harmful CO2 during the process of production.
- **Green Hydrogen:** When hydrogen is produced from clean energy sources like wind energy or solar energy, then it is termed as Green hydrogen. Green hydrogen can also be termed as “zero-emission” hydrogen as it is obtained from renewable sources like wind and sun and there is no release of greenhouse gases, during the process of synthesis. For this reason, the process of Green energy generation is considered environment friendly when compared to Grey hydrogen generation process. There are different ways to generate Green hydrogen, the most popular amongst those is the electrolysis of water into hydrogen and oxygen.

1.1.2. Advantages of Green Hydrogen:

1. Green hydrogen is created using renewable energy sources: Green hydrogen is created when surplus electricity generated by renewable energy sources is transformed into hydrogen at power-to-gas facilities. It is a portable clean energy source.
2. Green hydrogen stabilises the supply of heat and energy. Hydrogen that is created from renewable sources may be easily transformed into heat or electricity and used for home energy production and electricity supply. By doing this, it guarantees that renewable energy is consistently accessible in appropriate amounts in the case of power variations caused by the weather.
3. Green hydrogen is adaptable and may be creatively employed. The most abundant element on Earth, hydrogen provides a lot of opportunity for innovation. It may produce energy and heat, act as a fuel or coolant and be utilised as a raw material in manufacturing. Fuel-cell systems are already being utilised effectively today, and electrolysis technologies are already on the rise.

4. CO_2 emissions are reduced via green hydrogen. Carbon dioxide from the traditional production process leaks into the atmosphere, harming the environment. However, water is electrolyzed into hydrogen and oxygen in the power-to-gas process. The by-product oxygen can either be put to other uses or simply discharged into the environment while the hydrogen is still being used.

Additionally, as of 2019, India was releasing a net 2.9 gigatons of carbon dioxide equivalent annually [6]. Industries like automobile, aviation, power, steel, cement, and agriculture, are responsible for the major part of the emissions. Most of these industries would benefit from a shift towards carbon reduction.

1.1.3. Latest developments in green hydrogen

The realm of green hydrogen has a lot of news. In several nations, such the US, Russia, China, Germany, and France, the use of hydrogen as a fuel is now commonplace, and other countries are advancing their research even farther [13].

Hydrogen's adaptability makes it perfect for some industries that present difficulties in the decarbonization process, such as heavy manufacturing, aviation, and marine transport. While it will probably take many decades before hydrogen is used as a fuel for passenger aircraft, a number of initiatives have been started in recent years, especially inside the EU.

Although this requires the pipes to be modified, research is still being done on using natural gas pipelines to carry hydrogen. In France, 100 households' gas grids already included hydrogen as part of a test programme. As a backup during periods of high demand, it is also feasible to convert natural gas power plants to burn hydrogen. Research into the potential for manufacturing green hydrogen through the electrolysis of saltwater in order to prevent future depletion of the planet's freshwater resources is one fascinating area of study.

Many carbon-intensive and hard-to-abate sectors are going to be benefitted from the adoption of green hydrogen in India. However, others sectors will be benefitted by this decision. Hydrogen is widely used in India's industrial activities, including those in the energy, petrochemical, and chemical industries. The whole amount of hydrogen used originates from fossil fuels. With the expansion of the Indian economy, the present use of hydrogen (> 6 million tonnes annually) is anticipated to rise even higher [14]. However, it is anticipated that by 2050, about 80% of the hydrogen generated in India would be "green," created using electrolysis and renewable energy [13,14].

An attempt to lower prices and tightening policy to encourage hydrogen is what is driving the huge cost decreases in major production technologies like electrolyzers and solar PV, which are also partially driven by their widespread deployment in India and throughout the world. Green hydrogen becomes economically viable in India earlier than in other areas of the world due to a lack of indigenous natural gas supply and the prohibitive cost of imports.

The principal industries that stand to gain from the implementation of green hydrogen technology are listed below:

1. Transportation: India’s carbon emissions are mostly the result of the transportation industry. By powering hydrogen fuel cell cars or combining it with natural gas for better combustion, green hydrogen can play a significant part in the decarbonization of transportation. Various areas of mobility, heavy-duty vehicles, public transportation, and long-distance logistics might all gain from the use of green hydrogen as an alternative fuel.

2. Power Generation: Green hydrogen is a clean fuel that may be used in the production of electricity. Fuel cells may use hydrogen to generate power with no greenhouse gas emissions. Hydrogen is a dependable and sustainable energy source, and its use in power generation can assist lower carbon emissions from the electrical industry.

3. Industrial Processes: Industries like steel, chemicals, and refining may use green hydrogen in their manufacturing processes to their advantage. In industrial operations, hydrogen may be utilised as a fuel or feedstock to replace fossil fuels and cut carbon emissions. Industrial processes that use green hydrogen can be more sustainable and cleaner.

4. Energy Storage: In order to combat the erratic nature of renewable energy sources, green hydrogen may be used as energy storage. Electrolysis may produce hydrogen from surplus renewable energy, which can stored and used later. When the production of renewable energy is low, this stored hydrogen may be utilised as fuel or converted back into electricity, ensuring grid stability.

5. Heating and Cooling: Green hydrogen may be utilised in industrial, commercial, and residential settings for heating and cooling purposes. It can contribute to the decarbonization of the heating and cooling industry by taking the place of fossil fuel-based heating systems like natural gas boilers.

It is significant to highlight that depending on elements like infrastructure needs, cost effectiveness, and technology maturity, the viability and potential of green hydrogen adoption may differ across industries. Green hydrogen may be effectively used in the aforementioned industries to cut carbon emissions and move India towards a sustainable energy future.

Today, a number of technical advancements are combining to make it possible for hydrogen to successfully enter the energy grid. These include comprehensive decarbonization of energy systems, supply-side innovation in production technologies (electrolyzers and renewables), handling of excess renewable power, long-term electricity storage, and demand in end-use industries. With regard to the deployment of hydrogen in the energy networks of numerous important economies, these elements are starting to create a challenging loop. India may participate in this developing vital circle since hydrogen may be a key component of a low-emissions, economically viable, and less import-dependent Indian energy industry.

India has the potential to develop into one of the world's top centres for hydrogen production in the next decades, able to both meet its own needs and those of other nations. Petrochemical and chemical companies will undoubtedly top the list of domestic hydrogen consumers. Along with them, it is anticipated that a sizeable portion of the hydrogen will also be used by the steel (in their mandate to decarbonize steel production) and energy sectors. Goal has already been set by India in achieving Net Zero by 2070 and energy independence by 2047 [14]. The transition in the energy sector in India is focused on maximising the usage of renewable energy across all economic sectors in order to meet this goal. A potential substitute for facilitating this shift is green hydrogen.

1.1.4. Different pathways of production of Hydrogen

I) Steam Reforming: At present, **Grey Hydrogen** is being produced commercially via steam methane reforming reaction (Figure 1.3), mainly because of the high energy conversion efficiency. Steam reforming of oil involves breakdown of molecular bonds in oil by passing steam at a high temperature to produce hydrogen and carbon monoxide, the partial oxidation of waste oil on the other hand is the controlled combustion of the fuel-air mixture to produce hydrogen (H_2) and carbon monoxide (CO). The water gas shift reaction further converts carbon monoxide upon reacting with water/steam to generate more hydrogen [Eq. 1.2]. This reaction is endothermic in nature and takes place at a temperature of 700°C-900°C, using nickel supported alumina as a catalyst. This process emits carbon dioxide, which is a harmful greenhouse gas and is a threat to the nature.

$CH_4 + H_2O$ (+ heat) $\rightarrow CO + 3H_2$ $\Delta H = +206.2$ KJ mol^{-1} (1.1)

$CO + H_2O(l) \rightarrow CO_2(g) + 3H_2(g)$ $\Delta H = -41.2$ KJ mol^{-1} (1.2)

$CH_4 + 2H_2O \rightarrow 4H_2(g) + CO_2(g)$ $\Delta H = +165$ KJ mol^{-1} (1.3)

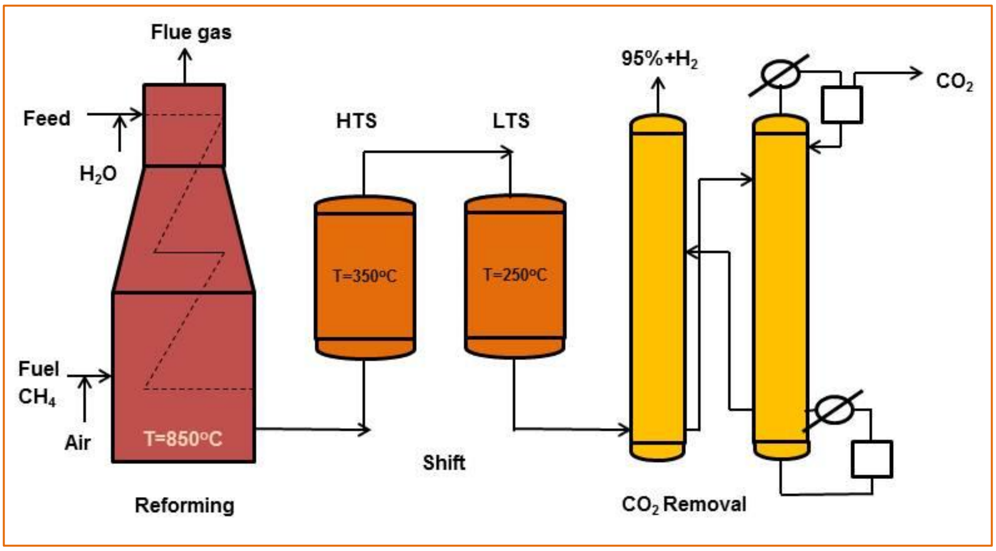

Figure 1.3. Production of hydrogen by steam methane reforming

II) Gasification of Coal: Coal is non-renewable source from which hydrogen can be obtained. **Brown Hydrogen** can be produced mainly by coal gasification and partial oxidation of coal. Coal is a rich source of carbon and coal gasification involves the breakdown of bonds in coal producing hydrogen and carbon-monoxide in presence of steam. Partial oxidation involves the controlled combustion of fuel-air mixture which produces hydrogen and carbon monoxide. This carbon monoxide is converter to carbon dioxide and more hydrogen by water gas shift reaction. The reaction may be as below:

$C_nH_m + {}^{n}/_{2}\, O_2 \rightarrow n\, CO + {}^{m}/_{2}\, H_2$ (1.4)

(where m ~ number atoms of hydrogen and n~ atoms of carbon)

III) Pyrolysis of Methane: Turquoise Hydrogen can be produced from Methane. The thermal decomposition of methane by pyrolysis of Methane involves into hydrogen and carbon, is known as pyrolysis of methane. The energy input in this process is very high, as the reaction is endothermic and the efficiency is low. This process can be labelled as low-emission hydrogen generation process. The equation may be as below:

$CH_4 \rightarrow C + 2\, H_2$ (1.5)

Till now hydrogen production via conventional processes have been discussed, where the evolved CO_2 gas, generated during combustion of the fuels, is being released in the atmosphere. The emission of the CO_2 gas can be either be checked and controlled, like in the case of Turquoise Hydrogen production, which is coined as a low emission process, or the CO_2 can be sequestered and captured, as in the case of **Blue Hydrogen** production. Green Hydrogen generation, on the other hand involves the production of hydrogen from renewable sources, without the emission of green house gases. As discussed earlier, **Yellow Hydrogen** and **Pink Hydrogen** can be categorized as a sub type of Green Hydrogen generation.

IV) Electrolysis of water utilizing nuclear energy: Pink Hydrogen can be obtained by electrolysis of water, utilizing the nuclear power source.

V) Electrolysis of water utilizing solar energy: Yellow hydrogen can be procured splitting water into hydrogen and oxygen, by electrolysis of water, utilizing the solar energy.

VI) Electrolysis of water: The most well known pathway of **Green Hydrogen** generation is by electrolysis of water using source of electricity as the driving force. It is the most popular route of green hydrogen generation. However the amount of energy required for the water splitting reaction is more than that energy obtained by producing hydrogen making the process energy inefficient. PEM (polymer electrolyte membrane cells) SOEC (Solid Oxide Electrolysis Cells) and AEC (Alkaline Electrolysis Cell Electrolysers) can be used to generate hydrogen by splitting water.

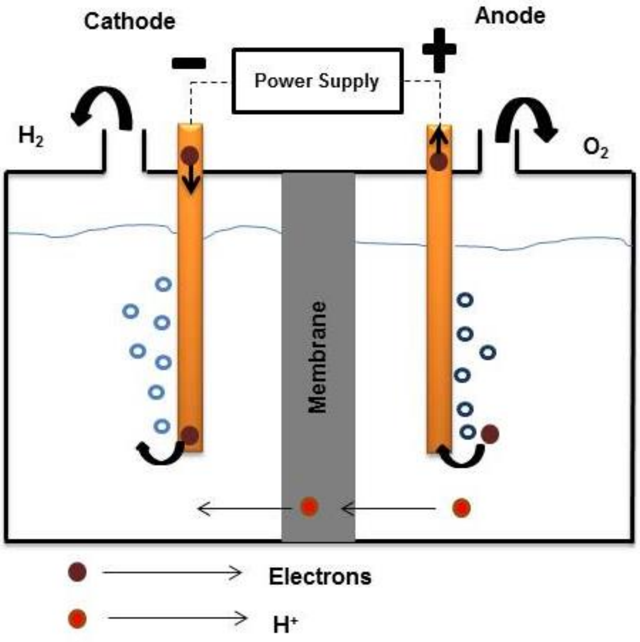

Figure 1.4 Hydrogen generation by electrolysis of water

By lowering the quantity of electrical energy needed for electrolysis, the overall cost of hydrogen production can be reduced. PEM electrolysis cells operate below 100°C, however AECs operate at 200°C. Microbial electrolysis cells can also be used for this purpose. About 4% of the global hydrogen is produced by the electrolysis of water [15].

Cathode: $2H_2O+2e^- \rightarrow H_2 + 2OH^-$ (1.6)

Anode: $4OH^- \rightarrow O_2+2H_2O+4e^-$ (1.7)

Overall: $2H_2O \rightarrow 2H_2+O_2$ (1.8)

In the following sections, few more generative pathways for emission less Green Hydrogen have been discussed:

VII) Thermochemical method: Thermochemical method involves the splitting water into hydrogen and oxygen by using high temperature heat, unlike electricity, in case of electrolysis of water. Much of the heat is lost as waste heat in the process plants. Solar energy can also be harnessed using tower concentrators, to produce high energy, thereby utilizing the energy for hydrogen production. Thermochemical method of energy conversion is mainly carried out by means of steam gasification, supercritical water gasification, and rapid pyrolysis followed by steam reforming of bio-oil. The cost of operation is high in this process of H_2 production. Techniques like combined slow pyrolysis and steam gasification can also be devised for hydrogen generation at cheaper rates and higher efficiency [16].

VIII) Hydrolysis of chemical hydrides: Hydrolysis of chemical hydrides like Sodium Borohydride can be a solution in generating hydrogen and for the storage of onboard hydrogen. The equation involving the hydrolysis of Sodium Borohydride is as follows:

$NaBH_4+2H_2O \rightarrow NaBO_2+4H_2O$ ΔH=-75 KJ/mol H_2 (1.9)

The reaction is highly exothermic, generating a lot of heat. This process of hydrolysis of chemical hydrides has been utilized to produce hydrogen for use in fuel cell. However, the byproducts generated in the process are toxic in nature, which can diminish the performance of fuel cell. [17].

IX) Biomass reforming: Hydrogen can be obtained by gasification of biomass and wastes. The gasification of biomass is an environmentally friendly and efficient process. The gasifying agents can be of different types: air, steam, air-steam, steam-oxygen etc., depending upon which the processes can further be classified [18]. The major drawback of this process is the low yield of hydrogen.

X) Biological hydrogen production: In case of biological hydrogen generation, hydrogen is being generated using hydrogen-production enzymes. Though hydrogen is released in trace amount, presently researches are being conducted to make this process commercially viable [19].

XI) Photo-induced hydrogen generation: Photo-induced production of hydrogen can be classified in four major processes viz. photobiological method, photovoltaic method, photoelectrochemical method (PEC), photocatalytic method. Photobiological method involves the production of hydrogen using microorganisms such as algae [20]. Primarily, algae are grown photosynthetically in ambient condition, and then cultured in anaerobic conditions for hydrogen production. Renewable hydrogen could be prepared using solar electric energy from photovoltaic modules coupled with electrolyzer without emitting carbon dioxide. Here the efficiency of solar-to-hydrogen conversion is particularly important ause lesser conversion efficiency indicates larger area requirement for capturing solar energy which impacts the overall cost of the system. In this case two schemes, namely, integrated PV-electrolysis system and stand-alone PV-electrolysis system could be used for solar hydrogen generation [21]. PEC devices use photoelectrode formed of photocatalyst to split water utilizing external voltage [Figure 1.5] [22], whereas photocatalysis process includes the involvement of semiconductor materials and light irradiation. In 1972, Honda and Fujishima first provided evidence that hydrogen can be procured by splitting of water, when hydrogen evolved in a photoelectrochemical (PEC) cell using a TiO_2 electrode along with a Pt counter electrode [24]. Allen Bard then observed the same principle during hydrogen evolution in a particulate system [25].

The reactions for PEC water splitting are:

At photocathode: $2H_2+2e^-\rightarrow H_2$ (1.10)

At photoanode: $H_2O\rightarrow\frac{1}{2}O_2+2H^++2e^-$ (1.11)

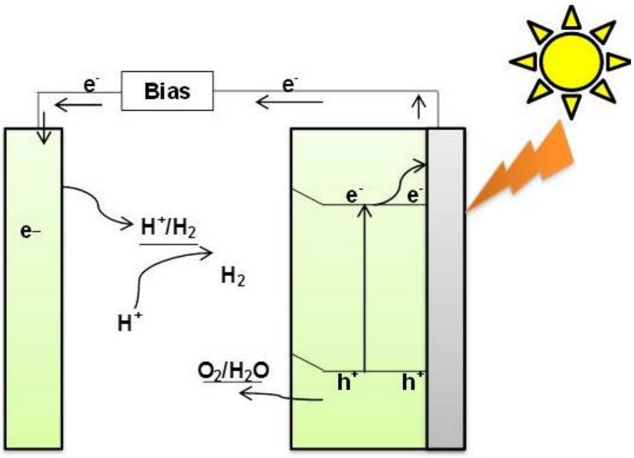

Figure 1.5 Hydrogen generation by photoelectrochemical process

In photocatalytic water splitting, water is being splitted, utilizing source of irradiation like solar energy.

1.2 Photocatalytic water splitting: Present state of the Art

In photocatalytic water splitting, hydrogen is produced in presence of photocatalyst utilizing source of irradiation, by harnessing photons of the light waves by the electrons, which creates a series of reactions [23].

The following are the advantages of Photocatalytic water splitting:

a. Photocatalytic water splitting produces Green Hydrogen
b. This process of green hydrogen production is cost-effective compared to Electrolysis of water and PEC water splitting. The extra cost due to the application of external bias, as in the case of PEC water splitting is not required.
c. The process is simple: design and synthesis of photocatalyst is relatively simple
d. Water is an abundant natural resource, which can easily be used for photocatalytic water splitting

Therefore, Photocatalytic water splitting seems to be a promising pathway of obtaining hydrogen, considering the environmental friendliness, cost-effectivity. Photocatalytic water splitting is a means of conversion of solar energy to hydrogen when the splitting of water into hydrogen and oxygen takes place utilising a semiconductor catalyst upon irradiation of light.

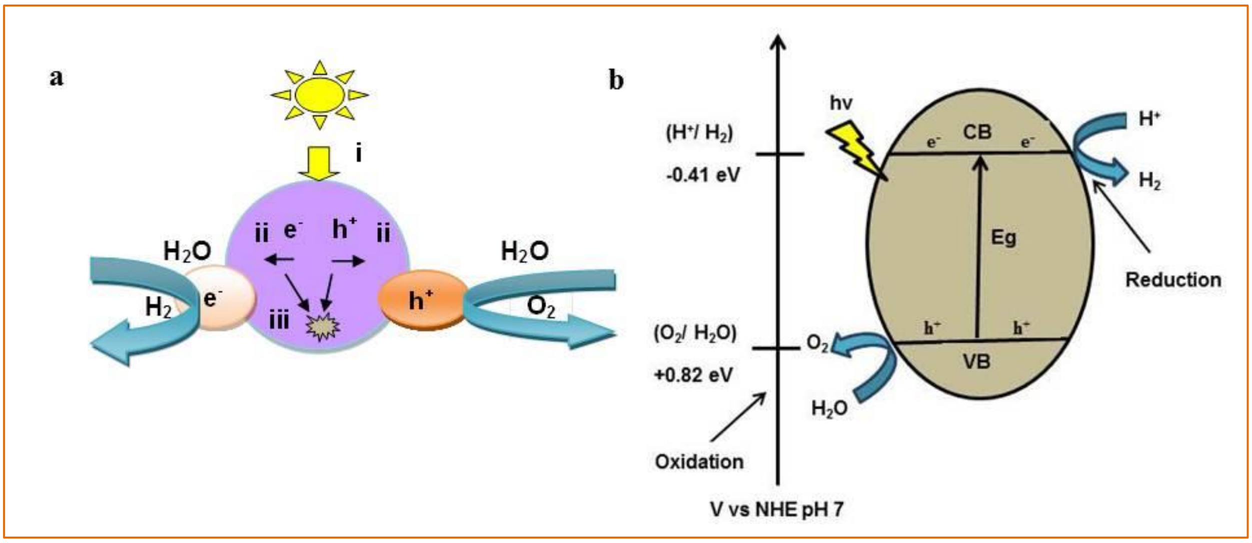

Figure 1.6 a Photocatalytic mechanism of hydrogen and Figure 1.6 b hydrogen generation by photocatalytic splitting of water (V vs NHE pH 7)

The basic mechanism of the process can be explained by three major steps [**Fig 1.6 a**]: [26-28]

i. generation of electrons and holes upon irradiation by absorption of photons

ii. migration of the photogenerated electrons and holes to various sites of the photocatalyst

iii. reduction of water by these photoinduced electrons to produce H_2 on the surface of the photocatalyst

The basic steps of reactions involved are as follows:

$$H_2O + 2h^+_{VB} \longrightarrow \frac{1}{2} O_2 + 2H^+ \qquad E^o = 0.82V \qquad (1.12)$$

$$2H^+ + 2e^-_{CB} \longrightarrow H_2 \qquad E^o = -0.41V \qquad (1.13)$$

$$\text{Overall reaction: } H_2O\,(l) \xrightarrow{hv} H_2\,(g) + \frac{1}{2} O\,(g) \qquad \Delta G = +237.2 \text{ kJ/mol} \qquad (1.14)$$

$$\text{Bandgap} = (hc/\lambda) = 1240/\lambda(\text{nm}) \qquad (1.15)$$

where λ is the wavelength of light, h is the Planck's constant, and c is the velocity of light, h^+ and e^- refers to energized holes and electrons, respectively. The standard Gibbs free energy for the splitting of water to hydrogen (H_2) and oxygen (O_2) is +237.2 kJ/mol which equates to 1.23 eV per electron transferred (**Eq. 1.14**) [26-28]. This means the reaction is thermodynamically a non-spontaneous reaction. The wavelength of the irradiated light should be greater than or equal to the bandgap of the semiconductor for the initiation of the process.

The band edge position should be able to generate hole-electron pairs upon irradiation. This is possible when the bottom of the conduction band is more negative than the redox potential of H^+/H_2 [0 V vs NHE (normal hydrogen electrode), pH = 0], while the top of the valence band should be more positive than the redox potential of O_2/H_2O (1.23 V). However the recombination of the photogenerated electron and holes may lead to decreased efficiency of the process producing water. The presence of adequate reactive sites for hydrogen generation centres is an important factor for a photocatalyst. For this reason cocatalysts are developed. Cocatalysts are used as sites for reaction, thereby catalyzing reactions and aiding in the separation of the charges [29]. Several sacrificial agents (electron donors/acceptors) are used to minimize the recombination rate of electron hole pairs, increasing the efficiency of the process [30].

1.2.1. Heterogeneous photocatalysis

Heterogeneous photocatalysis can be defined as the photoreaction in presence of a photocatalyst; usually particulate photocatalysts are suspended in photocatalytic reactors. Heterogeneous photocatalytic reactions are usually performed in a slurry-type reactor where the catalyst particles are suspended in the water [31].

Heterogeneous photocatalytic process involves five steps of reaction [**Figure 1.7**]: (i) the first step is the step of diffusion of reactants towards the surface of the photocatalyst, (ii) the second step is the adsorption of reactants on the surface of photocatalyst, (iii) the subsequent reaction step takes place on the surface of the photocatalyst (iv) the fourth step is the desorption of the reacted substances or products from the surface of the photocatalyst and (v) finally the diffusion of products occurs from the surface of the photocatalyst [32].

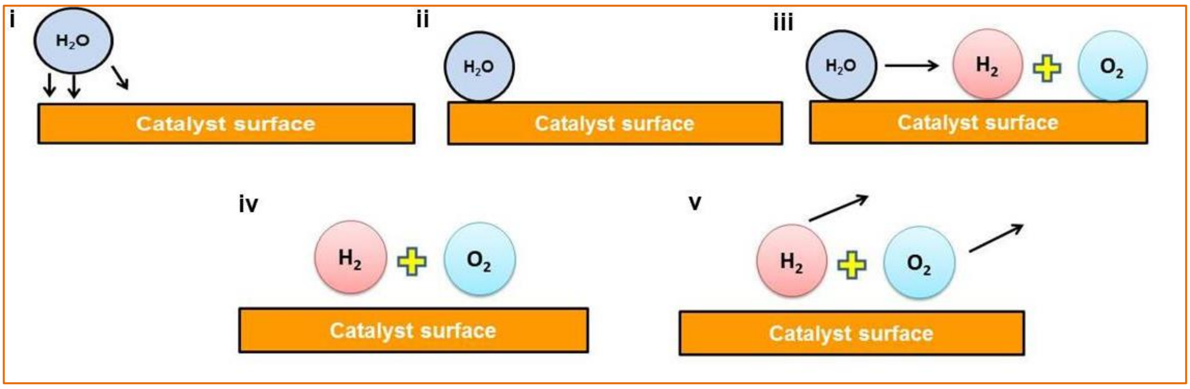

Figure 1.7 Steps of heterogeneous photocatalysis

Photocatalytic water splitting involves adsorption, surface reaction and desorption.

The herat of the overall process is the photocatalytic reaction. The water splitting reaction is an uphill reaction, following slow kinetics, hence adsorption and high retention time of water molecule on active site of photocatalyst is a crucial step for high hydrogen yield.

1.2.2. Semiconductors as photocatalysts for water splitting

As previously mentioned, the band edge (conduction band minimum) should be positioned lower than that of the reduction potential of H^+/H_2. The band gap of a visible-light-driven photocatalyst should be lower than 3.0 eV (λ >415 nm) to harness the visible range [29]. **Table 1.1** below shows the band gap of few semiconductor photocatalysts:

Table 1.1 Valence band (E_{VB}), conduction band (E_{CB}) and band gap (E_g) of semiconductor photocatalysts at pH 1 [33]

Name of semiconductors	E_{VB} (V vs SCE)	E_{CB} (V vs SCE)	E_g
CdSe	1.4	-0.3	1.7
CdS	2.2	-0.2	2.4
$SrTiO_3$	3.0	-0.2	3.2
ZnO	2.9	-0.1	3.0
SnO_2	3.8	-0.3	3.5
TiO_2	3.0	0.0	3.0
CdTe	1.4	0.0	1.4

If the band gap of a photocatalyst is lower than 3.0 eV, then it can termed as narrow band gap semiconductor photocatalyst, whereas if the band gap of a photocatalyst is greater than 3.0 eV, then it can be denoted as wide band gap semiconductor.

i. Wide band gap semiconductors

Wide band gap semiconductors with bandgap higher than 3.0 eV, are usually active in the wavelength, mainly in the ultraviolet region (≤300 nm). This might be due to the reason because the valence bands (VB) of these photocatalysts, comprises of O 2p orbitals with a potential of 3 eV vs. NHE, whereas the conduction bands (CB) are more negative than 0 eV. Oxide photocatalysts consisting of d^0 metal cations such as Titanates, Niobates, Tantalates, Zirconates ($Ti^{4+,}$ $Nb^{5+,}Ta^{5+}$ Zr^{4+}) display the nature of wide band gap semiconductor photocatalyst [29]. Layered titanates, doped titanates have shown considerable hydrogen generation in presence of UV-irradiation. TiO_2 (3.2 eV) is one such fascinating photocatalyst that finds wide application in various fields like decontamination, pollution degradation, hydrogen generation etc. [34 a,b].Yamaguti et al. developed NaOH-coated Rh/TiO_2 and Pd/TiO_2 photocatalyst, which resulted in simultaneous generation hydrogen and oxygen with an activity of 449 $\mu molh^{-1}$ [35]. 1837 $\mu molh^{-1}$ of hydrogen and 850 $\mu molh^{-1}$ of oxygen were produced using $K_4Nb_6O_{17}$ using nanosize Au cocatalyst as dopant [36]. Kato and Kudo developed several alkaline and alkali earth tantalates like $NaTaO_3$, $KTaO_3$, $LiTaO_3$, $MgTa_2O_6$, $BaTa_2O_6$, out of which $BaTa_2O_6$ showed highest photocatalytic activity, whereas 2180 $\mu molh^{-1}$ H_2 was produced using $NaTaO_3$ [37]. The photocatalytic reduction activity for Zirconia based photocatalysts was studied by Sayama et al, where 19.5 $\mu molh^{-1}$ of hydrogen and 10.8 $\mu molh^{-1}$ of oxygen were generated [38].

ii. Narrow band gap semiconductors

Narrow band gap semiconductors exhibit excellent photocatalytic activity in the visible range of the spectrum (380-780 nm). Several sulfides, oxy-sulfides and oxy-nitrides can absorb 600 nm of visible spectrum of light and are labeled as narrow band gap semiconductor photocatalysts [29]. The band gap narrowing might be due to the reason of the position of the valence bands: the valence bands consist of S 3p and of N 2p orbitals, along with O 2p orbitals. These photocatalysts can also be used for photoelectrochemical water splitting. Domen group developed $LaTiO_2N$ photocatalyst which displayed an activity of 30 $\mu molh^{-1}$ H_2 and 41 $\mu molh^{-1}$ O_2 was produced using IrO_2 co-catalyst [29, 39]. Photocatalytic activity of Lanthanum-Indium Oxysulfides were checked by Domen group, displaying 10 $\mu molh^{-1}$of H_2 generated [40]. Metal sulfides like CdS (2.4 eV) is a well-known visible light active photocatalyst. Various research groups designed CdS linked ZnS (3.6eV) based photocatalysts for efficient hydrogen generation by splitting water [41, 42].

1.2.3. Role of transition metals as photocatalysts

As discussed in the previous sections, metal sulphides, metal oxides, metal oxy-sulphides and oxy nitrides exhibit photocatalytic activities. Often the metallic component of the photocatalyst consists of a transition metal ion. Transition metal cations have partially filled d orbitals, as a result variation in the oxidation states can be observed [45]. The photocatalytic activity of the photocatalyst can be tuned by varying parameters like oxidation state, ionic radius, spin states etc. [46]. The bandgap energy is a strong function of the number of oxidized sites and oxidation degree of the material. In transition metals, appearance of t_{2g} and

e_g levels during splitting of d orbital takes place, t_{2g} is at a slightly higher energy level compared to e_g. These e_g and t_{2g} levels in the band gap are advantageous for absorbing visible spectrum of light and in increasing photocatalytic activity [47]. Basically, e_g is a subset of two orbitals i.e d_{z2} and d_{x2-y2} and t_{2g} of three orbitals that is d_{xy}, d_{yz} and d_{zx}. The migration of the photogenerated electrons can take place in two different pathways as shown in Figure 1.8 a and Figure 1.8 b. Upon inclusion of impurity in the form of doping, the electrons in the VB can either migrate to t_{2g} level by absorbing photons and then to CB leaving holes in the VB (**Figure 1.8 a**), or can migrate to e_g by absorbing photons of higher energy and then to CB (**Figure 1.8b**). As a result, an efficient separation of photogenerated electron-hole pairs takes place during transition metal doping

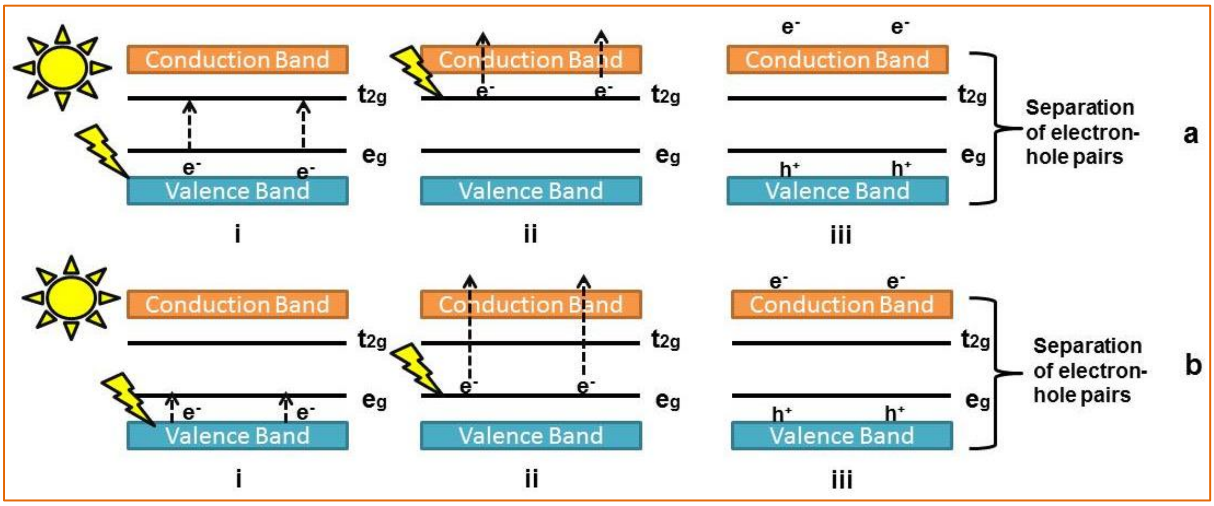

Figure 1.8a Migration of photogenerated electrons from Valence Band (VB) to t_{2g} and then to Conduction Band (CB) Figure 1.8 b Migration of photogenerated electrons from VB to e_g and then to CB

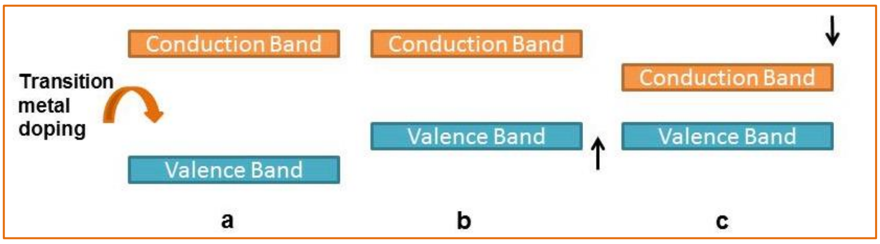

Figure 1.9 a-c Shift of conduction band and valence band by transition metal doping

Transition metal doping into wide band gap photocatalyst is done when a decrease in the band gap is observed as the impurity states is dragged near the Fermi level, making it ideal for electron transfer and photocatalytic reactions. Moreover doping creates excess free electrons, displaying coulombic attraction or repulsion, which contributes in shift of the position of band edges. The hybridization of the s-p and p-d orbitals occurs when the transition metal dopant is added to a photocatalyst, thereby reducing the band gap [48]. Depending upon the atomic number of the dopant, the shift of the valence band in the upward direction and the shift of the conduction band in the downward direction, takes place [**Figure 1.9 a-c**], which lowers the band gap of the photocatalyst.

1.2.4. Heterojunction

Two semiconductor photocatalysts with unequal band gaps can be coupled to develop heterojunction photocatalysts. Apart from doping, loading of metals, designing of heterojunction photocatalyst can be one strategy for the separation of photogenerated electrons and holes, in an attempt to reduce the rate of recombination for efficient photocatalytic water splitting. Due to the difference in band gap, an interface is created between the two semiconductors, causing various types of band alignments. The heterojunctions can be divided according the nature of the band alignment.

1.2.4.1 Different Types of Heterojunctions

Serpone et al. in 1984, [43] for the first time inducted the concept of interparticle electron transfer. Different types of heterojunction photocatalysts have been developed since then. Generally there are three main types of heterojunctions which are as follows [44]:

i. Type-I Heterojunction

Type-I Heterojunction is also known as “Straddling gap” type heterojunction. In the Type-I heterojunction photocatalytic system (vide **Figure 1.10 a**), the conduction band (CB) and the valence band (VB) of Photocatalyst I (PC-I) are higher and lower than that of Photocatalyst-II (PC-II), respectively.Upon irradiation, accumulation of the photogenerated electrons and holes occur at the CB and the VB bands of PC-II, respectively. Due to accumulation of electrons and holes happen on the same semiconductor photocatalyst, the effective separation of electrons and holes is not possible in Type-I heterojunction photocatalyst. Also, the redox reactions occur on the photocatalyst with lower redox potential, reducing the redox ability of heterojunction photocatalytic system.

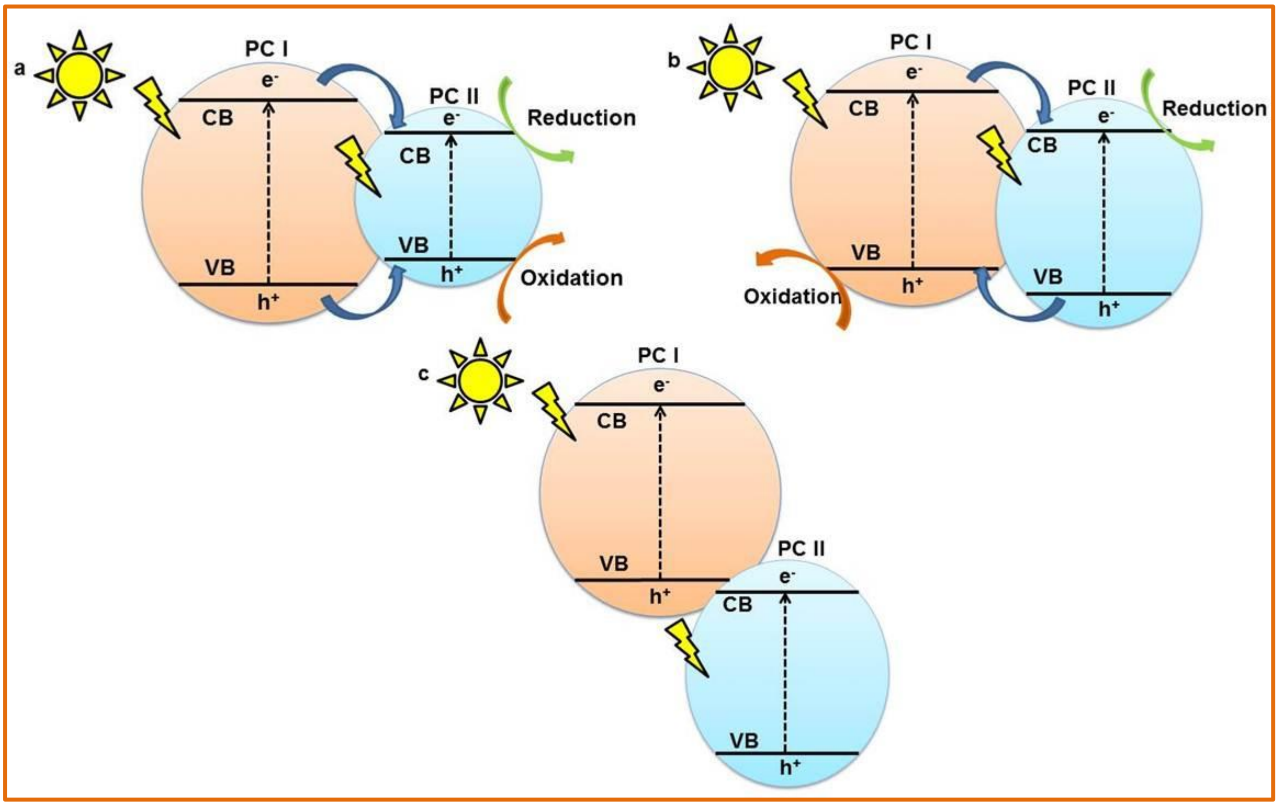

Figure 1.10 a Type I Heterojunction, Figure 1.10 b Type II Heterojunction and Figure 1.10 c Type III Heterojunction

ii. **Type II Heterojunction**

Type II Heterojunction is also known as "Staggered gap" type heterojunction. In Type-II heterojunction photocatalytic system, the CB and the VB bands of PC-I are higher than that of the PC-II. When the system is irradiated, the photogenerated electrons will migrate to PC-II, whereas the photogenerated holes will transfer to PC-I, creating a spatial separation of photogenerated electrons and hole. Effective separation of photogenerated electrons and holes happens in Type-II Heterojunction. However, the redox ability of the type-II heterojunction photocatalytic system will be low, like that of Type-I, because the reduction reaction happens on PC-II with lower reduction potential and the oxidation reaction on PC-I with lower oxidation potential.

iii.Type-III Heterojunction

Type III, is also termed as "Broken gap" type Heterojunction. In Type-III heterojunction photocatalytic system (**Figure 1.10 c**) the bandgap alignment is such that the bandgaps do not overlap at all. As a result, the migration of electron–hole pairs and the subsequent separation between the two photocatalysts does not occur at all in the Type-III heterojunction. Hence efficient separation is not possible in Type-III heterojunction. Therefore, Type-II heterojunction is the most suitable heterojunction, out of all the three systems for enhancing photocatalytic activity due to the efficient separation of photogenerated electron and holes.

1.2.4.2 Importance of Heterojunction Photocatalytic systems

As discussed in previous section 1.2.4.1., development of heterojunction photocatalytic can be a strategy to tackle the problem of rapid the rate of recombination by effective separation of photogenerated electron-hole pairs, for enhanced yield of hydrogen and photocatalytic activity.

Two semiconductor photocatalysts with non-identical band gaps has to be selected for designing heterojunction photocatalysts.

1.3 Two-step photoexcitation: Z scheme photocatalytic systems

Photocatalytic production of hydrogen can be done via two-step photoexcitation using two different types semi-conductor photocatalysts along with a reversible donor/acceptor pair (shuttle redox mediator), thereby formulating a separation of charges, leading to a higher photocatalytic efficiency with a high redox ability [71, 72]. In two component photocatalytic system a hydrogen evolution photocatalyst (HEP) and an oxygen evolution photocatalyst (OEP) are selectively chosen.

Several metal oxides have been used as photocatalysts for single component single step water splitting, but the prime hindrance has been the following:

(1) the band gap should be preferably be lower than 3 eV, for absorption of visible spectrum

(2) suitable position of band-edge for overall water splitting

(3) stability of the photocatalyst and the photocatalytic reaction

1.4 Preface of Graphene: Role of Graphene in Photocatalytic water splitting

Graphene, one of the breakthrough discoveries of the twenty-first century, is actually a uniatomic layer of sp^2 bonded carbon atoms. It is unique for its various remarkable properties including a very large specific surface area (2630 $m^2\ g^{-1}$), exceptional electronic mobility (200,000 $cm^2V^{-1}s^{-1}$) outstanding optical transparency (~97.7 %) and an excellent thermal conductivity (3000-5000 $W\ m^{-1}K^{-1}$) [49-50]. This may be due to the band structure of graphene.

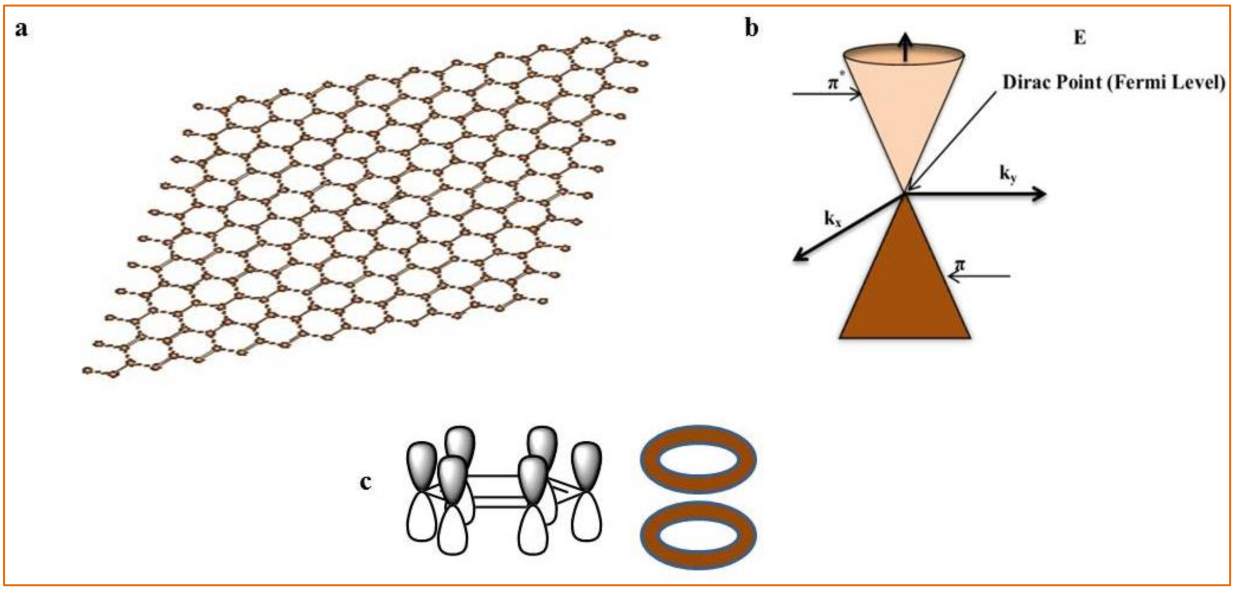

Figure 1.11 a. Graphene sheet and Figure 1.11 b. Band structure of graphene withcones touching at Dirac point, Figure 1.11 c Delocalised orbital cloud of graphene

The bonding π and antibonding π*orbitals in graphene, a zero band-gap semiconductor, touch each other at the Dirac point with the Fermi level between the valence and the conduction bands [51]. Moreover, the Fermi level can be shifted by doping of heteroatoms or electrostatic field tuning [52]. The electronic properties of graphene can be readily tuned via chemical doping with oxygen functionalities that withdraw electrons or nitrogen groups that donate electrons chemical to form p-doped or n-doped semiconductors respectively [26]. Graphene oxide (GO), a derivative of graphene, on the other hand is an insulator due to the disruption of delocalized π conjugation in graphene [53]. Formation of C-O covalent bonds, damage the original orbitals. This oxygen coverage leads to the separation of bonding and anti-bonding orbitals [28]. The valence band maximum (VBM) shifts from the π orbital of graphene to the 2p orbital of oxygen when more oxygen is added, expanding the band gap. Though the (π*) orbital remains as the conduction band minimum (CBM). The electronic and structural properties of graphene can be partially restored by reducing the GO [53]. Reduced GO (rGO) consists of aromatic sp^2 domains with few nanometers in the centre and sp^3-hybridized carbon atoms in the periphery. Hence modifying the degree of reduction helps in changing the bandgap of graphene [54]. So, functionalization of graphene can effectively promote in synthesizing graphene based nanocatalysts. Graphene can therefore be utilised as [55-58]:

i) **Electron sink/electron transporter:** Graphene has a high work function (4.42 eV) and very high conductivity. Thus it can easily accept electrons from the conduction bands of the photocatalyst semiconductors thereby checking the recombination of the photogenerated electrons and holes and increasing the efficiency of the process. Graphene can easily transport electrons through the 2D carbon matrix to the reactive sites for hydrogen generation. Semiconductors having a wide bandgap, such as, ZnS, ZnO, TiO_2 have been combined with graphene for photocatalytic reactions under UV-light and with narrow band gap photocatalysts like CdS absorbing an appreciable fraction of visible light. Graphene acts as an electron acceptor and transporter in such a composite and hence effectively suppress electron-hole recombination leading to higher quantity of hydrogen generation. Moreover, a number of variables have been discovered to impact function of graphene in this regard, including the graphene content of the composite, the interfacial interaction, and the contact area between graphene and the semiconductor. Three main graphene based photocatalyst systems can be fabricated, namely, graphene-semiconductor binary system, graphene-semiconductor trinary system and dye-sensitized graphene based system.

ii) **Cocatalyst:** As the reduction potential of graphene is more negative than the reduction potential of $H^+/_{H2}$ (-0.08eV), it can be used as a cocatalyst to replace most commonly used costly noble metal cocatalyst (Pt).

iii) **Photocatalyst:** Functionalized graphene can be used to absorb solar spectra and can be used for solar water splitting as photocatalyst. The conduction band minimum of rGO is greater than that needed for hydrogen generation. (-0.52 eV vs NHE, pH=0) and the valence band maximum consists of mainly O 2p orbital that can be altered with varying degrees of reduction.

iv) **Photosensitizer:** Graphene can be tuned to be used as a photosensitizer in light driven water splitting reactions. The electrons in the photosensitizer are generated upon absorption of photon energy; these are then accepted in CB of the photocatalysts to produce hydrogen. Thus the research objective is to develop graphene based semiconductor photocatalyst that is able to absorb the visible spectra for the generation of hydrogen from water. The emphasis should be on the fabrication of an economical, efficient, reproducible, reusable photocatalyst.

1.5 Immobilized photocatalytic system: Hydrogel encapsulated photocatalyst into three-dimensional (3D) network microstructures

Photocatalytic water splitting is a heterogeneous reaction and adsorption is a prime step of this process. Adsorption is a rate controlling step. For this reason, the design of the photocatalytic system should be done in a way so that it provides higher retention time for the reactionIn case of powder photocatalyst, as seen in most of the literatures are powdered nanoparticles, which displayed a number of setbacks, including metal aggregation and metal loss during recovery, which greatly diminished the metal loading during catalyst recovery and lowered the catalytic activity [59-60]. The recovery of catalyst nanoparticles from the reactor is a complex process that is essential for safe hydrogen production. Catalyst recycling, which has a strong impact on operating costs, is one of the challenges for photocatalytic systems comprising nanoparticles.Moreover, the majority of these structured powder catalyst systems operate in batch mode and cannot be used to control the rate of hydrogen generation rate. On substrates such as carbons [61], Ni substrate [62-63], polymers [64], metal phosphides [65] and ceramics [66], catalyst nanoparticles are typically immobilised. Recently, immobilisation and encapsulation of active nanoparticle photocatalysts into three-dimensional (3D) network microstructures have gained much interest and intense focus among researchers for photocatalytic applications with separation-free titles [67-68]. Metal-organic frameworks (MOFs) have been proposed to support the nanoparticles of the alloys [61] in order to prevent metal aggregation during the reaction and to increase catalytic activity. The porosity, high surface area and well-defined pore structure, enabled the metal-organic framework to stabilise metal nanoparticles. As catalyst carriers, various bio-based materials, such as wood and rattan, have been used [67-68]. Recently, hydrogel-based materials possessing robust absorption capacities, has evolved as a topic of research, amongst the scientists, because of their expanded three-dimensional network topologies and their hydrophilicity, which encourages chemisorption. along with physisorption of water confined in the channels, and good thermal and mechanical stability have attracted a lot of attention from researchers. Hydrogel is explored as a miniature reactor to enhance the photocatalytic hydrogen generation activity of CdS, ZnS quantum dot photo catalysts [69]. CdS embedded in cationic hydrogel is reported [70] to enhance photocatalytic hydrogen generation. The water adsorption capacity of the photocatalyst demonstrates the difficulty of stronger adsorption inhibiting the subsequent desorption of hydrogen and the synthesis of semiconductors with particular crystal planes and a reduced molecular adsorption energy [71-

72]. Understanding the mechanism of photocatalytic water dissociation hinges on the interfacial structure of water in contact with the photocatalyst; interaction between physically sorbed and chemisorbed water molecules may result in superhydrophilicity of the photocatalyst. Water stabilised in the nano confinement space behaves differently from the water molecule on the surface of the bulk photocatalyst [73–74]. Water in nanoconfinement exhibits properties different from that of bulk water [73]. Due to the nano-confinement of water, change in various properties can be seen, like the change in density, surface tension and melting or freezing point. With the increase in the spatial confinement of water, the change in hydrogen bonding network can be seen. Due to the change in O-H stretching, the water uptake increases. As a result of the cross linkage, in the hydrogel (Sodium Alginate) encapsulated photocatalyst a 3D Metal Organic Framework (MOF) microstructure is created which helps in water retention. Capturing water in a microporous organic framework or hydrogel can be an optimal system for enhancing "nano-confined water molecules" on the interior active sites of a photocatalyst in comparison to a bulk water system. Surface photocatalytic reactions to alter water molecule distribution and chemical adsorption properties on active sites of the photocatalyst, from which it can proceed on demand at a viable reaction state to enhance hydrogen evolution reaction activity [75] are of significant interest.

In this current thesis, the problem of the powder photocatalyst has been addressed by the development of a concept of hydrogel encapsulated photocatalytic system for enhancement of photocatalytic activity. The presence of crosslinked network in hydrogel aids in the adsorption and retention of water molecules. Hydogel materials display strong absorption, hydrophilicity that allows both chemisorption and physisorption of water, that remain confined in the channels [76,77]. Modification of the photocatalytic system is done by selecting suitable hydrogel for encapsulation of the powder photocatalyst, which in turn will improve the retention time. The variation of the mode of operation of photocatalytic water splitting from the conventional batch to continuous can also be made possible by the encapsulation of powder photocatalyst.

1.6. Process Bottlenecks of photocatalytic water splitting

The major process bottlenecks of the photocatalytic water splitting in the process of becoming a commercially viable process are:

- Recombination of photo-generated electrons and holes

- Rapid reverse reaction of formation of water from hydrogen and oxygen
- Inability to utilize visible light
- Low extent of water retention
- Metal loss aggregation of powder type photo-catalysts
- Low hydrogen production rate

In view of the present state of the art, the following research aims and objectives are presented as follows:

1.7 Research Aims and Objectives:

The proposed research aims and objectives are:

1. Synthesis, characterization of reduced graphene oxide (rGO) based composites and transition metal -based nano-hybrid powder photo-catalysts
2. Enhancement of photo-response and quantum efficiency by utilizing heterojunction comprising of hydrogen evolution catalyst and oxygen evolution catalyst and rGO based as electron transporter
3. Enhancement of photo-response and quantum efficiency by utilizing Z scheme with rGO as the solid-state mediator
4. Encapsulation of powder like heterojunction and Z scheme photocatalytic system with Hydrogel: Synthesis, characterization of environment friendly, recyclable, hydrogel encapsulated 3D milli spherical bead like photo-catalysts having high water retention capacity for batch and continuous mode of hydrogen generation: Enhancement of yield and efficiency.
5. Development of laboratory scale set up for production of hydrogen using photocatalytic water splitting. Testing of performance of synthesized photocatalysts for generation of hydrogen from water, along with analysis of photo-response of catalysts
6. Performance mapping and determination of optimum conditions
7. Cost analysis for each catalysts

1.8 Overview of the Thesis

The focus and goal of this thesis is the enhancement of yield of hydrogen, activity, photo-response, redox ability and quantum efficiency by utilizing heterojunction and two step photoexcitation photocatalytic schemes by development of reduced graphene oxide (rGO) based composites and transition metal -based nano-hybrid powder photo-catalysts. Moreover, encapsulation of powder like heterojunction and Z scheme photocatalytic system with hydrogel has been done in an attempt to develop environment friendly, recyclable hydrogen photocatalyst with high water retention for batch and sustainable constant continuous mode hydrogen generation. In view of the present state of the art, efforts have been put forward to synthesize, characterize, test and study the performance analysis of different types of photocatalyst powder and hydrogel encapsulated photocatalysts. The synthesized materials has thereby being characterized and the performance analysis has been done by varying process parameter. The determination of optimum conditions has been done and a comparative cost analysis study has been done for the different photocatalytic systems in an attempt to address the process bottlenecks as roadblocks in the pathway of commercialization of photocatalytic water splitting.

A schematic of the overview of thesis is given in the following section: [Scheme 1.1]:

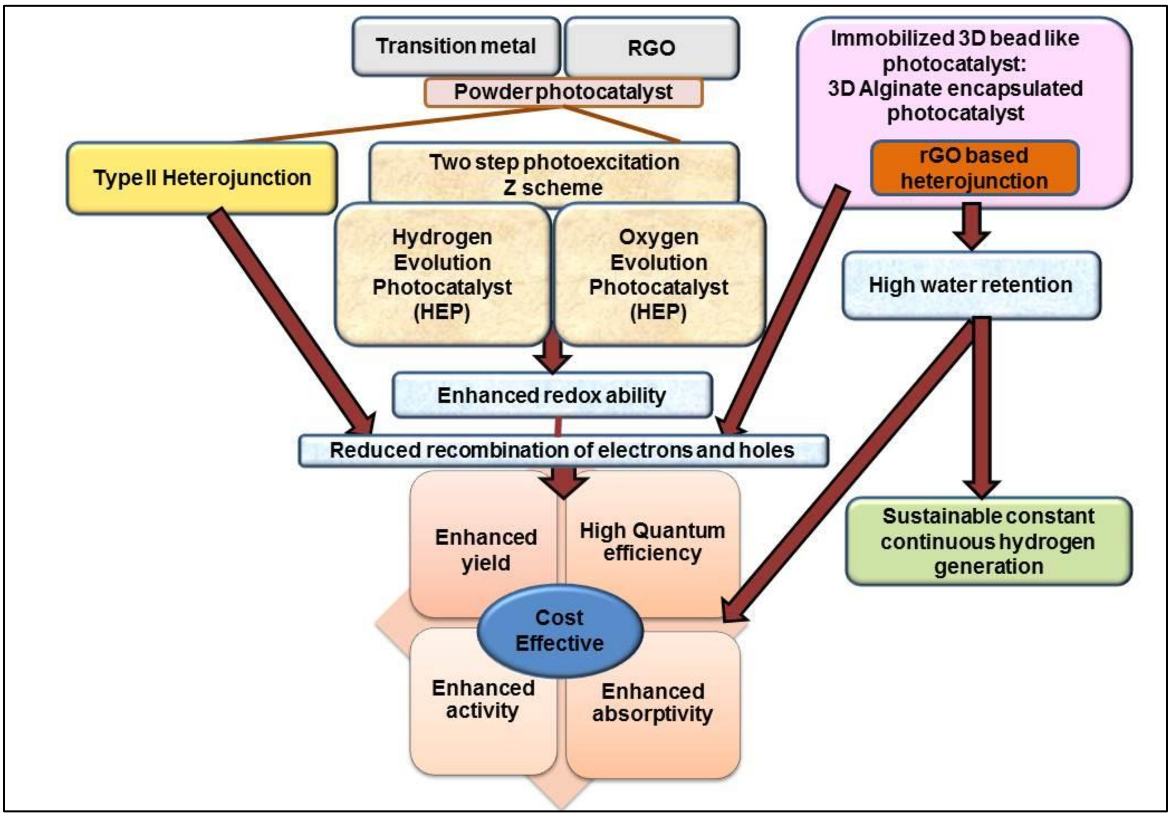

Scheme 1.1 Overview of the thesis

According to the objectives, at first the selection of the material has been done:

1.9. Choice of material

Choice of material is a crucial step for photocatalytic water splitting reaction. Photocatalytic material should be:

a. Visible light active

b. Narrow band gap semiconductor with low recombination rate

c. High porosity

d. Optimum surface area

e. Adsorbent based visible light active photocatalyst

f. High photocatalytic activity

g. High recyclability

h. High water retention capacity

i. Super hydrophilicity

1.9.1 Choice of Photocatalyst

The selection of a suitable photocatalyst for efficient water splitting, capturing the visible range of the solar spectrum has remained a topic of discussion amongst the global scientific community. There are very few numbers of semiconductors that satisfy the necessary requirements for both water reduction and oxidation simultaneously. The position of the bandedge of the photocatalyst is one key determining factor in that case.

1.9.1.1. Selection of ZnO

Zinc oxide (ZnO) is a transparent semiconductor that belongs to the II-VI family. It has unique properties such as a 3.37eV direct band gap energy, high electron mobility, environment-friendly, high room-temperature luminescence and a good thermal and chemical stability, making it suitable for a wide range of applications including light emitting diodes, solar cells, sensors, field emission displays and UV-laser applications ZnO as a photocatalyst is stable, non-toxic and highly photosensitive, making it a suitable candidate for photocatalytic water splitting. [78, 79].

1.9.1.2 Selection of Cadmium Sulfide (CdS)

Cadmium Sulphide is a II–VI semiconductor. CdS exists in two main crystal structure, in nature: one is wurtzite and another is zinc blende structure [80]. The band edge position of Cadmium Sulfide (vide: **Table 1.1**) (E_g of 2.42 eV), makes it suitable as one of the most well-known visible light active photocatalyst materials. The position of the conduction band of CdS is more negative than the reduction potential of H^+/H_2. Due to this reason CdS is chosen as a component, as a hydrogen evolution photocatalyst (HEP) of the Z scheme system.

1.9.1.3 Selection of Tungsten Trioxide (WO_3)

Tungsten trioxide (WO_3) exhibits interesting properties: visible light responsive with a hole mobility of 10 $cm^2V^{-1}s^{-1.}$ Moreover, WO_3 has photosensitivity and stability against photostability. The valence band edge of WO_3 is (E_{VB} = 3.0 V vs. NHE at pH = 0) is such that it is able to straddle the redox potential of O2/H2O, thereby acting as an oxygen evolution photocatalyst. During the design of two component Z scheme photocatalytic system, WO_3 acts like an O_2 evolution photocatalyst and CdS as H2 evolution photocatalyst.

1.9.2 Selection of Sodium Alginate as Hydrogel

Sodium Alginate ($C_6H_2NaO_6$)n, is a biopolymer, comprises of hydroxyl functional groups. Alginate can be derived in the form of fibers, beads, capsules etc. and there is numerous application of Alginate in drug delivery, food processing, pollutant removal etc. [81]. Alginate is build up of two monomers, α-L Guluronic acid (G) and (1–4) linked β-D Mannuronic acid (M) linked up as block copolymers. The covalent metals of the photocatalyst interacts with the carboxylate groups of alginate by ionic cross linking, forming ordered “egg-box” structures [82–85].In this way the immobilization of the metal ions in the polymer matrix takes place. Sodium Alginate is inexpensive, easily available and can be a component of the Metal Organic Framework (MOF), along with the photocatalyst for boosting photocatalytic hydrogen generation.

After the selection of the photocatalyts, the materials are synthesized and characterized. A brief discussion on the methodology of the processes has been discussed in the next few sections:

1.10 Methodology

1.10.1 Synthesis of photocatalysts

a. Synthesis of Graphene Oxide (GO):

Graphene oxide (GO) has been synthesized by Improved Hummers method [28] In this method, concentrated H_2SO_4 and H_3PO_4 are mixed maintaining 9:1 (360 ml: 40 ml) ratio and added to graphite flakes (3.0 g, 1 wt. equiv.). $KMnO_4$ (18.0 g. 6 wt. equiv.) is added slowly to the mixture under continuous stirring as the reaction is exothermic in nature. The mixture is kept stirring for 6 hours maintaining 50^oC temperature. It is then cooled at room temperature, diluted with deionised water (400 ml) and treated with 30% H_2O_2 to reduce residual permanganate and manganese dioxide. The resultant solution is centrifuged several times and treated with HCl and further by ethanol. After centrifugation and washing with deionised water a chocolate brown colour residue is obtained. It is dried, stored and used as per requirement.

b. Synthesis of reduced Graphene Oxide (rGO) based nanocomposites:

The photocatalysts and the nanocomposite photocatalysts are synthesized by employing hydrothermal technique and precipitation method. The synthetic processes are discussed in details in each chapter.

1.10.2 Characterization Study

a. Morphological analysis: The morphological analysis of the photocatalysts has been done by utilizing Scanning Electron Microcopy and Transmission Electron Microscopy

Scanning Electron Microscopy (SEM) involves the scanning of the sample surface with high energy beam of electrons to produce high resolution images. The samples are studied using scanning electron microscope utilizing 15.0 kV of voltage, for charging electrons. Energy Dispersive X-ray spectroscopy (EDS) set up attached with the SEM instrument is used to detect the elemental composition of the samples.

Transmission Electron Microscopy (TEM) involves the transmission of electrons through sample to form an image. The TEM micrographs are obtained by utilizing a electron beams at a voltage of 200 kV.

b. Identification of bonds: The identification of bonds and the detection of the functional groups present in the synthesized photocatalysts has been determined by Fourier Transform Infrared Spectroscopy (FTIR) in FTIR spectrophotometer by forming KBr pellets.

c. Crystallinity Study: The crystalline nature of the synthesized photocatalysts has been studied by using X-ray Diffraction (XRD) in X-ray Diffractometer applying 40 kV voltages, 30 mA current, 1.2 kW power in the 2θ range for all samples from 10 to 90^o. The crystallite size is determined by Scherrer equation which is as follows:

$$D = K\lambda/\beta cos\theta \tag{1.16}$$

d. Optical property measurement

UV-Vis Spectrocopy

The optical nature of the samples is analysed using UV-Vis Spectroscopy using UV-Vis Spectrophotometer. UV-Vis Spectroscopy is a type of spectroscopy technique where the electronic transitions are studied when the sample is exposed to light. The band gap of the synthesized photocatalysts are determined by Tauc plot analysis following the equation:

$$\alpha h\nu = A(h\nu - E_g)^n \tag{1.17}$$

Photoluminescence Spectroscopy

The photoluminescence spectroscopy (PL) of the samples is done to study the degree of rate of recombination between the photogenerated electrons and holes. The PL spectroscopy is done in a Fluorescence Spectrophotometer.

e. **Surface Chemical State Analysis:** The surface chemical states of the different elements present in the photocatalyst composites are studied using X-ray Photoelectron Spectroscopy (XPS) The binding energy of the elements are analysed and the shift of the electron clouds signifies the formation of heterostructures in these nanocomposites.XPS is done employing mono-energetic Al kα x-rays.

1.10.3 Performance Study and analysis

1.10.3.1 Photocatalytic Hydrogen Generation:

The photocatalytic performance study of the photocatalysts are done by utilizing LED lamp (45 W) and solar simulator (100 W, 1.5 G A.M.) as sources of illumination.

1.10.3.1.1 Components of Photocatalytic water splitting reaction setup

The photocatalytic reaction setup constitutes of the two major components:

a. Photoreactor

The photocatalytic reactions are carried out in photoreactor systems which are irradiated by sources of illumination. The design of the photoreactor systems has to be done for maximized output by absorbing the photon energy of the light source. Most commonly used design of photocatalytic reactors constitutes of annular photoreactor,parabolic trough photoreactors etc. In this work, cylindrical type photoreactor has been designed for the photocatalytic water splitting reactions. Solar Simulator and LED has been used as sources of irradiation.

b. Source of Irradiation

i. Solar Simulator

Solar simulator or sunlight simulator is a scientific apparatus used in controlled lab settings to simulate sunshine. It is crucial for the study and testing of processes and systems that either depend on sunlight or are impacted by it, such as solar fuels, sunscreens, solar cells, polymers, coatings, and other photosensitive materials. The light source is the primary element of the solar simulator. Short- and long-arc Xenon (Xe) lamps are the most commonly utilized light sources, but other light sources are also employed, such as metal halide (MH) arc lamps and quartz tungsten halogen lamps and more recently light-emitting diodes (LEDs). Oriel® LCS-100TM small area Sol.1A series solar simulator has been used in this thesis. Following are the basic components of a solar simulator

1. Light Source

2. Power Supply

The Xenon bulb displays a comparatively continuous spectrum from 300 nm to 2000 nm. Due to this reason, Xenon arc lamp is famous in the market for the last forty years and in this work, simulator used have ozone free Xenon lamp.

ii .Band Pass Filter

Filters that pass a set of wavelengths, while restricting other wavelengths, are known as bandpass filters. They are common filters suitable for a wide range of optical applications. Bandpass optical filters transmit only a defined range of energy of the electromagnetic spectrum. Two types of band pass filters have been used in this work: 350 nm and 420 nm. Evaluation of apparent quantum efficiency (AQE) using visible range band pass filter (420 nm) with solar simulator.

iii.LED

LED or Light Emitting Diode is basically semiconductor device that emitting light when electric current is passed through it. Electrons in the semiconductor recombine with the holes, when electric current is passed through it, and energy is released in the photonic form. This energy is utilised as source of light. The power consumption is low in LED devices. LED light is used as source of light in various photocatalytic water splitting reactions. In this work, 45 W LED light has been used.

1.10.3.1.2 Modes of operation

Usually, photocatalytic water splitting reactions is carried out in batch mode photoreactor setup. Continuous mode of operation is also carried out during the experimental studies while testing the photocatalytic activity of hydrogen encapsulated photocatalyst system.

An overview of the batch and contintinuous modes of operation has been discussed in the following sections:

a) Batch mode of operation:

In this mode fixed volume of water is kept in the reactor along with the photocatalyst. . First and foremost the photocatalytic reactor was purged with inert gas. Photo-catalyst was then introduced in the water, inside the reactor. Sacrificial agent (methanol) might be added Continuous stirring of the solution was done by magnetic stirring. The photograph of the reactor setup was shown below:

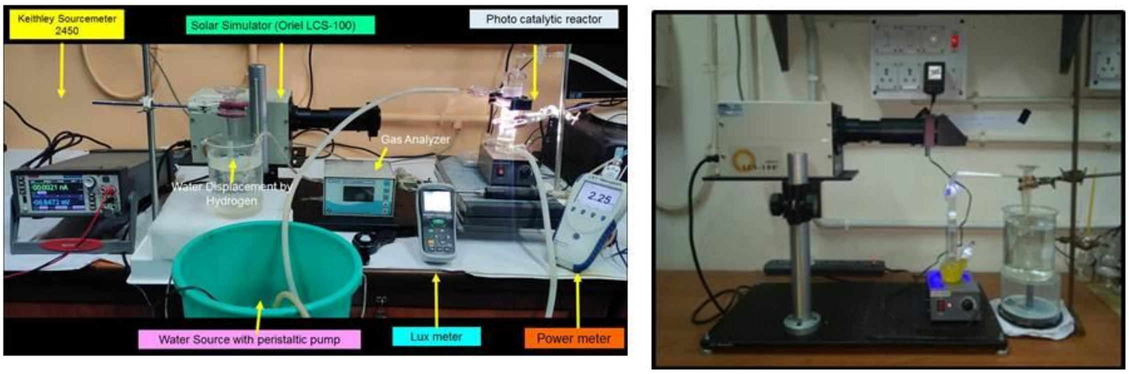

Figure 1.12 Photocatalytic Reactor Set Up: Batch mode

After some time, gradual bubble formation was observed. The gas was passed through oxygen trapping setup containing alkaline pyrogallate solution. The time and the volume of gas generated were noted down.

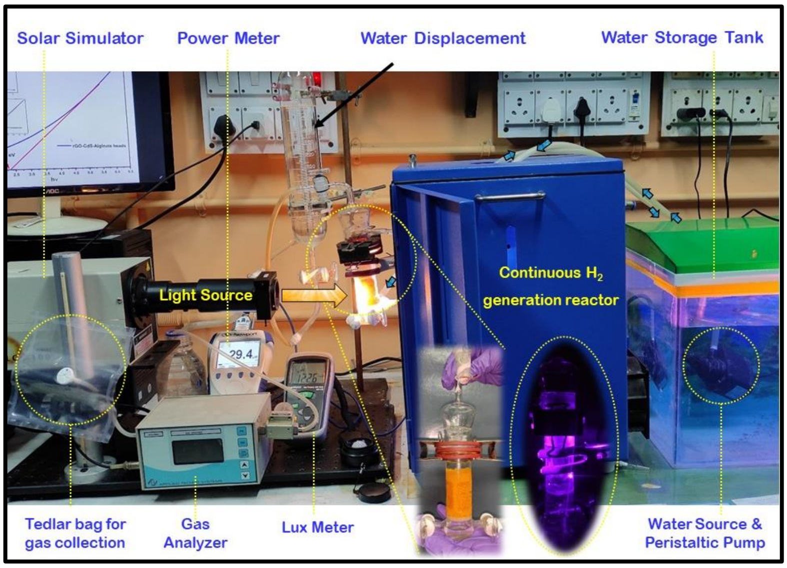

Figure 1.13 Continuous Mode Photocatalytic Reactor Setup using spherical bead water-adsorbent cum photocatalyst

b) Continuous mode: Water is continuously fed to the bed of photocatalyst through peristaltic pump. Packed bed reactor is filled with beads like photo-catalyst and water/ water vapor is fed continuously through the bed. The experimental setup for continuous mode of photocatalytic hydrogen generation using hydrogel encapsulated bead photocaalyst is depicted in Figure 1.13.

1.10.3.1.3 Performance Analysis of Photocatalytic water splitting

The performance of a specific photocatalyst is analysed in terms of photocatalytic activity and apparent quantum efficiency (AQE). Whereas Solar to Hydrogen (STH) conversion efficiency is another such metric to measure the efficiency of a photocatalytic reaction and this is applicable for systems when the source of irradiation is solar energy.

a.Calculation of STH (%):

STH is an absolute standard of measurement of performance of photocatalysts in presence of sunlight or simulated sunlight. The definition can be presented in the form of the equation:

$$\frac{r_{H_2} \times \Delta G_{H_2O} \times 100}{I \times S} \tag{1.18}$$

Here r_{H_2}, $\Delta G_{H_2O,}$ I and S represent Hydrogen evolution rate, Gibbs Free Energy of water splitting, light energy flux and the irradiation area respectively.

b. Calculation of AQE (%):

Quantum yield is a factor to determine the performance of photocatalysts during splitting of water. It can be defined as:

$$\text{Q.Y.(\%)}=\frac{Number\ of\ reacted\ electrons}{Number\ of\ incident\ photons}\times 100 \qquad (1.19)$$

If a photon (E_{photon}) of wavelength of λ_{inc} (nm) is incident during a photocatalytic water splitting reaction, the energy of this one photon calculated using the equation:

$$E_{photon} = \frac{hc}{\lambda_{inc}} \qquad (1.20)$$

where h (J·s) is Planck's constant, c ($\text{m}\cdot\text{s}^{-1}$) is the speed of light , λ_{inc} (m) is the wavelength of the monochromatic light that is incident. The energy of the incident monochromatic light (E_{total}) is calculated using the following equation:

$$E_{total} = P\ s\ t \qquad (1.21)$$

here P ($\text{W}\cdot\text{m}^{-2}$) is the power density of that incident monochromatic light,
S (m^2) is area that is being irradiated , t (s) is the duration of the exposure of the incident light
The total number of incident photons can be determined from the given equation:

$$\text{Number of incident photons} = \frac{E_{total}}{E_{photon}} = \frac{P\ s\lambda_{inc}\ t}{hc} \qquad (1.22)$$

Apparent Quantum Yield is twice the ratio between number of hydrogen molecules evolved by number of incident photons multiplied by 100.

$$\text{A.Q.Y(\%)}=\frac{2\times Number\ of\ hydrogen\ moleculed\ generated}{Number\ of\ incident\ photons}\times 100 \qquad (1.23)$$

This can be seen from the equation

A.Q.Y (%) = $\frac{2n_{H2,t}\,N_A\,hc}{P\ s\lambda_{inc}\ t}\times 100$; Where $n\text{H}_{2,t}$ (mol) is number of molecules of hydrogen evolved over the duration t of the incident light N_{A} (mol^{-1}) is Avogadro's constant

1.10.3.2 Photo-electro-catalytic (PEC) Performance

In this thesis, the Photo-electro-catalytic water splitting was carried out in a three electrode cell. The working electrode was developed by layering the synthesized heterostructure photocatalyst, reference electrode was that of Ag/AgCl electrode and the counter electrode was Pt electrode. The electrolyte was 0.5M solution of Sodium Sufate (Na_2SO_4). The source of irradiation was solar simulator (1.5 G A.M.).

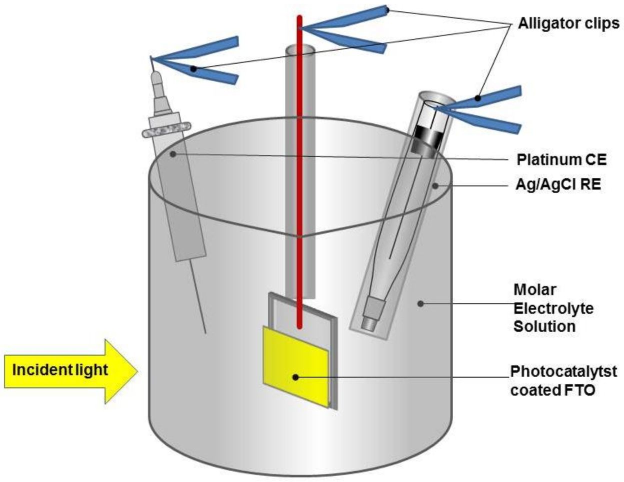

Figure 1.14 Setup for PEC performance analysis

Photoelectrodes: The photoelectrodes were prepared by coating photocatalyst on the Fluorine Doped Tin Oxide (FTO) coated glass substrates employing techniques like hydrothermal method, spraying, spray pyrolysis etc. FTO glass substrates are electrically conducting by nature. One side of the FTO glass is coated with Fluorine Doped Tin Oxide and is conducting by nature, while another side is highly insulating in nature.

IPCE (Incident Photon to Current Density) Calculation

Incident Photon to Current Density is a measurement of efficiency of photon to current conversion, defined by the ratio between the photocurrent obtained as output to the number of incident photons as input, for a particular wavelength.

$$\textbf{IPCE}= \frac{\boldsymbol{1240 \times j_{ph}}}{\boldsymbol{\lambda \times I}} \times \mathbf{100\%} \qquad (1.24)$$

Here, $\boldsymbol{j_{ph}}$ is photocurrent density (in A) at a specific wavelength $\boldsymbol{\lambda}$, $\boldsymbol{\lambda}$ is the wavelength of the incident light and $\boldsymbol{I}$ is the intensity of light for the wavelength at the film surface, here the value of $\boldsymbol{I}$ is 100 mW/cm^2.

1.11 Brief description of research work

The chapters in the subsequent segments of the thesis are as follows:

Chapter 2: Synthesis, characterization and performance analysis of rGO and transition metal based hetero-junction photocatalytic system ZnO-rGO-WO_3 for enhanced yield of hydrogen by water splitting

Chapter 3: Exploration of solid state mediator rGO based dual component CdS-rGO-WO_3, Z scheme photo-catalytic system for enhanced hydrogen generation from water splitting

Chapter 4: Organic alginate encapsulated rGO-WO_3 based photocatalyst for continuous solar green hydrogen generation

The entire research work is schematically presented in Scheme. 1.2

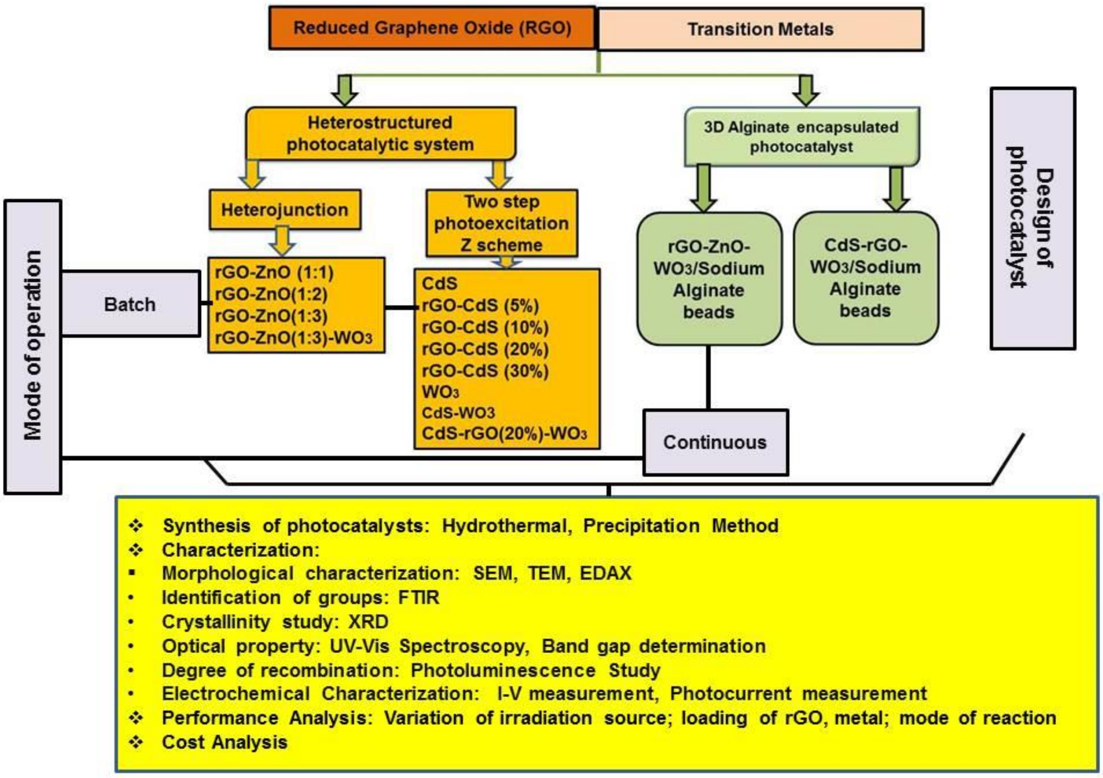

Scheme 1.2 Schematic representation of research carried out in the present thesis

1.11.1 Chapter wise Research Description

Subsequent few paragraphs are dedicated to brief on the chapters presented in this thesis.

Chapter 2

In Chapter 2, exploration of transition metal based heterojunction photocatalytic system had been done. ZnO (band gap 3.37eV) had been chosen as the photocatalyst along with transition metal WO_3 considering their bandgap for harnessing the wide solar spectrum, from UV to visible range. Pristine ZnO, nanocomposites of rGO-ZnO had been prepared by hydrothermal technique by varying the loading of ZnO, keeping loading of rGO constant in the ratio: 1:1, 1:2, 1:3, 1:4. Heterojunction rGO-ZnO-WO_3 had been developed by a facile hydrothermal technique. ZnO hexagonal nanorods and nanocuboids of WO_3 was found in the Scanning Electron Microscopy study. Photocatalytic performance study of rGO-ZnO (1:1, 1:2, 1:3, and 1:4 weight ratios) was done to get optimal ZnO loading in rGO for maximum hydrogen production, which is 1:3. Modification of optimal rGO-ZnO(1:3) photocatalyst by WO_3 was done to obtain best photoactive rGO-ZnO/WO_3 heterojunction photocatalyst for increasing the yield of hydrogen production. According to Tauc plots the optical band gaps of pure ZnO, ZnO-WO_3, rGO-ZnO (1:3), and rGO-ZnO (1:3)/WO_3 photocatalysts are 2.69, 2.58, 2.50, and 2.11 eV, respectively. PL study showed the decrease in the degree of recombination of electrons and holes. The performance analysis was done by varying the process parameters: like the source of irradiation, using LED and Solar Simulator.About 5.13 times higher yield of H_2 was obtained for rGO-ZnO-WO_3 (13.2 mmol/gh), when compared to pristine ZnO (2.57 mmol/gh). rGO-ZnO-WO_3 displayed an AQE of 3.40% at 420 nm. Subsequent cost analysis was done, which showed that considering 4 cycles of recyclability the cost for production of 1 mole of H2 is $ 652.5. Chapter 2 is schematically represented as Scheme 1.3 as below:

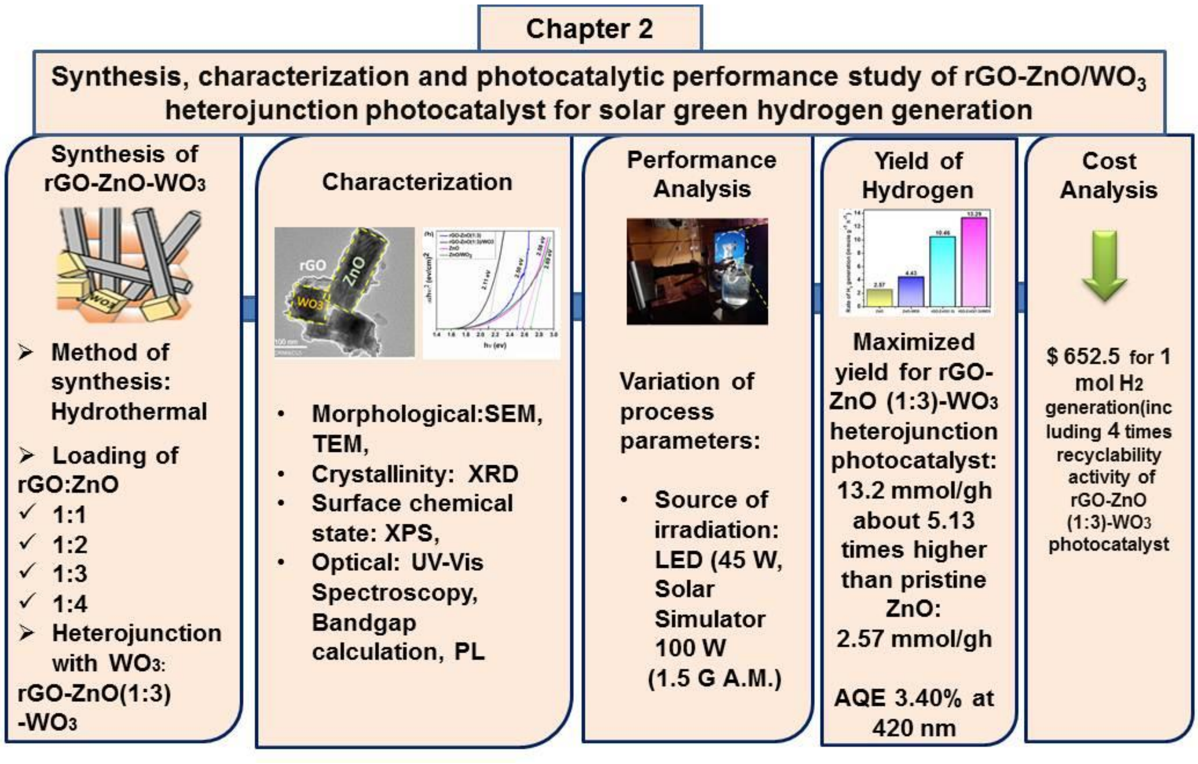

Scheme 1.3 Schematic representation of Chapter 2

The role of heterojunction in the enhancement of photocatalytic H2 and the plausible mechanism activity has been discussed in Chapter 2.

Chapter 3

In Chapter 3, exploration of two step photoexcitation scheme had been done. Chapter 3 is schematically represented as Scheme 1.4. CdS(band gap 2.42eV) and WO_3 (band gap 2.48 eV), were selected due to their suitable band edge positions where CdS played the role of Hydrogen Evolution Photocatalyst (HEP) and WO_3 as Oxygen Evolution Photocatalyst (OEP) and rGO as an excellent electron transporter acted as a solid- state mediator, between two photocatalysts: CdS (HEP) and WO_3 (OEP). Pristine CdS, WO_3, rGO-CdS, CdS-rGO-WO_3 had been prepared by hydrothermal techniques.Subsequently the variation of loading of rGO had been done as follows: 10%, 20%, 30%, 40%. The optimal loading of rGO had been determined to be 20% based on the performance study. The heterostructure CdS-rGO-WO_3 had been prepared based on this loading of rGO. The Z scheme photocatalytic system of CdS-rGO-WO_3 had been tested and characterized by various characterization techniques. CdS nanorods and nanoplates of WO_3 scattered on sheet of rGO

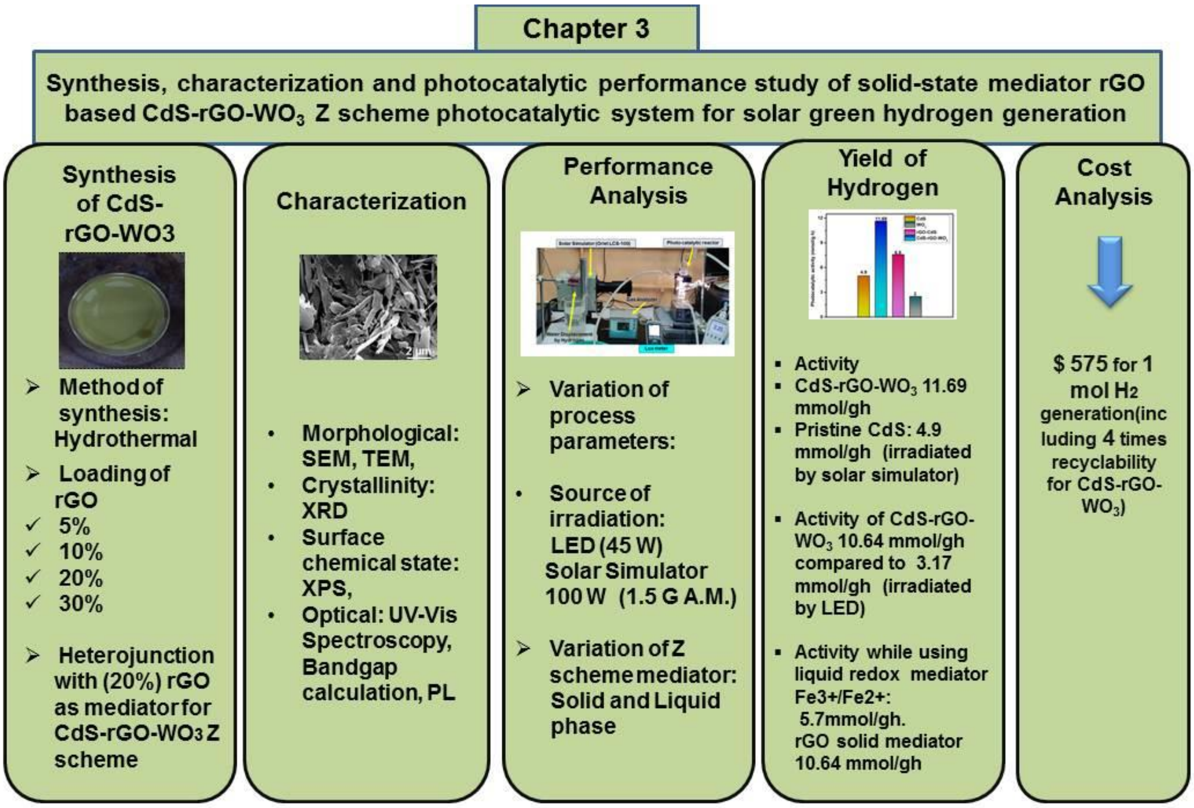
Chapter 3

Synthesis, characterization and photocatalytic performance study of solid-state mediator rGO based CdS-rGO-WO_3 Z scheme photocatalytic system for solar green hydrogen generation

Synthesis of CdS-rGO-WO3

- ➢ Method of synthesis: Hydrothermal
- ➢ Loading of rGO
  - ✓ 5%
  - ✓ 10%
  - ✓ 20%
  - ✓ 30%
- ➢ Heterojunction with (20%) rGO as mediator for CdS-rGO-WO_3 Z scheme

Characterization

- Morphological: SEM, TEM,
- Crystallinity: XRD
- Surface chemical state: XPS,
- Optical: UV-Vis Spectroscopy, Bandgap calculation, PL

Performance Analysis

- ➢ Variation of process parameters:
- Source of irradiation: LED (45 W) Solar Simulator 100 W (1.5 G A.M.)
- ➢ Variation of Z scheme mediator: Solid and Liquid phase

Yield of Hydrogen

- Activity
- CdS-rGO-WO_3 11.69 mmol/gh
- Pristine CdS: 4.9 mmol/gh (irradiated by solar simulator)
- Activity of CdS-rGO-WO_3 10.64 mmol/gh compared to 3.17 mmol/gh (irradiated by LED)
- Activity while using liquid redox mediator Fe3+/Fe2+: 5.7mmol/gh. rGO solid mediator 10.64 mmol/gh

Cost Analysis

\$ 575 for 1 mol H_2 generation(including 4 times recyclability for CdS-rGO-WO_3)

Scheme 1.4 Schematic representation of Chapter 3

were found in SEM study. The calculated band gaps of CdS, WO_3, rGO-CdS, CdS-WO_3 and CdS-rGO-WO_3 are found to be 2.40, 2.48, 2.36, 2.30, 2.20 eV respectively. The effect of rGO loading in increasing absorptivity and tuning the band gap of the photocatalyst is confirmed by the band gap calculation. Surface chemical states had been studied by X-ray Photoelectron spectroscopy, also the formation of the Z scheme had been verified by XPS,. Photoluminescence Spectroscopy was done to determine the degree of recombination of the electron-hole pairs.Urbach energy plot was done to determine the defect state. Zeta Potential study was done to identify the surface charges and the stabiliy of the as synthesized nanocomposite in a colloidal system. The performance analysis was done by varying the process parameters: like the source of irradiation, using LED and Solar Simulator.About times 3.35 times higher yield of H2 was obtained for CdS-rGO-WO_3 (10.64 mmol/gh), when compared to pristine CdS (3.17 mmol/gh), using LED as light source, activity was also checked using solar simulator when 11.69 mmol/gh activity was seen for CdS-rGO-WO_3 and 4.9 mmol/gh for CdS.. The effect of enhancement of activity using solid redox mediator in Z scheme compared to liquid redox mediator ($Fe^{3+/}Fe^{2+}$) was found to be about 1.8 times more. IPCE of 0.549 (1.23 vs RHE) was obtained for CdS-rGO-WO_3, during photoelectrochemical performance study . The Solar to Hydrogen Efficiency (STH %) for the nano-heterojunction CdS-rGO-WO_3 was calculated to be 0.62 and the Apparent Quantum Efficiency (AQE %) was estimated to be 1.5 (λ=420 nm) during operation using solar simulator. Subsequent cost analysis was done, which showed that considering 4 cycles of recyclability, the cost for production of 1 mole of H2 is $ 575. The plausible mechanism of the CdS-rGO-WO_3 Z scheme photocatalytic activity had also been discussed in Chapter 3.

Chapter 4 A novel 3D millisphere of organic alginates hydrogel-encapsulated graphene-supported CdS-rGO-WO_3 and rGO-ZnO-WO_3 photocatalyst with high water retention capability was designed in Chapter 4. The water uptake or sorption characteristics of rGO-CdS-Alginate, rGO-CdS-WO_3-alginate and rGO-CdS-ZnO-alginate at the room temperature (20^0C) was studied, which were 96.9% and 97.7%, respectively. Water in a microporous organic framework or hydrogel may be an optimum method for boosting "nano-confined water molecules" on the inner active sites of a photocatalyst. Surface photocatalytic reactions to change the distribution of water molecules and chemical adsorption qualities on photocatalyst active sites, from which it may continue on demand at a viable reaction state to boost hydrogen evolution reaction activity are of great interest. Therefore, the high water retention capability was investigated for enhanced solar hydrogen production from water using batch and continuous modes of operation for a pressure-driven flow-through system under full band solar irradiation. It was observed that below a critical flow rate, this steady rate of hydrogen generation becomes and the the slope of the curve of amount of evolved hydrogen generation versus time becomes almost constant and attains the steady rate of hydrogen generation, which is invariant of the inlet flow rate and attains almost a constant value of 29.16 mmol/h. The photocatalytic activity of rGO-CdS-WO_3-alginate and rGO-ZnO-WO_3-alginate were obtained to be 81.8 mmol h^{-1} g^{-1} and 90.63 mmol h^{-1} g^{-1}, the enhancement addressing the issue of high photo charge carrier recombination rate, short hole diffusion length, and sluggish water oxidation kinetics. The recyclability of the photocatalyst was investigated over the course of four successive cycle and it is found that after one month (30 days), rGO-CdS-WO_3-Alginate millisphere photocatalyst loses 5.92% of its initial activity. Chapter 4 is schematically represented as Scheme 1.5.

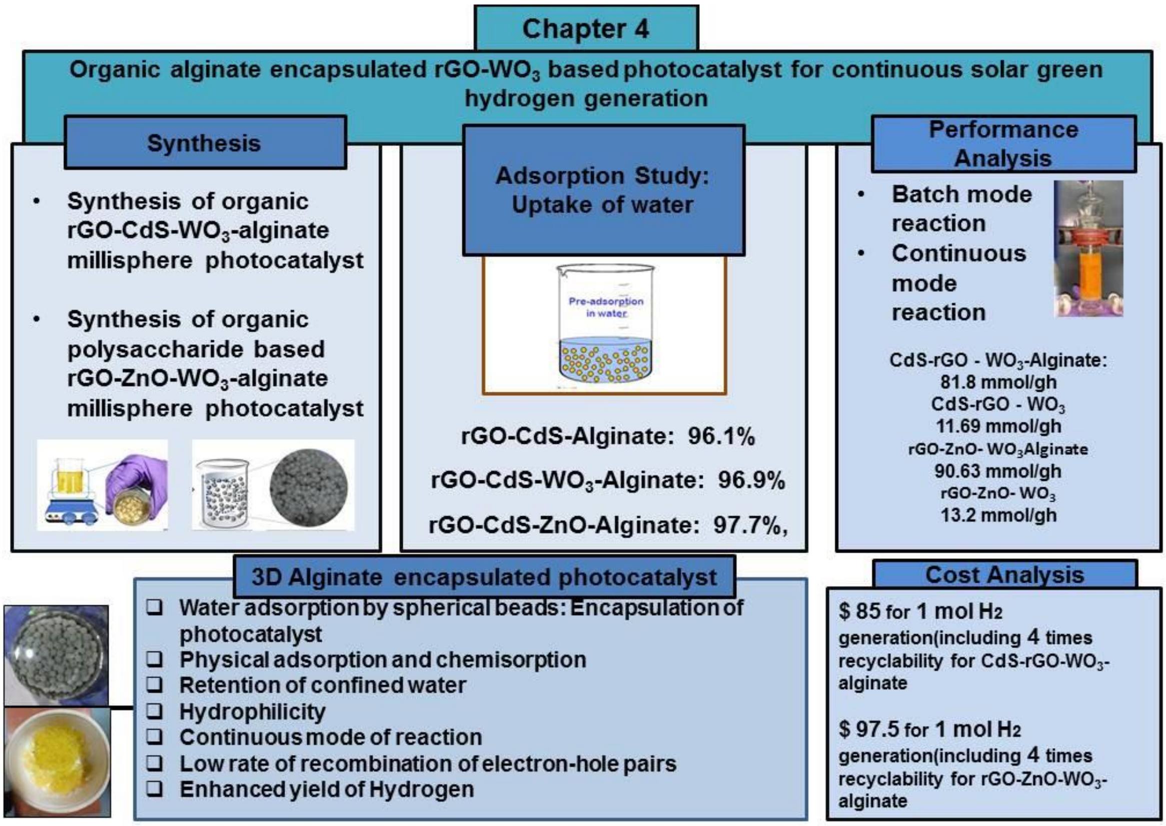

Scheme 1.5 Schematic representation of Chapter 4

The toxicity and the photocorrosion problems of the CdS based photocatalyst was addressed by encapsulation of the photocatalyst by 3D Alginate organic framework as revealed in the cell viability test: the percentage of cell for the alginate encapsulated photocatalyst was much higher than the powdered photocatalyst. Subsequent cost analysis was done, which showed that considering 4 cycles of recyclability, the cost for production of 1 mole of H2 is $ 85 for 1 mol H2 generation(including 4 times recyclability for CdS-rGO-WO_3-alginate and 97.5 for 1 mol H2 generation including 4 times recyclability for rGO-ZNO-WO_3-alginate.

Chapter 5 concludes the outcome of the research work presented in this thesis and mentions the future scope of research in the related field.

1.11.2 Supporting work

Annexure-I reports the synthesis, characterization and photocatalytic performance study of rGO-$SnFe_2O_4$ photocatalyst for solar hydrogen generation

1.12 References

1. Short, W., Packey, D.J. and Holt, T. (2005) *A Manual for the economic evaluation of Energy Efficiency and Renewable Energy Technologies*. Honolulu, HI: University Press of the Pacific.

2. Khare, V. (2023). Chapter 4 - Productivity and manufacturing economics of solar energy system, *Decision science and operations management of solar energy system*. London, England: Elsevier. 111-145

3. Jones, G. A., & Warner, K. J. (2016). The 21st century population-energy-climate nexus. *Energy Policy*, *93*, 206–212.

4. Zou, C., Zhao, Q., Zhang, G., & Xiong, B. (2016). Energy revolution: From a fossil energy era to a new energy era. *Natural Gas Industry B*, *3*(1), 1–11.

5. Kapoor,V., Malviya, M. (2021). Chapter 15 - Assessment of mechanisms and instruments of climate finance: a global perspective, *Environmental Sustainability and Economy*, Elsevier 297-324

6. https://www.ucsusa.org/resources/each-countrys-share-co2-emissions.

7. Renewables 2022 Global Status Report, https://www.ren21.net/wpcontent/uploads/2019/05/GSR2022_Full_Report.pdf

8. Energy Statistics Report-2022, Ministry of Statistics and Programme Implementation https://www.mospi.gov.in/publication/energy-statistics-india-2022

9. Turner, J. A. (1999). A realizable renewable energy future. *Science*, *285*(5428), 687–689.

10. Brun, K., & Allison, T. (2022). *Machinery and energy systems for the Hydrogen Economy*. Amsterdam, Netherlands: Elsevier.

11. https://www.weforum.org/agenda/2021/07/clean-energy-green-hydrogen/

12.https://www.worldenergy.org/assets/downloads/WEInsights-Brief-New-Hydrogen-economy-Hype-or-Hope-ExecSum.pdf

13. Global Hydrogen Review 2022 IEA https://iea.blob.core.windows.net/assets/c5bc75b1-9e4d-460d-9056-6e8e626a11c4/GlobalHydrogenReview2022.pdf

14. National Green Hydrogen Mission, January 2023, Ministry of New and Renewable Energy https://mnre.gov.in/img/documents/uploads/file_f-1673581748609.pdf

15. Shiva Kumar, S., & Lim, H. (2022). An overview of water electrolysis technologies for Green Hydrogen production. *Energy Reports*, *8*, 13793–13813.

16. Chapter 4-Thermochemical hydrogen production. (1979). *Solar-Hydrogen Energy Systems*, 81–114.

17. Aiello, R. (1999). Production of hydrogen from chemical hydrides via hydrolysis with steam. *International Journal of Hydrogen Energy*, *24*(12), 1123–1130.

18. Gao, N., Li, A., Quan, C., & Gao, F. (2008). Hydrogen-rich gas production from biomass steam gasification in an updraft fixed-bed gasifier combined with a porous ceramic reformer. *International Journal of Hydrogen Energy*, *33*(20), 5430–5438.

19. Parthasarathy, P., & Sheeba, K. N. (2014). Combined slow pyrolysis and steam gasification of biomass for Hydrogen Generation-A Review. *International Journal of Energy Research*, *39*(2), 147–164.

20. Sakurai, H., Masukawa, H., Kitashima, M., & Inoue, K. (2013). Photobiological hydrogen production: Bioenergetics and challenges for its practical application. *Journal of Photochemistry and Photobiology C: Photochemistry Reviews*, *17*, 1–25.

21. Tributsch, H. (2008). Photovoltaic hydrogen generation. *International Journal of Hydrogen Energy*, *33*(21), 5911–5930.

22. Ahmed, M., & Dincer, I. (2019). A review on photoelectrochemical hydrogen production systems: Challenges and future directions. *International Journal of Hydrogen Energy*, *44*(5), 2474–2507.

23. Christoforidis, K. C., & Fornasiero, P. (2017). Photocatalytic hydrogen production: A rift into the future energy supply. *ChemCatChem*, *9*(9), 1523–1544.

24. Fujishima, A., & Honda, K. (1972). Electrochemical photolysis of water at a semiconductor electrode. *Nature*, *238*(5358), 37–38.

25. Bard, A. J. (1979). Photoelectrochemistry and heterogeneous photo-catalysis at semiconductors. *Journal of Photochemistry*, *10*(1), 59–75.

26. Xie, G., Zhang, K., Guo, B., Liu, Q., Fang, L., & Gong, J. R. (2013). Graphene-based materials for hydrogen generation from light-driven water splitting. *Advanced Materials*, *25*(28), 3820–3839.

27. Xiang, Q., & Yu, J. (2013). Graphene-based photocatalysts for hydrogen generation. *The Journal of Physical Chemistry Letters*, *4*(5), 753–759.

28. Xiang, Q., Yu, J., & Jaroniec, M. (2012). Graphene-based semiconductor photocatalysts. *Chemical Society Reviews*, *41*(2), 782–796.

29. Bahrani, S., Khafri, H., & Ghaedi, M. (2021). New materials for water-splitting. *Photocatalysis: Fundamental Processes and Applications*, 791–870.

30. Kudo, A., & Miseki, Y. (2009). Heterogeneous photocatalyst materials for water splitting. *Chemical Society Reviews*, *38*(1), 253–278.

31. Kamat, P. V. (2012a). Manipulation of charge transfer across semiconductor interface. A criterion that cannot be ignored in photocatalyst design. *The Journal of Physical Chemistry Letters*, *3*(5), 663–672.

32. Ibhadon, A., & Fitzpatrick, P. (2013). Heterogeneous photocatalysis: Recent advances and applications. *Catalysts*, *3*(1), 189–218.

33. Somasundaran, P.,(2006) *Encyclopedia of Surface and Colloid Science*, CRC Press, 2312.

34.a.Wu, X. (2022). Applications of titanium dioxide materials. *Titanium Dioxide - Advances and Applications*. IntechOpen

34.b. Huang, A., Cao, L., Chen, J., Spiess, F.-J., Suib, S. L., Obee, T. N.,Freihaut, J. D. (1999). Photocatalytic degradation of triethylamine on titanium oxide thin films. *Journal of Catalysis*, *188*(1), 40–47.

35. Yamaguti, K., & Sato, S. (1985). Photolysis of water over metallized powdered titanium dioxide. *Journal of the Chemical Society, Faraday Transactions 1: Physical Chemistry in Condensed Phases*, *81*(5), 1237.

36. Iwase, A., Kato, H., & Kudo, A. (2006). Nanosized Au particles as an efficient cocatalyst for photocatalytic overall water splitting. *Catalysis Letters*, *108*(1–2), 7–10.

37. Kato, H., & Kudo, A. (1998). New tantalate photocatalysts for water decomposition into H_2 and O_2. *Chemical Physics Letters*, *295*(5–6), 487–492.

38. Sayama, K., & Arakawa, H. (1993). Photocatalytic decomposition of water and photocatalytic reduction of carbon dioxide over Zirconia catalyst. *The Journal of Physical Chemistry*, *97*(3), 531–533.

39. Kashahara, A., Nukumizu, K., Hitoki, G., Takata, T., Kondo, J.N., Hara, M., Kobayashi, H., Domen, K., (2002) Photoreactions on $LaTiO_2N$ under Visible Light Irradiation *The Journal of Physical Chemistry A*, *106 (29)*, 6750–6753

40. Ogisu, K., Ishikawa, A., Teramura, K., Toda, K., Hara, M., & Domen, K. (2007). Lanthanum–indium oxysulfide as a visible light driven photocatalyst for water splitting. *Chemistry Letters*, *36*(7), 854–855.

41. Xing, C., Zhang, Y., Yan, W., & Guo, L. (2006). Band structure-controlled solid solution of Cd_{1-X} Zn_xS photocatalyst for hydrogen production by water splitting. *International Journal of Hydrogen Energy, 31*(14), 2018–2024.

42.Reber, J. F., & Rusek, M. (1986). Photochemical hydrogen production with platinized suspensions of cadmium sulfide and cadmium zinc sulfide modified by silver sulfide. *The Journal of Physical Chemistry*, *90*(5), 824–834.

43. Serpone, N., Borgarello, E., & Grätzel, M. (1984). Visible light induced generation of hydrogen from H_2S in mixed semiconductor dispersions; improved efficiency through inter-particle electron transfer. *Journal of the Chemical Society Chemical Communications,* (6), 342–344.

44. Low, J., Yu, J., Jaroniec, M., Wageh, S., & Al-Ghamdi, A. A. (2017). Heterojunction photocatalysts. *Advanced Materials*, *29*(20), 1601694.

45. Twilton, J., Le, C., Zhang, P., Shaw, M. H., Evans, R. W., & MacMillan, D. W. (2017). The merger of transition metal and photocatalysis. *Nature Reviews Chemistry*, *1*(7).

46. Li, Y., Bahamon, D., Sinnokrot, M., & Vega, L. F. (2022). Computational screening of transition metal-doped CdS for photocatalytic hydrogen production.*npj Computational Materials*, *8*(1).

47. TM Yang, K., Li, D.-F., Huang, W.-Q., Xu, L., Huang, G.-F., & Wen, S. (2016). Origin of enhanced visible-light photocatalytic activity of transition-metal (Fe, Cr and Co)-doped CeO_2: Effect of 3d orbital splitting. *Applied Physics A*, *123*(1).

48. Suo, Z., Dai, J., Gao, S., & Gao, H. (2020). Effect of transition metals (Sc, Ti, V, Cr and Mn) doping on electronic structure and optical properties of CdS. *Results in Physics*, *17*, 103058.

49. Du, X., Skachko, I., Barker, A., & Andrei, E. Y. (2008). Approaching ballistic transport in suspended graphene. *Nature Nanotechnology*, *3*(8), 491–495.

50. Geim, A. K. & Novoselov, K. S. (2007). The rise of graphene. *Nature Materials*,*6*(3), 183–191

51. Avouris, P. (2010). Graphene: Electronic and photonic properties and devices. *Nano Letters*, *10*(11), 4285–4294.

52. Guo, B., Fang, L., Zhang, B., & Gong, J. R. (2011). Graphene doping: A Review. *Insciences Journal*, 80–89.

53. Mao, S., Pu, H., & Chen, J. (2012). Graphene oxide and its reduction: Modeling and experimental progress. *RSC Advances*, *2*(7), 2643.

54. Eda, G., Mattevi, C. Yamaguchi, H., Kim, H., & Chhowalla, M. (2009). Insulator to semimetal transition in graphene oxide. *The Journal of Physical Chemistry C*, *113*(35), 15768–15771.

55. Wang, X., Zhi, L., & Müllen, K. (2007). Transparent, conductive graphene electrodes for dye-sensitized solar cells. *Nano Letters*, *8*(1), 323–327.

56. Zhang, J., Yu, J., Jaroniec, M., & Gong, J. R. (2012). Noble metal-free reduced graphene oxide-$Zn_xCd_{1-x}S$ nanocomposite with enhanced solar photocatalytic H_2-production performance. *Nano Letters*, *12*(9), 4584–4589.

57. Yeh, T.-F., Syu, J.-M., Cheng, C., Chang, T.-H., & Teng, H. (2010). Graphite oxide as a photocatalyst for hydrogen production from water. *Advanced Functional Materials*, *20*(14), 2255–2262.

58. Zhang, Y., Zhang, N., Tang, Z.-R., & Xu, Y.-J. (2012). Graphene transforms wide band gap ZnS to a visible light photocatalyst. The new role of graphene as a macromolecular photosensitizer. *ACS Nano*, *6*(11), 9777–9789.
Here are the references converted to APA 6 format:

59. Liu, Q., Zhang, S., Liao, J., Feng, K., Zheng, Y., Pollet, B., & Li, H. (2017). CuCo2O4 nanoplate film as a low-cost, highly active and durable catalyst towards the hydrolytic dehydrogenation of ammonia borane for hydrogen production. Journal of Power Sources, 355, 191-198.

60. Saha, S., Basak, V., Dasgupta, A., Ganguly, S., Banerjee, D., & Kargupta, K. (2014). Graphene supported bimetallic G–Co–Pt nanohybrid catalyst for enhanced and cost-effective hydrogen generation. International Journal of Hydrogen Energy, 39(22), 11566-11577.

61. Tu, K., Büchele, S., Mitchell, S., Stricker, L., Liu, C., Goldhahn, C., ... Keplinger, T. (2022). Natural wood-based catalytic membrane microreactors for continuous hydrogen generation. ACS Applied Materials & Interfaces, 14(6), 8417-8426.

62. Zhang, L., et al. (2022). Ni(OH)2 nanoparticles encapsulated in conductive nanowire array for high-performance alkaline seawater oxidation. Nano Research, 15(7), 6084-6090.

63. Chen, J., et al. (2023). High-efficiency overall alkaline seawater splitting: Using a nickel-iron sulfide nanosheet array as a bifunctional electrocatalyst. Journal of Materials Chemistry A, 11(3), 1116-1122.

64. Ning, X., Li, J., Yang, B., Zhen, W., Li, Z., Tian, B., & Lu, G. (2017). Inhibition of photocorrosion of CdS via assembling with thin film TiO2 and removing formed oxygen by artificial gill for visible light overall water splitting. Applied Catalysis B: Environmental, 212, 129-139.

65. Tian, J., et al. (2015). Cobalt phosphide nanowires: Efficient nanostructures for fluorescence sensing of biomolecules and photocatalytic evolution of dihydrogen from water under visible light. Angewandte Chemie, 127(18), 5583-5587.

66. Masai, H., et al. (2020). Photocatalytic hydrogen generation of monolithic porous titanium oxide-based glass-ceramics. Scientific Reports, 10(1).

67. Li, J., Ma, R., Lu, Y., Wu, Z., Su, M., Jin, K., ... Jiang, Z. (2020). A gravity-driven high-flux catalytic filter prepared using a naturally three-dimensional porous rattan biotemplate decorated with Ag nanoparticles. Green Chemistry, 22(20), 6846-6854.

68. Hui, B., Li, J., Lu, Y., Zhang, K., Chen, H., Yang, D., ... Huang, Z. (2021). Boosting electrocatalytic hydrogen generation by a renewable porous wood membrane decorated with Fe-doped NiP alloys. Journal of Energy Chemistry, 56, 23-33.

69. Jiang, Z., et al. (2019). Hydrogel as a miniature hydrogen production reactor to enhance photocatalytic hydrogen evolution activities of CdS and ZnS quantum dots derived from the modified gel crystal growth method. Chemical Engineering Journal, 373, 814–820.

70. Li, F., et al. (2020). Enhanced photocatalytic hydrogen production of CdS embedded in cationic hydrogel. International Journal of Hydrogen Energy, 45(3), 1969-1980.

71. Farstad, M., Ragazzon, D., Walle, L., Schaefer, A., Sandell, A., & Borg, A. (2015). Water adsorption on TiOx thin films grown on Au(111). The Journal of Physical Chemistry C, 119(12), 6660-6669.

72. Wei, Z., Sinko, R., Keten, S., & Luijten, E. (2018). Effect of surface modification on water adsorption and interfacial mechanics of cellulose nanocrystals. ACS Applied Materials & Interfaces, 10(9), 8349-8358.

73. Wang, H., Xi, X., Kleinhammes, A., & Wu, Y. (2008). Temperature-induced hydrophobic-hydrophilic transition observed by water adsorption. Science, 322(5898), 80-83.

74. Hummer, G., Rasaiah, J., & Noworyta, J. (2001). Water conduction through the hydrophobic channel of a carbon nanotube. Nature, 414(6860), 188-190.

75. Tu, S., Zhao, X., Cheng, M., Sun, P., He, Y., & Xu, Y. (2019). Uniform mesoporous MnO2 nanospheres as a surface chemical adsorption and physical confinement polysulfide mediator for lithium-sulfur batteries. ACS Applied Materials & Interfaces, 11(11), 10624-10630.

76. Abdallah, A. M. (2019). The effect of hydrogel particle size on water retention properties and availability under water stress. International Soil and Water Conservation Research, 7(3), 275–285.

77. Allangawi, A., Aziz Aljar, M. A., Ayub, K., El-Fattah, A. A., & Mahmood, T. (2023). Removal of methylene blue by using sodium alginate-based hydrogel; Validation of Experimental Findings via DFT calculations. Journal of Molecular Graphics and Modelling, 122, 108468.

78. Sharma, P., Sreenivas, K., & Rao, K. V. (2003). Analysis of ultraviolet photoconductivity in ZnO films prepared by unbalanced magnetron sputtering. *Journal of Applied Physics*, *93*(7), 3963–3970.

79. Yuvaraj, D., Sathyanarayanan, M., & Narasimha Rao, K. (2013). Deposition of ZnO nanostructured film at room temperature on glass substrates by activated reactive evaporation. *Applied Nanoscience*, *4*(7), 801–808.

80. Zhang, K., & Guo, L. (2013). Metal sulphide semiconductors for photocatalytic hydrogen production. *Catalysis Science & Technology*, *3*(7), 1672.

81. Partovinia, A., & Vatankhah, E. (2019). Experimental investigation into size and sphericity of alginate micro-beads produced by electrospraying technique: Operational condition optimization. *Carbohydrate Polymers*, *209*, 389–399.

82. Zhao, W., Qi, Y., Wang, Y., Xue, Y., Xu, P., Li, Z., & Li, Q. (2018). Morphology and thermal properties of calcium alginate/reduced graphene oxide composites. *Polymers*, *10*(9), 990.

83. Wang, Z., Kale, G. M., Yuan, Q., & Ghadiri, M. (2012). X-ray micro-tomography of freeze dried nickel alginate beads and transformation into NiO nanopowders. *RSC Advances*, *2*(26), 9993.

84. Gombotz, W. (1998). Protein release from alginate matrices. *Advanced Drug Delivery Reviews*, *31*(3), 267–285.

85. Chen, W., Luo, M., Yang, K., & Zhou, X. (2020). Simple pyrolysis of alginate-based hydrogel cross-linked by bivalent ions into highly porous carbons for energy storage. *International Journal of Biological Macromolecules*, *158*, 265–274.

Chapter 2

Synthesis, characterization and photocatalytic performance study of rGO-ZnO/WO_3 heterojunction photocatalyst for solar green hydrogen generation

Highlights:

- **Synthesis of rGO-ZnO photocatalyst using different weight ratios to provide the best ZnO loading in rGO for the highest possible hydrogen production.**
- **Modification of optimal rGO-ZnO (1:3) by WO_3 to obtain the best photoactive rGO-ZnO(1:3)/WO_3 heterojunction photocatalyst for increasing the yield of hydrogen production.**
- **The rGO-ZnO (1:3)/WO_3 heterojunction photocatalyst shows the greatest hydrogen generation rate of 13.29 mmol g^{-1} h^{-1} under visible light irradiation of solar simulator.**

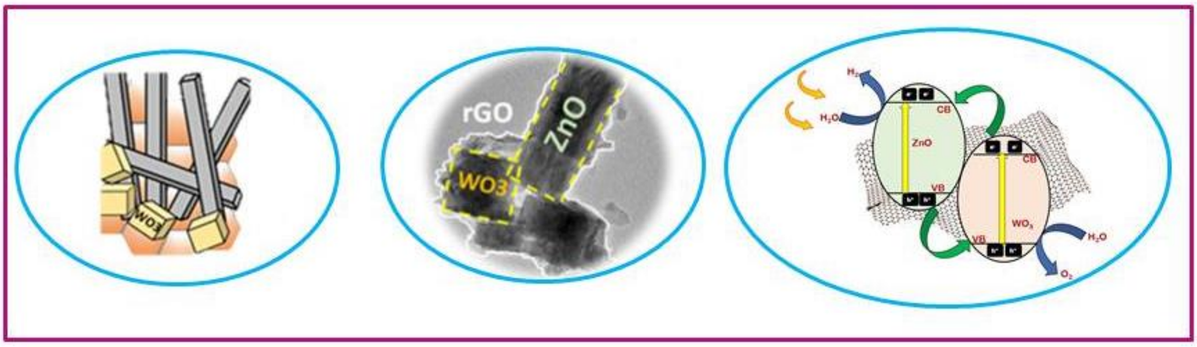

2.1. Introduction

The rapid consumption of fossil fuels is a key factor in the development of contemporary industrial society. Governments, scientists, and the general public, however, have become acutely aware of the depletion of fossil fuel resources and the ensuing environmental problems in recent decades. Today, the investigation of renewable energy sources is receiving a growing amount of focus and emphasis [1-3]. The most plentiful and renewable source of sustainable energy is solar energy. One of the most promising methods to address the aforementioned energy crisis and environmental challenges is the environmentally benign, economically viable, and efficient solar-to-fuel conversion [4-6]. Since hydrogen is a clean energy carrier and water and unlimited solar energy are endless, photocatalytic hydrogen generation from water splitting offers a potentially sustainable solution to meet the future demand for green energy without causing environmental harm. In order to address all of these problems, a phenomenon known as photocatalysis is quite promising. In this process, the electrons are excited from valence band (VB) to conduction band (CB) by light irradiation resulting in photoinduced electron-hole (e^- & h^+) pairs, which can be used to produce clean energy and clean up the environment [7-10]. A crucial prerequisite for cost-effective photocatalysis applications is a semiconductor photocatalyst that is stable, effective, and affordable, has a large number of adsorption sites and active centres on its surface, and can harvest light from the entire solar spectrum. A significant area of scientific interest is the identification of photocatalysts with improved potential for various photocatalytic processes employing solar energy [11-13].

In this present work Zinc oxide (ZnO) photocatalyst is preliminary chosen for photocatalytic hydrogen production study beacase ZnO has received the most attention among the metal oxide semiconductor photocatalysts due to its potent oxidation and reduction capabilities, non-toxicity, and tunable shape. Although ZnO has a confined light response zone and a reasonably substantial direct band gap energy (3.2 eV) and excitation binding energy (60 meV) at ambient temperature, its use in photocatalysis is severely constrained. Additionally, low photocatalytic activity of ZnO is caused by its rapid electron-hole (e^--h+) recombination rate as a single-component photocatalyst [14-18]. Therefore, photocatalytic performance of ZnO needs to be further enhanced from the perspective of practical use and economic advantages [19-20]. The morphology and structure design of ZnO for better light absorption, such as nanorods, nanosheets, nanowires, and hollow structures, have attracted a lot of study attention in order to increase photocatalytic activity [21-23]. These distinctive architectures will give ZnO excellent advantages over bulk ZnO, such as increased surface area, a shorter charge carrier transit path, and more active reaction sites, all of which are essential for improving photocatalytic performance. In this work ZnO nanorods are synthesized for the photocatalytic performance study because the nanorod structures play a key role in the field of catalysis due to a high light absorptivity, abundance of active sites while assisting the mass transfer process.However, the high recombination rate of the photogenerated e^-h^+ pairs still limits the enhancement in photocatalytic performance of nanorod ZnO [24-28].

Further graphene or reduced graphene oxide (rGO) has been included into ZnO nanorod photocatalyst to help with these issues and to enhance the charge separation of ZnO nanorods because graphene, is a 2D sp^2 carbon-based uniatomic sheet that has been extensively used to produce hydrogen and storage of hydrogen. Graphene has a wide base of application in the field of photocatalysis, supercapacitors and electronic gadgets due to its excellent conductivity ($\sim$15,000 $m^2\ V^{-1}\ s^{-1}$ at room temperature), high chemical stability, a large theoretical specific surface area ($\sim$2600 $m^2\ g^{-1}$), pore size distribution and remarkable capacitive performance. Graphene or reduced graphene oxide also enhances the active sites and the adsorption in a photocatalytic system for hydrogen generation. This is due to the large specific surface area of Graphene. [29-33].

In this work the optimal amount of ZnO and rGO has been coupled into multicomponent heterojunctions to create good photocatalysts which has been further investigated to improve the photocatalytic activity. An enhanced adsorptivity of reactant, superior absorption of light and effective charge transfer and separation can be found with an enhancement in photocatalytic efficiency of rGO-ZnO (1:3) composites, can be observed in the present study [9]. Further Tungsten oxide (WO_3) is also incorporated into rGO-ZnO (1:3) nanocomposites to form rGO-ZnO (1:3)/WO_3 heterojunction photocatalysts to boost the yield of visible light-driven hydrogen production. Actually WO_3 stands out as a potential candidate with its outstanding optical properties, tuneable bandgap, and significant visible light absorption and it is also nontoxic, inexpensive, and stable in acidic and oxidative settings. Because of its unique electrical and optoelectronic properties, excellent photo-corrosion stability, and ease of recycling, it has potential applications in enhanced photocatalytic hydrogen production. Binary nanocomposites consisting of WO_3 and rGO-ZnO (1:3) show greater cumulative photo-efficiency than corresponding pure nanostructures due to the formation of Type-II heterojunction. The majority of Z-scheme photocatalysts have the drawback of requiring an electron/redox mediator; however, Type-II heterojunctions between two semiconductors permits a beneficial cyclic movement of photo-induced e^- and h+ couples, causing spatial separation and eliminating this necessity. To comprehensively characterise the synthesised nanocomposites, XRD, SEM, TEM, EDX, and PL are utilised.

The focus of this chapter is the synthesis of rGO-ZnO/WO_3 heterojunction photocatalysts, their characterization and their photocatalytic activity study for green hydrogen production. The specific objectives are enlisted below:

I. The synthesis of rGO-ZnO photocatalysts hydrothermally with various ZnO loadings in fixed rGO concentrations (1:1, 1:2, 1:3, and 1:4 weight ratios, respectively).
II. Photocatalytic performance study of rGO-ZnO (1:1, 1:2, 1:3, and 1:4 weight ratios) to get optimal ZnO loading in rGO for maximum hydrogen production.
III. Modification of optimal rGO-ZnO photocatalyst by WO_3 to obtain best photoactive rGO-ZnO/WO_3 heterojunction photocatalyst for increasing the yield of hydrogen production.
IV. Structural and morphological characterization of the synthesized photocatalyst.
V. Photocatalytic performance study of rGO-ZnO/WO_3 photocatalyst under visible light illumination.
VI. Identification of the Product.
VII. Photocatalytic activity study.

The major research problem is addressed in this chapter; the problem definition is as follows:

Problem definition:

Synthesis, characterization and photocatalytic performance study of rGO-ZnO(1:3)/WO_3 heterojunction photocatalyst for solar green hydrogen generation

2.2. Experimental

2.2.1 Materials and Methods

All reagents namely zinc nitrate [$Zn(NO_3)_2.6H_2O$], KOH, sodium tungstate dihydrate ($Na_2WO_4.2H_2O$), sodium chloride (NaCl), hydrochloric acid , ammonia (25%), graphite flakes (Loba Chemi, extra pure 99.5 %, 50 µm average sizes, bulk density 20-30 gm. /100 ml), sulphuric acid (H_2SO_4) (Merck, 98%), phosphoric acid (H_3PO_4) (Merck, 88%) potassium permanganate ($KMnO_4$) (Merck, 99% purity), hydrogen peroxide (H_2O_2) (Merck, 30%), hydrochloric acid (HCl) (merck-35%), ethanol (C_2H_5OH) (Merck, 99.9% purity), deionized water (with resistivity of 18.25 MΩ), of analytical grade, procured from Sigma Aldrich are used without any further purification.

2.2.2 Synthesis of ZnO nanocomposite:

In the direct precipitation method, zinc nitrate and KOH are utilised as precursors to generate ZnO nanocomposite. Deionized water is utilised in this investigation to make aqueous solutions of 0.2 M $Zn(NO_3)_2.6H_2O$ and 0.4 M KOH. To make a white suspension, forcefully mix the zinc nitrate solution while gradually adding the KOH solution. The white residue was centrifuged at 5000 rpm for 30 minutes, then washed three times with distilled water and once more with ethanol. The finished product is calcined in an air atmosphere for three hours at 500°C.

2.2.3 Synthesis of rGO-ZnO:

To study the effect of ZnO loading on the photocatalytic H_2 production, the synthesis of rGO-ZnO nanorod is performed with different amount of ZnO loading of 1:1, 1:2, 1:3 and 1:4 weight ratio, respectively, with a fixed concentration of rGO solution. Different amount of zinc nitrate hexahydrate [$Zn(NO_3)_2.6H_2O$] are separately added to 50 mL of GO solution which is synthesised by the modified Hummers method. The pH value of four different rGO/ZnO with weight ratio of 1:1, 1:2, 1:3 and 1:4 is set to 11 by ammonia (25%) under stirring for 3 hours. After stirring, the four mixed solutions are transferred separately to 100 ml Teflon-sealed autoclaves for 24 hours of heat treatment at 180°C. rGO-ZnO (1:1), rGO-ZnO (1:2) rGO-ZnO (1:3) and rGO-ZnO (1:4) nanocomposites are collected after cooling by extensively filtering and washing with water and ethanol and drying in a hot air oven at 75°C for 8 hours.

2.2.4 Synthesis of ZnO-WO_3 nanocomposite:

Hydrothermal processing of synthesised ZnO nanocomposite, sodium tungstate dihydrate ($Na_2WO_4.2H_2O$), and sodium chloride (NaCl) results in ZnO-WO_3 nanocomposite. As a surfactant, hydrochloric acid is employed in this procedure. 1 g of synthesised ZnO nanocomposite, 2 g of ($Na_2WO4.2H_2O$), and 0.74 g of NaCl are combined in 70 ml of deionized water and agitated for 60 minutes at 700 rpm. During the stirring procedure, 8 ml of HCl is added to the aforementioned solution drop by careful drop. After that, the mixture is continued churning for an additional 60 minutes. The solution turned pale yellow after the addition of HCl. After 60 minutes of stirring, the whitish yellow solution is placed in a Teflon-lined autoclave and heated in the muffle furnace at 180°C for 24 hours. Finally, the synthesised catalyst is washed three times with distilled water and ethanol before being dried in a hot air furnace at 75°C.

2.2.5 Synthesis of rGO–ZnO(1:3)/WO_3 heterojunction photocatalyst:

It has been revealed that rGO/ZnO(1:3) exhibits the enhanced photocatalytic hydrogen generation of all the synthesised rGO/ZnO photocatalysts [Figure 2.6 a]. So that to form rGO–ZnO(1:3)/WO_3 heterojunction photocatalyst for achieving highest yield of H_2 production a solution of sonicated rGO-ZnO (1:3) is combined with sodium tungstate dihydrate ($Na_2WO_4.2H_2O$) and sodium chloride (NaCl). In this 60-minute stirring operation, the aforementioned solution is delivered as a surfactant by hydrochloric acid. Following magnetic stirring, the solution is transported to a Teflon-lined autoclave and placed in a furnace for 24 hours of heat treatment at 180°C. After filtering and washing with water and ethanol, the rGO-ZnO (1:3)/WO_3 heterojunction photocatalyst is dried at 75°C for 8 hours. Figure 2.1 represents the schematic image of synthesis procedure of rGO-ZnO(1:3)/WO_3 heterojunction photocatalyst.

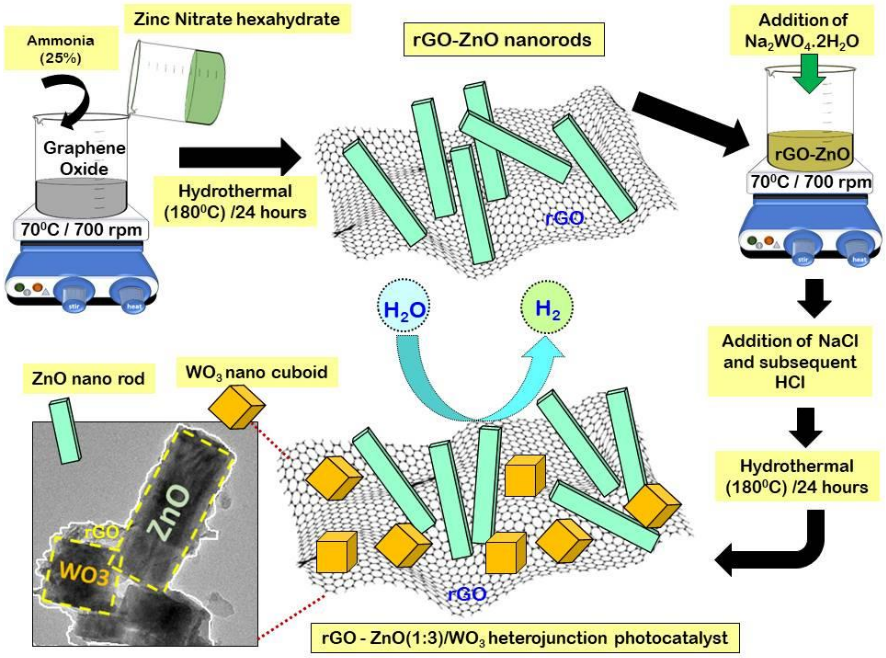

Figure 2.1: Schematic representation of synthesis procedure of rGO-ZnO(1:3)/WO_3 heterojunction photocatalyst

2.2.6. Characterization:

The morphological structure of the synthesised nanocomposite is examined using scanning electronic microscopy (SEM - JEOL JSM-7600) and transmission electronic microscopy (JEOL JEM 2100). The crystallographic characteristics of the resulting nanocomposite are examined using an X-ray diffractometer (Xpert-PRO diffractometer system). The UV-Vis absorbance spectra of synthesised visible light-active nanocomposite are examined using a PerkinElmer Lambda 35 UV-Vis spectrophotometer to determine the absorption edge and band gap energy. To assess the lifetime of the photogenerated charges, photoluminescence (PL) spectra are performed using a TRIAX 320 detector (excitation wavelength: 380 nm). X-ray photoelectron spectroscopy (XPS: AXIS Supra Model with Al K - 1486.6 eV Dual Al K / Mg Ka chromatic X-ray source) is used to examine the defect type, concentration, chemical state composition, and variation in band structure in the sample.

2.2.7. Photocatalytic Hydrogen Generation:

The photocatalytic performance of the synthesised nanocomposite is assessed by producing H_2 through water splitting. The experiment utilised a solar simulator (manual shutter, Newport Oriel LCS-100) and the intensity was set to 113 mW cm^{-2}. The AM 1.5G air mass filter installed in the LCS-100 solar simulator (Class ABB) can accomplish class A spectral performance in conformance with the output of 1 sun irradiance as specified by IEC and ASTM standards. Photocatalytic hydrogen generation of all catalysts was performed at room temperature using a specially designed glass photocatalytic reactor which is represented in Figure 2.2. 0.2 g of the photocatalyst was dispersed in 100 ml of deionized water, and 5 ml CH_3OH was used as sacrificial agent. Before each photocatalytic reaction experiment, the developed glass reactor was purged to remove O_2 (air) via a vacuum pump (Rivotek, 30 LPM). The photocatalytic reaction is continued for more than 7 hours until the rate of hydrogen generation decays to zero.

The performance of a specific photocatalyst is analysed in terms of photocatalytic activity and apparent quantum efficiency. The photocatalytic activity (of the different photocatalysts is evaluated from the cumulative hydrogen production versus time data. Experiments are performed using the full band spectra of the solar simulator as well as bandpass filters at 420 nm. Apparent quantum yields (AQYs) are determined using a 420 nm band pass filter. The light intensity was adjusted to $100\,\mathrm{mW\,cm^{-2}}$ which was measured using a power meter (Newport 843-R). The radius was irradiated across an area of $14.44\,\mathrm{cm^2}$. The number of incident photons from the solar simulator (Newport LCS-100) was measured with a power meter (843-R, Newport). Apparent quantum yields (AQYs) were calculated by the following equation (2.1), as previously reported [34].

$$\mathrm{AQE}(\%) = \frac{2\times\text{The number of evolved Hydrogen molecules}}{\text{The number of incident photons}} \times 100 \qquad (2.1)$$

Figure 2.2: Experimental set-up for photocatalytic performance study of rGO-ZnO(1:3)/WO_3 heterojunction photocatalyst using solar simulator as visible light source

2.3. Results and discussion

2.3.1 Morphologies and structure of rGO-ZnO (1:3) /WO_3 heterojunction photocatalyst

2.3.1.1 XRD analysis:

As-produced ZnO, rGO-ZnO (1:3), ZnO-WO_3 and rGO-ZnO(1:3)/WO_3 crystal quality and orientation are examined using X-ray diffraction (XRD), as seen in Figure 2.3 a. Sharp peaks can be seen in all synthesised nanocomposites patterns, proving that all nanocomposites are extremely crystalline. The XRD spectra of synthesized ZnO nanorods show several reflections at $2\theta = 31.33°, 34.45°, 36.20°, 47.46°, 56.32°, 62.56°, 66.36°, 67.74°$, and $69.22°$, indicating typical diffraction peaks of hexagonal wurtzite crystal structure ZnO nanorods with crystallographic planes of (100), (002), (101), (102), (110), (103), (200), (112), and (201) respectively (JCPDS No. 36-1451) [9,18,34]. Peaks in the XRD spectra of WO_3 nanocuboids are located at $2\theta = 23.76°, 25.84°, 28.65°, 30.27°, 33.54°, 41.24°$, and $55.16°$ in that these are indexed to the formation of (002), (120), (112), (204), (220), (222), and (420) planes (JCPDS card No. 43-1035), respectively, which attributed to growth of WO_3

nanocuboids into monoclinic crystal phase [35-37]. The diffraction peak at 2θ = 24.3° in rGO-ZnO (1:3) /WO_3 heterojunction photocatalysts reveal the presence of reductive graphene oxide and also indicates a complete reduction of GO by hydrothermal process during the growth of ZnO [19-20]. Furthermore, the XRD spectra of rGO-ZnO (1:3) /WO_3 heterojunction photocatalyst displays diffraction peaks for ZnO nanorods as well as small, distinct peaks at about 2θ = 16.7° and 17.3° can be assigned to WO_3, affirming the combination of ZnO and WO_3 in the nanocomposite photocatalyst.

2.3.1.2 XPS analysis:

XPS has been performed to investigate the surface chemical states of the rGO-ZnO (1:3) /WO_3 heterojunction photocatalyst. Figure 2.3 b shows the high-resolution Zn 2p spectra of rGO-ZnO (1:3)/WO_3 heterojunction photocatalyst under visible light irradiation that reveals two symmetrical peaks corresponding to the main peaks at 1022.78 eV (Zn 2p3/2) and 1045.96 eV (Zn 2p1/2) correspond to + 2 valence state of Zn ions. In the W 4f spectrum of W, shown in Figure 2.3 c, the main peaks are observed at 38.59 and 36.47 eV approximately, which result from W $4f_{5/2}$ and W $4f_{7/2}$, respectively indicating the existence of the W^{6+} species of WO_3.

Figure 2.3 d shows that the XPS of C 1s pattern of the rGO-ZnO (1:3)/WO_3 composite can be deconvoluted into three peaks at 285.85, 287.48, and 289.66 eV, which can be assigned to the surface adventitious epoxide (C–C), hydroxyl (C–O), and carboxyl (O–C=O) groups, respectively. The results confirmed the existence of rGO. The O 1s XPS pattern in Figure 2.3-e displayed three peaks at 531.56, 532.92 and 535.16 eV, corresponding to lattice O (Zn–O, W–O), hydroxyl O (–OH), and the O of the O-C-Zn/W bonds, respectively. Figure 2.3-f shows the survey scan of X-ray photoelectron spectra (XPS) of the rGO-ZnO/WO_3 heterojunction photocatalyst. The XPS patterns of rGO-ZnO(1:3)/WO_3 suggests that electrons transferred from WO_3 to rGO or ZnO or at the interfaces. Therefore, both ZnO and WO_3 has been successfully anchored on the rGO nanosheets [33,35,40,41].

2.3.1.3 SEM & TEM analysis:

Figure 2.4 (a-c) displays the SEM images of pristine ZnO, rGO-ZnO (1:3), ZnO-WO_3, and rGO-ZnO (1:3) /WO_3 photocatalysts. The hexagonal cross section of a ZnO nanorod in SEM picture of ZnO-WO_3 of Figure 2.4 b is an indication of a hexagonal wurtzite structure supported by WO_3 nanocuboids. The hexagonal nanorod structures formed by the rGO and

WO_3 nanocuboids are encased in the rGO-ZnO (1:3) /WO_3 heterojunction photocatalyst in figure 2.4-f, and the ZnO-WO_3 nanorods have an average diameter of 206 nm and 120 nm, respectively. Moreover, figure 2.4-c clearly depicts the close surface contact between rGO-ZnO (1:3) and WO_3, which is also visible in TEM picture of figure 2.4-f.

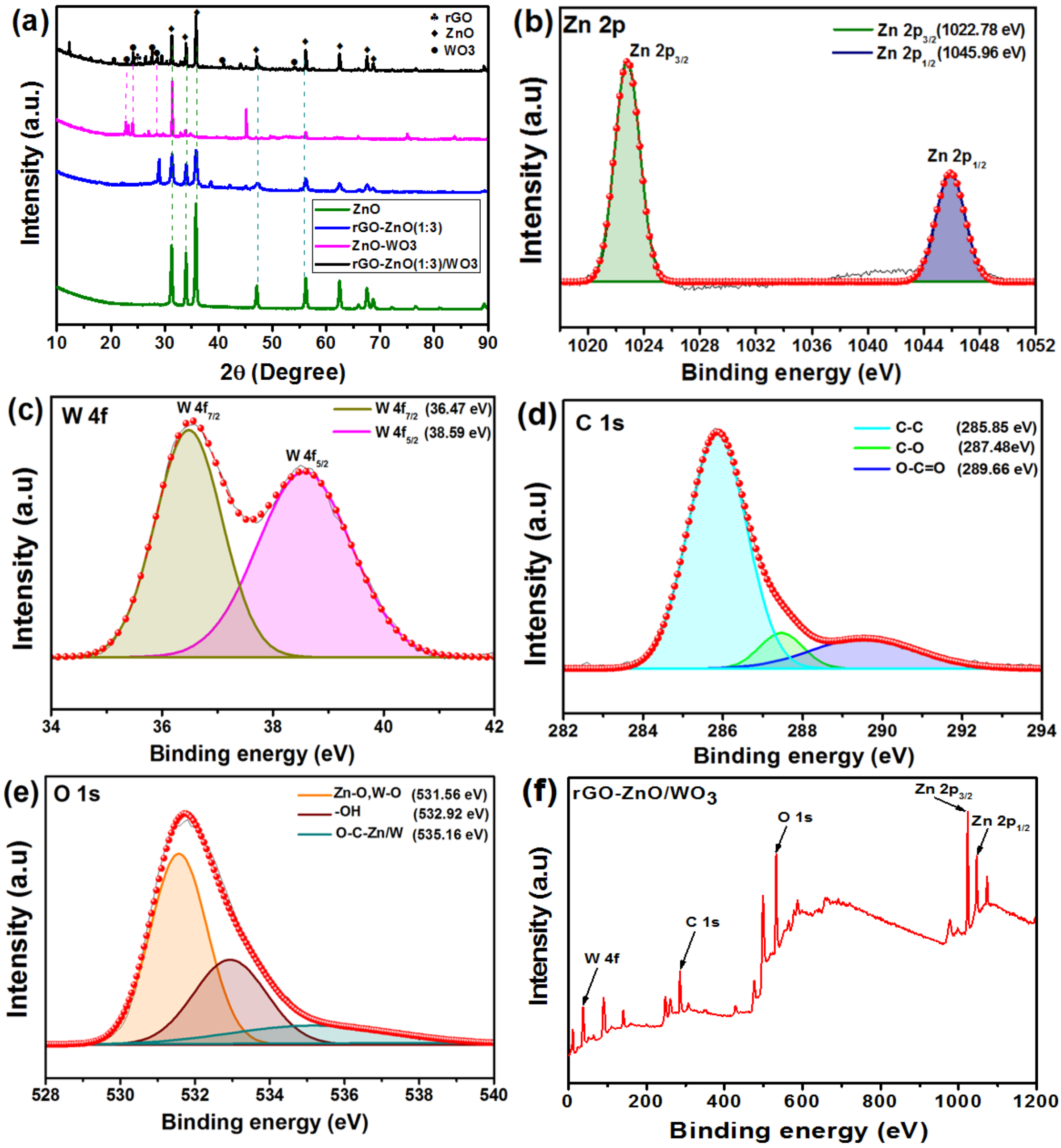

Figure 2.3: (a) XRD analysis of ZnO, rGO-ZnO(1:3), ZnO-WO_3 and rGO-ZnO(1:3)/WO_3 heterojunction photocatalysts, Core level XPS scan of (b) Zn 2p, (c) W 4f, (d) C 1s, and (e) O 1s, (f) survey scan of X-ray photoelectron spectra (XPS) of the rGO-ZnO/WO_3 heterojunction photocatalyst.

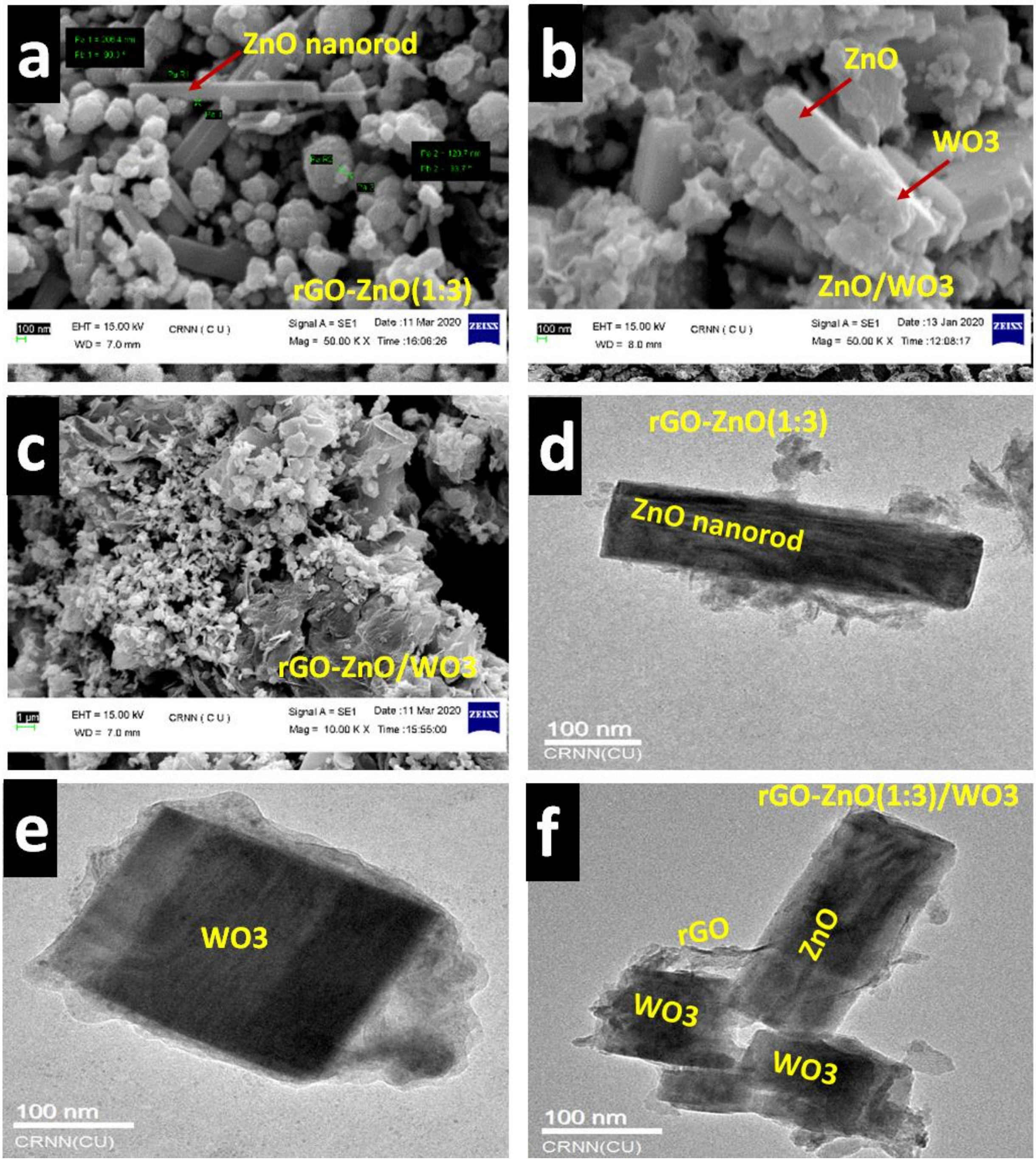

Figure 2.4: SEM images of (a) rGO-ZnO(1:3), (b) ZnO-WO$_3$, (c) rGO-ZnO(1:3)/WO$_3$ nanohybrid and TEM images of (d) rGO-ZnO (1:3), (e) WO$_3$, (f) rGO-ZnO (1:3)/WO$_3$.

TEM picture of Figure 2.4-d shows the ZnO hexagonal nanorod is embedded in the sheet of rGO; TEM image of figure 2.4-e shows the unique nanocuboid structure of WO$_3$. The interfacial charge transfer during light illumination is boosted as a result of appropriate contact between rGO-ZnO (1:3) and WO$_3$, and this might be useful for the enhanced photocatalytic activity [38-40]

2.3.2 Optical Studies

2.3.2.1 UV-Vis spectra and Band gap energy analysis:

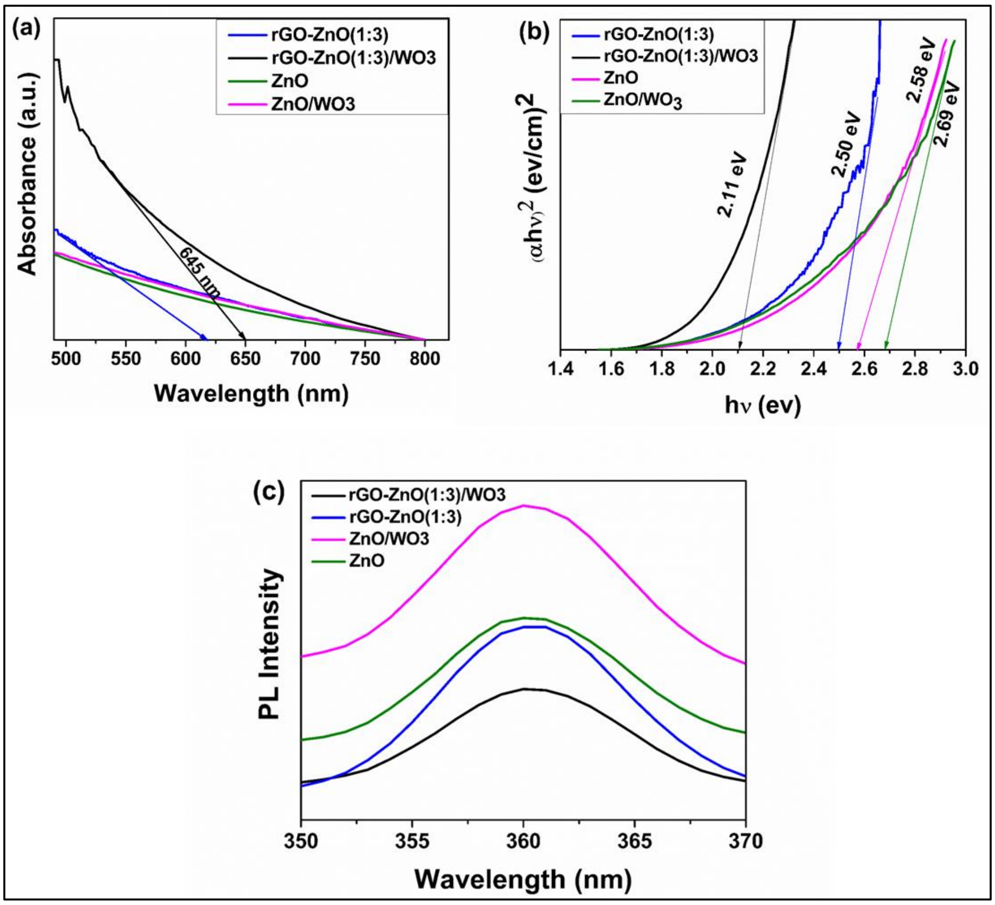

Figure 2.5: (a) UV-Vis absorbance spectra of ZnO , rGO-ZnO (1:3), ZnO-WO_3 and rGO-ZnO (1:3)/ WO_3 nanohybrid, (b)Tauc plot of ZnO, rGO-ZnO (1:3) , ZnO-WO_3 and rGO-ZnO, (c) Photoluminescence spectra (PL) of ZnO, rGO-ZnO(1:3), ZnO-WO_3 and rGO-ZnO(1:3)/WO_3 nanohybrid.

Figure 2.5 (a & b) displays the UV-vis absorbance spectra and Tauc plot [$(\alpha h\nu)^2$ vs. $(h\nu)$] of pure ZnO, rGO-ZnO (1:3), ZnO-WO_3, and rGO-ZnO (1:3) /WO_3 heterojunction photocatalysts, respectively. In contrast to rGO-ZnO (1:3), rGO-ZnO (1:3) /WO_3 displays a red shift in the absorption edge in the visible light range, allowing photo-generated electrons and holes to move more easily. According to studies, pure WO_3 and pure ZnO have small band gaps of 2.6-2.8 eV and 3.37 eV, respectively. Pure ZnO also has a band width that is greater than the band width that is strictly prohibited for pure WO_3. The absorption edge of the rGO-ZnO (1:3) photocatalyst in Figure 2.5 a is 617 nm, whereas the absorption edge of the rGO-ZnO (1:3)/WO_3 heterojunction photocatalyst is increased to 645 nm due to the addition of WO_3, which changes the forbidden band width of the nanocomposite and enhances optical absorption performance in the visible light region. Tauc plots may be used to calculate the band gap (E_g) of photocatalysts using the equation (2.2):

$$\alpha h\nu = A(h\nu - E_g)^n \tag{2.2}$$

In this equation, the photon energy is indicated by 'h', the absorption coefficient by 'α', and the proportionality constant by 'A'. According to Tauc plots in Figure 2.5-b, the optical band gaps of pure ZnO, ZnO-WO_3, rGO-ZnO (1:3), and rGO-ZnO (1:3)/WO_3 photocatalysts are 2.69, 2.58, 2.50, and 2.11 eV, respectively. These findings imply that the optical band gap value of rGO-ZnO (1:3)/WO_3 heterojunction photocatalysts is decreasing. ZnO and WO_3 are both n-type semiconductors with variable band gap energies [29]. As a consequence, when rGO-ZnO (1:3) and WO_3 are joined to form a composite material, numerous unoccupied states with varying energies may be identified inside the band gap. As a result of the narrowing of the band gap energy in the rGO-ZnO (1:3)/WO_3 heterojunction due to the development of oxygen vacancies, photo electron transfer under visible light irradiation has been accelerated, resulting in enhanced photocatalytic hydrogen generation.

2.3.2.2 Photoluminescence (PL) spectrum analysis:

The photoluminescence (PL) spectrum may be used to investigate the photo-recombination rate of electron-hole pairs. At an excitation wavelength of 380 nm, figure 2.5-c shows the composite PL spectrum of pure ZnO, ZnO-WO_3, rGO-ZnO (1:3), and rGO-ZnO (1:3)/WO_3 photocatalysts. The change in absorption strength towards higher wavelengths is clearly seen in the absorption spectra, as previously indicated in figure 2.5-a. When the heterojunction photocatalyst is stimulated at this wavelength, a strong emission peak develops at 645 nm for all of them. The PL emission spectra reveal a change in intensity with regard to WO_3 loading rather than a shift to higher wavelength. The intensity changes in the order of rGO-ZnO (1:3)/WO_3 < rGO-ZnO (1:3) < ZnO < ZnO-WO_3, accordingly. Using rGO-ZnO (1:3), the PL intensity is reduced in the presence of WO_3. The suppression of the electron-hole recombination rate is directly related to the decrease in intensity. The lowered recombination rate demonstrates effective charge transfer inside the rGO-ZnO (1:3)/WO_3 photocatalysts, implying that rGO primarily accelerates electron transfer from ZnO to WO_3, increasing the rate of hydrogen evolution owing to the photocatalytic performance of rGO-ZnO (1:3)/WO_3 heterojunction photocatalysts [15,24].

2.3.3 Photocatalytic Hydrogen generation

At first the photocatalytic performances of all weight ratios of rGO-ZnO nanocomposites are evaluated by the rates of the photocatalytic H_2 production by using 3.3 vol% methanol aqueous solution under visible light irradiation of Light Emitting Diode (LED) lamp for 7 h. A comparable study of the photocatalytic H_2 production rate of all rGO-ZnO nanocomposites is shown in figure 2.6-b. Methanol is used as holes sacrificial reagent under visible light irradiation in order to maintain high rates of reaction and large scale production of H_2. It is clearly observed in the figure 2.6-a that different ratios of rGO-ZnO show better performance in order of rGO-ZnO (1:3) (58.75 mmol g^{-1}) > rGO-ZnO (1:2) (44.95 mmol g^{-1}) > rGO-ZnO (1:4) (36.02 mmol g^{-1}) > rGO-ZnO (1:1) (23.856 mmol g^{-1}) to produce hydrogen during 7h visible light illumination of LED lamp. In figure 2.6-b it is observed that rGO-ZnO (1:3) shows the best photocatalytic H_2 production rate of 8.393 mmol g^{-1} h^{-1} among all different rGO-ZnO compositions.

After that the photocatalytic performances of rGO-ZnO(1:3) along with ZnO, ZnO-WO_3 and rGO-ZnO (1:3)/WO_3 nanocomposites are evaluated by the rates of the photocatalytic H_2 production by using 3.3 vol% methanol aqueous solution under irradiation of solar simulator for 7 h to achieve highest yield of H_2 production. Again a comparable study of the photocatalytic H_2 production rate of all above mentioned nanocomposites is shown in figure 2.6-d. Methanol is used as holes sacrificial reagent under visible light irradiation in order to maintain high rates of reaction and large scale production of H_2. It is clearly observed in the figure 2.6-c that pure ZnO, ZnO-WO_3, rGO-ZnO (1:3), and rGO-ZnO (1:3)/WO_3 heterojunction photocatalyst show better performance in order of ZnO (18 mmol g^{-1}) <ZnO-WO_3 (31.03 mmol g^{-1}) <rGO-ZnO (1:3) (73.2 mmol g^{-1}) <rGO-ZnO (1:3)/WO_3 (93 mmol g^{-1}) to produce H_2 during 7h visible light illumination. In figure 2.6-d the pure ZnO shows photocatalytic H_2 production rate of 2.57 mmol g^{-1} $h^{-1,}$ which is a very low photocatalytic activity because of its fast recombination of photogenerated electron-hole pairs. The incorporation of WO_3 nanocuboid in ZnO nanorod enhances photocatalytic H_2 production rate up to the 4.43 mmol g^{-1} h^{-1} for ZnO-WO_3 nanocomposites, which is about 1.72 times higher than that of ZnO. The incorporation of optimal amount of ZnO in rGO significantly enhances the photocatalytic H_2 production rate upto 10.46 mmol g^{-1} h^{-1} for rGO-ZnO (1:3) nanocomposites, which is about 2.36 times higher than that of ZnO-WO_3 nanocomposites.

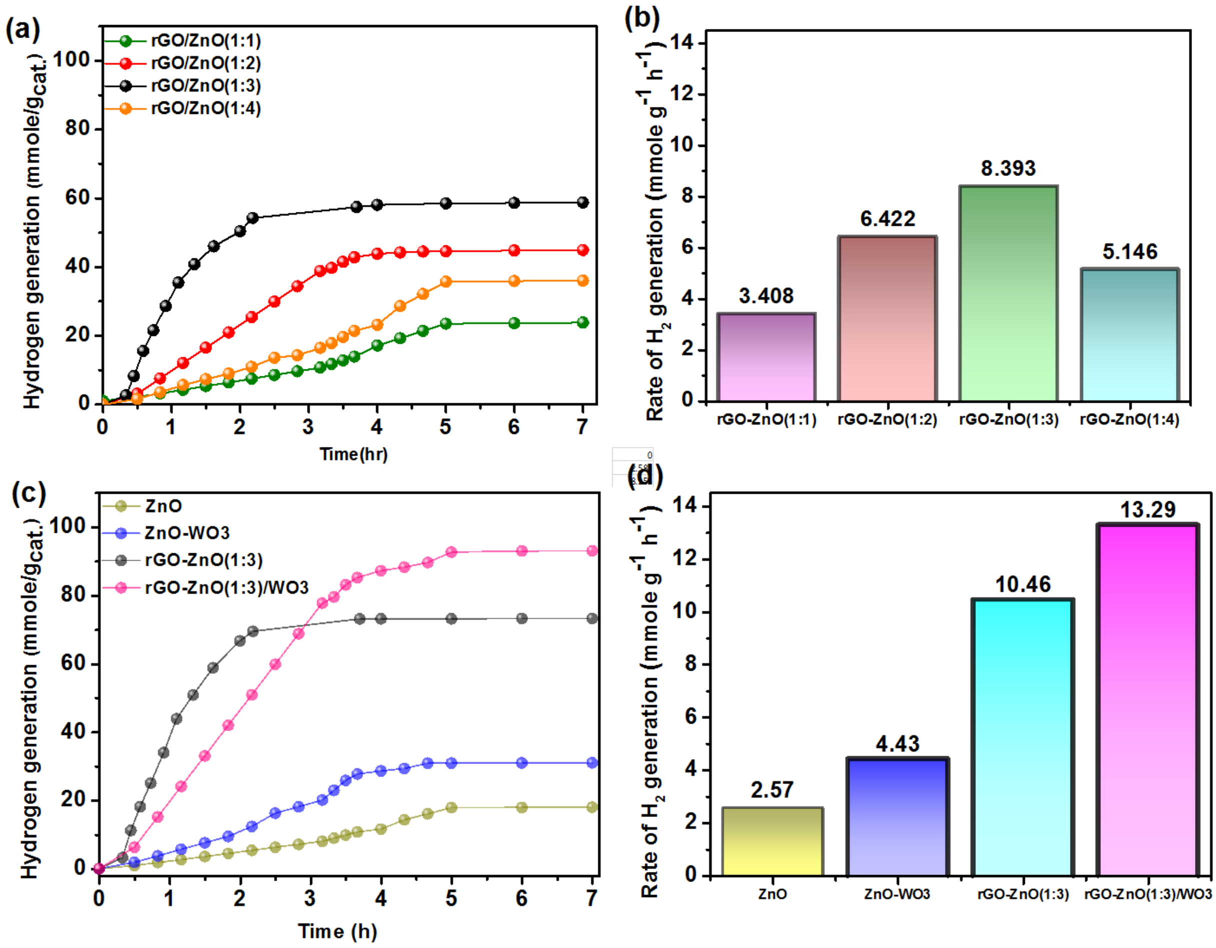

Figure 2.6: (a) Photocatalytic hydrogen generation using rGO/ZnO photocatalysts having different ratios of rGO and ZnO under visible light irradiation of LED (b) Photocatalytic activity study of different rGO/ZnO (1:1, 1:2, 1:3, 1:4) photocatalysts under visible light irradiation of LED (c) Photocatalytic hydrogen generation using ZnO, ZnO-WO_3, rGO-ZnO (1:3) and rGO-ZnO (1:3)/WO_3 Photocatalyst and irradiation of solar simulator (d) Photocatalytic activity study of ZnO, ZnO-WO_3, rGO-ZnO (1:3) and rGO-ZnO (1:3)/WO_3 photocatalysts using solar simulator.

The incorporation of WO_3 in rGO-ZnO (1:3) further enhances the photocatalytic H_2 production rate up to 13.29 mmol g^{-1} h^{-1} for rGO-ZnO (1:3)/ WO_3 heterojunction photocatalysts which is about 1.27 times higher than that of rGO-ZnO (1:3). The result suggests that the incorporation of rGO and WO_3 in ZnO nanorods enhance the visible light absorption and suppress the recombination of electron hole pairs in rGO-ZnO (1:3)/WO_3 to enhance the charge separation, which is demonstrated in the photoluminescence (PL) study. With further enhancement of the amount of ZnO in rGO, the photocatalytic activity decreases due to a reduction in active sites for hydrogen production reaction. Lastly rGO-ZnO

(1:3)/WO_3 heterojunction photocatalysts show the best visible active photocatalytic H_2 production. An apparent quantum yield (AQY) of 3.40% is determined for the rGO-ZnO (1:3)/WO_3 heterojunction photocatalyst at 420 nm. Table 2.1 compares the photocatalytic activities of different photo-catalyst of this study with those of literature reported value.

Table 2.1: Comparative photocatalytic activity data of different photo catalyst

Photocatalyst	**Light Source**	**Activity (mmole g^{-1} h^{-1})**	**References**
WO_3/TiO_2/rGO	Solar simulator	0.245	**[17]**
WO_3/TiO_2	Solar simulator	0.105	**[18]**
ZnO nanoparticle	Solar simulator	4.90	**[38]**
ZnO–graphene	Solar simulator	4.35	**[39]**
$WO_3/ZnIn_2S_4$	Solar simulator	1.945	**[40]**
g-C_3N_4/WO_3	Solar simulator	0.963	**[41]**
rGO-ZnO (1:3)	Solar simulator	10.46	**This work**
rGO-ZnO(1:3)/WO_3	**Solar simulator**	**13.29**	**This work**

2.4. Mechanism for enhanced performance of rGO-ZnO (1:3)/WO_3 heterojunction photocatalysts

WO_3 and rGO-ZnO (1:3) nanocomposite are the typical semiconductors. Figure 2.7 depicts the computative energy shift of rGO-ZnO (1:3) in the presence of WO_3 when both are exposed to visible light. The greater photocatalytic activity of the rGO-ZnO (1:3)/WO_3 composite is due to the difference in energy levels between WO_3 and rGO-ZnO, which reduces the band gap. In the current system, WO_3 operates as an absorber as it can harness the the visible spectra, while the low band gap (2.7 eV) enables electron-hole pair recombination via coupling with rGO-ZnO (1:3). When a rGO-ZnO (1:3)/WO_3 mixed oxide composite is exposed to visible light, due to the large gap in absorption, the activation of ZnO is not possible for producing photogenerated electron-hole pairs, whereas narrow band gap WO_3 efficiently absorbs the visible light, to generate photon excited electron-hole pairs.

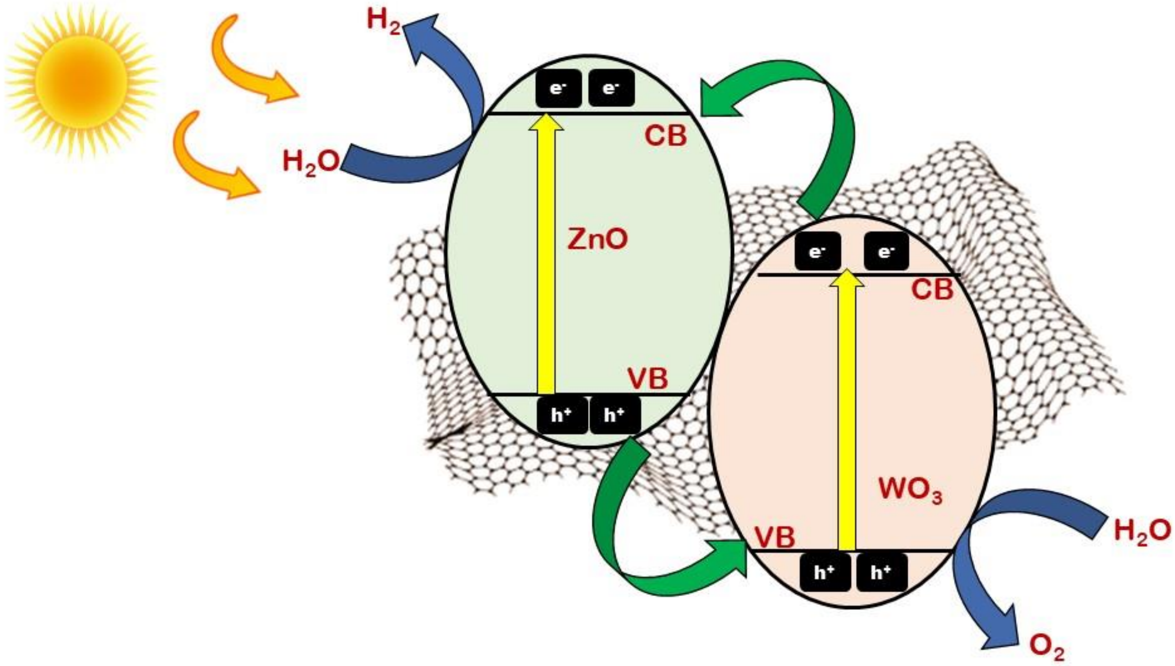

Figure 2.7: Mechanism of enhanced H_2 evolution process in the rGO-ZnO (1:3)/WO_3 composite under visible light irradiation.

Due to the high electronic conductivity of rGO, photogenerated electrons generated in WO_3 transfer their electrons to the conduction band (CB) of ZnO, reducing the possibility of recombination of photogenerated electron-hole pairs. Finally, photogenerated electrons are transferred from the conduction band of ZnO to the surface of rGO sheet. As a result, photogenerated charge-hole-electron pair recombination on the surface of ZnO-WO_3 is considerably decreased, successfully separating photogenerated carriers. Following that, the photogenerated electrons transferred from the ZnO CB to the surface-active sites of rGO nanosheets have a high reducing power, and the photogenerated electrons reduce the diffused water molecules in the photocatalytic reaction and accompanied by oxidising sacrificial reagent by the photogenerated holes to generate H_2. The transmission of photogenerated electrons happens as a "step" from a macroscopic perspective, with ZnO functioning as a "bridge." Moreover, the high specific surface area and dense pore structure of rGO-ZnO (1:3)/WO_3 improve photocatalytic H_2 generation yield.

2.5 Detailed cost-analysis of rGO-ZnO/WO_3

Table 2.2

Chemical used	Chemicals	Approx. quantity	Cost (Rs.)	Cost (Dollar)
rGO-ZnO/WO_3	Graphite flakes	0.02 g	281.8	3.4
	Sodium tungstate dihydrate	3.806	349.6	4.22
	Zinc nitrate	8 g	249.2	3.00
	Ammonia	10 ml	207.3	2.50
	NaCl	1.5	3.6	0.043
	KOH	4.0	21.908	0.26
	Oxalic acid	1	512.8	6.19
	Deionized water	2 L	120	1.45
	Phosphoric Acid	10 ml	264.1	3.19
	Hydrogen Peroxide	10 ml	57.48	0.69
	Hydrochloric Acid	40 ml	13.8	0.17
	Ethanol (for synthesis & washing)	20 ml	12	0.14
	Sulphuric Acid	10 ml	9.8	0.12
Electricity Involved	Stirring	54.6 unit (30 hours)	485.9	5.87
	Drying	13 unit (10 hours)	115.7	1.40
	Calcination	20 unit (42 hours)	178	2.15
Total			2882.99	34.79

1 g of the synthesised rGO-ZnO-WO_3 photo catalyst typically costs $34.79.

The stirring and drying cost has been calculated using the following equation (2.3):

$$\text{Stirring, Drying cost} = \frac{\text{Instrument power (watt)} \times \text{time} \times \text{unit cost}}{1000} \quad (2.3)$$

2.6. Conclusions

- A hydrothermal process is enrooted to synthesised rGO-ZnO (1:3)/WO_3 nanohybrid powder photocatalysts. The characterization results confirm that the ZnO nanorods and WO_3 nanocuboids are connected by rGO sheets in synthesised rGO-ZnO (1:3)/WO_3 photocatalyst.

- The optimal loading of ZnO in rGO with the ratio of 1:3 shows the enhanced hydrogen production under visible light irradiation.
- Here WO_3 is used as a strong electron transport channel, the hydrogen generation activity of rGO-ZnO/WO_3 is significantly increased.
- The rGO-ZnO (1:3)/WO_3 heterojunction photocatalyst has the greatest hydrogen generation rate of 13.29 mmol g^{-1} h^{-1}, which is roughly 5.17 times greater than pure ZnO and 3 times higher than the ZnO-WO_3 nanocomposite. Most notably, under the same conditions, the rGO-ZnO (1:3)/WO_3 heterojunction photocatalyst exhibits much greater hydrogen evolution activity than the rGO-ZnO (1:3).
- An apparent quantum yield (AQY) of 3.40% is determined for the rGO-ZnO (1:3)/WO_3 heterojunction photocatalyst at 420 nm.
- Inclusion of rGO and WO_3 can boost electron transport capacities while inhibiting recombination of electron-hole pairs, resulting in increased hydrogen evolution activity. This work proposes a method for developing a robust rGO-ZnO(1:3)/WO_3 heterojunction photocatalyst that is both environmentally friendly and affordable in cost for solar green hydrogen production.

2.7 References

1. Tong, H., Ouyang, S., Bi, Y., Umezawa, N., Oshikiri, M., & Ye, J. (2012). Nano-photocatalytic materials: Possibilities and challenges. *Advanced Materials*, 24(2), 229.
2. Hisatomi, T., Kubota, J., & Domen, K. (2014). Recent advances in semiconductors for photocatalytic and photoelectrochemical water splitting. *Chemical Society Reviews*, 43(22), 7520.
3. Tahir, M., Tasleem, S., & Tahir, B. (2020). Recent development in band engineering of binary semiconductor materials for solar driven photocatalytic hydrogen production. *International Journal of Hydrogen Energy*, 45(28), 15985.
4. Lee, S. L., & Chang, C. J. (2019). Recent Progress on Metal Sulfide Composite Nanomaterials for Photocatalytic Hydrogen Production. *Catalysts*, 9(5), 457.
5. Jia, L., Tan, X., Yu, T., & Ye, J. (2022). Mixed Metal Sulfides for the Application of Photocatalytic Energy Conversion. *Energy & Fuels*, 36(18), 11308.
6. Ahmed, M., & Xinxin, G. (2016). A review of metal oxynitrides for photocatalysis. *Inorganic Chemistry Frontiers*, 3(5), 578.

7. Yang, H., Amari, H., Liu, L., Zhao, C., Gao, H., He, A.,…Cooper, A. I. (2020). Nano-assemblies of a soluble conjugated organic polymer and an inorganic semiconductor for sacrificial photocatalytic hydrogen production from water. *Nanoscale*, 12(39), 24488.
8. Bai, Y., Wilbraham, L., Slater, B. J., Zwijnenburg, M. A., Sprick, R. S., & Cooper, A. I. (2019). Accelerated Discovery of Organic Polymer Photocatalysts for Hydrogen Evolution from Water through the Integration of Experiment and Theory. *Journal of the American Chemical Society*, 141(23), 9063.
9. Wang, S., Zhu, B., Liu, M., Zhang, L., Yu, J., & Zhou, M. (2019). Direct Z-scheme ZnO/CdS hierarchical photocatalyst for enhanced photocatalytic hydrogen-production activity. *Applied Catalysis B: Environmental*, 243, 19.
10. Wu, Z., Li, Y., Gao, L., Wang, S., & Fu, G. (2016). Synthesis of Na-doped ZnO hollow spheres with improved photocatalytic activity for hydrogen production. *Dalton Transactions*, 45(31), 11145.
11. Guo, S., Zhao, T., Jin, Z., Wan, X., Wang, P., Shang, J., & Han, S. (2015). Self-assembly synthesis of precious-metal-free 3D ZnO nano/microspheres with excellent photocatalytic hydrogen production from solar water splitting. *Journal of Power Sources*, 293, 17.
12. Reli, M., Edelmannová, M., Šihor, M., Praus, P., Svoboda, L., Mamulová, K. K., ... Kocˇí, K. (2015). Photocatalytic hydrogen generation from aqueous ammonia solution using ZnO photocatalysts prepared by different methods. *International Journal of Hydrogen Energy*, 40(22), 8530.
13. Khan, S., Je, M., Ton, N. N. T., Lei, W., Taniike, T., Yanagida, S., ... Katsumata, K. -I. (2021). C-doped ZnS-ZnO/Rh nanosheets as multijunctioned photocatalysts for effective hydrogen generation from pure water under solar simulating light. *Applied Catalysis B: Environmental*, 297, 120473.
14. Xiang, Q., & Yu, J. (2013). Graphene-Based Photocatalysts for Hydrogen Generation. *The Journal of Physical Chemistry Letters*, 4(5), 753.
15. Ghorbani, M., Abdizadeh, H., Taheri, M., & Golobostanfard, M. R. (2018). Enhanced photoelectrochemical water splitting in hierarchical porous ZnO/Reduced graphene oxide nanocomposite synthesized by sol-gel method. *International Journal of Hydrogen Energy*, 43(17), 7754.

16. Gang, R., Xu, L., Xia, Y., Zhang, L., Wang, S., & Li, R. (2021). Facile One-step Production of 2D/2D ZnO/rGO Nanocomposites under Microwave Irradiation for Photocatalytic Removal of Tetracycline. *ACS Omega*, 6(5), 3831.
17. He, F., Meng, A., Cheng, B., Ho, W., & Yu, J. (2020). Enhanced photocatalytic H2-production activity of WO3/TiO2 step-scheme heterojunction by graphene modification. *Chinese Journal of Catalysis*, 41(1), 9.
18. Wang, J., Wang, G., Jiang, J., Wan, Z., Su, Y., & Tang, H. (2020). Insight into charge carrier separation and solar-light utilization: rGO decorated 3D ZnO hollow microspheres for enhanced photocatalytic hydrogen evolution. *Journal of Colloid and Interface Science*, 564, 322.
19. Raja, A., Son, N., Swaminathan, M., & Kang, M. (2021). Facile synthesis of sphere-like structured ZnIn2S4-rGO-CuInS2 ternary heterojunction catalyst for efficient visible-active photocatalytic hydrogen evolution. *Journal of Colloid and Interface Science*, 602, 669.
20. Lin, H., Sui, X., Wu, J., Shi, Q., Chen, H., Wang, H., ... Tam, K. C. (2022). Robust visible-light photocatalytic HYDROGEN evolution on 2D RGO/Cd0.15Zn0.85In2S4–Ni2P hierarchitectures. *Catalysis Science & Technology*, 12(12), 4181.
21. Sadeghzadeh-Attar, A. (2020). Boosting the photocatalytic ability of hybrid BiVO4-TiO2 heterostructure nanocomposites for hydrogen production by reduced graphene oxide (rGO). *Journal of the Taiwan Institute of Chemical Engineers*, 111, 325.
22. Xie, X., Wang, R., Liu, E., Fan, J., Chen, B., & Hu, X. (2019). Fabrication of a Cu2-xSe/rGO heterojunction photocatalyst to achieve efficient photocatalytic hydrogen generation. *International Journal of Hydrogen Energy*, 44(63), 32042.
23. Yan, H., Liu, Y. -H., Yang, Y., Zhang, H. -Y., Liu, X. -R., Wei, J. -Z., ... Zhang, F. -M. (2022). Covalent organic framework based WO_3@COF/rGO for efficient visible-light-driven hydrogen evolution by two-step separation mode. *Chemical Engineering Journal*, 431, 133404.
24. Katsumata, H., Tachi, Y., Suzuki, T., & Kaneco, S. (2014). Z-scheme photocatalytic hydrogen production over WO_3/g-C3N4 composite photocatalysts. *RSC Advances*, 4(41), 21405.
25. Ma, L., Xu, J., Li, L., Mao, M., & Zhao, S. (2020). Hydrothermal synthesis of WO_3/CoS2 n-n heterojunction for Z-scheme photocatalytic hydrogen evolution. *New Journal of Chemistry*, 44(42), 18326.

26. Fu, J., Xu, Q., Low, J., Jiang, C., & Yu, J. (2019). Ultrathin 2D/2D WO_3/g-C3N4 step-scheme hydrogen-production photocatalyst. *Applied Catalysis B: Environmental*, 243, 556.
27. Grant, G. T., Morris, E. R., Rees, D. A., Smith, P. J. C., & Thom, D. (1973). Biological interactions between polysaccharides and divalent cations: The egg-box model. *FEBS Letters*, 32(1), 195.
28. Kumar, S., Reddy, N. L., Kushwaha, H. S., Kumar, A., Shankar, M. V., Bhattacharyya, K., ... Krishnan, V. (2017). Efficient electron transfer across ZnO-MoS2-RGO heterojunction for remarkably enhanced sunlight driven photocatalytic hydrogen evolution. *ChemSusChem*, 10(18), 3588.
29. Manzoor, M. F., Ahmed, E., Ahmad, M., Ahmad, I., Rana, A. M., Ali, A., ... Aziz, M. T. (2020). Enhanced photocatalytic activity of hydrogen evolution through Cu incorporated ZnO nano composites. *Materials Science in Semiconductor Processing*, 120, 105278.
30. Hamid, S. B. A., Teh, S. J., Lai, C. W., Perathoner, S., & Centi, G. (2017). Applied bias photon-to-current conversion efficiency of ZnO enhanced by hybridization with reduced graphene oxide. *Journal of Energy Chemistry*, 26, 302.
31. Xu, T., Zhang, L., Cheng, H., & Zhu, Y. (2011). Significantly enhanced photocatalytic performance of ZnO via graphene hybridization and the mechanism study. *Applied Catalysis B: Environmental*, 101(3-4), 382.
32. Yan, W., Wang, L., Wang, H. -Y., Chen, Q. -D., & Sun, H. -B. (2019). Ultrafast Spectroscopic Study of Insulator–Semiconductor–Semimetal Transitions in Graphene Oxide and Its Reduced Derivatives. *The Journal of Physical Chemistry C*, 123(37), 22550.
33. Ponnusamy, R., Venkatesan, R., Gangan, A., Samal, R., Chakraborty, B., Late, D. J., & Rout, C. S. (2019). Experimental and density functional theory investigations of catechol sensing properties of ZnO/RGO nanocomposites. *Applied Surface Science*, 495, 143588.
34. Prabhu, Y. T., Rao, V. N., Shankar, M. V., Sreedhar, B., & Pal, U. (2019). The facile hydrothermal synthesis of CuO@ZnO heterojunction nanostructures for enhanced photocatalytic hydrogen evolution. *New Journal of Chemistry*, 43(17), 6794.
35. Chaudhary, K., Shaheen, N., Zulfiqar, S., Sarwar, M. I., Suleman, M., Agboola, P. O., ... Warsi, M. F. (2020). Binary WO_3-ZnO nanostructures supported rGO ternary

nanocomposite for visible light driven photocatalytic degradation of methylene blue. *Synthetic Metals*, 269, 116526.

36. Zheng, J. Y., Haider, Z., Van, K. T., Pawar, A. U., Kang, M. J., Kim, C. W., & Kang, Y. S. (2015). Tuning of the crystal engineering and photoelectrochemical properties of crystalline tungsten oxide for optoelectronic device applications. *CrystEngComm*, 17(31), 6070.
37. Peng, F., Wang, S., Yu, W., Huang, T., Sun, Y., Cheng, C., ... Dai, N. (2020). Ultrasensitive ppb-level hydrogen gas sensor at room temperature based on WO_3/rGO hybrids. *Journal of Materials Science: Materials in Electronics*, 31(6), 5008.
38. Jiang, J., Wang, G., Shao, Y., Wang, J., Zhou, S., & Su, Y. (2022). Step-scheme ZnO@ZnS hollow microspheres for improved photocatalytic H2 production performance. *Chinese Journal of Catalysis*, 43(2), 329.
39. Xu, J., Cui, Y., Han, Y., Hao, M., & Zhang, X. (2016). ZnO–graphene composites with high photocatalytic activities under visible light. *RSC Advances*, 6(102), 96778.
40. Wang, Y., Chen, D., Hu, Y., Qin, L., Liang, J., Sun, X., & Huang, Y. (2020). An artificially constructed direct Z-scheme heterojunction: WO_3 nanoparticles decorated ZnIn2S4 for efficient photocatalytic hydrogen production. *Sustainable Energy & Fuels*, 4(4), 1681.
41. Sun, X. -Y., Zhang, F. -J., & Kong, C. (2020). Porous g-C3N4/WO_3 photocatalyst prepared by simple calcination for efficient hydrogen generation under visible light. *Colloids and Surfaces A: Physicochemical and Engineering Aspects*, 594, 124653

Chapter 3

Synthesis, characterization and photocatalytic performance study of solid-state mediator rGO based CdS-rGO-WO_3 Z scheme photocatalytic system for solar green hydrogen generation

Highlights:

- **Design of an in-situ rGO solid state mediator based CdS-rGO-WO_3 photocatalytic system comprising of nano-rods of CdS and nanoplates of WO_3 by a simple hydrothermal technique**
- **Characterisation and performance analysis for photocatalytic hydrogen generation by varying parameters: sources of illumination, type of mediators, loading of rGO**
- **An enhanced photocatalytic activity of 11.69 $mmolg^{-1}h^{-1}$ which was almost 2.4 times than pristine CdS (4.9 $mmolg^{-1}h^{-1}$), in presence of simulated solar light**

3.1 Introduction

The gradual decrease in the number of fossil fuel reserves due to the overconsumption of the natural resources is one of the major challenges of the twenty-first century. The problem of energy security is also significant in this context [1, 2]. The need of the hour is a renewable clean energy based technology. Hydrogen, in the recent years has emerged as a probable alternative form of energy due to its high energy density, compared to other fuels like coal, gasoline etc. [3, 4]. Currently hydrogen is being produced commercially by steam reforming of methane. During this process harmful greenhouse gases (CO_2) are emitted, contributing to global pollution. Also, the steam reforming process is expensive with high energy consumption and a low efficiency. Photocatalytic water splitting is a comparatively simple and cost-effective process and can be an effective way to generate hydrogen. Honda and Fujishima were the first ones to report the hydrogen evolution in a PEC cell, in presence of UV irradiation using TiO_2 electrode and Pt counter electrode, in 1972 [5]. Since the discovery, extensive research has been carried out to develop photocatalyst for efficient photocatalytic water splitting. Due to the high photostability and abundance of TiO_2, a broad range of application of TiO_2 as photocatalyst can be found [6-9]. However, TiO_2, a wide band gap semiconductor, is active only in the ultraviolet (UV) range of the solar spectrum. Narrow band gap semiconductors like Cadmium Sulfide (CdS) with a bandgap of 2.4 eV, exhibited improved photoresponse in the visible spectrum, acting as hydrogen evolution photocatalyst [10-14], but there were several drawbacks like photo-corrosion [15], resulting in low photocatalytic activity of water splitting reaction. Besides, slow reaction kinetics and recombination of photogenerated electrons and holes [16,17] are impediments that lowered the yield of evolved hydrogen. Also, there is a tendency of CdS particles to aggregate, forming larger particles, leading to reduced surface area with a faster recombination rate of photogenerated electron-hole pairs [18]. The photogenerated holes upon irradiation accumulate on the outer surface of the sulfide resulting in the oxidation of sulfides to sulphates [19]. Also, nascent oxygen (O^{2-} radical) is formed during the process which accelerates the photo-corrosion of CdS [15,19]. Different strategies have been adopted to solve the problem of photo-corrosion to enhance the efficiency of photocatalytic water splitting. Some of these strategies are heteroatom doping, loading of carbon based material (reduced graphene oxide) and development of heterojunction photocatalytic system [18, 21-24]. Amongst these, the design of a heterojunction photocatalytic system seems a promising approach to achieve enhanced photocatalytic performance. Z-scheme photocatalytic system, a type of heterojunction photocatalytic system, consists of two photocatalytic semiconductors, one Hydrogen Evolution Photocatalytst (HEP) and another Oxygen Evolution Photocatalytst (OEP), involving multiple photo-excitation steps [25]. WO_3, a transition metal oxide based semiconductor, with a band gap of 2.6 eV, used generally as photochromic and electrochromic materials, gas sensors, humidity sensors [26-29] can also be used as an oxygen evolution photo-catalyst [30, 31]. The oxygen vacancies in WO_3 function as sites for reactions [32, 33] and as electron donating sites [34-35]. In 1979, the concept of Z-scheme was first established by Bard *et al*. depending on the concept of artificial photosynthesis [36]. In a single component catalytic process, usually a narrow bandgap of the semiconductor photocatalyst is preferred for wide light harvesting. But, this narrow band gap creates a barrier to higher redox ability [37]. For the creation of separated oxidative and reductive active sites, a wide bandgap is necessary [25]. Therefore, a high redox activity along with a broad light absorption range, simultaneously, can be achieved with a multi-component (Z-scheme) photocatalytic system [25, 37]. In a Z-scheme photocatalytic system, electron mediators play an important role by helping in the promotion of the electron transfer between the two semiconductors. In the conventional shuttle redox mediator Z-scheme photocatalytic system, generally IO^3/I^-, or Fe^{3+}/Fe^{2+} like ionic redox couples are used as electron mediators [38]. However, backward reactions occur in these reversible redox mediator Z-scheme photocatalytic systems, due to the competitive oxidation of I^- by the holes in the OEP while using IO_3^-/I^- as redox mediator. The reaction efficiency of reversible redox mediator Z-scheme photocatalytic system is thereby reduced [25, 37-38]. Moreover, the redox mediators strongly absorb visible light, reducing the light absorption of semiconductor photo-catalysts [25, 37]. So, solid state mediated Z-scheme systems without the reversible redox pair mediators are being explored in recent years [39, 40]. Some advances have been made in this field; CdS/WO_3 nano-heterojunction was developed by Zhang *et al.*, where the hydrogen generation rate reached upto 369 μmol $g^{-1}h^{-1}$ and further increased to reach a value of 2900 μmol $g^{-1}h^{-1}$, when noble metal Platinum (Pt) was incorporated in the system, which boosted the charge transfer between CdS and WO_3 [41]. Huang *et al.* developed a Z scheme photocatalytic system by physically mixing composites of rGO-CdS nanosheets and WO_3 nanosheets together by sonication, which displayed a hydrogen generation rate of 119.4 ±4.0 μmol h^{-1} [42]. Zhang *et al.* obtained a yield of 736.89 μmol of hydrogen by modifying $CdS@WO_3$ photocatalyst with a cobalt based co-catalyst, Cobalt Phosphide (CoP) [43]. Li *et al.* fabricated an oxygen deficiency induced CdS/WO_{3-x} Z scheme photocatalytic system, with MoS_2 cocatalyst and attained a hydrogen production rate of 2852.5 μmol $g^{-1}h^{-1}$ [44].

However, most of the researches on CdS/WO_3 heterojunctions involved the use of a co-catalyst for improving the photocatalytic activity. In many cases, expensive metals like Pt had been used, which in turn increased the cost of the process. Here, an attempt has been made to enhance the photocatalytic activity without the utilization of a co-catalyst, by placing a charge transporter (rGO), which accelerated the transport of electrons at the interface, promoting charge separation. After an extensive literature review, it was found that there were no such reports on the in-situ fabrication of graphene (rGO) incorporated solid mediator-based Z-scheme photocatalytic system with a high photocatalytic activity.

3.2 Mechanism of Z-scheme photocatalytic system

The schematic of reaction are as follows:

$$2\,H^+ + 2e^- \longrightarrow H_2 \tag{3.1}$$

$$D + nh^+ \longrightarrow A \tag{3.2}$$

$$A + ne^- \longrightarrow D \tag{3.3}$$

$$2H_2O + 4h^+ \longrightarrow O_2 + 4H^+ \tag{3.4}$$

D: electron donor; A: electron acceptor

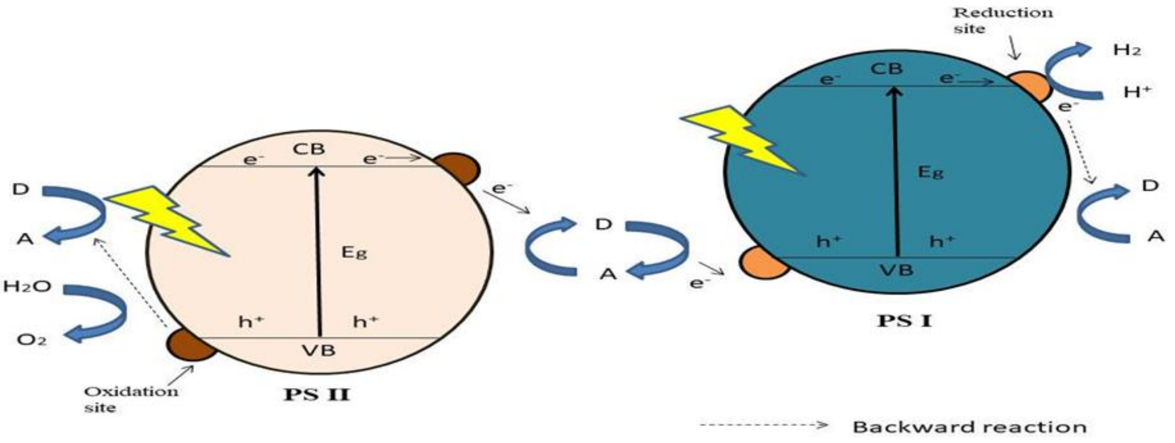

Figure 3.1 Mechanism of Z scheme photocatalytic system

The advantages of the Z-Scheme photocatalytic system are:

- more efficient utilization of visible spectrum of light
- reduction of energy required to drive each photocatalyst

- reverse reaction is suppressed

The concept of Z-scheme water splitting was first proposed by Bard et al. in 1979 [36].

Z scheme can broadly be classified, depending upon the type of mediators:

3.2.1 Shuttle Redox Mediator mediated Z-Scheme System

Reversible liquid state redox mediators like Fe^{3+}/ Fe^{2+}, IO_3^-/I^-, NO_3^-/NO_2^- had been used as electron mediators in Z-scheme water splitting. However, backward reactions occurred in the reversible redox mediator Z-scheme photocatalytic systems. The undesirable backward reaction was mostly caused due to the competitive oxidation of I^- by holes in the O_2 evolution photo-catalyst when using IO_3^-/I^- as redox mediator. In this way, the reaction efficiency of reversible redox mediator Z-scheme photocatalytic system was reduced. Also, the redox mediators strongly absorb visible light, thereby reducing the light absorption of semiconductor photo-catalysts [85]. Domen et al. developed a Pt-loaded ZrO_2/TaON as hydrogen and Pt-loaded WO_3 as oxygen evolution photocatalysts, respectively, with a photocatalytic activity of 7.5 µmol h-^{1} for H_2 generation using IO^{3-}/I^-as redox mediator [86]. The effect of co-catalysts (Rh, Ru, Pt, Fe_2O_3, Ni and RuO_2) on $SrTiO_3$:Rh/WO_3 was studied by Kudo et al. using Fe^{3+}/Fe^2 as redox mediator [87].

3.2.2 Z-Scheme Systems without Redox Mediators

The backward reactions and the shielding effect in the shuttle redox mediator based Z scheme system can be eliminated by formulating Z-scheme systems without redox mediators. Heterojunction is formed between two semiconductor photocatalysts and the charge transfer takes place at the interface. The difference between Type-II heterojunction system and Z scheme system without redox mediator is that, in Type-II heterojunction, the electrons migrate from CB of semiconductor 1 to that of semiconductor 2 and the route of holes is exactly the opposite. The chemical bond created at the interface due to surface conjugation between Photosystem I (PS I) and Photosystem II (PS II) aids in the effective charge transfer, in these Types Z scheme systems [85]. A ZnO/CdS Z-scheme photocatalytic system was fabricated by Wang et al. which offered a high photocatalytic H_2 activity of 1805 µmol h-^{1} g-^{1}[88]. Tian et al. designed a Z-scheme of $BiVO_4$/g-C_3N_4 using g-C_3N_4 and $BiVO_4$ which displayed high photocatalytic degradation activity [89].

3.2.3 Solid state mediator based Z scheme systems

In this type of Z scheme system, the mediator used between Photosystem I (PS I) and Photosystem II (PS II) is a solid state mediator, instead of the previously mentioned liquid state redox mediator. The problems of backward reactions and the shielding effect in the shuttle redox mediator- based Z scheme system was solved in this type of Z scheme systems. Au, Ag type Noble-metal particles (such as Au, Ag) and reduced graphene oxide (RGO). Tada et. al. designed a solid-state Z scheme of CdS/Au/TiO_2 system, using a facile photochemical process and this was the first reported solid state Z scheme photocatalytic scheme [90]. A solid state $ZnRh_2O_4$/Ag/$Ag_{1-x}SbO_{3-y}$ Z scheme using Ag as mediator was prepared by Kobayashi et al, where an AQE value of 0.037% was obtained at 420 nm [91].

The issue of aggregation of CdS nanoparticles during synthesis was solved by utilizing reduced graphene oxide (rGO) as a supporting matrix to develop layered composite like structure, which could resist the aggregation of ultrathin nanostructure with the aid of coupling mechanism of rGO [45]. Moreover, rGO as an excellent electron transporter (with a work function 4.42 eV, and an electron mobility of 200000 $cm^2\ V^{-1}\ s^{-1}$) [46, 47] acted as a solid- state mediator, between two photocatalysts: CdS (HEP) and WO_3 (OEP). The CdS-rGO-WO_3 Z-scheme composite was prepared hydrothermally, which exhibited enhanced photocatalytic activity, compared to pure CdS. Series of characterization studies was performed to verify the formation of the heterojunction and the pathway of charge transfer. This report will offer valuable insight on the charge transfer pathway in heterojunctions, beneficial in engineering advanced photocatalytic systems for improved photocatalytic activity.

3.3 Objective

Reduced graphene oxide (rGO) solid mediator based CdS-rGO-WO_3 Z scheme photocatalytic system

The specific objectives are enlisted below:

1. Synthesis of CdS- rGO-WO_3 photocatalyst.
2. Characterization of CdS- rGO-WO_3
3. Performance analysis
4. Recyclability test (stability) of photocatalyst.

The major research problem is addressed in this chapter; the problem definition is as follows:

Problem definition:

Synthesis, characterization and photocatalytic performance study of solid-state mediator rGO based CdS-rGO-WO_3 Z scheme photocatalytic system for solar green hydrogen generation

3.4 Experimental

3.4.1 Materials for synthesis of CdS-rGO-WO_3

Cadmium acetate dihyrate [$Cd(CH_3CO_2)_{2}.2H_2O$] (Sigma-Aldrich, 98% purity), Thio-urea ($SC(NH_2)_2$) (Sigma-Aldrich, 99% purity), Sodium tungstate dihydrate ($Na_2WO_4.2H_2O$) (Sigma-Aldrich, 99% purity), Oxalic acid ($C_2H_2O_4$) (Sigma-Aldrich, 98% purity), graphite flakes (Luba Cheme, extra pure 99.5 %, 50 µm avg sizes, bulk density 20-30 gm. /100 ml), Sulphuric Acid (H_2SO4) (MERCK, 98%), Phosphoric Acid (H_3PO4) (MERCK, 88%) Potassium Permanganate (KMnO4) (MERCK, 99% purity), Sodium Hydroxide (NaOH), (MERCK, 98%) Hydrogen Peroxide (H_2O_2) (MERCK, 30%), Hydrochloric Acid (HCl) (MERCK-35%), Ethanol (C_2H_5OH) (MERCK, 99.9% purity) were used as received. Deionized water (DI) (with resistivity of 18.25 MΩ) was used for the purpose of synthesis.

3.4.2 Synthesis of composite photocatalyst

3.4.2.1 Synthesis of CdS Nano-rods

0.5 (M) solution of Cadmium acetate was prepared by adding Cadmium acetate to 50 ml. of de-ionized water and stirring was done for 1 h [48, 49]. 3.806 g of thiourea was then added to 50 ml. deionized water and was stirred for an hour. Subsequently, these two prepared solutions were mixed together in a beaker and stirred for 10 hours at 80°C for preparation of Cadmium sulfide solution. Color change was the indication of CdS formation. Orange color solution of Cadmium sulfide solution was obtained after calcination at 300°C for 0.5 h. Then this solution was filtered and dried at 70°C for 3 h. Powder CdS was obtained by grinding this dried mass.

3.4.2.2 Synthesis of WO_3 Nanoplates

At first 100 ml 15mM Sodium tungstate ($Na_2WO_4.2H_2O$) was prepared by adding 0.4947 g Sodium tungstate into 100ml de-ionized water. After that 40 ml 6(N) HCl was prepared by diluting 12(N) HCl. Then these prepared solutions were mixed and stirred continuously for 3 h at 5°C. Then 1g Oxalic acid was added to the mixture and the colour of the solution was changed to yellow [50]. After that, it was centrifuged and washed to collect the precipitate. Then this precipitate was dried at 60°C for 2-3 h in a tube furnace to obtain powder WO_3.

3.4.2.3 Synthesis of rGO-CdS

This composite was synthesized via hydrothermal procedure. 0.1 g Graphene oxide (GO) powder was added to 50 ml water in a beaker and solution was sonicated for about 2 h for the preparation of homogeneous GO solution. GO was synthesized by following Improved Hummers Method [51-54]. Quantity of GO was varied to prepare different loadings (5%, 10%, 20%, 30%) of rGO-CdS composite. Precursors of Cd and S were obtained by adding Cadmium acetate and thiourea to this prepared GO solution and stirred at 80°C until the homogeneous mixture was formed, while maintaining pH at 9 using NaOH [55]. Then this solution was taken into an autoclave and kept for 18 h in a muffle furnace. After that solution was washed and centrifuged repeatedly using ethanol. Then it was dried under vacuum chamber at 70°C and powder sample was collected.

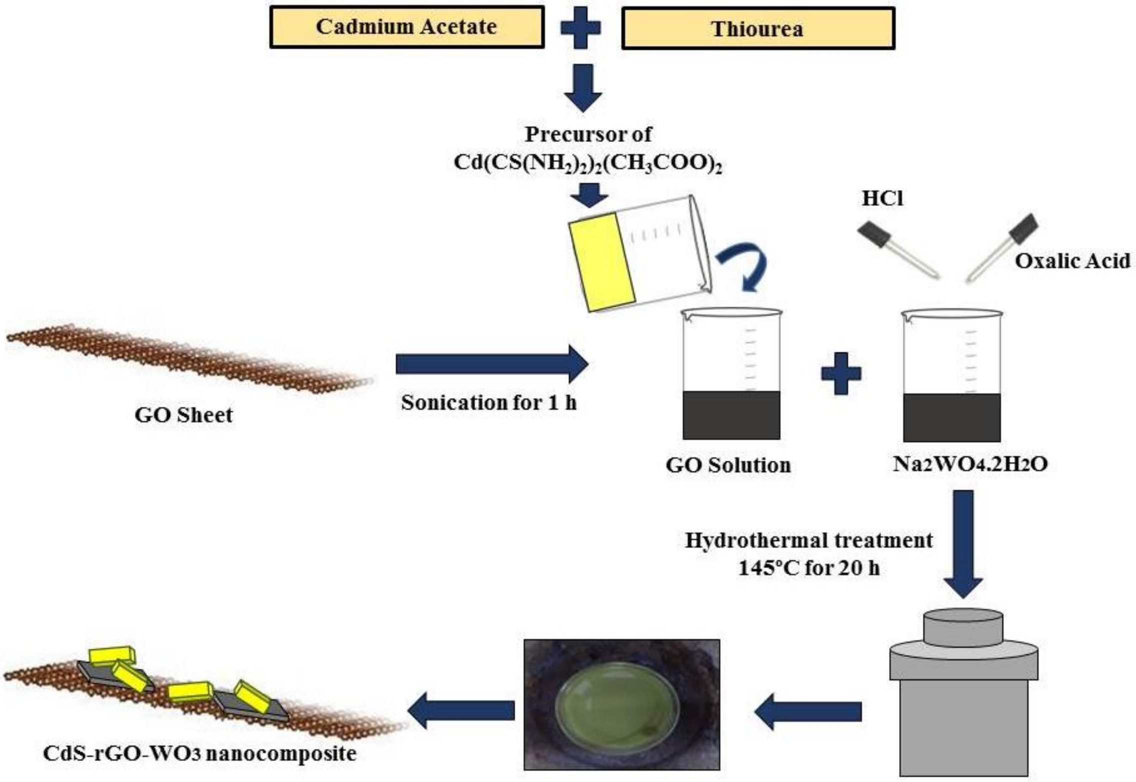

Figure 3.2 Schematic of synthesis procedure of CdS-rGO-WO_3 nanocomposite

3.4.2.4 Synthesis of CdS-rGO-WO_3

This composite was synthesized via hydrothermal procedure. 0.5 g of Sodium Tungstate was added to the previously prepared solution of rGO-CdS by dispersing and sonicated for about an hour. The pH value of the solution was moderated and maintained at 2, using HCl. This mixture was then sealed inside a 100ml Teflon lined autoclave and kept in a furnace at a temperature of 145°C for about 20 h. Next day the solution was washed several times using ethanol and then dried in a vacuum oven at a temperature of 80°C [Figure 3.2].

3.4.3 Characterization

Transmission Electron Microscopy (TEM) (JEOL JEM-2100F) and Scanning Electron Microscopy (SEM) (Model Hitachi S-3400, JEOL JSM-7600F) (accelerating voltage of 15.0 kV) coupled with Energy Dispersive X-ray Spectroscopy (EDS) were utilized to characterize surface morphology and elemental analysis of the nanomaterial. Field Emission Scanning Electron Microscopy (FESEM) analysis of the sample was done to study the morphological changes after photocatalytic water splitting reaction, using FEI, Inspect F50. The ultraviolet-visible absorbance (UV-vis absorbance) of the synthesized photocatalysts was measured by Perkin Elmer 365 UV-Vis Spectrophotometer. X-ray Diffraction (XRD) was used to analyze the composition and crystal structure of the materials using a Cu Kα source (λ= 0.154178 nm) with Rigaku, Ultima III Diffractometer. Perkin Elmer Spectrum-2 was used for FTIR analysis of different synthesized photo-catalyst for identification of bonds. X-ray Photoelectron Spectroscopy (XPS) with Al K_α irradiation was used to study the surface elemental interactions using Model AXIS Supra *HORIBA*, Kratos Analytical Ltd. *Jobin Yvon NanoLog* spectrofluorometer was used for photoluminescence spectroscopic study of the synthesized hybrid photocatalyst (at excitation wavelength of 370 nm).

3.4.4 Photocatalytic Hydrogen Generation

Table 3.1 Process parameters for photocatalytic hydrogen generation

Parameters		
Temperature	20 °C	20 °C
Phase	Liquid	Liquid
Volume of water	50 ml	50 ml
Loading of photocatalyst	10 mg	13 mg
Stirring speed	600 rpm	600 rpm
Light intensity/flux	4500 lumens	113 µW/cm^2 1.0 sun (100 mW/ cm^2)
Source of illumination	LED (45 W)	Solar simulator Newport LCS-100 (Class ABB)
Surface area of irradiation	25.8 cm^2	14.44 cm^2

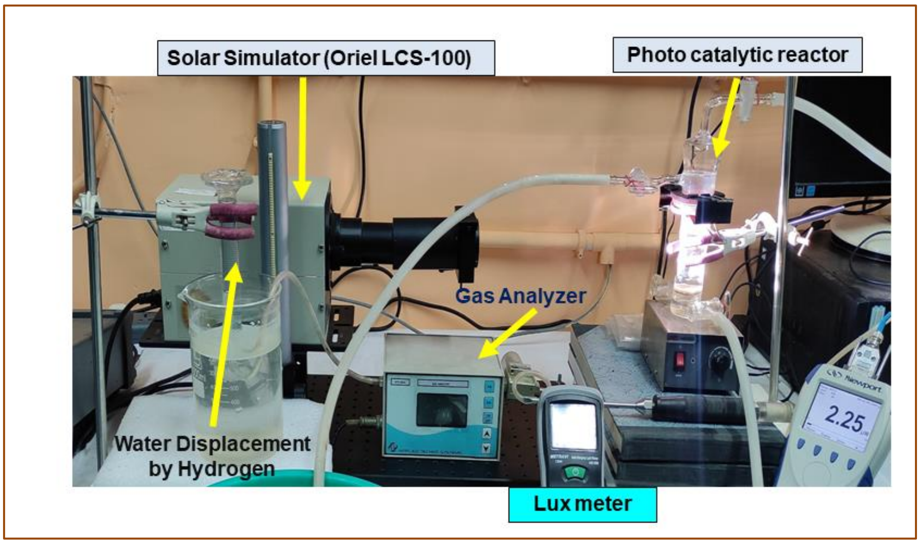

Figure. 3.3 Real-life picture of Photocatalytic Hydrogen Generation setup

A real- life picture of photocatalytic hydrogen generation set up is given in Figure 3.3. For a typical batch study, 50 ml of deionized water was used. Powder photocatalyst was taken for dispersion in water and the solution was sonicated after adding few drops of methanol as sacrificial agent. Then the reactor setup was purged with inert gas like Argon/N_2 for 30 min. Room temperature was maintained during the reaction by circulating cooling water outside the photo reactor. A 100 W Solar simulator (94011A, Manual shutter, Newport Oriel LCS-100), equipped with an AM1.5G air mass filter, was utilized as the source of illumination. The solar simulator with full spectra was used for simulating solar light and the intensity was fixed at 100 mW cm^{-2}. Thereafter data was collected after regular time intervals.

3.4.5. Degree of Photon Absorption

In photocatalytic reactions photons are being absorbed by the semiconductor photocatalyst and the excitation of an electron from its ground state to an excited state occurs. However, the wavelength of light is of prime importance for the initiation of the process of photon absorption. Practically, it is difficult to measure the degree of photon absorption by a photocatalyst. It is assumed that the irradiated photons are utilized effectively for the process of absorption.

Solar to Hydrogen (STH) conversion efficiency is one such metric to measure the efficiency of a photocatalytic reaction and this is applicable for systems when the source of irradiation is solar energy. Another metric of measurement is the Apparent Quantum Efficiency (AQE) which is used for the evaluation of performance of photocatalytic reaction and can be broadly defined as the ratio of number of reacted electrons to the number of incident photons.

Apparent Quantum Efficiency Calculation

Quantum yield is a parameter to determine the performance of photocatalysts during splitting of water. It can be defined as:

$$\text{Q.Y. (\%)} = \frac{Number\ of\ reacted\ electrons}{Number\ of\ incident\ photons} \times 100 \tag{3.5}$$

If a photon (E_{photon}) of wavelength of λ_{inc} (nm) is incident during a photocatalytic water splitting reaction, the energy of this one photon calculated using the equation:

$$E_{photon} = \frac{hc}{\lambda_{inc}} \tag{3.6}$$

where h (J·s) is Planck's constant,

c ($\text{m}\cdot\text{s}^{-1}$) is the speed of light

λ_{inc} (m) is the wavelength of the monochromatic light that is incident.

The total energy of the incident monochromatic light (E_{total}) is calculated using the following equation:

$$E_{total} = P\ s\ t \tag{3.7}$$

here P ($\text{W}\cdot\text{m}^{-2}$) is the power density of that incident monochromatic light, S (m^2) is area that is being irradiated and t (s) is the duration of the exposure of the incident light

The total number of incident photons can be determined from the given equation:

$$\text{Number of incident photons} = \frac{E_{total}}{E_{photon}} = \frac{P\ s\lambda_{inc}\ t}{hc} \tag{3.8}$$

In order to calculate the Apparent Quantum Efficiency (AQE) additional experimentation on hydrogen generation was performed using a 420 nm Band pass filter. A power meter (Model: 843-R, Newport) was used for measuring the number of incident photons, in the irradiated light of the solar simulator (Oriel LCS-100). Apparent Quantum Efficiency (AQE) was calculated according to the equation as follows [53]:

$$\text{AQE}(\%) = \frac{2\times \text{The number of evolved Hydrogen molecules}}{\text{The number of incident photons}} \times 100 \tag{3.9}$$

Solar to Hydrogen Conversion Efficiency (STH) Calculation

Another parameter to measure the performance of photocatalytic water splitting reaction is the Solar to Hydrogen Conversion Efficiency (STH). This can be calculated from the below mentioned equation:

$$\frac{\boldsymbol{r_{H_2}\times\Delta G_{H_2O}\times 100}}{\boldsymbol{I\times S}} \tag{3.10}$$

Here r_{H_2}, $\Delta G_{H_2O,}$ I and S represent Hydrogen evolution rate, Gibbs Free Energy of water splitting, light energy flux and the irradiation area, respectively.

3.4.6. Photoelectrochemical Hydrogen Generation

Photo-electro-chemical analysis was performed using an electrochemical workstation (Keithley Source-meter 2450) using a three-electrode system, comprising of a working electrode, a reference electrode (Ag/AgCl electrode), and a counter electrode (Pt electrode). The transient photocurrent response of the samples was carried out in a 0.5 mol/L Na_2SO_4 electrolyte solution. The source of illumination is the same (100 W Solar simulator) as that used during photocatalytic hydrogen generation. The working electrode was prepared on pre-cleaned Fluorine doped Tin Oxide (FTO) coated glass substrate (1cm ×2 cm) in a step by step method using hydrothermal and spray pyrolysis techniques[Figure 3.4] [56-58].

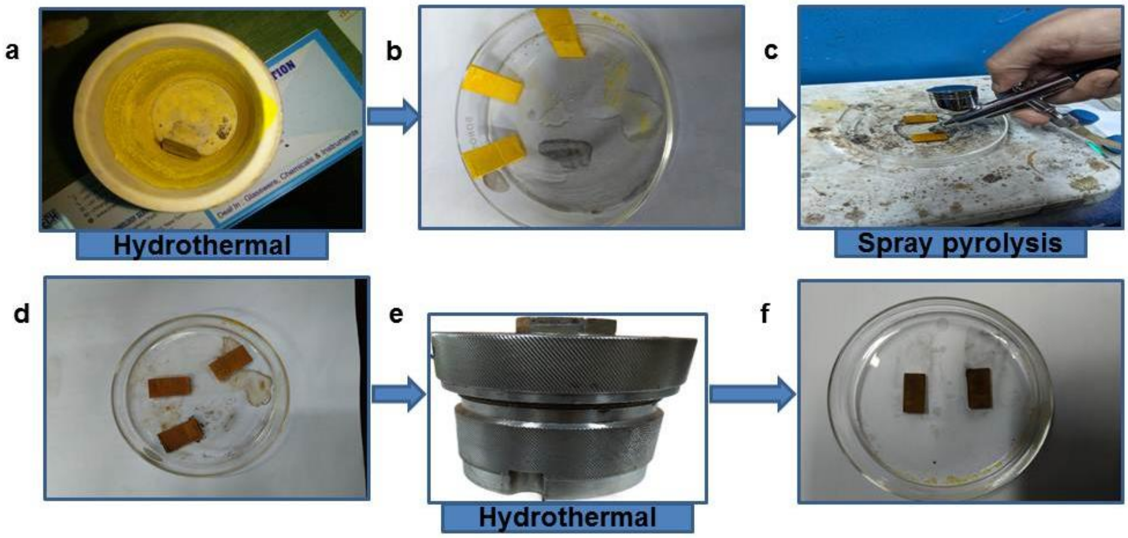

Figure 3.4 (a-d) Fabrication of CdS-rGO-WO3 photoelectode

3.4.6.1Preparation of CdS and CdS-rGO-WO_3 photoelectrodes

At first the FTO coated glass is cleaned ultrasonically by using an ultrasonic bath by acetone, ethanol and deionized water for about 15 min. Then, two slides of FTO glass substrate with conductive faces up and down, respectively, were laid flat in the bottom of autoclave. The hydrothermal method was used to prepare CdS nanofilm with the conductive side facing up and down, using Cadmium Acetate and Thiourea as precursors.The hydrothermal reaction took place in a stainless steel Teflon lined autoclave for 10h. The obtained samples were filtered and washed several times with deionized water and ethanol absolute and then dried at 60°C for 12 h (Figure 3.4 a-b). GO solution was prepared by dispersion in Dimethyl Formamide (DMF). One of thus coated FTO slides was then coated by spray pyrolysis using a spray gun, by keeping the substrates on a hot plate at a temperature of about 120°C (Figure 3.4 c). Thereafter Sodium Tungstate dihydrate powder ($Na_2WO_4.2H_2O$, 1.32 g) was dissolved in 40 ml deionized water. The solution was acidified to pH 2 with HCl (3 M). The resulting solution was stirred for 30 min and then transferred into a 50 ml Teflon lined stainless steel autoclave by vertically orienting the slides at an angle of 45°. In this way coated CdS and CdS-rGO-WO_3 coated photoelectrodes were prepared and were tested by photocurrent measurement. The current density vs. potential was obtained, using 0.5 mol/L Na_2SO_4 as the electrolyte solution.

The general equation for the conversion at any pH using Ag/AgCl reference electrode to Reference Hydrogen Electrode (RHE), using Nernst Equation is

$$\boldsymbol{E_{RHE} = E_{Ag/AgCl} + 0.059\,pH + E^{\circ}_{Ag/AgCl}} \tag{3.11}$$

where $E^{\circ}_{Ag/AgCl}$= 0.1976 V at 25ºC (3M KCl) and $E_{Ag/AgCl}$is the working potential. Here the pH of 0.5 M Na_2SO_4 solution is ~ 7. This equates to $E_{RHE} = E_{Ag/AgCl} + 0.6106$**.**

IPCE (Incident Photon to Current Density) Calculation

Incident Photon to Current Density is a measurement of efficiency of photon to current conversion, defined by the ratio between the photocurrent obtained as output to the number of incident photons as input, for a particular wavelength.

$$\textbf{IPCE}= \frac{\boldsymbol{1240 \times j_{ph}}}{\boldsymbol{\lambda \times I}} \times \mathbf{100\%} \tag{3.12}$$

Here, $\boldsymbol{j_{ph}}$ is photocurrent density (in A) at a specific wavelength $\boldsymbol{\lambda}$, $\boldsymbol{\lambda}$ is the wavelength of the incident light and $\boldsymbol{I}$ is the intensity of light for the wavelength at the film surface, here the value of $\boldsymbol{I}$ is 100 mW/cm^2.

3.5 Results and Discussion

3.5.1 Morphology and Elemental Analysis

The surface morphology of the synthesized photo catalysts can be obtained from SEM analysis. From Figure 3.5(a), it can be seen that pure WO_3 exhibits rectangular plates like structures. At first a layered structure of $WO_3 \cdot H_2O$ was formed from $[WO(OH)_4\ (OH_2)]$, obtained from H_2WO_4 precursor, by the stable hydrogen bonding between the terminal oxygen atoms and the adjacent water molecules [59]. Oxalic acid played a significant role by assisting the stacking growth and in phase transformation of WO_3 [50, 59]. In Figure 3.5(b), it can be seen that pure CdS displays rods like structure with uniform thickness and length. During the synthesis, decomposition of complex precursors occurred, leading to an increase of concentration of S^{2-} ions which then reacted with Cd^{2+} ions to form tiny CdS crystals. For the purpose of reduction in surface energy, these tiny CdS crystals then coalesced with adjacent tiny CdS to form CdS seeds in the reaction solution [60]. The faster rate of growth along the c-axis orientation led to the formation of rod like morphology in CdS as energetically it is more favorable [60].

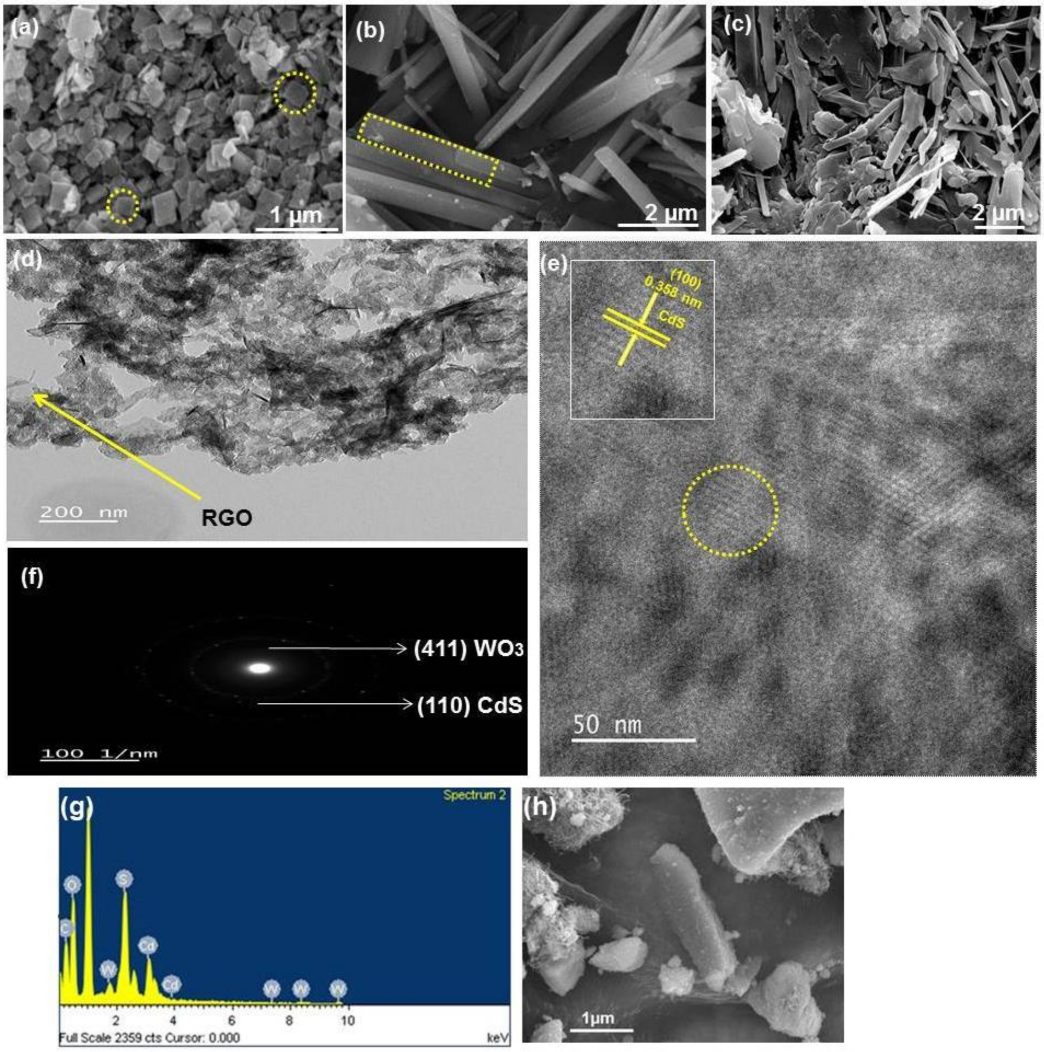

Figure 3.5. SEM images of (a) CdS (II) (b) WO_3, (c) CdS- rGO-WO_3, (d) TEM image of CdS- rGO-WO_3 (e and f) Lattice fringes and SAED pattern of CdS- rGO -WO_3,(g) EDS of CdS- rGO-WO_3, (h) FESEM of CdS-rGO-WO_3 after 24 h of reaction

It can be found from Figure3.5c that non-homogeneously distributed nano rods of CdS and nano plates of WO_3 strewn over graphene sheet. Scattered sheets of graphene can be observed in the from the TEM image of CdS- rGO-WO_3 (Figure 3.5d). The lattice fringe as seen in Figure 3.5e (marked by yellow dotted circle) with a d spacing of 0.358 nm corresponded to (100) crystal plane of hexagonal CdS [61]. The ring patterns observed in the Selected Area Electron Diffraction (SAED) pattern (Figure 3.5f) indicated the formation of polycrystalline material. Interplanar distance between the crystal planes was measured by calculating the diameter of the ring. In the SAED pattern, the (110) crystal plane can be assigned to hexagonal CdS whereas the (411) crystal plane confirmed the presence of WO_3, in the as-prepared nanocomposite [62,63]. The obtained EDS spectrum (Figure 3.5g) of CdS-rGO-WO_3 showed the appearance of Cd and W peaks confirming the presence of Cadmium and Tungsten. The atomic composition (Table 3.1) of Cd and W were 2.75% and 0.28%, respectively. This value varies slightly from the atomic percentage determined by XPS analysis, the reason might be XPS is a surface characterization analytical technique, whereas EDS determines the bulk atomic concentration ratio [64] (Table 3.2)

Table 3.2 Element wise percentage composition of CdS-rGO-WO_3

Element	**From EDS**		**From XPS**
	Weight%	**Atomic%**	
C	15.83	25.25	64%
O	54.52	65.27	15%
S	10.79	6.45	9.82%
Cd	16.14	2.75	10.38%
W	2.72	0.28	0.27%
Total	100.00	100.00	100.00

The atomic concentration (from X-ray Photoelectron Spectroscopy or XPS) is obtained by using equation:

$$\boldsymbol{Atomic}\,\% = \frac{\frac{I_x}{S_x}}{\sum i\frac{I_i}{S_i}} \times \mathbf{100}\% \qquad (3.13)$$

Here I_x is the relative peak area formed by the photoelectrons from element x, whereas the atomic sensitive factor of element x is denoted by S_x. $\sum i\frac{I_i}{Si}$ is basically the ratio between peak areas to atomic sensitive factors of all other elements. The peak area is calculated from ORIGIN Lab software. The FESEM image of the CdS-rGO-WO_3 sample after 24 hours of reaction can be seen from Figure3.3h, displaying scattered rods and plates of CdS-rGO-WO_3 nanocomposite.

3.5.2 Phase Structure Analysis

The X-ray diffraction (XRD) study was done to obtain phase structures of CdS, WO_3, CdS-rGO-WO_3, CdS-WO_3, as can be seen from Figure 3.4a. The values of 2θ at 25.22°, 26.67°, 28.37°, 43.98°, 48° and 52.24° could be indexed to (100), (002), (101), (110), (103) and (112) planes respectively, for pristine CdS, as indexed in JCPDS 41-1049 [65]. The major diffraction peaks of CdS are assigned to hexagonal phase of CdS. From the XRD patterns, it can be observed that the WO_3 nanoplates have an orientation growth in the (100) direction due to increase in peak intensity for the (100) reflection relative to other peaks, at 2θ of 18.56°. The diffraction peaks of WO_3 corresponded to the hexagonal phase JCPDS 33-1387 [66]. From the diffraction pattern of CdS-WO_3 and CdS- rGO-WO_3, it is noticed that the diffraction peaks of CdS are retained and are prominent rather than WO_3. The XRD peaks are in well accordance with the SAED pattern and lattice fringes obtained from TEM images of CdS- rGO-WO_3. The mean grain sizes of the crystallites are calculated using Scherrer equation [67]:

$$D = K\lambda/\beta cos\theta \tag{3.14}$$

Here, D=Size of the crystallites, K=0.9 (Scherrer constant), λ= 0.15406nm (wavelength), β=FWHM (radians), θ=Peak positions (radians). The calculated average grain size of different photo-catalyst was found in the range nearly 8nm to11nm. Table 3.2 depicts the average crystallite size, along with the values of dislocation densities and strain calculation. The dislocation density and lattice strain were calculated from the following equation:

$$\beta = 4\varepsilon tan\theta \tag{3.15}$$

where ε corresponds to the lattice strain and δ refers to the dislocation density where $\delta = \frac{1}{D^2}$. Due to the doping of heteroatoms, the presence of defects induces a shift or dislocation resulting from the stress in the crystal lattice. An increase in lattice strain and dislocation density in C`dS-rGO-WO_3 can be found when compared to CdS-WO_3, upon incorporation of reduced graphene oxide, as evident from Table 3.3

Table 3.3 Average grain size, dislocation density and lattice strain calculation of different photo-catalysts

Name of the photo-catalyst	Average size(nm)	Dislocation density (δ)	Strain(ε)
CdS	4.2303	0.058	0.003411
WO_3	10.0664	0.00826	0.000216
CdS-WO_3	7.9049	0.0153	0.001621
CdS-rGO-WO_3	8.0855	0.0164	0.00277

3.5.3 Optical Property Analysis

An inspection through the FTIR spectra can provide details about the presence of the bonds and the functional groups, in the synthesized nano-heterostructure.

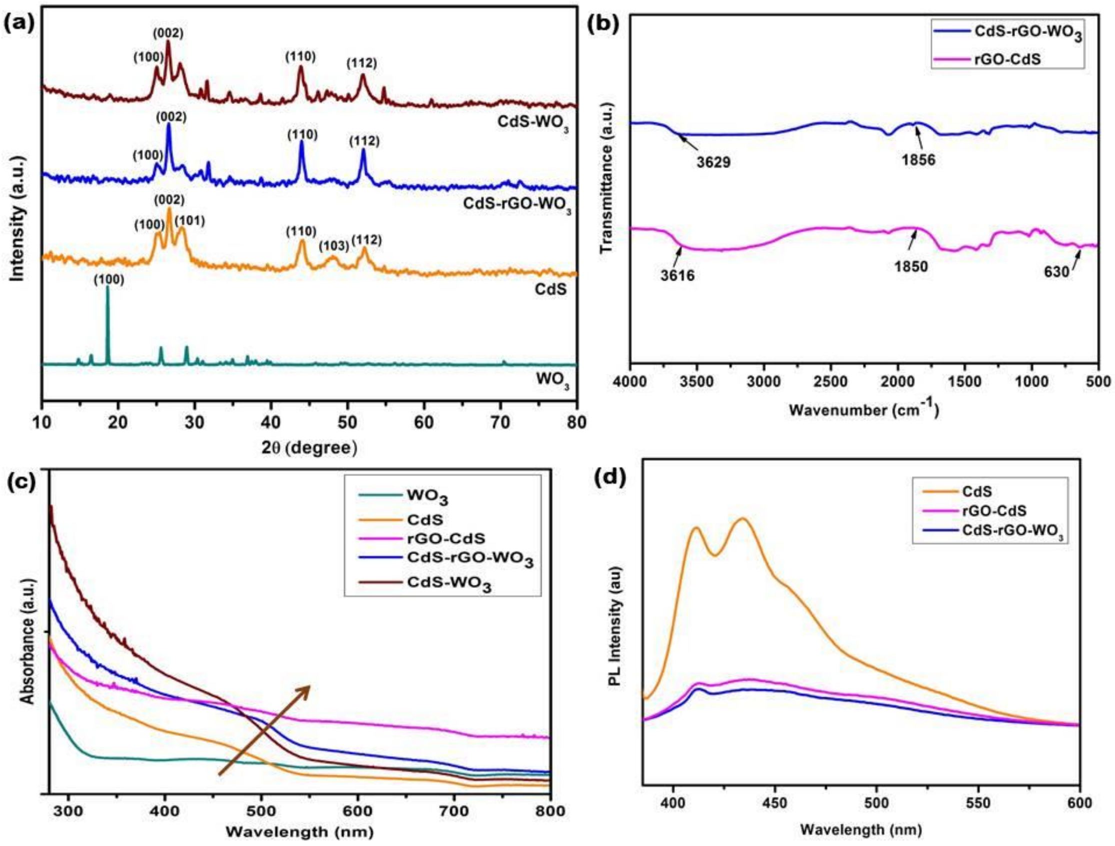

Figure 3.6a. XRD pattern of CdS, WO_3, CdS-rGO-WO_3, CdS-WO_3 Figure 3.6b FTIR spectra of rGO –CdS and CdS-rGO- WO_3 Figure 3.6c UV−Vis spectra of CdS, WO_3, CdS-WO_3, rGO-CdS and CdS-rGO-WO_3 Figure 3.6d Photoluminescence Spectra of CdS, rGO-CdS and CdS- rGO-WO_3

In Figure 3.6b the FTIR spectra of rGO–CdS and CdS-rGO-WO_3 are shown. The stretching vibration due to the O-H stretching could be observed at 3616 cm^{-1} and 3629 cm^{-1} in rGO-CdS and CdS-rGO-WO_3, respectively [68]. The C=O stretching of COOH groups in reduced graphene oxide (rGO) was observed at 1856 cm^{-1} and 1850 cm^{-1} in CdS-rGO-WO_3 and rGO-CdS, respectively [69]. The peak at 630 cm^{-1} corresponded to the Cd-O stretching [70] and the stretching peaks near 969 cm^{-1} could be ascribed to W=O and W-O bond formation [71].

UV-Vis spectroscopic analysis is necessary to determine the optical properties of the as prepared photocatalyst. Peak at 452 nm was observed for CdS [72], at 470 nm for rGO-CdS and at 502 nm for CdS-rGO-WO_3, thereby denoting a red-shift, in Figure 3.6 c. This shifting of absorption edge towards the visible region of the spectrum (red-shift) causes a boost in the absorption of light in the visible region, implying the nano-heterostructure to be visible light active, which can also be tallied with the photocatalytic performance data, as discussed later. Band gaps of the synthesized nanomaterials were calculated from Tauc relation as below [73]:

$$\alpha h\nu = A(h\nu - E_g)^n \qquad (3.16)$$

Where, $h\nu$ = Photon energy α=Absorption coefficient, A = Constant, n =Constant depending on transition. Here, A =1 and n =1/2 for direct allowed transition, so, the equation can be written as $(\alpha h\nu)^2 = (h\nu - E_g); \quad h\nu = hc/\lambda$ (3.17)

A graph was plotted (Figure3.7) between as $(\alpha h\nu)^2$an ordinate and $h\nu$ as abscissa. The extrapolation of straight line to $(\alpha h\nu)^2 = 0$ as provided the value of band gap.

The calculated band gap for the nanocomposite CdS-rGO-WO_3 was determined to be 2.20 eV, whereas the band gap for CdS was found to be 2.40 eV, implying a band narrowing effect, tuning the absorptivity towards the visible spectrum. All of the calculated band gaps and the corresponding Tauc plots can be found in Table 3.4.

Table 3.4 Calculated values of Band gap and Urbach Energy

Sl. No.	**Sample**	**Bandgap (eV)**	**Urbach Energy (eV)**
a.	CdS	2.40	1.65
b.	WO_3	2.48	0.66
c.	rGO-CdS	2.36	4.27
d.	CdS-WO_3	2.30	1.65
e.	CdS-rGO-WO_3	2.20	2.20

A high value of Urbach energy means an increase in localized states. From Table 3.4 it can be seen that, upon incorporation of rGO, with the infusion of defects states, Urbach energy rose to a high value of 4.27 eV for rGO-CdS from 1.65 eV for that of pristine CdS. However, a decrease in the value of Urbach energy was seen for CdS-rGO-WO_3 (2.20 eV), which is still higher than that of CdS, may be due to the formation of oxygen vacancies, resulting in the subsequent band gap narrowing.

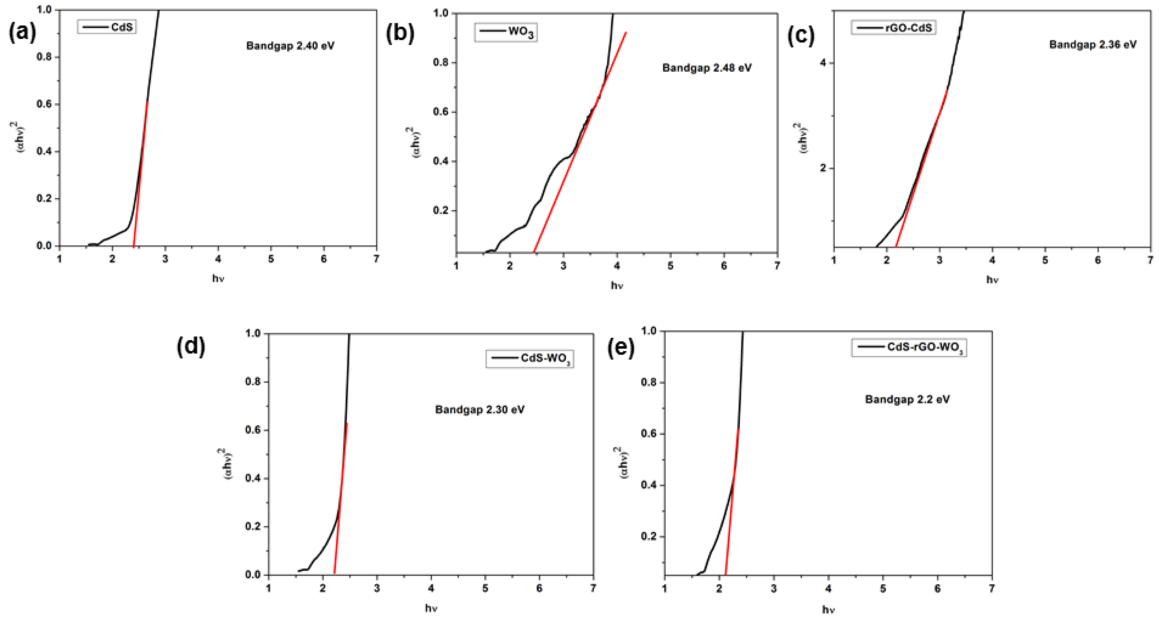

Figure 3.7 Calculated band gaps of a) CdS, b) WO_3, c) rGO-CdS, d) CdS-WO_3 and CdS-rGO-WO_3

Due to the absorption of photons, transition of the electrons from the valence band (VB) to the conduction band (CB) occurs. Defect states induced by doping leads to the extension of tail states through the energy band gap. The tail is being referred to the Urbach tail and Urbach energy is a metric for measuring the density of electronic states [74].

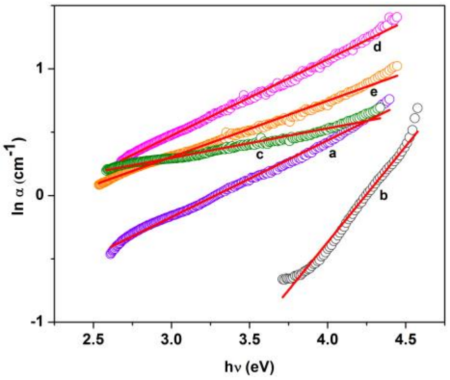

Figure 3.8 Urbach Energy plots of a) CdS, b) WO_3, c) rGO-CdS, d) CdS-WO_3 and e) CdS-rGO-WO_3

The value of Urbach Energy is calculated from the following equation:

$$\alpha = \alpha_0 + \exp\left(\frac{E}{E_u}\right) \tag{3.18}$$

Here, E is the photon energy, α is the absorption coefficient and Urbach energy is represented by E_u. $\ln(\alpha)$ vs E was first plotted, as can be seen from Fig 3.8. The value of Urbach energy was derived by calculating the reciprocal of the slope of the linear fit of the plot $\ln(\alpha)$ vs E.The Urbach energy values are tabulated in Table 3.4.

Photoluminescence spectroscopic study involves the plot of photoluminescence intensity as a function of wavelength for a fixed excitation wavelength (λ=370 nm) [43]. From the photoluminescence spectra (Figure 3.6d) it can be found that the PL intensity of rGO-CdS and CdS-rGO-WO_3 Z-scheme photocatalytic system is much lower than that of the pristine CdS. Strong PL intensity denotes high rate of recombination of photogenerated electrons and holes. The weak intensity of CdS-rGO-WO_3 implies lowering of the rate of recombination of photogenerated electron-hole pairs [75]. Incorporation of rGO lowered the recombination of electrons and holes, further lowering might have been caused due to the creation of the oxygen vacancies [76], thereby improving the charge separation, which is demonstrated by the enhanced photocurrent.

3.5.4 Surface Chemical State Analysis

The surface oxidation states and the elemental composition of the nanocomposite were reviewed by XPS analysis. The survey scan (Fig 3.9(c)) demonstrated the existence of elements Cd, S, W, O and C in the synthesized nanomaterial. XPS spectra of Cd 3d in Fig 3.9(a) exhibits two peaks at 405.20 eV and 411.94 eV, which corresponds to Cd $3d_{5/2}$ and Cd $3d_{3/2}$ states of Cd^{2+}[56], respectively. In the W 4f spectra (Figure 3.9(b)), two dominant peaks at 35.28 eV and 37.49 eV could be attributed to the W $4f_{7/2}$ and $4f_{5/2}$ states of W^{6+}[44], respectively. Meanwhile the C 1s spectra (Figure 3.9(d)) could be deconvoluted to three distinct peaks: 284.9 eV, 286.31 eV and 288.79 eV [77]. The peak at 284.9 eV corresponded to sp^2 hybridized graphitic carbon (C=C) bond, whereas the peaks at 286.31 eV and 288.79 eV corresponded to the C-O and C=O bonds, respectively [78]. The decrease in the relative intensity of peaks of the C-O bonds, indicate that the GO has been reduced to rGO [79]. Meanwhile the O 1s spectra (Figure 3.9(e)) could be deconvoluted to give rise to two peaks, at 532.27 eV, which could be attributed to the W-O bonding and at 533.68 eV, which could be ascribed to the adsorbed oxygen, caused due to the oxygen vacancy states [44]. In Figure

3.9(f), peaks at 161.47 eV and 162.59 eV of the XPS spectra of S 2p corresponds to the S $2p_{3/2}$ and S $2p_{1/2}$ states, respectively [44]. Therefore, XPS analysis confirms the construction of CdS-rGO-WO_3 heterostructure. A shift of the binding energy in the XPS spectra is an indicator of the transfer of electron density; if the shift is towards the positive direction, this suggests a loss of electron density and if the shift is towards the negative direction, this means gain of electron density. After speculating the binding energy shift, a prediction can be made about the charge transfer pathway [37].

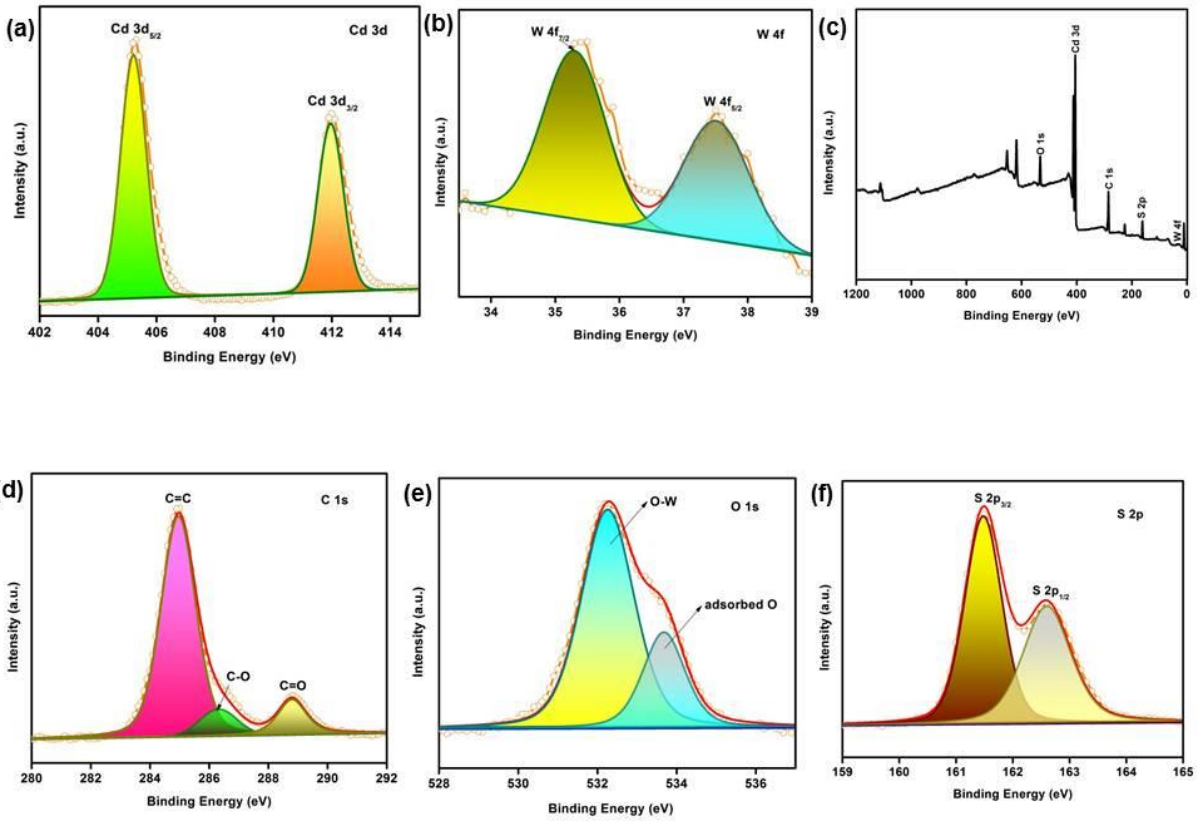

Figure 3.9 XPS Spectra 3(a)Cd 3d (3b)W 4f (3c) survey scan of CdS-rGO-WO3 (3d) C 1s, (3e) O 1s and (3f) S 2p

When compared to previous reports, the characteristic peaks at 405.20 eV and 411.94 eV for Cd 3d showed a shift in the negative direction, indicating an enhancement of electron density [44]. For W 4f, the characteristic peaks at 35.28 eV and 37.49 eV displayed a positive shift, when tallied with previous reported data [80], suggesting a decrease in electron density. Therefore, the charge migration occurred from WO_3 to CdS, resulting in the formation of a Z scheme heterojunction.

3.5.5 Zeta Potential Measurement

Zeta Potential measurement is an analytical technique to estimate the surface charges of nanoparticles dispersed in a colloidal system. The stability of the emulsions depends on the values of the Zeta Potential. Zeta Potential of a sample is measured by determining the velocity of the charged particles moving towards an electrode, on applying an external electric field. The values of Zeta Potential might vary within the range of -100mV to +100 mV. A high zeta potential of nanoparticles in a colloidal solution indicates that the force of repulsion is more dominant compared to the force of attraction, leading to the formation of a comparatively more stabilized system. On the other hand, nanoparticles with low zeta potential tend to flocculate or form coagulates, resulting in low stability of the system.

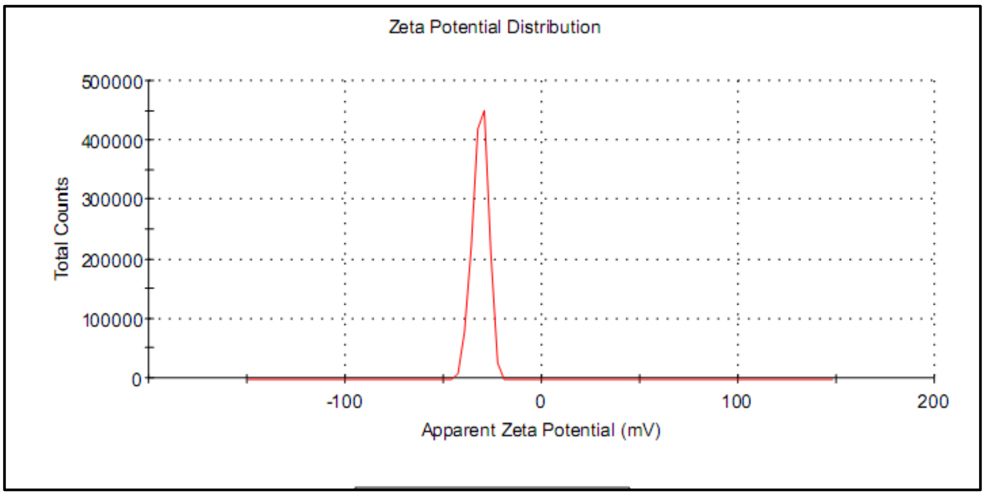

Figure 3.10 Zeta Potential of CdS-rGO-WO_3 dispersion

From Figure 3.10, it can be found that the Zeta potential of CdS-rGO-WO_3 dispersion is negatively charged with a value of about -31.4 mV. Thus, the stability of CdS-rGO-WO_3 dispersion is confirmed under ambient condition.

3.6 Photocatalytic activity for hydrogen generation

Hydrogen evolution by the reduction of water during photocatalytic water splitting was measured at specific interval of time and the yield of hydrogen was derived.The photocatalytic activity was studied by varying different process parameters like:

i) source of illumination: a) LED (45 W) and b) Solar simulator (100 W)

ii) types of mediator used: liquid state redox mediator and solid state mediator

iii) loading of reduced graphene oxide

i). Role of source of illumination

a. Photocatalytic hydrogen generation using LED

The rates of yield of hydrogen by comparing the five different photocatalysts are shown in Figure 3.11 a along with the activity plot (Figure 3.11 b). Photocatalytic hydrogen generation is generally characterized by photocatalytic activity (moles of hydrogen generated/gm.of catalyst.hour). Pristine CdS showed a photocatalytic activity of 3.17 mmol g^{-1} h^{-1}, the activity was further enhanced to 10.64 mmol g^{-1} h^{-1} for CdS- rGO-WO_3, due the effective separation of photogenerated electrons and holes as Z-scheme heterojunction was formed.

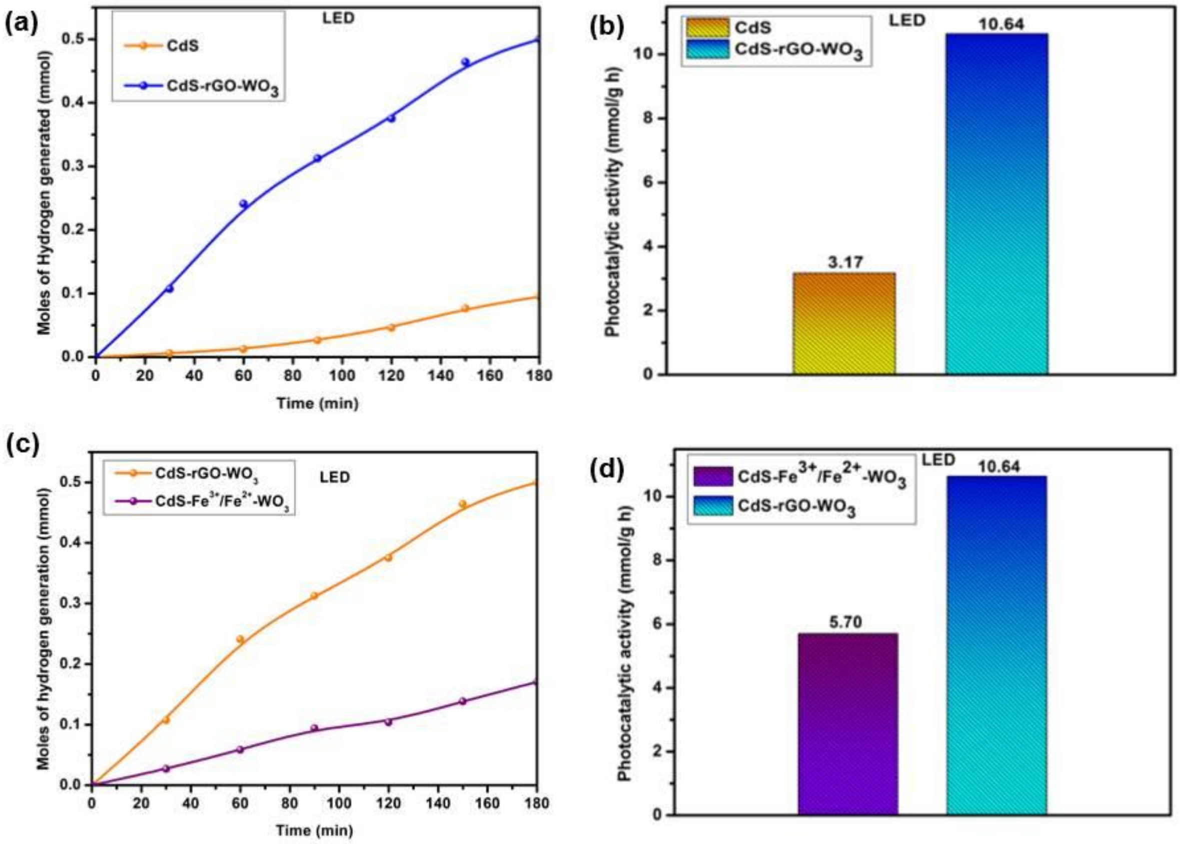

Figure 3.11 (a) Rate of production of hydrogen of two different photo-catalysts: CdS and CdS- rGO-WO_3, using LED as source of irradiation (b) Photocatalytic activities of CdS and CdS-rGO-WO_3 (c) Comparison between the rates of generation of hydrogen using rGO solid state mediator and Fe^{3+}/Fe^{2+} redox mediator for Z scheme nanocomposite (d) Comparison between the corresponding activity rates for rGO solid state mediator and Fe^{3+}/Fe^{2+} redox mediator

ii) Role of nature of mediator:

Different reversible redox mediators like Fe^{3+}/ Fe^{2+}, IO_3^-/I^-, NO_3^-/NO_2^- had been used as electron mediators in Z-scheme water splitting. However, undesirable backward reactions occurred due to the competitive oxidation of I^- by holes in the O_2 evolution photo-catalyst, while using IO_3^-/I^- as redox mediator [38]. Besides, the absorption of visible light by the redox mediators affects the light absorption of semiconductor photo-catalysts, thereby reducing the reaction efficiency of reversible redox mediator Z-scheme photocatalytic system. For this reason, solid state mediated Z-scheme systems without the reversible redox pair mediators are being explored in recent years. From Figure 3.11 c comparative analysis between solid state mediated Z scheme photocatalytic system and liquid state redox mediator based Z scheme photocatalytic system can be seen. Reduced graphene oxide (rGO) was used as the solid state mediator and the liquid state redox mediator ($Fe^{3+/}Fe^{2+}$) i.e. redox cycle of trivalent and divalent Fe ions was used. The activity rate almost doubled (10.64 mmol g^{-1} h^{-1}) for rGO based solid state electron mediator when compared to the $Fe^{3+/}Fe^{2+}$ based electron mediator (5.70 mmol g^{-1} h^{-1}) for the CdS- rGO-WO_3, nanocomposite (Figure 3.11 d).

b. Photocatalytic hydrogen generation using Solar Simulator

The cumulative volume of hydrogen generated with respect to time was plotted. The rates of yield of hydrogen were studied by comparing the four different photocatalysts as shown in Fig 3.12a along with the activity plot (Fig 3.12b). Photocatalytic hydrogen generation is generally characterized by photocatalytic activity. Pristine CdS displayed a photocatalytic activity of 4.9 mmol g^{-1} h^{-1} and the value of pristine WO_3 was 2 mmol g^{-1} h^{-1}. Due to the synergistic effect between rGO and CdS, the value of photocatalytic activity rose to a value of 6.9 mmol g^{-1} h^{-1}. This value was further increased to 11.69 mmol g^{-1} h^{-1}, by effective charge separation due to the formation of Z-scheme heterojunction. The effect of percentage of rGO on the photocatalytic activity (Figure 3.12c) was further studied by varying the percentage of rGO in the nanocomposite photocatalyst.

iii) Role of loading of rGO

The loading of reduced Graphene Oxide was varied, which had a direct effect on the performance of the rGO-CdS nanocomposite. rGO-CdS with rGO loading of 5%, 10%, 20% and 30% of rGO was developed and the photocatalytic activity was measured. It was seen (Figure 3.12c) that with increase in the loading of rGO from 5% the yield of hydrogen gradually increased (0.16 mmol) till 20% rGO loading (0.48 mmol) beyond which there is a decrease in the photocatalytic activity. Thus, 20% rGO loading was selected as the optimized rGO loading.

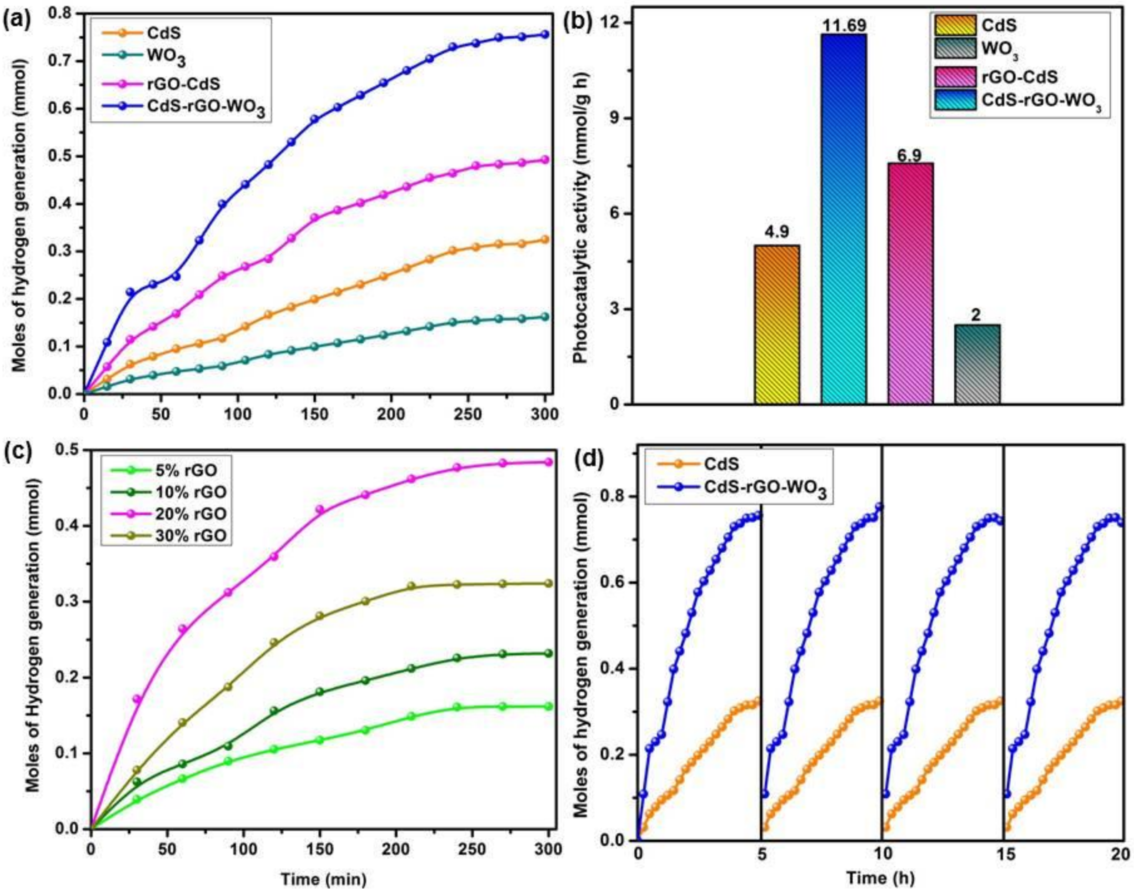

Figure 3.12 (a) Rate of production of hydrogen under the irradiation of solar simulator, full spectrum (b) Photocatalytic activities of four different photo-catalysts: CdS, rGO-CdS, WO_3, and CdS- rGO-WO_3, (c) Photocatalytic activities by varying the loading of rGO and (d) Time course evolution of hydrogen for CdS and CdS- rGO-WO_3

The long term photostability of the nanocomposite photocatalyst was also studied for four consecutive cycles. Each cycle was carried out for 5 h, after which the hydrogen gas was purged out by using inert gas nitrogen, every single time, keeping the reaction condition same. It can be seen from Figure 3.12 d that the hydrogen evolution was slightly increased in the second recycle for the nanocomposite CdS-rGO-WO_3 and the hydrogen generation rate reduced only after the fourth cycle by about 1.9%, exhibiting photostability when compared to pristine CdS. Thus, the photocatalyst can be reused multiple times, without any decrease in photocatalytic activity.

Table 3.5 Comparison of values of STH and AQE for the Z scheme photocatalytic system for the two different photocatalysts (CdS, CdS-rGO--WO_3)

Sl No.	Name of photocatalyst	STH (%) Source of illumination: LED	AQE(%) (3 h operation)	STH (%) Source of illumination: SS	AQE(%) (5 h operation)
1	**CdS**	0.13	0.314	0.27	0.64
2	**CdS-rGO-WO_3**	0.41	1.65	0.62	1.5

The Solar to Hydrogen Efficiency (STH %) and the Apparent Quantum Efficiency (AQE %) of both the systems are compared and the data is tabulated as given in **Table 3.5**. The Solar to Hydrogen Efficiency (STH %) for the nano-heterojunction CdS-rGO-WO_3 was calculated to be 0.62 and the Apparent Quantum Efficiency (AQE %) was estimated to be 1.5 (λ=420 nm) during operation using solar simulator, whereas 0.41 (STH%) and 1.65 (AQE %) was obtained during operation using LED. The value of AQE is dependent on the total number of hours of reaction, the operation using LED was carried out for 3h and the operation using solar simulator was carried out for 5h. The reading was taken in the full band range of the solar simulator and the for AQE calculation, 420 nm bandpass filter was used for allowing a single wavelength, that is monochromatic light (λ=420 nm).

Table 3.6 compares the photocatalytic activities of different photo-catalyst of this study with those of literature reported value

Table 3.6: Comparative photocatalytic activity data of different photo catalyst

Photocatalyst	Light Source	Activity (mmole g^{-1} h^{-1})	References
CdS-WO_3/Pt	500 W Xenon Lamp	2.9	**[41]**
CdS/ RGO-WO_3	300 W Xenon Lamp	0.12	**[42]**
CdS@WO_3/CoP	Xenon Lamp (λ=420)	0.73	**[43]**
CdS/WO_{3-x}/MoS_2	350 W Xenon Lamp	2.85	**[44]**
CdS-RGO-WO_3	**Solar simulator**	**11.69**	**This work**

3.7 Photoelectrochemical hydrogen generation

The photocurrent responses of the CdS and CdS-rGO-WO_3 were studied to analyse the photoelectrochemical phenomenon occurring on the surface of the photocatalyst. The transient photocurrent response was observed under intermittent irradiation of visible light.

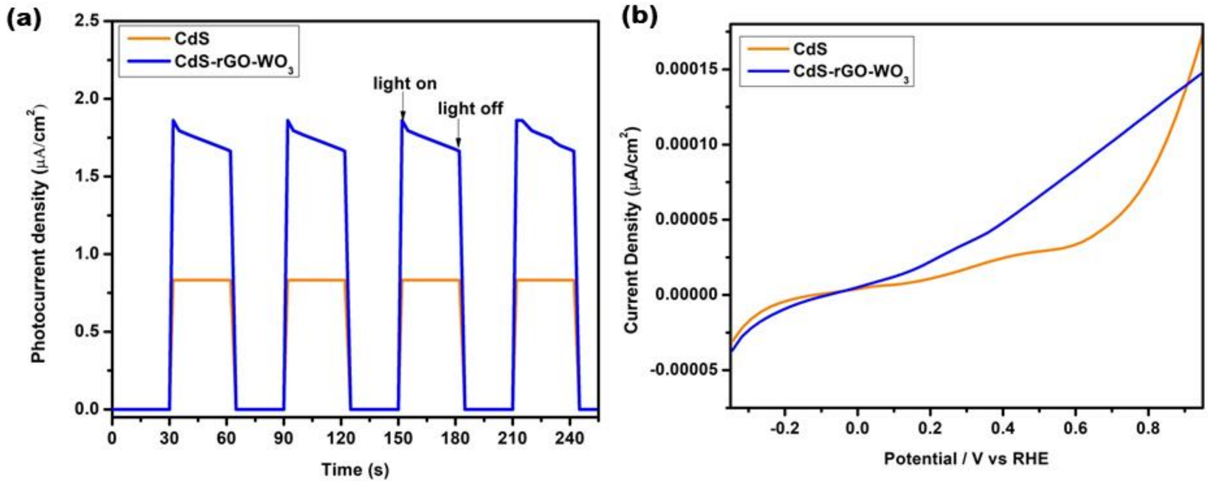

Figure 3.13 (a) Photocurrent comparison between CdS and CdS-rGO-WO_3 (b) Current vs Potential Plot of CdS and CdS-rGO-WO_3 in 0.5 mol/L Na_2SO_4 solution

From Figure 3.13a, it was found that photocurrent value reached zero in absence of light, while the value reached a high value in presence of light. For CdS-rGO-WO_3 nanocomposite, the photocurrent density was the maximum, while the photocurrent density for CdS was the lowest. A higher value of photocurrent density implied a higher value of degree of absorption of photons and a better mobility of charge transport, thereby signifying a reduction in the rate of recombination, which could also be verified from the PL study. Linear Sweep Voltammetry (LSV) study was done to observe the onset potential for H^+ reduction. From Figure 3.13b it could be seen that the onset potential for CdS-rGO-WO_3 nano-heterojunction displayed a negative shift compared to pure CdS, which suggests better HER performance, as also proved from the photocurrent analysis. The incident photon to current efficiency (IPCE) at 1.23 vs RHE was calculated to be 0.549 V.

3.8 Plausible Photocatalytic Reaction Mechanism

Z-scheme hetero-structure of CdS-rGO-WO_3 was typically designed to achieve efficient photo reduction of water to produce hydrogen. A plausible mechanism was predicted base on

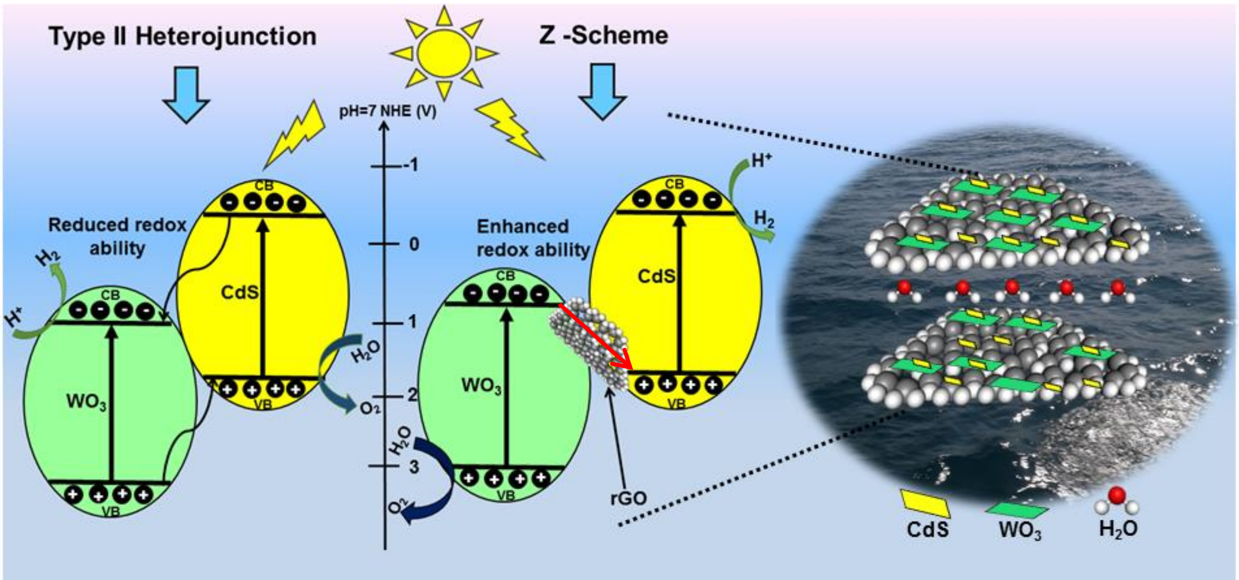

Figure 3.14 Plausible Mechanism

the obtained results and analysis, as can be seen in the Figure 3.14.

The calculated band gap of CdS was found to be 2.40 eV and that of WO_3 was 2.48 eV. The VB and CB can be calculated from the following the empirical formulae [83]:

$$E_{VB} = X - E^e + 0.5E_g \tag{3.19}$$

$$E_{CB} = E_{VB} - E_g \tag{3.20}$$

Here X is the electronegativity of the semiconductor, E_{VB} and E_{CB} represent the valence band and the conduction band potential, the value of E^e (energy of free electrons on hydrogen scale) is about 4.5eV [84]. Electronegativity of an atom is determined by obtaining the arithmetic mean of the ionization energy and electron affinity of that particular atom. The values of X of CdS and WO_3 are estimated to be about 5.19 eV and 6.59 eV, respectively. Therefore, the calculated values of E_{VB} and E_{CB} of CdS are 1.89 eV and -0.51 eV, while the E_{VB} and E_{CB} values of that of WO_3 are 3.33 eV and 0.85 eV, respectively.

Electron migration took place from the CB of CdS to the CB of WO_3, because of the potential difference and the position of the conduction band edges of CdS (-0.51 eV) and WO_3 (0.85 eV). rGO as an electron mediator, allowed the charge transfer at the interface of the heterojunction. This however resulted in reduced redox ability as photogenerated electrons gathered at the CB of WO_3, whereas photogenerated holes gathered at the VB of CdS. Z-Scheme heterojunction photocatalytic system was more favourable than that of Type-II photocatalytic system. This was also emphasized by the shift of electron cloud density from

WO_3 to CdS as observed from the XPS and PL spectra analysis. In case of Z-scheme photocatalytic system due to electrostatic attraction between electron and holes, migration of photogenerated electron occurred easily from the CB of the WO_3 to the photogenerated hole rich VB of the CdS, causing recombination of weaker photogenerated electrons and holes. In CdS-rGO-WO_3 Z-scheme nano heterojunction photogenerated electrons migrated from WO_3 to CdS via rGO, whereas holes of WO_3 remains intact in the VB. Therefore, reduction reaction occurred on the CdS, having higher reduction potential and oxidation reaction occurred on the WO_3, having higher oxidation potential respectively. Therefore utilization of the higher redox potential and minimization of the rate of recombination of more reactive photogenerated electron-hole pairs in Z-scheme heterojunction, aids in enhancing the photocatalytic performance.

3.9 Detailed cost-analysis of CdS-rGO-WO_3

Table 3.5

Chemical used	Chemicals	Approx. quantity	Cost (Rs.)	Cost (Dollar)
CdS- rGO-WO_3	Graphite flakes	0.02 g	281.8	3.4
	Cadmium Sulphide	0.05	1.78	0.022
	Sodium tungstate dihydrate	3.806	349.6	4.22
	Oxalic acid	1	512.8	6.19
	Deionized water	2 L	-	-
	Phosphoric Acid	10 ml	264.1	3.19
	Hydrogen Peroxide	10 ml	57.48	0.69
	Hydrochloric Acid	40 ml	13.8	0.17
	Ethanol (for synthesis & washing)	20 ml	12	0.14
	Sulphuric Acid	10 ml	9.8	0.12
Electricity Involved	Stirring	54.6 unit (30 hours)	485.9	5.87
	Drying	13 unit (10 hours)	115.7	1.40
	Calcination	20 unit (42 hours)	178	2.15
Total			2282.57	27.56

1 g of the synthesised rGO-ZnO-WO_3 photo catalyst typically costs $27.56.

The stirring and drying cost has been calculated using the following equation (3.21):

$$\text{Stirring, Drying cost} = \frac{\text{Instrument power (watt)} \times \text{time} \times \text{unit cost}}{1000} \tag{3.21}$$

3.10. Conclusions

- A solid mediator-based Z-scheme CdS-rGO-WO_3 nano-heterostructure was synthesized by an in-situ hydrothermal process.
- Photocatalytic performance study of rGO-CdS (varying rGO loading: 5%,10% 20% and 30%) to get optimal rGO loading that is 20%.
- Modification of optimal rGO-CdS photocatalyst by WO_3 to obtain best photoactive CdS-rGO-WO_3 nanocomposite photocatalyst for increasing the yield of hydrogen production.
- The formation of a direct Z-scheme CdS-rGO-WO_3 heterojunction was verified by using different sets of characterization techniques such as SEM, TEM, XRD, FTIR, UV-Vis and XPS.
- Photocatalytic performance study of CdS-rGO-WO_3 photocatalyst under LED and solar light illumination.
- Pristine CdS displayed a photocatalytic activity of 3.17 mmol g^{-1} h^{-1}whereas a value of 10.64 mmol g^{-1} h^{-1} for CdS-rGO-WO_3 photocatalyst was obtained which was almost 3.3 times than pristine CdS, in presence of LED as source of light.
- Pristine CdS displayed a photocatalytic activity of 4.9 mmol g^{-1} h^{-1} whereas a value of 11.69 mmol $g^{-1}h^{-1}$ for CdS-rGO-WO_3 photocatalyst was obtained which was almost 2.4 times than pristine CdS, in presence of solar simulator. This enhanced photocatalytic performance of the nanocomposites is suggestive of an efficient Z-scheme charge transfer at the interface of the heterojunction, as also evident from the generated photocurrent measurement. This research work offers a valuable insight in designing newer categories of heterojunction
- The incident photon to current efficiency (IPCE) at 1.23 vs RHE obtained as 0.549 V.

3.11 References

1. Cherp, A., & Jewell, J. (2014). The concept of Energy Security: Beyond the four As. *Energy Policy*, 75, 415–421..

2. Chaule, S., Hwang, J., Ha, S., Kang, J., Yoon, J., & Jang, J. (2021). Rational design of a high performance and robust solar evaporator via 3D-Printing technology. *Advanced Materials*, 33, 2102649.

3. Veziroğlu, T. N., & Şahi˙n, S. (2008). 21st century's energy: Hydrogen Energy System. *Energy Conversion and Management*, 49, 1820–1831.

4. Hwang, H. T., & Varma, A. (2014). Hydrogen storage for fuel cell vehicles. *Current Opinion in Chemical Engineering*, 5, 42–48.

5. Fujishima, A., & Honda, K. (1972). Electrochemical photolysis of water at a semiconductor electrode. *Nature*, 238, 37–38.

6. Cheng, H., Wang, J., Zhao, Y., & Han, X. (2014). Effect of phase composition, morphology, and specific surface area on the photocatalytic activity of TiO2 nanomaterials. *RSC Advances*, 4, 47031–47038.

7. Damkale, S. R., Arbuj, S. S., Umarji, G. G., Rane, S. B., & Kale, B. B. (2021). Highly crystalline anatase TiO2 nanocuboids as an efficient photocatalyst for hydrogen generation. *RSC Advances*, 11, 7587–7599.

8. Ma, Y., Wang, X., Jia, Y., Chen, X., Han, H., & Li, C. (2014). Titanium dioxide-based nanomaterials for photocatalytic fuel generations. *Chemical Reviews*, 114, 9987–10043.

9. Li, R., Weng, Y., Zhou, X., Wang, X., Mi, Y., Chong, R., et al. (2015). Achieving overall water splitting using titanium dioxide-based photocatalysts of different phases. *Energy & Environmental Science*, 8, 2377–2382.

10. Wei, R.-B., Huang, Z.-L., Gu, G.-H., Wang, Z., Zeng, L., Chen, Y., et al. (2018). Dual-cocatalysts decorated rimous CdS spheres advancing highly-efficient visible-light photocatalytic hydrogen production. *Applied Catalysis B: Environmental*, 231, 101–107.

11. Mkhalid, I.A. (2022). Solution-based synthesis of NiS/CdS nanocomposite heterojunction for efficient visible-light-driven hydrogen evolution. *Optical Materials*, 133, 113049.

12. Bi, Y., Wang, G., Wang, J., Liu, Q., Zhang, Y. (2022). Ni2P–Ni2P4O12 Enhanced CdS nanowires for efficient visible light photocatalytic hydrogen production. *Journal of Solid State Chemistry*, 314, 123407.

13. Wang, Y., Chen, J., Liu, L., Xi, X., Li, Y., Geng, Z., et al. (2019). Novel Metal Doped Carbon Quantum Dots/CdS composites for efficient photocatalytic hydrogen evolution. *Nanoscale*, 11, 1618–1625.

14. Cao, W., Zhang, X., Zheng, Y., Wang, K., Dai, H. (2017). Controlled One-step synthesis of CdS@ZnS core–shell particles for efficient photocatalytic hydrogen evolution. *International Journal of Hydrogen Energy*, 42, 2924–2930.

15. Ning, X., Lu, G. (2020). Photocorrosion inhibition of CdS-based catalysts for photocatalytic overall water splitting. *Nanoscale*, 12, 1213–1223.

16. Kokane, S.B., Sartale, S.D., Girija, K.G., Jagannath, Sasikala, R. (2015). Photocatalytic performance of Pd decorated TiO2–CdO composite: Role of in situ formed CdS in the photocatalytic activity. *International Journal of Hydrogen Energy*, 40, 13431–13442.

17. Ning, X., Wu, Y., Ma, X., Zhang, Z., Gao, R., Chen, J., et al. (2019). A novel charge transfer channel to simultaneously enhance photocatalytic water splitting activity and stability of CdS. *Advanced Functional Materials*, 29, 1902992.

18. Li, Q., Guo, B., Yu, J., Ran, J., Zhang, B., Yan, H., et al. (2011). Highly efficient visible-light-driven photocatalytic hydrogen production of CdS-cluster-decorated graphene nanosheets. *Journal of the American Chemical Society*, 133, 10878–10884.

19. Meissner, D., Memming, R., Kastening, B. (1988). Photoelectrochemistry of Cadmium Sulfide. Part 1. Reanalysis of photocorrosion and flat-band potential. *Journal of Physical Chemistry*, 19, 3476-3483.

20. Fermín, D.J., Ponomarev, E.A., Peter, L.M. (1999). A kinetic study of CdS photocorrosion by intensity modulated photocurrent and photoelectrochemical impedance spectroscopy. *Journal of Electroanalytical Chemistry*, 473, 192–203.

21. Lv, J.-X., Zhang, Z.-M., Wang, J., Lu, X.-L., Zhang, W., & Lu, T.-B. (2018). In situ synthesis of CdS/graphdiyne heterojunction for enhanced photocatalytic activity of hydrogen production. *ACS Applied Materials & Interfaces*, 11, 2655-2661.

22. Qian, L., Hou, Y., Yu, Z., Li, M., Li, F., Sun, L., et al. (2018). Metal-induced Z-scheme CdS/Ag/g-C3N4 photocatalyst for enhanced hydrogen evolution under visible light: The Synergy of MIP effect and electron mediator of Ag. *Molecular Catalysis*, 458, 43–51.

23. Li, J., Peng, Y., Qian, X., & Lin, J. (2018). Few-layer Co-doped MoS2 nanosheets with rich active sites as an efficient cocatalyst for photocatalytic H2 production over CdS. *Applied Surface Science*, 452, 437–442.

24. Neelgund, G.M., & Oki, A. (2011). Photocatalytic activity of CdS and Ag2S quantum dots deposited on poly(amidoamine) functionalized carbon nanotubes. *Applied Catalysis B: Environmental*, 110, 99–107.

25. Li, H., Tu, W., Zhou, Y., Zou, Z. (2016). Z-scheme photocatalytic systems for promoting photocatalytic performance: Recent progress and future challenges. *Advanced Science*, 3, 1500389.

26. He, Y., Wu, Z., Fu, L., Li, C., Miao, Y., Cao, L., et al. (2003). Photochromism and size effect of WO_3 and WO_3-TiO2 aqueous sol. *Chemistry of Materials*, 15, 4039–4045.

27. Danine, A., Cojocaru, L., Faure, C., Olivier, C., Toupance, T., Campet, G., et al. (2014). Room temperature UV treated WO_3 thin films for electrochromic devices on paper substrate. *Electrochimica Acta*, 129, 113–119.

28. Polleux, J., Gurlo, A., Barsan, N., Weimar, U., Antonietti, M., & Niederberger, M. (2006). Template-free synthesis and assembly of single-crystalline Tungsten oxide nanowires and their gas-sensing properties. *Angewandte Chemie International Edition*, 45, 267–271.

29. Rocha, K.O., Zanetti, S.M. (2011). Structural and properties of nanocrystalline WO_3/TiO2-based humidity sensors elements prepared by high energy activation. *Sensors and Actuators B: Chemical*, 157, 654–661.

30. Chen, D., Gao, L., Yasumori, A., Kuroda, K., Sugahara, Y. (2008). Size- and shape-controlled conversion of tungstate-based inorganic-organic hybrid belts to WO_3 nanoplates with high specific surface areas. *Small*, 4, 1813–1822

31. Pihosh, Y., Turkevych, I., Mawatari, K., Asai, T., Hisatomi, T., Uemura, J., et al. (2014). Nanostructured WO_3 /BiVO4 photoanodes for efficient photoelectrochemical water splitting. *Small*, 10, 3692–3699

32. Zhang, M., Lai, C., Li, B., Huang, D., Liu, S., Qin, L., et al. (2019). Ultrathin oxygen-vacancy abundant WO_3 decorated monolayer Bi2WO6 nanosheet: A 2D/2D heterojunction for the degradation of ciprofloxacin under visible and NIR Light Irradiation. *Journal of Colloid and Interface Science*, 556, 557–567.

33. Lei, F., Sun, Y., Liu, K., Gao, S., Liang, L., Pan, B., et al. (2014). Oxygen vacancies confined in ultrathin Indium oxide porous sheets for promoted visible-light water splitting. *Journal of the American Chemical Society*, 136, 6826–6829

34. Chen, W., Fu, W., Qian, G., Zhang, B., Chen, D., Duan, X., et al. (2020). Synergistic Pt-WO_3 dual active sites to boost hydrogen production from Ammonia Borane. *iScience*, 23, 100922.

35. Sachs, M., Park, J.-S., Pastor, E., Kafizas, A., Wilson, A.A., Francàs, L., et al. (2019). Effect of oxygen deficiency on the excited state kinetics of WO_3 and implications for photocatalysis. *Chemical Science*, 10, 5667–5677.

36. Bard, A.J. (1979). Photoelectrochemistry and heterogeneous photocatalysis at semiconductors. *Journal of Photochemistry*, 10, 59–75.

37. Ng, B., Putri, L.K., Kong, X.Y., Teh, Y.W., Pasbakhsh, P., Chai, S. (2020). Z-scheme photocatalytic systems for solar water splitting. *Advanced Science*, 7, 1903171.

38. Maeda, K. (2013). Z-scheme water splitting using two different semiconductor photocatalysts. *ACS Catalysis*, 3, 1486–1503.

39. Li, H., Zhou, Y., Tu, W., Ye, J., Zou, Z. (2015). State-of-the-art progress in diverse heterostructured photocatalysts toward promoting photocatalytic performance. *Advanced Functional Materials*, 25, 998–1013.

40. Zhou, P., Yu, J., Jaroniec, M. (2014). All-solid-state Z-scheme photocatalytic systems. *Advanced Materials*, 26, 4920–4935.

41. Zhang, L.J., Li, S., Liu, B.K., Wang, D.J., Xie, T.F. (2014). Highly efficient CdS/WO_3 photocatalysts: Z-scheme photocatalytic mechanism for their enhanced photocatalytic H2 evolution under visible light. *ACS Catalysis*, 4, 3724–3729.

42. Huang, Y., Liu, Y., Zhu, D., Xin, Y., Zhang, B. (2016). Mediator-free Z-scheme photocatalytic system based on ultrathin CdS nanosheets for efficient hydrogen evolution. *Journal of Materials Chemistry A*, 4, 13626–13635.

43. Zhang, Y., Hao, X., Ma, X., Liu, H., Jin, Z. (2019). Special Z-scheme CdS@WO_3 hetero-junction modified with CoP for efficient hydrogen evolution. *International Journal of Hydrogen Energy*, 44, 13232–13241.

44. Li, F., Hou, Y., Yu, Z., Qian, L., Sun, L., Huang, J., et al. (2019). Oxygen deficiency introduced to Z-scheme CdS/WO_3-x nanomaterials with MoS2 as the cocatalyst towards enhancing visible-light-driven hydrogen evolution. *Nanoscale*, 11, 10884–10895.

45. Xie, G., Zhang, K., Guo, B., Liu, Q., Fang, L., Gong, J.R. (2013). Graphene-based materials for hydrogen generation from light-driven water splitting. *Advanced Materials*, 25, 3820–3839.

46. Geim, A.K., Novoselov, K.S. (2007). The rise of graphene. *Nature Materials*, 6, 183–191.

47. Saha, S., Basak, V., Dasgupta, A., Ganguly, S., Banerjee, D., Kargupta, K. (2014). Graphene supported bimetallic G–Co–Pt nanohybrid catalyst for enhanced and cost effective hydrogen generation. *International Journal of Hydrogen Energy*, 39, 11566–11577.

48. Sarkar, A., Chaule, S., Mandal, S., Saha, S., Ganguly, S., Banerjee, D., et al. (2023). Enhanced photocatalytic hydrogen generation by splitting water using Sodium Alginate decorated RGO-CdS hybrid photo-catalyst. *Materials Today: Proceedings*.

49. Yu, Y., Ding, Y., Zuo, S., Liu, J. (2011). Photocatalytic activity of nanosized cadmium sulfides synthesized by complex compound thermolysis. *International Journal of Photoenergy*, 2011, 1–5.

50. Li, L., Zhao, J., Wang, Y., Li, Y., Ma, D., Zhao, Y., et al. (2011). Oxalic acid mediated synthesis of WO_3•H2O nanoplates and self-assembled nanoflowers under mild conditions. *Journal of Solid State Chemistry*, 184, 1661–1665.

51. Marcano, D.C., Kosynkin, D.V., Berlin, J.M., Sinitskii, A., Sun, Z., Slesarev, A., et al. (2010). Improved synthesis of graphene oxide. *ACS Nano*, 4, 4806–4814.

52. Saha, S., Maitra, S., Chattopadhyaya, M., Sarkar, A., Haque, S., Roy, S., et al. (2022). Unveiling the electrocatalytic activity of crystal facet-tailored cobalt oxide-rGO heterostructure toward selective reduction of CO2 to ethanol. *ACS Applied Nano Materials*, 5, 10369–10382.

53. Ghosh, P., Mandal, S., Majumdar, S., Sarkar, A., Ganguly, S., Kargupta, K. (2020). Enhanced Power Generation, faster transient response and longer durability of HT-PEMFC using composite polybenzimidazole electrolyte membrane with optimum RGO loading. *International Journal of Hydrogen Energy*, 45, 16708–16723.

54. Mandal, A., Maitra, S., Roy, S., Hazra, B., Ray, K., Kargupta, K. (2023). Selective Photo-reduction of CO2 to methanol using Cu-doped 1d-Bi2S3/rGO nanocomposites under visible light irradiation. *New Journal of Chemistry*, 47, 1422–1434.

55. Indhumathy, M., Prakasam, A. (2019). A one pot hydrothermal stimulated CdS-reduced graphene oxide (CdS/rGO) hybrid nanocomposite for high performance photovoltaic applications. *Journal of Materials Science: Materials in Electronics*, 30, 15444–15451..

56. Maitra, S., Sarkar, A., Maitra, T., Halder, S., Kargupta, K., Roy, S. (2021). Solvothermal phase change induced morphology transformation in CdS/CoFe2O4@Fe2O3 hierarchical nanosphere arrays as ternary heterojunction photoanodes for solar water splitting. *New Journal of Chemistry*, 45, 12721–12737.

57. Kumari, S., Suthar, D., Himanshu, Kannan, M.D., Kumari, N., Dhaka, M.S. (2022). Understanding the grain growth mechanism in CdS thin films by CdCl2 treatment and thermal annealing evolution. *Optical Materials*, 123, 111900.

58. Liu, Y., Cui, Y., Huang, F., Yang, X. (2016). Controllable synthesis of CdS/WO_3 heterostructures with enhanced photoelectrochemical performance. *RSC Advances*, 6, 16668–16672.

59. Hu, W.-H., Han, G.-Q., Dong, B., Liu, C.-G. (2015). Facile synthesis of highly dispersed WO_3•H2O and WO_3 nanoplates for electrocatalytic hydrogen evolution. *Journal of Nanomaterials*, 2015, 1–6.

60. Liang, Y.-C., Lung, T.-W. (2016). Growth of hydrothermally derived CdS-based nanostructures with various crystal features and photoactivated properties. *Nanoscale Research Letters*, 11.

61. Poulose, A.C., Veeranarayanan, S., Yoshida, Y., Maekawa, T., Sakthi Kumar, D. (2012). Rapid synthesis of triangular CdS nanocrystals without any trap emission. *Journal of Nanoparticle Research*, 14.

62. Zhang, C., Cheng, X., Liu, B., Guo, Z., He, G., Lv, Z. (2021). Noble-metal-free hexagonal wurtzite CdS nanoplates with exposed (110) and (112) crystal facets for efficient visible-light H2 production. *New Journal of Chemistry*, 45, 217–222.

63. Mohamed, M.M., Salama, T.M., Hegazy, M.A., Abou Shahba, R.M., Mohamed, S.H. (2019). Synthesis of hexagonal WO_3 nanocrystals with various morphologies and their enhanced electrocatalytic activities toward hydrogen evolution. *International Journal of Hydrogen Energy*, 44, 4724–4736.

64. Xiong, Z., Zhao, X.S. (2014). Preparation of layered titanate with interlayer Cadmium sulfide particles for visible-light-assisted dye degradation. *RSC Advances*, 4, 61960–61967.

65. Yang, F., Tian, X., Zhang, K., Zhang, X., Liu, L. (2018). The morphology–property effect and synergetic catalytic effect of CdS as electrocatalysts for dye-sensitized solar cells. ECS *Journal of Solid State Science and Technology*, 7.

66. Duan, X., Xiao, S., Wang, L., Huang, H., Liu, Y., Li, Q., et al. (2015). Ionic liquid-modulated preparation of hexagonal tungsten trioxide mesocrystals for lithium-ion batteries. *Nanoscale*, 7, 2230–2234.

67. Scherrer, P. (1912). Bestimmung der inneren struktur und der Größe von Kolloidteilchen Mittels Röntgenstrahlen. *Kolloidchemie Ein Lehrbuch*, 387–409.

68. Imran Din, M., Ahmed, M., Ahmad, M., Saqib, S., Mubarak, W., Hussain, Z., et al. (2023). Novel and facile synthesis of carbon quantum dots from chicken feathers and their application as a photocatalyst to degrade methylene blue dye. *Journal of Chemistry*, 2023, 1–11.

69. Barra, G.M.O., Crespo, J.S., Bertolino, J.R., Soldi, V., Pires, A.T. (1999). Maleic anhydride grafting on EPDM: Qualitative and quantitative determination. *Journal of the Brazilian Chemical Society*, 10, 31–34.

70. Kumar, S., Sharma, J.K. (2016). Stable phase CdS nanoparticles for optoelectronics: A study on surface morphology, structural and optical characterization. *Materials Science-Poland*, 34, 368–373.

71. Najafi-Ashtiani, S.H., Bahari, A., Gholipour, S., Hoseinzadeh, S. (2017). Structural, optical and electrical properties of WO_3–Ag nanocomposites for the electro-optical devices. *Applied Physics A*, 124.

72. Rengaraj, S., Venkataraj, S., Jee, S.H., Kim, Y., Tai, C., Repo, E., et al. (2010). Cauliflower-like CdS microspheres composed of nanocrystals and their physicochemical properties. *Langmuir*, 27, 352–358.

73. Tauc, J., Grigobovici, R., Vancu, A. (1966). Optical properties and electronic structure of amorphous germanium. *Physica Status Solidi B Basic Research*, 1966.

74. Janani Archana, K., Christy Preetha, A., Balasubramanian, K. (2022). Influence of urbach energy in enhanced photocatalytic activity of Cu doped ZnO nanoparticles. *Optical Materials*, 127, 112245.

75. Huang, L., Wang, X., Yang, J., Liu, G., Han, J., Li, C. (2013). Dual cocatalysts loaded type I CdS/ZnS core/shell nanocrystals as effective and stable photocatalysts for H2 evolution. The *Journal of Physical Chemistry C*, 117, 11584–11591.

76. Influence of defect structure on colour tunability and Magneto optical behaviour of WO_3 nanoforms. *RSC Advances*, 9, 20536–20548.

77. Prabhakar Vattikuti, S.V., Devarayapalli, K.C., Zeng, J., Shim, J., Nguyen Dang, N. (2023). Ternary nanocomposites of CdS/WO_3/g-C3N4 for hydrogen production. *Physical Chemistry Chemical Physics*, 25, 3758–3765.

78. Jerng, S.-K., Yu, D.S., Lee, J.H., Kim, C., Yoon, S., Chun, S.-H. (2011). Graphitic carbon growth on crystalline and amorphous oxide substrates using molecular beam epitaxy. *Nanoscale Research Letters*, 6.

79. Chen, C., Long, M., Xia, M., Zhang, C., Cai, W. (2012). Reduction of graphene oxide by an in-situ photoelectrochemical method in a dye-sensitized solar cell assembly. *Nanoscale Research Letters*, 7.

80. Chen, D., Li, T., Chen, Q., Gao, J., Fan, B., Li, J., et al. (2012). Hierarchically plasmonic photocatalysts of Ag/AgCl nanocrystals coupled with single-Crystalline WO_3 nanoplates. *Nanoscale*, 4, 5431.

81. Dotan, H., Mathews, N., Hisatomi, T., Grätzel, M., Rothschild, A. (2014). On the solar to hydrogen conversion efficiency of Photoelectrodes for water splitting. *The Journal of Physical Chemistry Letters*, 5, 3330–3334.

82. Yu, Y.-G., Chen, G., Hao, L.-X., Zhou, Y.-S., Wang, Y., Pei, J., et al. (2013). Doping La into the depletion layer of the Cd0.6Zn0.4S photocatalyst for efficient H2 Evolution. *Chemical Communications*, 49, 10142.

83. Cheng, H., Huang, B., Dai, Y., Qin, X., Zhang, X. (2010). One-step synthesis of the nanostructured AgI/BiOI composites with highly enhanced visible-light photocatalytic performances. *Langmuir*, 26, 6618–6624.

84. Peng, J., Xu, J., Wang, Z., Ding, Z., Wang, S. (2017). Developing an efficient NiCo2S4 cocatalyst for improving the visible light H2 evolution performance of CdS nanoparticles. *Physical Chemistry Chemical Physics*, 19, 25919–25926.

85. Ng, B., Putri, L. K., Kong, X. Y., Teh, Y. W., Pasbakhsh, P., Chai, S., & Zou, Z. (2020). Z-scheme photocatalytic systems for solar water splitting. *Advanced Science*, 7, 1903171.

86. Maeda, K. (2013). Z-scheme water splitting using two different semiconductor photocatalysts. *ACS Catalysis*, 3, 1486-1503.

87. Li, H., Zhou, Y., Tu, W., Ye, J., & Zou, Z. (2015). State-of-the-art progress in diverse heterostructured photocatalysts toward promoting photocatalytic performance. *Advanced Functional Materials*, 25, 998-1013.

88. Zhou, P., Yu, J., & Jaroniec, M. (2014). All-solid-state Z-scheme photocatalytic systems. *Advanced Materials*, 26, 4920-4935.

89. Tian, N., Huang, H., He, Y., Guo, Y., Zhang, T., & Zhang, Y. (2015). Mediator-free direct Z-scheme photocatalytic system: Bivo4/g-C3N4 organic–inorganic hybrid photocatalyst with highly efficient visible-light-induced photocatalytic activity. *Dalton Transactions*, 44(9), 4297–4307.

90. Tada, H., Mitsui, T., Kiyonaga, T., Akita, T., & Tanaka, K. (2006). All-solid-state Z-scheme in CdS–Au–TiO2 three-component nanojunction system. *Nature Materials*, 5(10), 782-786.

91. Kobayashi, R., Kurihara, K., Takashima, T., Ohtani, B., & Irie, H. (2016). A silver-inserted zinc rhodium oxide and bismuth vanadium oxide heterojunction photocatalyst for overall pure-water splitting under Red Light. *Journal of Materials Chemistry A*, 4(8), 3061-3067.

Chapter 4

Organic alginate encapsulated rGO-WO_3 based photocatalyst for continuous solar green hydrogen generation

Highlights:

- **Remarkable (81.8 mmol g^{-1} h^{-1}) solar hydrogen generation through water splitting using an alginate-encapsulated rGO-CdS-WO_3-alginate millisphere photocatalyst and a full-band spectrum of solar irradiation.**
- **Notable (90.63 mmol g^{-1} h^{-1}) solar hydrogen generation through water splitting using an alginate-encapsulated rGO-ZnO-WO_3-alginate millisphere photocatalyst and a full-band spectrum of solar irradiation.**
- **Dependence of the rate of hydrogen evolution on the extent of hydration and the time frame of pre-adsorption of the water (hydration) in the photocatalyst millisphere. Steady, constant rate of sustainable continuous hydrogen generation from flow reactors.**

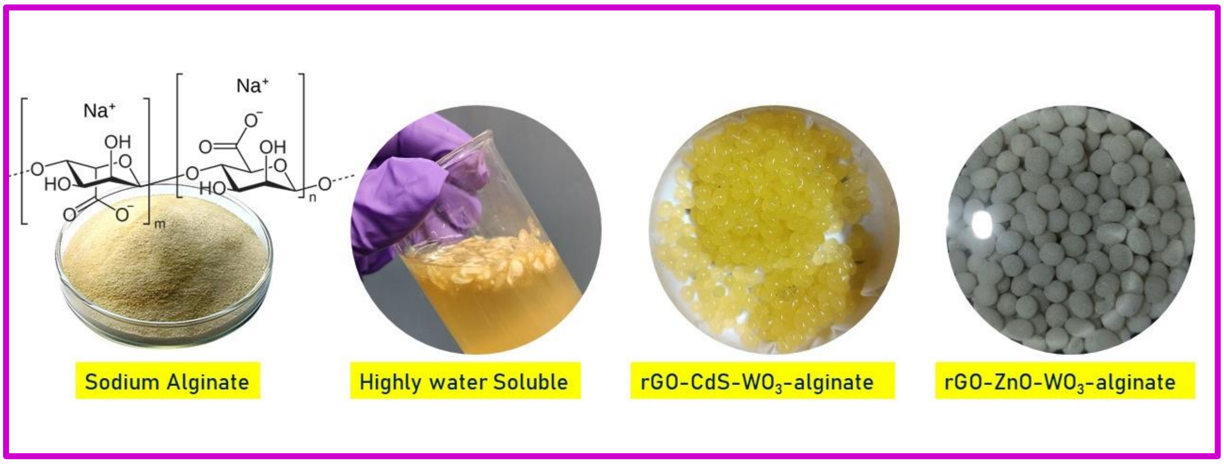

4.1 Introduction

The solar green hydrogen generation via photocatalytic water splitting depends on various factors which includes intensity of light [1], activity of the efficiency light conversion, the photocatalyst materials [2], photo-corrosion [3] and the recombination of photocarriers [4]. Numerous investigations have been undertaken in order to generate highly efficient photocatalytic materials capable of solving the issues experienced by presently used photocatalytic materials. To be a high-performance photocatalytic material, it should ideally be visible light-driven, highly resistant to photo-corrosion, have a correct band edge position, and be capable of smooth photo-charge carrier migration and separation [5-7]. Slow reaction kinetics, fast recombination of photo generated electrons and holes, a very poor hydrogen yield, metal aggregation, and metal loss are further challenges to commercialization of photocatalytic water splitting [8]. Photocatalysts with high water adsorption and retention capabilities are critical for viable solar hydrogen generation from water in batch or continuous modes of operation. The HER process is a heterogeneous catalytic reaction process that includes diffusion of water molecules towards the catalyst surface, physical and/or chemical adsorption of water molecules on the active sites, surface reactions, and hydrogen desorption. Because surface catalytic reactions are limited, improving photocatalyst performance still remains a serious issue.

The heterogeneous photocatalytic reaction occurs particularly on the active sites at the photocatalyst's surface, where all resident photo charges commence the activity. Thus, the performance of water splitting may be improved by tailoring the surface structure of photocatalytic materials [9-10]. The majority of photocatalyst systems for water splitting reported in the literature were powdered nanoparticles, which had a number of disadvantages, including metal aggression and metal loss during recovery, which greatly reduced metal loading during catalyst recovery and lowered catalytic activity [11-12]. Recovery of catalyst nanoparticles from the reactor is a complicated operation that is required for safe hydrogen generation in practical applications. One of the issues for photocatalytic systems using nanoparticles is catalyst recycling, which has a significant influence on running costs.

Furthermore, the majority of these structured powder catalyst systems work in batch mode and lack control over the pace of hydrogen production. Catalyst nanoparticles are commonly immobilised on substrates such as carbons [13], Ni substrates [14-15], polymers [16], metal phosphides [17], and ceramics [18]. Immobilisation and encapsulation of active nanoparticle photocatalyst into three-dimensional (3D) network microstructures have recently piqued the attention of researchers for separation-free photocatalytic applications [19-20]. Metal-organic frameworks (MOFs) have been suggested to support the alloy's nanoparticles [13], preventing metal agglomeration and increasing catalytic activity.

The metal-organic framework (MOFs) was able to stabilise metal nanoparticles due to its large surface area, well-defined pore structure, and porosity. Various bio-based materials, such as wood and rattan, have been used as catalyst carriers [19-20]. Transparent hydrogel-based materials with strong absorption capabilities due to their swollen 3D network structures, hydrophilicity that promotes chemisorption as well as physisorption of water confined in the channels, and good thermal and mechanical stability have recently piqued researchers' interest. The use of hydrogel as a small reactor to boost the photocatalytic hydrogen production activity of CdS and ZnS quantum dot photocatalysts is being investigated [21]. It has been shown [22] that CdS incorporated in cationic hydrogel improves photocatalytic hydrogen production. [23] describes a PVA hydrogel integrated with ZnO/ZnS as a separation-free photocatalyst with good recycling performance for increased photocatalytic hydrogen production. In general, the adsorption and distribution characteristics of water molecules in hydrogel micropores and on active sites play a critical role in regulating the efficacy of heterogeneous catalytic processes, particularly for hydrogel-encapsulated photocatalysts [24-27]. The photocatalyst's water adsorption capacity illustrates the difficulties of greater adsorption limiting subsequent hydrogen desorption and the production of semiconductors with specific crystal planes and a lower molecular adsorption energy [28-29]. Understanding the process of photocatalytic water dissociation is dependent on the interfacial structure of the water in contact with the photocatalyst; interactions between physically and chemically sorbed water molecules may result in superhydrophilicity of the photocatalyst [30]. According to the literature, water stabilised in the nano confinement area acts differently from water molecules on the bulk photocatalyst's surface [31-32]. In compared to a bulk water system, capturing water in a microporous organic framework or hydrogel may be an optimum method for boosting "nano-confined water molecules" on the inner active sites of a photocatalyst.

Surface photocatalytic reactions to change the distribution of water molecules and chemical adsorption qualities on photocatalyst active sites, from which it may continue on demand at a viable reaction state to boost hydrogen evolution reaction activity [25] are of great interest. The distribution and adsorption of water molecules impact the efficacy of a heterogeneous photocatalytic process [33-34]. The diffusion and adsorption of water molecules on the surface of the catalyst, as well as surface reactions, are involved in the heterogeneous catalytic hydrogen evolution reaction mechanism [35]. Any regulated increase in the pace or quantity of water diffusion towards the active sites of the photocatalyst will result in increased photocatalytic activity. Furthermore, at different time scales, charge carrier recombination and interaction with surface adsorbates are critical to the efficacy of the photocatalytic water splitting process. According to a recent- research, the hydrated material has increased hole mobility; the adsorbed water may successfully stabilise photogenerated charge carriers in nanocrystalline photocatalyst (TiO_2) and prevent their recombination on a time scale of minutes [36].

The focus of this Chapter 4 is the synthesis, characterization of the alginate based 3D-organic photocatalyst and study of solar green hydrogen evolution performance using the photocatalyst.

4.2 Objectives

(a) Alginate encapsulated reduced graphene oxide based CdS-WO_3

(b) Alginate encapsulated reduced graphene oxide based ZnO-WO_3

The specific objectives are enlisted below:

1. Synthesis of organic polysaccharide based rGO-CdS-WO_3-alginate millisphere photocatalyst.
2. Synthesis of organic polysaccharide based rGO-ZnO-WO_3-alginate millisphere photocatalyst.
3. Water uptake dynamics study of organic alginate based millisphere photocatalyst.
4. Batch and continuous study of solar hydrogen generation using both millisphere alginate based photocatalyst.
5. Recyclability test (durability) of organic alginate based millisphere photocatalyst.
6. Cell viability assay of both powder based and alginate based millisphere photocatalyst.
7. Cost Analysis comparison of both organic alginates based millisphere photocatalyst.

The major research problem is addressed in this chapter; the problem definition is as follows:

Problem definition:

Organic alginate encapsulated rGO-WO_3 based photocatalyst for continuous solar green hydrogen generation

Cadmium sulphide (CdS) is one of numerous visible-light-driven photocatalysts that have long been employed in the study of photocatalytic water splitting [37]. Cadmium sulphide's 2.4 eV band gap makes it an appealing active material for visible-range applications, and its band edge is at an ideal position for water-splitting Hydrogen [38-39]. A single CdS molecule application is restricted by characteristics such as its high photo charge carrier recombination rate, short hole diffusion length, and sluggish water oxidation kinetics [7]. To address these issues, several research groups have employed various ways to develop heterostructure system [40-41]. Graphene has received a great deal of interest in recent years due to its extraordinary features like as high optical transparency, excellent electrical conductivity, and a large theoretical specific surface area. Because of its conjugation structure, graphene, a uni-atomic layer of sp^2-hybridised carbon atoms, works as an excellent electron transporter and may therefore be utilised to reduce the rate of recombination of photo-generated electron-hole pairs [42-43]. Because of its unique qualities such as increased surface area, improved charge migration, and band-gap tuning capability, graphene-based catalytic devices are recognized for enhanced hydrogen production. Because of its remarkable optical characteristics, tunable bandgap, and considerable visible light absorption Tungsten oxide (WO_3) stands out as a viable choice. WO_3 is also nontoxic, cheap, and stable in acidic and oxidative environments, which is fascinating. It is generally established that a variety of synthetic techniques may be used to create photocatalysts with varying morphologies, sizes, and structures, each of which has a distinct impact on their catalytic efficiency. It has prospective uses in gas sensing, electrocatalysts, and lithium-ion batteries due to its unique electrical and optoelectronic characteristics, good photo-corrosion stability, and ease of recycling [44-47]. ZnO stands out among them as a dependable semiconductor material with a band gap of 3.3 eV for the synthesis of solar hydrogen due to its non-toxicity, high charge carrier mobility, chemical stability, and ease of availability. Despite this, because to the quick recombination of photogenerated electrons and holes, pure ZnO has a poor hydrogen generation efficiency [48]. In recent years, significant attempts have been made to increase ZnO effectiveness in visible light-driven photocatalysis, either by increasing the light-harvesting duration by reducing the bandgap or by improving charge separation efficiency [49-51]. As a consequence, doping with metals or non-metals [52], or linking with other semiconductors or nano-carbons such as graphene or reduced graphene oxide [53], may considerably enhance the efficiency of ZnO solar hydrogen generation [54].

4.3 Alginate as a 3D Metal-Organic Framework (MOF's) as photocatalyst support / encapsulation

Sodium alginate is an organic polysaccharide biopolymer composed mostly of L-guluronic acid (G) and D-mannuronic acid (M). Alginate is generally extracted from brown algae (Phaeophyceae) such as Laminaria hyperborea, Laminaria digitata, Laminaria japonica, Ascophyllum nodosum, and Macrocystis pyrifera [55] using aqueous alkali solutions, most often NaOH. To precipitate alginate, the extract is filtered and either sodium or calcium chloride is added to the filtrate. By treating this alginate salt with weak HCl, it may be converted into alginic acid. Water-soluble sodium alginate power is obtained after additional purification and conversion [56]. The existence of M/G and the sequence are determined by the source of alginic acid, which might be bacteria [57] or brown algae [58]. Alginate concentration in Ascophyllum nodosum is 22-30% by dry weight and 25-44% in Laminaria digitata [59]. When compared to other hydrogels, sodium alginate has a higher degree of porosity, swelling behaviour, gel strength, biodegradability, and biocompatibility, all of which have a substantial impact on their delivery carrier applications. [55]. The recommended biopolymer (organic moiety) for the catalyst-encapsulated millispheres is sodium alginate, which is commercially generated from brown seaweed extract. Alginate is an anionic polymer that is extracted from brown seaweed, which has been investigated and utilised for various sectors like in foods, textiles, drug delivery, bio-medical and pharmaceutical applications because to its biocompatibility, low toxicity, cheap cost, and moderate gelation caused by the addition of divalent cations. By increasing the molecular weight of alginate, the physical properties of the resultant gels may be enhanced. A high molecular weight polymer-generated alginate solution, on the other hand, becomes quite viscous, which is often undesirable in processing [60]. Manipulation of the molecular weight and its distribution may control both the viscosity of the pre-gel solution and the stiffness of the post-gelling solution independently. Immobilisation of metal ions during the gelation process resulted in the production of various metal-polymer composites throughout time by various research groups. Alginate was employed as a template to create nanostructures utilising components such as Co, Ni, Zn, and Fe [61-65]. During the synthesis of alginate hydrogels, divalent Ca^{2+} cations interact with two nearby diaxially linked G residues, resulting in the construction of a cavity that serves as a binding site for the egg-box buckling Ca^{2+} arrangement.

Figure 4.2: Calcium alginate as foam and millisphere beads, 3D model image of Calcium alginate

Chemical and/or physical cross-linking of hydrophilic polymers is a common method for forming hydrogels, and their physicochemical properties are highly dependent on the cross-linking type and density, as well as the polymers' molecular weight and chemical composition [66]. Combining an aqueous alginate solution with ionic cross-linking agents, such as divalent cations (i.e., Ca^{2+}), is the most popular approach for creating hydrogels (Figure 4.1). Because the structure of the guluronate blocks allows for a high degree of coordination of the divalent ions, the divalent cations are thought to bind only to guluronate blocks of the alginate chains. In what is known as the "**egg-box**" model of cross-linking, the guluronate blocks of one polymer chain connect with the adjacent neighbouring guluronate blocks, resulting in a gel structure [67]. Gels made from alginate with a high quantity of G residues, for example, are stiffer than those with a low level of G residues [68]. One significant disadvantage of ionically cross-linked alginate gels is their low long-term durability in physiological circumstances, since these gels may disintegrate owing to divalent ion release into the surrounding fluids as a result of exchange interactions with monovalent cations. Mammals cannot degrade alginate as alginase enzyme is not present that cleaves polymer chains, but metamorphically alginates are cross-linked gels that basically dissolves as reaction exchanges with cations that are monovalent like ions of sodium. Even if the gel dissolves, the average molecular weights of several commercially available alginates are greater than the renal clearance threshold of the kidneys, implying that the alginates will not be entirely eliminated from the body [69].

4.4 rGO-CdS-WO_3-alginate and rGO-ZnO-WO_3-alginate as 3D MOF photocatalyst for green solar hydrogen generation

Soft alginate hydrogel was selected as the organic carrier for the catalyst rGO-CdS-WO_3 and rGO-CdS-ZnO due to its benefits. Alginate hydrogel's long gelation process gives greater mechanical integrity and structural consistency [70]. Because the two G-blocks of neighbouring chains may create electronegative spaces for transporting cations, the alginate solution is readily transformed to alginate hydrogel by ionotropic gelation with a polyvalent metal ion (Ca^{2+}), resulting in the development of a 3D gel network [71]. The rGO-CdS-WO_3 and rGO-CdS-ZnO composite is ionic gelated/encapsulated in the alginate hydrogel by the external gelation method, in which soluble salt ($CaCO_3$) diffuses into the alginate sol phase to create heterogeneous hydrogels [72]. Greater water retention was achieved by increasing the concentration of alginate hydrogel, but the addition of rGO-CdS-WO_3 and rGO-CdS-ZnO increased photocatalytic efficiency. The performance of rGO-CdS-WO_3-Alginate and rGO-CdS-ZnO-Alginate in the context of solar hydrogen generation is investigated and compared; improved activity of alginate-encapsulated photocatalysts is assessed in comparison to pristine powder-like photocatalyst rGO-CdS-WO_3/ rGO-ZnO-WO_3 is evaluated. Water adsorption in the pores of alginate and on the active sites of the photocatalyst, as well as retention duration on the active sites of the photocatalyst, are important factors in regulating the overall pace of the water splitting process for hydrogen generation. The photocatalytic activity and rate of hydrogen evolution are examined in particular in relation to the level of hydration/pre-adsorption of water in the alginate-encapsulated photocatalyst milli-sphere. Furthermore, for the continuous mode of operation, the fluctuation of the production rate of solar hydrogen generation by water splitting with the change in incoming flow rate of water (residence time) has been investigated, which is seldom documented in the literature. In addition, the photo-corrosion characteristics were investigated using reusability and stability assessments. Cell viability testing is also used to demonstrate that encapsulated photocatalysts are less hazardous than virgin powder catalysts. Finally, a cost analysis is presented to address economic concerns. The organic polysaccharide polymer alginate nanocage, with its mesoporous pores and hydrophilic channels, offers itself as a suitable system for boosting water molecule transport and adsorption in the nano-confinement region. We used a rGO-CdS-WO_3-alginate/ rGO-ZnO-WO_3-alginate photocatalyst enclosed inside an organic polymer alginate nano-cage to allow water molecules to adsorb and the hydrogen evolution process to occur. The structure design facilitates the accumulation of reactant water molecules in the cavity of the rGO-CdS-WO_3-alginate/ rGO-ZnO-WO_3-alginate photocatalyst; the confined water molecules in the pores of the alginate and on the rGO-CdS-WO_3-alginate/ rGO-ZnO-WO_3-alginate surface through physical and chemical adsorption behave differently than the bulk water system and promote super hydrophilicity, thereby enhancing its photocatalytic performance. The intermolecular hydrogen bonds formed between the water molecule and the hydroxyl and acid groups of sodium alginate aid in water molecule binding and adsorption, allowing for the achievement of the goal of extending retention duration during the water-splitting process.

4.5 Materials for synthesis of rGO-CdS-WO_3-alginate millisphere photocatalyst:

Cadmium acetate dihyrate [$Cd(CH_3CO_2)_2.2H_2O$, 98% purity], Thio-urea ($SC(NH_2)_2$, 99% purity), Sodium tungstate dihydrate ($Na_2WO_4.2H_2O$), Sodium Alginate, Calcium Chloride ($CaCl_2$, 99.9%), Oxalic acid ($C_2H_2O_4$, 98% purity) were procured from Sigma-Aldrich. Graphite flakes (extra pure 99.5 %, 50 µm average sizes, bulk density 20-30 gm. /100 ml) and Sodium Alginate ($C_6H_9NaO_7$, 91%) was bought from Loba Chemie. Sulphuric Acid (H_2SO_4, 98%), Phosphoric Acid (H_3PO_4, 88%) Potassium Permanganate ($KMnO_4$, 99%), Hydrogen Peroxide (H_2O_2, 30%), Hydrochloric Acid (HCl, 35%), Ethanol (C_2H_5OH, 99.9%) were also procured from Merck. The chemical reagents used, were of analytical grade. Deionized water (DI) with a resistivity of 18.25 MΩ was utilised during the experimental process.

4.6 Synthesis of organic polysaccharide based rGO-CdS-WO_3-alginate millisphere photocatalyst.

The detailed synthesis of powder photocatalyst CdS-rGO-WO_3 has already been discussed in the Chapter No 3. The encapsulation of CdS-rGO-WO_3 in the organic Alginate matrix was done by the process of gelation, by ionic crosslinking. Hydrogel of Sodium Alginate forms due to the cross linkage between the carboxylate groups (COO^-) of Alginate and the divalent ions of Ca^{2+} (obtained from precursors like $CaCl_2$), creating ordered “egg box” like arrangement. [67] 1wt% aqueous solution of Sodium alginate was taken for synthesizing Alginate hydrogel. This solution was stirred at vigorously for 2 hours at a speed of 800 rpm in a magnetic stirrer (Tarson), until a homogeneous solution is obtained. Previously synthesized CdS-rGO-WO_3 (as mentioned in Chapter 3) was then added to this solution. The solution was then stirred for extra 4 hours with an increased speed of 1000 rpm. Meanwhile, 1 wt. % aqueous solution of $CaCl_2$ was prepared as a cross-linker. Then this $CaCl_2$ solution was dispensed with the help a micropipette, leading to the formation of uniform spherical beads. These microspheres were then kept in a petri dish for stabilization for 30 minutes (ageing time). These beads were then washed with deionized water for three times, followed by vacuum filtration and finally dried in vacuum oven ($\leq 80^0C$). Similarly, a Calcium-Alginate is synthesized in a same manner but without the addition of the photocatalyst powder.

4.7 Materials for synthesis of rGO-CdS-ZnO-alginate millisphere photocatalyst:

Zinc nitrate [$Zn(NO_3)_2.6H_2O$, 98% purity], Potassium Hydroxide (KOH, 99% purity), Sodium tungstate dihydrate ($Na_2WO_4.2H_2O$), Sodium Alginate, Calcium Chloride ($CaCl_2$, 99.9%), Sodium Chloride (NaCl) and Ammonia were procured from Sigma-Aldrich. Graphite flakes (extra pure 99.5 %, 50 µm average sizes, bulk density 20-30 gm. /100 ml) and Sodium Alginate ($C_6H_9NaO_7$, 91%) was bought from Loba Chemie. Sulphuric Acid (H_2SO_4, 98%), Phosphoric Acid (H_3PO_4, 88%) Potassium Permanganate ($KMnO_4$, 99%), Hydrogen Peroxide (H_2O_2, 30%), Hydrochloric Acid (HCl, 35%), Ethanol (C_2H_5OH, 99.9%) were also procured from Merck. All other chemical reagents were of analytical grade and used as received without further purification. Deionized water (DI) with resistivity of 18.25 MΩ was used during the experimental procedure.

4.8 Synthesis of organic polysaccharide based rGO-ZnO- WO_3 -alginate millisphere photocatalyst.

The detailed synthesis of powder photocatalyst CdS-rGO-WO_3 has been discussed in the chapter 3. The encapsulation of rGO-ZnO/WO_3 in the organic Alginate matrix was done by the process of gelation, by ionic crosslinking. Hydrogel of Sodium alginate forms due to the cross linkage between the carboxylate groups of Alginate and the divalent ions of Ca^{2+} (obtained from precursors like $CaCl_2$), creating ordered "egg box" like arrangement [67]. 1 wt% aqueous solution of Sodium Alginate was taken for synthesizing Sodium Alginate hydrogel. This solution was stirred at high speed for about two hours, until a homogeneous solution is obtained. Previously synthesized rGO-ZnO/WO_3 was then added to this solution. The solution was then stirred for two more hours. Meanwhile, 1 wt. % aqueous solution of $CaCl_2$ was prepared and chilled in a low temperature freezer. Then this $CaCO_3$ solution was dispensed with the help a micropipette (Inner diameter: 0.5 cm), leading to the formation of uniform spherical beads. The distance between nozzle and $CaCl_2$ solution was 8 cm and the solution was stirred slowly. These microspheres were then kept in a petri-dish in low temperature (4^0C) for stabilization. These beads were then washed with deionized water, followed by vacuum filtration and finally dried in vacuum oven (Figure 4.2).

Figure 4.3: Synthesis of rGO-ZnO-WO_3-Alginate millisphere beads

4.9 Material Characterizations of alginate based photocatalyst millisphere.

The morphologies of the synthesized alginate based millisphere photocatalysts were studied by employing Field Emission Scanning Electron Microscopy (FE-SEM) technique. Hitachi S-3400 SEM was used for analysis of the surface morphology of the samples collected at an accelerating voltage of 15.0 kV. The Energy Dispersive X-ray (EDX) study was performed to obtain the percentage of elements in the composite material.

4.9.1 Field emission scanning electron microscopy (FE-SEM) and Energy Dispersive X-ray (EDX) microanalysis

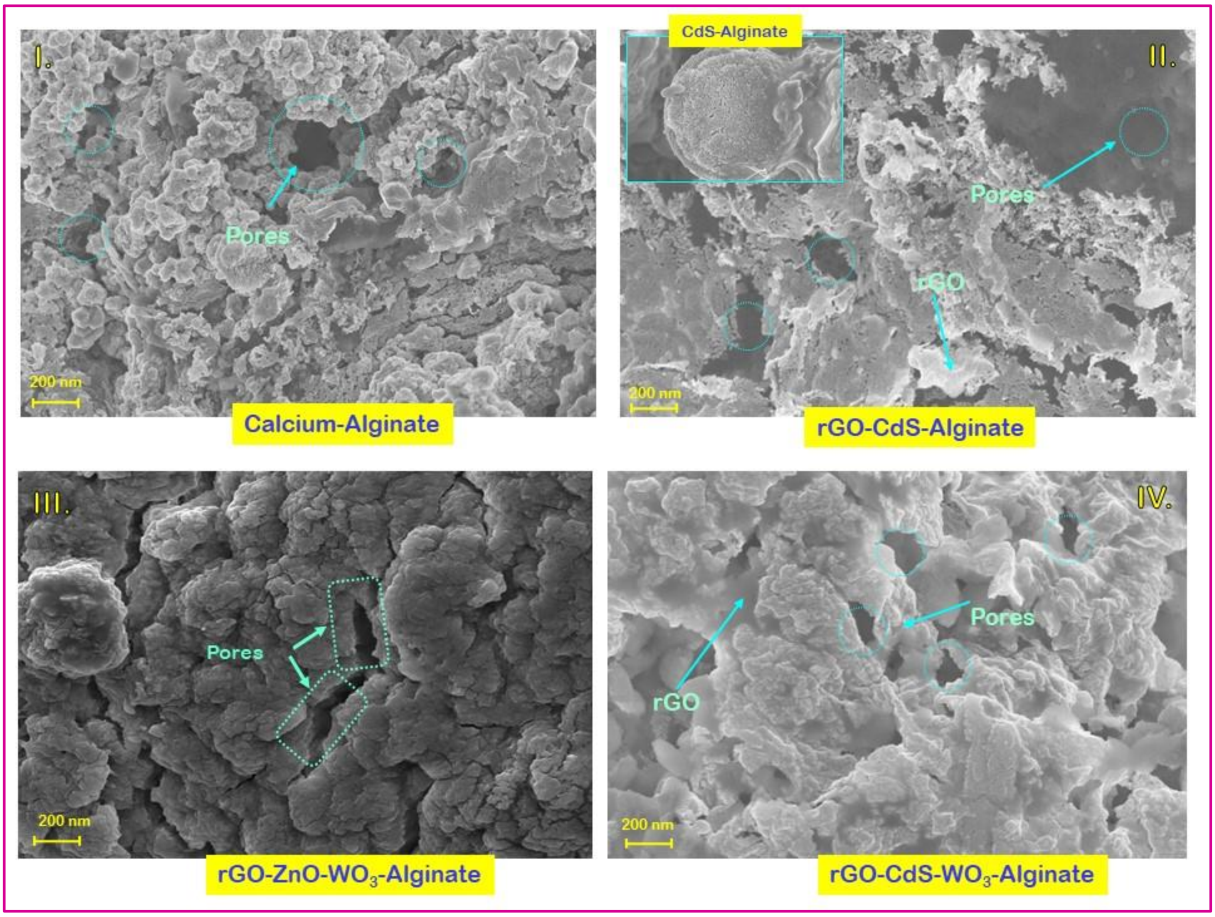

Figure 4.4: FE-SEM Image of (I) Calcium alginate (II) rGO-CdS-alginate, CdS-Alginate (Inset) (III) rGO-ZnO-WO$_3$-Alginate and (IV) rGO-CdS-WO$_3$-Alginate

The morphologies of Calcium alginate (Figure 4.3-I), CdS-Alginate (Figure 4.3-II, Inset), rGO-CdS-Alginate (Figure 4.3-II), rGO-ZnO-WO$_3$-Alginate (Figure 4.3-III) and rGO-CdS-WO$_3$-Alginate (Figure 4.3-IV) were investigated by scanning electron microscopy. The SEM analysis shown in Figure 4.3, depicts homogenously distributed sodium alginate nano-fibrils scattered with CdS nano-flowers in CdS-alginate (Figure 4.3-II, inset). All the alginate based photo catalyst morphologies displayed a porous structure. rGO-ZnO-WO$_3$-Alginate and rGO-CdS-WO$_3$-Alginate exhibits a denser pore structure compared to that of rGO-CdS-Alginate. This can be attributed to the fact that the incorporation of photocatalyst nanoparticles destroys the pristine alginate hydrogel network. The surface became rough because of the attachment of photocatalyst nanoparticles to the hydrogel surface. Figure II inset shows that the micro fibrils of sodium alginate can be seen interspersed with nano-flowers of CdS on the crumpled-up sheets of graphene in case of CdS- alginate. This crumpled-up nature of graphene may result from the restacking procedure and the exfoliation effect [73]. The pores observed in each alginate based photocatalyst shows the high water retention capacity within its 3D organic structure.

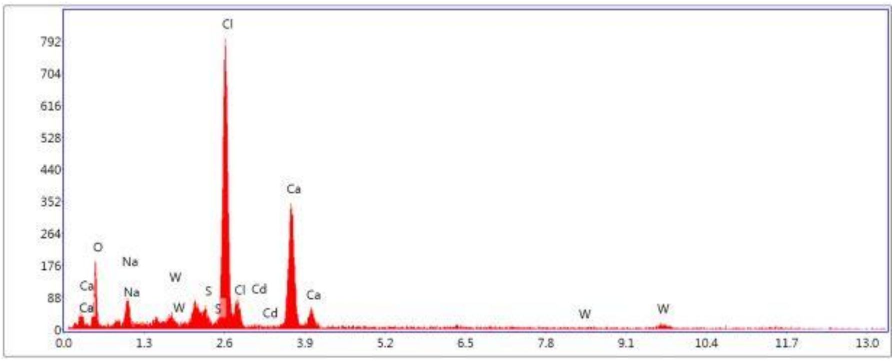

Figure 5.4 : EDX spectra of rGO-CdS-WO_3-Alginate

The obtained EDX spectrum of rGO-CdS-WO_3-Alginate (Figure 4.4) also confirmed the successful formation with the appearance of Cd, W, Ca and S peaks. The atomic composition of Cd, W and S was found to be 0.38, 0.74 % and 2.85 %, respectively. The atomic percent is almost equivalent to their nominal stoichiometry within the experimental error, according to the EDX spectra. Due to the encapsulation of photocatalyst in the alginate framework majority of the peaks correspond to carbon and oxygen. Other peak of Ca and Cl are due to the presence of cross linker in the organic framework of alginate.

Table 4.1: Composition tabulation by EDX spectra

Element	Weight %	Atomic %	Net Int.	Error %	Kratio	Z	R	A	F
O K	27.67	47.30	36.61	13.67	0.0378	1.1219	0.9325	0.1219	1.0000
NaK	5.38	6.40	19.36	15.23	0.0191	1.0226	0.9615	0.3466	1.0033
S K	2.85	2.43	24.73	9.70	0.0255	1.0063	0.9998	0.8484	1.0483
ClK	33.51	25.84	256.25	3.54	0.2885	0.9578	1.0064	0.8817	1.0195
CdL	0.38	0.09	1.12	68.54	0.0028	0.7536	1.2064	0.9336	1.0396
CaK	25.22	17.20	126.73	4.71	0.2137	0.9722	1.0242	0.8606	1.0132
W L	5.00	0.74	3.40	40.41	0.0371	0.6188	1.1763	1.0395	1.1533

4.10 Liquid water sorption of alginate based photocatalyst millisphere.

Hydrogels had the capacity to hold and absorb a particular amount of the water due to its 3D cage like structure. The sorption of liquid water was studied by quantifying water uptake over time while immersed in liquid water. At room temperature, vacuum-dried, pre-weighed dry alginate based hydrogel millisphere particles were submerged in deionized water. After dehydrating their surfaces with filter paper, their weight was attentively monitored at regular intervals until the millisphere hydrogel showed a constant weight. The fractional change in weight was converted to a percentage using empirical formulas. All investigations were conducted three times, and the mean results were used for calculations. Using a micrometre, the average diameter of dried crystals was determined using a micrometre (Kayco).

$$\text{Dynamic weight change } (\%) = \frac{(\text{Final weight} - \text{Initial weight})}{\text{Initial weight}} \times 100 \tag{4.1}$$

Alginate Millisphere	Average diameter (± 0.001 cm)	Water uptake (%)
Calcium alginate	0.61	98.6
rGO-CdS-Alginate	0.63	96.1
rGO-CdS-WO_3-alginate	0.64	96.9
rGO-ZnO-WO_3-alginate	0.58	97.7

Table 4.2: Average diameter and water uptake(%) of different millisphere photocatalyst

The water uptake or sorption characteristics of Ca-alginate, rGO-CdS-Alginate, rGO-CdS-WO_3-alginate and rGO-ZnO-WO_3-alginate at the room temperature (20^0C) are shown in the Figure 4.5 I. Since Ca-Alginate hydrogel have multiple Carboxyl group(COO^-) and hydroxyl (OH^-)group resulting maximum water uptake. For the time duration of 10 hour of water uptake the Ca-Alginate can achieves 98.6% and continues to swell, absorbs water in its larger pores. The inner pores of the Ca-alginate are higher compared to others prompting higher absorption of water molecules. Similarly, rGO-CdS-Alginate, rGO-CdS-WO_3-alginate and rGO-ZnO-WO_3-alginate shows the water uptake as 96.1%, 96.9% and 97.7%, respectively (Figure 4.5 II). The increased water uptake capacity of the alginate hydrogel encapsulated photocatalyst reflects the increase in the photocatalytic activity.

Calcium alginate has higher water uptake capacity but doesn't have any photocatalytic activity due to absence of any photocatalyst materials in it (00.00 mmole g^{-1} h^{-1}).

The water uptake of all the photocatalyst encapsulated alginate hydrogels is slowly increased up to 4 hours (point of inflection versus time elapsed; Figure-4.5-I) and then increased rapidly up to 8 hours followed by gradual increase until the equilibrium reached at around 12 hours. The dynamic water adsorption behaviour of alginate encapsulated photocatalyst is described by a two-stage kinetic model.

Stage-I: When swelling and pore size grow, the first stage contains sluggish rate of adsorption is far from equilibrium.

Stage-II: When the pore size crosses a threshold value, the dynamic adsorption follows an equilibrium controlled first order kinetics.

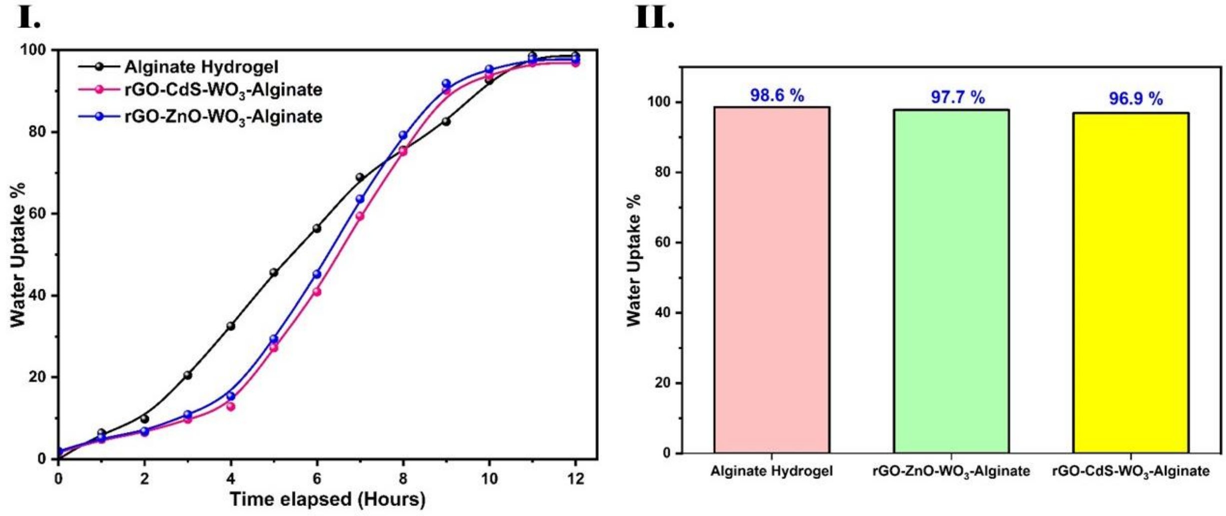

Figure 4.5: Comparison of water uptake of different alginate based photocatalyst

4.11 Photocatalytic Hydrogen Generation: batch and continuous mode of operation

The basic continuous photocatalytic hydrogen generating system is shown in Figure 4.6. Semi-batch and continuous tests were used to evaluate photocatalyst performance. The pH and dissolved solids of the water were examined using a portable pH/EC/TDS checker (Hanna Instruments, USA; HI991300P) for a specific semi-batch experimental investigation, and they were 6.53 and 0.009 ppm, respectively. To replicate, a solar simulator (manual shutter, Newport Oriel LCS-100) was used, with the intensity set to 100 mW cm^{-2}. The AM 1.5G air mass filter installed in the LCS-100 solar simulator (Class ABB) may achieve class A spectral performance in compliance with the IEC and ASTM specifications for 1 sun irradiation output. The hydrogen production was studied using the water column displacement method. All alginate based millisphere photocatalyst were used for hydrogen generation (semi-batch mode) at 20°C in a specifically built lab-scale glass photocatalytic reactor. There was no sacrificial agent utilized, and 0.5 g of the alginate encapsulated photocatalyst was distributed in 25 ml of deionized water. The created glass reactor was purged to remove O_2 (air) before to each photocatalytic reaction experiment using a vacuum pump (Rivotek, 30 LPM). Prior to the start of the photocatalytic reaction (by turning on the solar simulator), the photocatalyst milli sized beads were immersed in water for three, six, twelve, and eighteen hours to allow water to sorb into the pores of the alginate hydrogel and subsequent pre-adsorption of confined water into the pores to reach close proximity of the encapsulated photocatalyst.

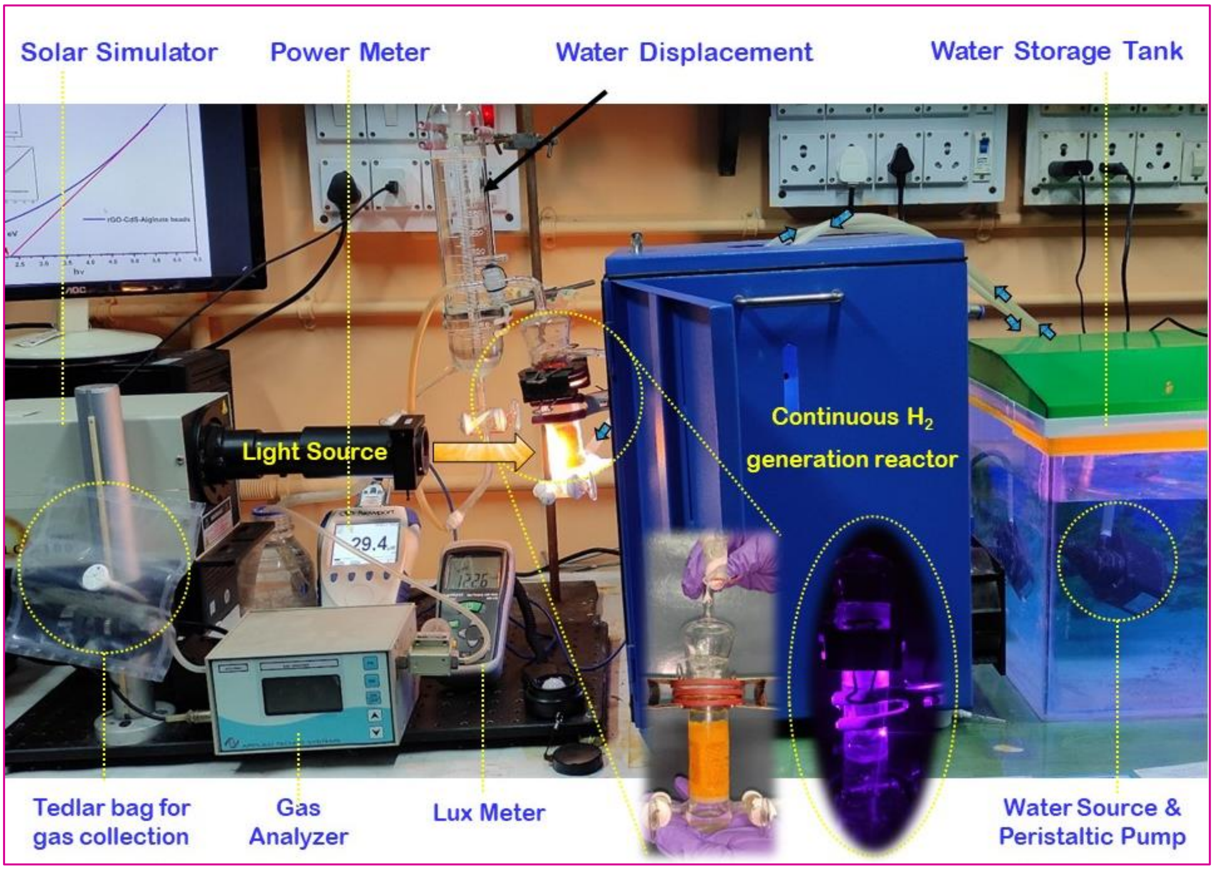

Figure 4.6: Real life picture of Continuous Hydrogen generation set-up

The photocatalytic process is carried out for more than 5 hours, or until the rate of hydrogen production reaches zero. The packed bed millisphere beads were used to create and develop the continuous photocatalytic splitting reactor. The deionized water was continually purged at a predetermined flow rate via the reactor's bottom valve by a peristaltic pump, and the flow was regulated by a water flow controller. The reactor was made out of an interior vessel that had packed millisphere catalytic beads and was filled with water. The reactor's water was withdrawn by the water outlet, while the hydrogen produced was collected via the gas outlet valve. The created gas was passed through a potassium pyrogallate solution to absorb the oxygen, and the displacement of water was used to calculate the cumulative hydrogen generation over time. For eight hours, the constant creation of hydrogen is recorded. To evaluate the recycling stability of the photocatalysts, each used milli sized bead photocatalyst was washed multiple times with deionized water and dried in an oven at 60 °C for 4 hours prior to each subsequent run under the same operating circumstances. In the glass reactor, the dried material was re-dispersed in 25 mL of deionized water. The photo catalyst’s recyclability was investigated over the course of four successive cycles.

The photocatalytic activity and apparent quantum efficiency of a given photocatalyst are measured. The cumulative hydrogen production versus time data is used to calculate the photocatalytic activity (mmol hydrogen g^{-1} hr^{-1}) of the various photocatalysts. Experiments are carried out utilizing the solar simulator's full band spectra as well as band pass filters at 420 nm. A 420 nm band pass filter is used to calculate apparent quantum yields (AQYs). The light intensity was set to 100 mW cm^{-2} and recorded using a power meter (Newport 843-R). The radius was irradiated across a 14.44 cm^2 region. A power metre (843-R, Newport) was used to measure the number of incoming photons from the solar simulator (Newport LCS-100).

Apparent quantum yields (AQYs) for different Alginate encapsulated photo-catalysts were calculated by the following equation, as previously reported [74] and tabulated in Table 4.3:

$$\mathrm{AQE}(\%) = \frac{2\times\text{The number of evolved Hydrogen molecules}}{\text{The number of incident photons}} \times 100 \qquad (4.2)$$

A novel 3D millisphere of organic alginates hydrogel-encapsulated graphene-supported CdS-WO_3 and CdS- ZnO photocatalyst with high water retention capability is investigated here for enhanced solar hydrogen production from water using batch and continuous modes of operation for a pressure-driven flow-through system under full band solar irradiation. The primary emphasis was put on the function of enhanced water molecule adsorption on the active sites of the photocatalyst on the performance of solar hydrogen generation. It is proven that alginate-encapsulated photocatalyst systems (rGO-CdS-WO_3-alginate and rGO-ZnO-WO_3-alginate) generate more hydrogen than competing powder catalysts. The photocatalytic activity of various catalysts is assessed using cumulative hydrogen production data for about 6 hours and compared to published data (Table 4.4). For comparison, pure sodium alginate millispheres were also evaluated for photoactivity, and organic sodium alginate was shown to have little photocatalytic activity. By adding CdS-alginate, the photocatalytic activity of pure CdS powder photocatalyst (2.6 mmol h^{-1} g^{-1}) may be improved by an order of magnitude. When rGO-CdS is utilised instead of CdS, the specific surface area increases, electrons flow faster, the band gap value decreases, and electron hole recombination decreases, as indicated in the powder photocatalyst PL spectra.

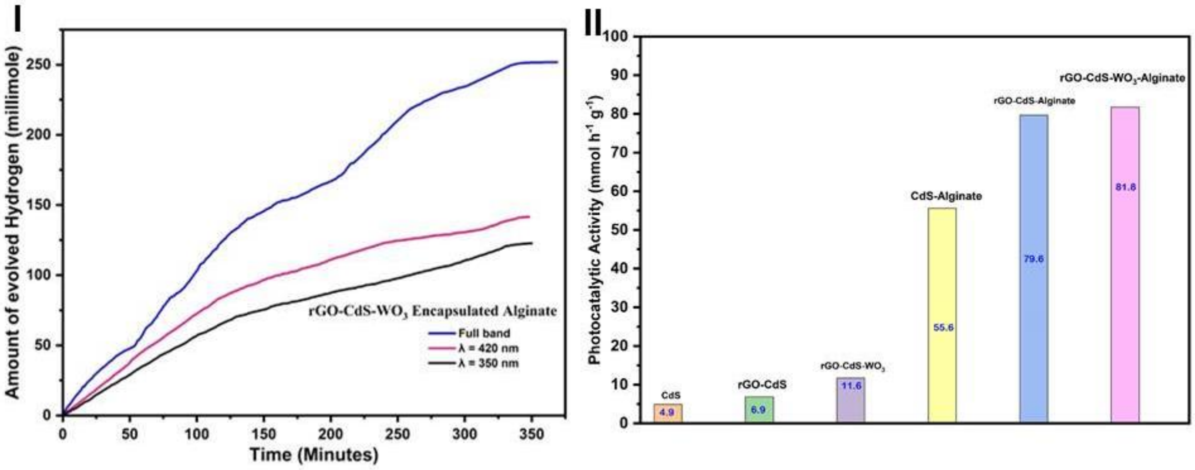

Figure 4.7 : (I)Batch Hydrogen generation from rGO-CdS-WO_3-Alginate (II) Activity comparison with its counterpart photocatalyst

Table 4.3: AQE(%) of different photocatalyst

Alginate based Photocatalyst	AQE(%)
CdS-Alginate	15.16
rGO-CdS-Alginate	19.51
rGO-CdS-WO_3-Alginate	21.9

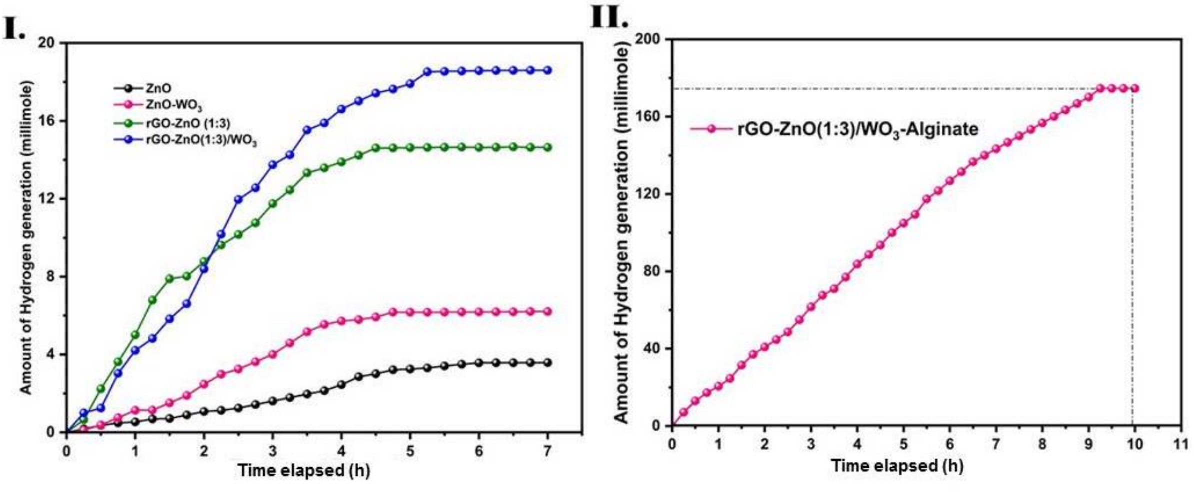

Figure 4.8: Batch Hydrogen generation from (I) powder photocatalyst (II) alginate based photocatalyst

The photocatalytic activity of rGO-CdS-WO_3-alginate and rGO-ZnO-WO_3-alginate increases to 81.8 mmol h^{-1} g^{-1} and 90.63 mmol h^{-1} g^{-1}, respectively (Figures 4.7 & 4.8). The strong visible light absorption and low band gap of the organic framework network contribute to the homogenous dispersion of photocatalyst nanoparticles. Furthermore, the increased surface area provided more surface reactive sites, which may improve water molecule capture and facilitate photocatalysis of rGO-CdS-WO_3-alginate and rGO-ZnO-WO_3-alginate photocatalysts. The performance of the alginate-based photocatalyst millisphere was improved, suggesting that the combination of its counter particle photocatalyst and the alginate network is good for photocatalytic activity.

Figure 4.9 depicts continuous hydrogen generation using an alginate-encapsulated bead-like photocatalyst.

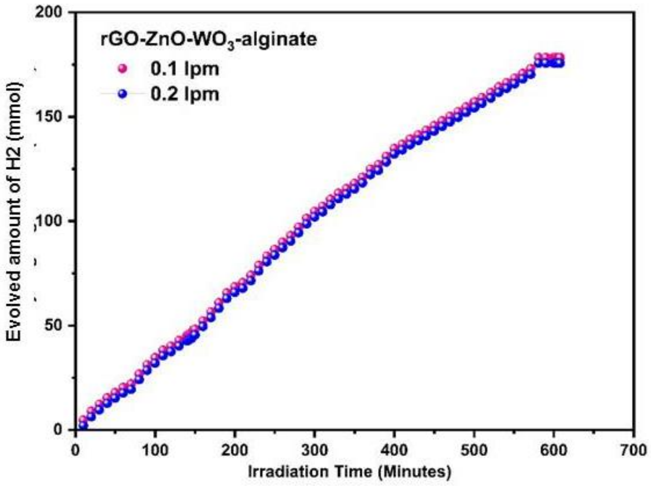

Figure 4.9: Continuous Hydrogen generation at different flow rate for rGO-CdS-WO_3-alginate

The hydrogel-encapsulated photocatalysts were soaked with water maintaning a pre-adsorption duration of six hours. Inlet flow rate is tested for the effect of the water flow rate on hydrogen generation. Beyond an initialization period, the curve of evolved hydrogen generation over time becomes constant and reaches the steady hydrogen generation rate. Below a critical flowrate, this steady hydrogen generation rate becomes invariant with the inlet flowrate and reaches almost a constant value 29.16 mmol/hr (Figure 4.9). The average of the hydrogen generation rates considering different inlet flow rates, for about eight hours of operation, are plotted, along with the steady hydrogen generation rate. The confined water trapped into the pores of alginate and on the active sites of the photocatalyst plays a significant role in a constant rate hydrogen production, below a critical flow rate (above a critical value of residence time). Upon continuation of the the dynamic adsorption, the hydrogen generation rate becomes invariant of the inlet flow rate, implying that each of the bead-like alginate-encapsulated spherical photocatalysts can be treated as a miniaturised photocatalytic reactor or hydrogen generator. The tuning of the continuous hydrogen generation process can be done by modifying the size of the beads and their water retention capacity, as well as the degree of pre-adsorbed confined water.

In summary, rGO-CdS-WO_3-alginate and rGO-ZnO-WO_3-alginate milli-spherical bead-like photocatalysts outperform pristine powder catalyst CdS and rGO-CdS in terms of photocatalytic activity, hydrogen production, and apparent quantum efficiency. From an operational standpoint, the addition of alginate enhances the photocatalyst's water retention capacity and activity, allowing for continuous hydrogen production. Each spherical catalyst has the potential to function as a miniature photo reactor. The presence of rGO narrows the band gap, minimises recombination, and boosts photocatalytic activity.

4.12 Activity Comparison

Table 4.4 Comparison of the Photocatalytic activity of different photocatalysts

Name of photocatalyst	Source of irradiation	Activity (mmole g^{-1} h^{-1})	Reference
CdS QD-sensitized TiO_2 photo anode	Solar simulator	8.5×10E^{-5}	[75]
WO_3/g-C_3N_4	Solar Simulator	0.066	[76]
WO_3/TiO_2	Xenon lamp, 350 W	0.105	[77]
WO_3/TiO_2/rGO	Xenon lamp, 350 W	0.245	[78]
$ZnIn_2S_4$-rGO-$CuInS_2$	Solar simulator	0.506	[79]
$BiVO_4$-TiO_2 /rGO	Solar simulator	1.42	[80]
ZnO/CdS	350 W Xenon lamp	1.54	[81]
CdS/NiO HHAs	Sunlight	1.77	[82]
WO_3/$ZnIn_2S_4$	Xenon lamp, 300 W	1.945	[83]
N doped carbon a dots (NCQDs) using g-C_3N_4	Solar simulator	2.306	[84]
$Cu_{2-x}Se$/3% rGO	Solar simulator	3.12	[85]
ZnO–graphene	Xenon lamp, 300 W	4.35	[86]
ZnO nanoparticle	Xenon lamp, 350 W	4.9	[87]
rGO-CdS	Solar simulator	5.5	[88]
WO_3@MoS_2/CdS	300W Xenon lamp	8.2	[89]
RGO/$Cd_{0.15}Zn_{0.85}In_2S_4$–$Ni_2P$	Solar simulator	14.56	[90]
WO_3/CdS- DETA (Diethylenetriamine)	300W Xenon lamp	15.522	[91]

WO_3-TpPa-1-COF/ rGO	Solar simulator	26.73	[92]
g-C_3N_4/WO_3	Xenon lamp, 300 W	0.963	[93]
rGO-CdS-Alginate	Xenon lamp, 300 W	0.5	[94]
ZnO-WO_3	Solar simulator	4.43	This work
rGO-ZnO (1:3)	Solar simulator	10.46	This work
rGO-ZnO-WO_3 (1:3)	Solar simulator	13.29	This work
rGO-CdS-WO_3-Alginate	Solar simulator	81.8	This work
rGO-ZnO-WO_3 (1:3)-Alginate	Solar simulator	90.63	This work
rGO-CdS-WO_3-Alginate	Solar simulator	81.8	This work

4.13 Recyclability test (durability) of organic rGO-CdS-WO_3-Alginate millispheres photocatalyst.

The recyclability of a catalyst refers to its ability to be recovered and reused in a chemical reaction multiple times without significant loss of activity or selectivity. Catalysts play a crucial role in chemical reactions by reducing the activation energy of a reaction allowing the reaction to occur, thereby increasing the reaction rate. Recycling catalysts is environmentally and economically beneficial, as it reduces waste generation, lowers the cost of catalyst production, and minimizes the need for continuous catalyst replacement. The recyclability of a catalyst depends on several factors: Stability of the catalyst, leaching, deactivation, regeneration, reaction mechanism and support materials.

For catalyst powders, separation by centrifugation or filtering is required, which may result in metal agglomeration and considerable losses, resulting in lower activity [13]. The photo catalyst’s recyclability was investigated over the course of four successive cycles. The deactivation of the catalyst happened with the passage of time, as seen in Figure 4.10-I. Based on six hours of operation, the new catalyst of rGO-CdS-WO_3-Alginate millisphere produced 18.58 mmoles of hydrogen during the first run of operation. After 7 days (2nd run), 15 days (3rd run), and 30 days (4th run), the rate of hydrogen production declined to 18.37 mmoles, 18.02 mmoles, and 17.48 mmoles, respectively (Figure-10-I). After one month (30 days), rGO-CdS-WO_3-Alginate millisphere photocatalyst loses about 5.92% of its initial activity. Following the reaction, just a little metal loss is seen.

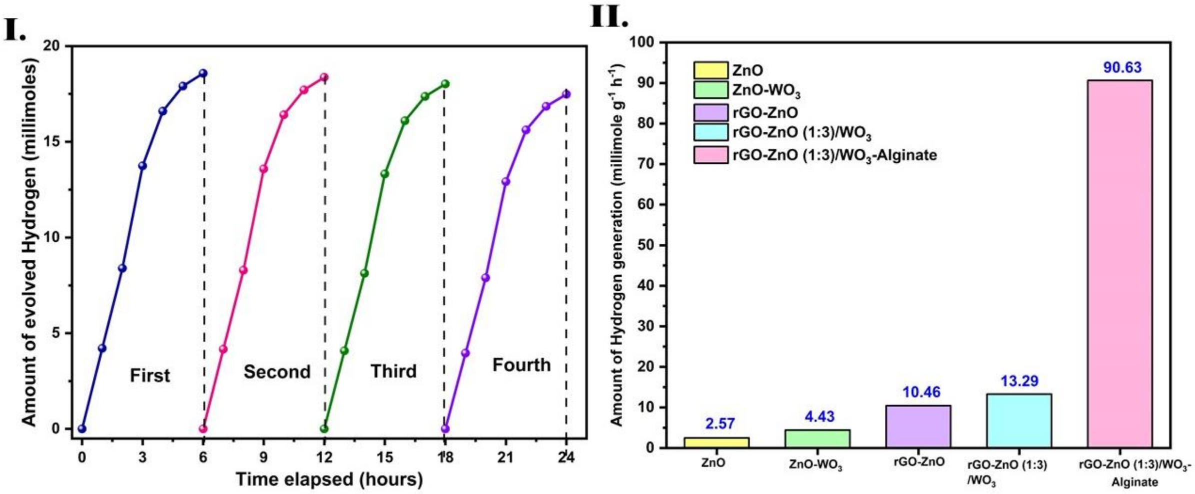

Figure 4.10: (I) Recyclability study after 24 hours (II) Photocatalytic activity comparison of rGO-ZnO-WO_3-alginate with its counterpart powder photocatalyst

4.14 Cell viability assay of both powder based and alginate based millisphere photocatalyst.

Solar green hydrogen generation is beneficial for the energy as well as environmental sustainability sector. The morphology and the composition of the photocatalyst is the backbone of the performance of the Hydrogen generation. Many studies are already performed to increase the rate and purity of the Hydrogen by modification of the photocatalyst. The important parts of a photocatalyst are the heavy metals which take part actively in the water splitting process leading to the Hydrogen generation. The heavy metals include Zinc, Cadmium, Tungsten, Arsenic, Lead and Aluminium etc. All the heavy metal powder photocatalyst has the high risk of heavy metal exposure in all components of environment including soil, water and air ultimately reach to human body [95].

One of our used photocatalyst contains Cadmium (Cd) is a naturally occurring heavy metal found in the Earth's crust widely used in industrial processes, batteries, pigments, and plastics, making it pervasive in various consumer products. However, Cd is highly toxic to humans and animals, posing severe health risks when exposure occurs as it is known as “long biological half-life”. The accumulation of Cd in the body can lead to a range of detrimental effects on multiple organ systems. The Cd exposure (“Itai Itai/ ouch-ouch disease”) occurs through contaminated soil, water and high risk of inhaling cadmium particles or absorbing it through their skin during work processes leading to its entry into the food chain. Similarly, Zinc (Zn) is an essential trace element required for numerous physiological processes in the human body, including immune function, DNA synthesis, cell division, wound healing, and the sense of taste and smell. While Zn is vital for overall health, excessive intake of this mineral can lead to Zn toxicity or zinc poisoning.

Cd is one of the most usage semiconductors (Chalcogenic material) due to its important direct intermediate bandgap (2.42 eV at 300K), high thermal and chemical stability, superior optical absorption, and various application purposes. Cd has been used as photocatalytic material but now a day its usage access has been denied in the real world due its high toxicity. Several attempt has been taken to minimise its toxicity level by using different chelating agents like ethylene diamine tetra-acetic acid (EDTA), dimercaprol, and di-thio-carbamates.

In the present chapter we focused in the alginate encapsulate photo catalyst millisphere where the organic polysaccharide polymer alginate completely encapsulated the powder material. Since Food and Drug Administration (FDA) defines food grade sodium alginate as a GRAS (generally recognised as safe) component in Title 21 of the Code of Federal Regulations (CFR) and specifies its usage as a stabiliser, emulsifier, gelling agent and thickener [96-97]. The European Commission (EC) approved alginic acid and its salts (E400-E404) as food additives.

We had also studied the toxicity of both powder and encapsulated alginate based photocatalyst by determination of cell viability assay for 72 hours.

The cells were seeded into a 96 well culture plates in MTS(3-(4,5-dimethylthiazol-2-yl)-2,5-diphenyltetrazolium bromide), supplemented with 10% FBS (Fetal Bovine Serum), 1% antibiotic-antimytotic solution, and 1% NEAA. The MTS reagent was added to each sample (powder & alginate encapsulated photocatalyst) and incubated (Thermo Scientific™ Forma™ CO_2 Incubators) at 37 ± 1°C in a 5% carbon di-oxide atmosphere for 4 hours. The period of incubation was done for a span of three days (72 hours). The formazan was formed during the period of incubation by the reduction of the metabolically active cells in the culture medium due to the reaction in the mitochondria of the living cells by the dehydrogenase enzymes. The 96 well plates are taken out from the incubator and the absorbance of the sample was recorded at the fixed wavelength of 590nm with a 96 well- plate reader (Perkin Elmer Microplate reader). The number of present living cells can be determined form the absorbance as it is directly proportional to the number of present active cells.

$$\text{Absorbance } \propto \text{number of present living cells}$$

After the duration of 72 hours, the cell viability percentage of cell for the alginate encapsulated photocatalyst is much higher than the powdered photocatalyst. Lower value of the cell viability assay denotes high toxicity of the photocatalyst. The detailed cell viability assay percentage of each photocatalyst has been tabulated in the following Table 4.5.

Table 4.5 Cell Viability Assay percentage of different powder Photocatalysts and Alginate encapsulated 3D Photocatalysts

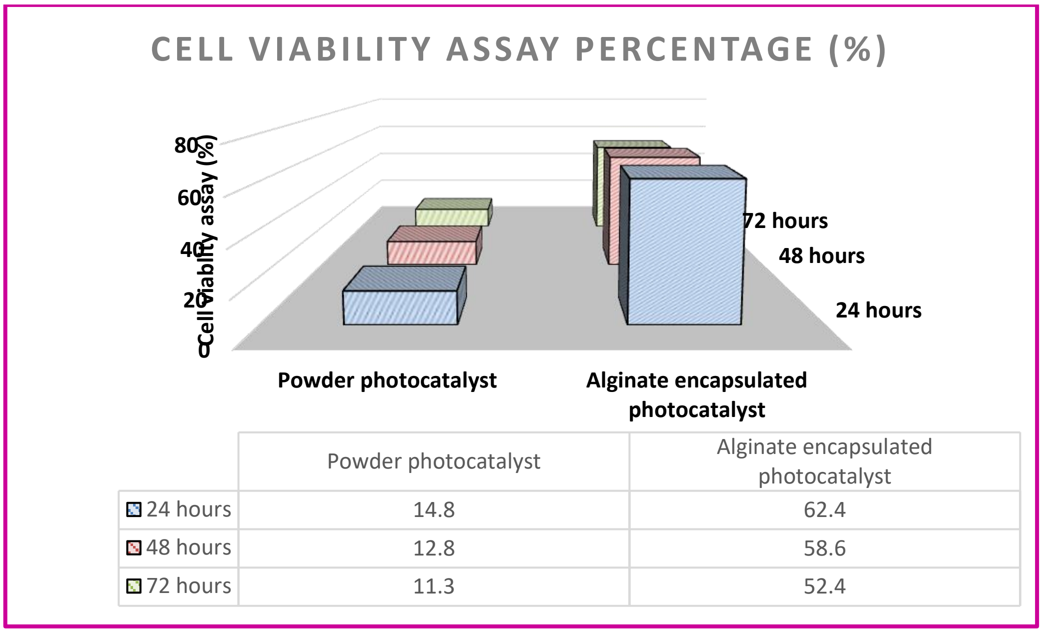

	Powder photocatalyst	Alginate encapsulated photocatalyst
▨ 24 hours	14.8	62.4
▨ 48 hours	12.8	58.6
▨ 72 hours	11.3	52.4

4.15 Estimation of Cost of rGO-CdS-WO_3-Alginate and rGO-ZnO-WO_3-Alginate

The biggest barrier to practical hydrogen generation is operational expense. The US Department of Energy's Office of Hydrogen and Fuel Cell Technologies is developing technologies to allow net-zero-carbon hydrogen generation at a cost of $2 per kg by 2025 and $1 per kg by 2030. The cost of producing hydrogen by photocatalytic water splitting includes the cost of the catalyst as well as the one-time expenditure of creating the hydrogen generating reactor. The choice and use of the catalyst (rGO-CdS-WO_3-Alginate and rGO-ZnO-WO_3) reduces the cost of hydrogen generation owing to its high reusability up to run 4. The anticipated cost of the synthesised catalyst was studied in this respect to underline its economic potential. The Food and Drug Administration (FDA) defines food grade sodium alginate as a GRAS (generally recognised as safe) component in Title 21 of the Code of Federal Regulations (CFR) and specifies its usage as a stabiliser, emulsifier, gelling agent and thickener [96]. The European Commission (EC) approved alginic acid and its salts (E400-E404) as food additives [97]. Tables show several components, as well as their estimated number and cost.

The stirring and drying cost has been calculated using the following equations (4.3):

$$\text{Stirring, Drying cost} = \frac{\text{Instrument power (watt)} \times \text{time} \times \text{unit cost}}{1000} \quad (4.3)$$

4.15.1 Detailed cost-analysis of rGO-CdS-WO_3-Alginate millisphere

Table 4.6 Cost Analysis for hydrogen generation using CdS-rGO-WO_3-Alginate milli-sphere photocatalysts

Chemical used	**Chemicals**	**Approx. quantity**	**Cost (Rs.)**	**Cost (Dollar)**
CdS- rGO-WO_3-Alginate	Graphite flakes	0.02 g	281.8	3.4
	Cadmium Sulphide	0.05	1.78	0.022
	Sodium tungstate dihydrate	3.806	349.6	4.22
	Oxalic acid	1	512.8	6.19
	Deionized water	2 L	-	-
	Phosphoric Acid	10 ml	264.1	3.19
	Hydrogen Peroxide	10 ml	57.48	0.69
	Hydrochloric Acid	40 ml	13.8	0.17
	Ethanol (for synthesis & washing)	20 ml	12	0.14
	Sulphuric Acid	10 ml	9.8	0.12
	Sodium Alginate	1 g	15.44	0.19
	Calcium Chloride	1 g	27.99	0.34
Electricity Involved	Stirring	54.6 unit (30 hours)	485.9	5.87
	Drying	13 unit (10 hours)	115.7	1.40
	Calcination	20 unit (42 hours)	178	2.15
Total			2326.19	28.09

1 g of the synthesised rGO-CdS-WO_3- Alginate millisphere photo catalyst typically costs $28.09.

4.15.2 Detailed cost-analysis of rGO-ZnO-WO_3-Alginate millispheres

Table 4.7 Cost Analysis for hydrogen generation using rGO- ZnO-WO_3-Alginate millisphere photocatalysts

Chemical used	Chemicals	Approx. quantity	Cost (Rs.)	Cost (Dollar)
rGO-ZnO-WO_3-Alginate	Graphite flakes	0.02 g	281.8	3.4
	Sodium tungstate dihydrate	3.806	349.6	4.22
	Zinc nitrate	8 g	249.2	1.50
	Ammonia	10 ml	207.3	2.50
	NaCl	1.5	3.6	0.043
	Oxalic acid	1	512.8	6.19
	Deionized water	2 L	120	1.45
	Phosphoric Acid	10 ml	264.1	3.19
	Hydrogen Peroxide	10 ml	57.48	0.69
	Hydrochloric Acid	40 ml	13.8	0.17
	Ethanol (for synthesis & washing)	20 ml	12	0.14
	Sulphuric Acid	10 ml	9.8	0.12
	Sodium Alginate	1 g	15.44	0.19
	Calcium Chloride	1 g	27.99	0.34
Electricity Involved	Stirring	54.6 unit (30 hours)	485.9	5.87
	Drying	13 unit (10 hours)	115.7	1.40
	Calcination	20 unit (42 hours)	178	2.15
Total			2882.99	35.32

1 g of the synthesised rGO-ZnO-WO_3- Alginate millisphere photo catalyst typically costs $35.32. The catalyst has high reusability and may be used for 4 runs with only a 5.92 % loss in activity; therefore, the hydrogen generation cost of is majorly reduced by using the rGO-ZnO-WO_3- Alginate millisphere photocatalyst. Thus, that in addition to being environmentally friendly, resusable and easy separation process, rGO-ZnO-

WO_3-Alginate millisphere catalyst is an ideal choice for producing commercially feasible hydrogen generation via photocatalytic water splitting.

4.16 Conclusion

- Synthesis of rGO-CdS-WO_3-alginateand rGO-ZnO-WO_3 -alginate millisphere by a simple ionic cross-linking process having remarkable solar hydrogen generation of 81.8 mmol g^{-1} h^{-1} and 90.63 mmol g^{-1} h^{-1} respectively through water splitting in a full-band spectrum of solar irradiation.
- .The presence of large cavity in the hydrogel results in the high water retention capcity resulting in the direct interaction with the water and increased HER.
- Extent of hydration and the time duration of pre-adsorption of water (hydration) in the photocatalyst milisphere affect the rate of hydrogen generation.
- Sustainable, continuous hydrogen generation at a steady, constant rate, from flow reactors.
- After the duration of 72 hours, the cell viability percentage of cell for the alginate encapsulated photocatalyst is much higher than the powdered photocatalyst. Lower value of the cell viability assay denotes high toxicity of the photocatalyst.
- Cost analysis of both the alginate based photocatalyst has been forwarded based on 1 mole of Hydrogen generation.

4.17 References

1. Bell, S., Will, G., & Bell, J. (2013). Light intensity effects on photocatalytic water splitting with a titania catalyst. *International Journal of Hydrogen Energy*, 38(17), 6938–6947.

2. He, Y., Hamann, T., & Wang, D. (2019). Thin film photoelectrodes for solar water splitting. *Chemical Society Reviews*, 48(7), 2182–2215.

3. Ning, X., & Lu, G. (2020). Photocorrosion inhibition of cds-based catalysts for photocatalytic overall water splitting. *Nanoscale*, 12(3), 1213–1223.

4. Kudo, A., & Miseki, Y. (2009). Heterogeneous photocatalyst materials for water splitting. *Chemical Soiecty. Reviews,* 38(1), 253–278.

5. Meng, S., Zhang, J., Chen, S., Zhang, S., Huang, W. (2019). Perspective on construction of heterojunction photocatalysts and the complete utilization of photogenerated charge carriers. *Applied Surface Science*, 476, 982-992.

6. Alarawi, A., Ramalingam, V., He, J. (2019). Recent advances in emerging single atom confined two-dimensional materials for water splitting applications. *Materials Today Energy*, 11, 1-23.

7. Tan, H., Abdi, F., Ng, Y. (2019). Heterogeneous photocatalysts: An overview of classic and modern approaches for optical, electronic, and charge dynamics evaluation. *Chemical Society Reviews*, 48(5), 1255-1271.

8. Zhang, Q., & Guan, J. (2020). Recent progress in single-atom catalysts for photocatalytic water splitting. *Solar RRL*, 4(9), 2000283

9. Wang, X., Li, Z., Shi, J., Yu, Y. (2014). One-dimensional titanium dioxide nanomaterials: Nanowires, nanorods, and nanobelts. *Chemical Reviews*, 114(19), 9346-9384.

10. Babu, V., Vempati, S., Uyar, T., Ramakrishna, S. (2015). Review of one-dimensional and two-dimensional nanostructured materials for hydrogen generation. *Physical Chemistry Chemical Physics*, 17(5), 2960-2986.

11. Liu, Q., Zhang, S., Liao, J., Feng, K., Zheng, Y., Pollet, B., Li, H. (2017). CuCo2O4 nanoplate film as a low-cost, highly active and durable catalyst towards the hydrolytic dehydrogenation of ammonia borane for hydrogen production. *Journal of Power Sources*, 355, 191-198.

12. Saha, S., Basak, V., Dasgupta, A., Ganguly, S., Banerjee, D., Kargupta, K. (2014). Graphene supported bimetallic G–Co–Pt nanohybrid catalyst for enhanced and cost effective hydrogen generation. *International Journal of Hydrogen Energy*, 39(22), 11566-11577.

13. Tu, K., Büchele, S., Mitchell, S., Stricker, L., Liu, C., Goldhahn, C., Allaz, J., Ding, Y., Günther, R., Zhang, Z., Sun, J., Stucki, S., Panzarasa, G., Zeeman, S., Burgert, I., Pérez-Ramírez, J., Keplinger, T. (2022). Natural wood-based catalytic membrane microreactors for continuous hydrogen generation. *ACS Applied Materials & Interfaces*, 14(6), 8417-8426.

14. Zhang, L. et al. (2022). Ni(OH)2 nanoparticles encapsulated in conductive nanowire array for high-performance alkaline seawater oxidation. *Nano Research*, 15(7), 6084–6090.

15. Chen, J. et al. (2023). High-efficiency overall alkaline seawater splitting: Using a nickel–iron sulfide nanosheet array as a bifunctional electrocatalyst. *Journal of Materials Chemistry A*, 11(3), 1116–1122.

16. Ning, X., Li, J., Yang, B., Zhen, W., Li, Z., Tian, B., Lu, G. (2017). Inhibition of photocorrosion of CdS via assembling with thin film TiO2 and removing formed oxygen by artificial gill for visible light overall water splitting. *Applied Catalysis B: Environmental*, 212, 129-139.

17. Tian, J. et al. (2015). Cobalt phosphide nanowires: Efficient nanostructures for fluorescence sensing of biomolecules and photocatalytic evolution of dihydrogen from water under visible light. *Angewandte Chemie*, 127(18), 5583–5587.

18. Masai, H. et al. (2020). Photocatalytic hydrogen generation of monolithic porous titanium oxide-based glass–ceramics. *Scientific Reports*, 10(1).

19. Li, J., Ma, R., Lu, Y., Wu, Z., Su, M., Jin, K., Qin, D., Zhang, R., Bai, R., He, S., Chen, Y., Jiang, Z. (2020). A gravity-driven high-flux catalytic filter prepared using a naturally three-dimensional porous rattan biotemplate decorated with Ag nanoparticles. *Green Chemistry*, 22(20), 6846-6854.

20. Hui, B., Li, J., Lu, Y., Zhang, K., Chen, H., Yang, D., Cai, L., Huang, Z. (2021). Boosting electrocatalytic hydrogen generation by a renewable porous wood membrane decorated with Fe-doped NiP alloys. *Journal of Energy Chemistry*, 56, 23-33.

21. Jiang, Z. et al. (2019). Hydrogel as a miniature hydrogen production reactor to enhance photocatalytic hydrogen evolution activities of CdS and ZnS quantum dots derived from modified gel crystal growth method. *Chemical Engineering Journal*, 373, 814–820.

22. Li, F. et al. (2020). Enhanced photocatalytic hydrogen production of CdS embedded in cationic hydrogel. *International Journal of Hydrogen Energy*, 45(3), 1969–1980.

23. Poliukhova, V. et al. (2022). ZnO/ZnS-polyvinyl alcohol hydrogel for photocatalytic H2-generation. *Catalysts*, 12(3), 272.

24. Li, H.; Chong, B.; Xu, B.; Wells, N.; Yan, X.; Yang, G. (2021). Nanoconfinement-induced conversion of water chemical adsorption properties in nanoporous photocatalysts to improve photocatalytic hydrogen evolution. *ACS Catalysis*, 11(22), 14076-14086.

25. Tu, S.; Zhao, X.; Cheng, M.; Sun, P.; He, Y.; Xu, Y. (2019). Uniform mesoporous MnO2 nanospheres as a surface chemical adsorption and physical confinement polysulfide mediator for lithium–sulfur batteries. *ACS Applied Materials & Interfaces*, 11(11), 10624-10630.

26. Kumar, P.; Short, M.; Yip, S.; Yildiz, B.; Grossman, J. (2013). High surface reactivity and water adsorption on NiFe2O4 (111) surfaces. *The Journal of Physical Chemistry C*, 117(11), 5678-5683.

27. Möller, C.; Barreto, J.; Stavale, F.; Tissot, H.; Shaikhutdinov, S.; Freund, H.; Nilius, N. (2018). Water adsorption to crystalline Cu2O thin films: Structural and vibrational properties. *The Journal of Physical Chemistry C*, 122(4), 2195-2199.

28. Farstad, M.; Ragazzon, D.; Walle, L.; Schaefer, A.; Sandell, A.; Borg, A. (2015). Water adsorption on TiOx thin films grown on Au (111). *The Journal of Physical Chemistry C*, 119(12), 6660-6669.

29. Wei, Z.; Sinko, R.; Keten, S.; Luijten, E. (2018). Effect of surface modification on water adsorption and interfacial mechanics of cellulose nanocrystals. *ACS Applied Materials & Interfaces*, 10(9), 8349-8358.

30. Hosseinpour, S., Tang, F., Wang, F., Livingstone, R. A., Schlegel, S. J., Ohto, T., … Backus, E. H. (2017). Chemisorbed and physisorbed water at the TIO2/water interface. *The Journal of Physical Chemistry Letters, 8*(10), 2195–2199.

31. Wang, H.; Xi, X.; Kleinhammes, A.; Wu, Y. (2008). Temperature-induced hydrophobic-hydrophilic transition observed by water adsorption. *Science,* 322(5898), 80-83.

32. Hummer, G.; Rasaiah, J.; Noworyta, J. (2001). Water conduction through the hydrophobic channel of a carbon nanotube. *Nature*, 414(6860), 188-190.

33. Kumar, P.; Short, M.; Yip, S.; Yildiz, B.; Grossman, J. (2013). High surface reactivity and water adsorption on NiFe2O4 (111) surfaces. *The Journal of Physical Chemistry C,* 117(11), 5678-5683.

34. Möller, C.; Barreto, J.; Stavale, F.; Tissot, H.; Shaikhutdinov, S.; Freund, H.; Nilius, N. (2018). Water adsorption to crystalline Cu2O thin films: Structural and vibrational properties. *The Journal of Physical Chemistry C*, 122(4), 2195-2199.

35. Lee, C.; Aikens, C. (2014). Water adsorption and dissociation processes on small Mn-doped TiO2 complexes. *The Journal of Physical Chemistry A*, 118(3), 598-605.

36. Litke, A., Su, Y., Tranca, I., Weber, T., Hensen, E. J., & Hofmann, J. P. (2017). Role of adsorbed water on charge carrier dynamics in photoexcited TiOs2. *The Journal of Physical Chemistry C*, *121*(13), 7514–7524.

37. Wang, H., Gao, Y., Liu, J., Li, X., Ji, M., Zhang, E., Cheng, X., Xu, M., Liu, J., Rong, H., Chen, W., Fan, F., Li, C., Zhang, J. (2019). Efficient plasmonic Au/CdSe nanodumbbell for photoelectrochemical hydrogen generation beyond visible region. *Advanced Energy Materials*, 9(15), 1803889.

38. Ning, X., Zhen, W., zh, Y., Lu, G. (2018). Inhibition of CdS photocorrosion by Al2O3 shell for highly stable photocatalytic overall water splitting under visible light irradiation. *Applied Catalysis B: Environmental*, 226, 373-383.

39. Ning, X., Lu, G. (2020). Photocorrosion inhibition of CdS-based catalysts for photocatalytic overall water splitting. *Nanoscale,* 12(3), 1213-1223.

40. Ning, X., Li, J., Yang, B., Zhen, W., Li, Z., Tian, B., Lu, G. (2017). Inhibition of photocorrosion of CdS via assembling with thin film TiO2 and removing formed oxygen by artificial gill for visible light overall water splitting. *Applied Catalysis B: Environmental*, 212, 129-139.

41. Liang, J. et al. (2022). Recent advances in nanostructured heterogeneous catalysts for N-cycle electrocatalysis. *Nano Research Energy*, 1.

42. Geim, A., & Novoselov, K. (2007). The rise of graphene. *Nature Materials*, 6(3), 183-191.

43. Xie, G., Zhang, K., Guo, B., Liu, Q., Fang, L., Gong, J. (2013). Graphene-based materials for hydrogen generation from light-driven water splitting. *Advanced Materials*, 25(28), 3820-3839.

44. Fei He, Aiyun Meng, Bei Cheng, Wingkei Ho, Jiaguo Yu. (2020). Enhanced photocatalytic H2-production activity of WO_3/TiO_2 step-scheme heterojunction by graphene modification. *Chinese Journal of Catalysis*, 41(1), 9-20.

45. Hideyuki Katsumata, Yusuke Tachi, Tohru Suzuki, Satoshi Kaneco , Z-scheme photocatalytic hydrogen production over WO_3/g-C3N4 composite photocatalysts. *RSC Advances*, 4, 21405.

46. Ma, L., Xu, J., Li, L., Mao, M., & Zhao, S. (2020). Hydrothermal synthesis of WO_3/CoS_2 N–N heterojunction for Z-scheme photocatalytic H2 evolution. *New Journal of Chemistry*, *44*(42), 18326–18336.

47. Junwei Fu, Quanlong Xu, Jingxiang Low, Chuanjia Jiang, Jiaguo Yu. (2019). Ultrathin 2D/2D WO_3/g-C_3N_4 step-scheme hydrogen-production photocatalyst. *Applied Catalysis B: Environmental*, 243, 556-565.

48. Sheng Wang, Bicheng Zhu, Mingjin Liu, Liuyang Zhang, Jiaguo Yu, Minghua Zhou. (2019). Direct Z-scheme ZnO/CdS hierarchical photocatalyst for enhanced photocatalytic hydrogen-production activity. *Applied Catalysis B: Environmental*, 243, 19-26.

49. Z. Wu, Y. Li, L. Gao, S. Wang, G. Fu. (2016). Synthesis of Na-doped ZnO hollow spheres with improved photocatalytic activity for hydrogen production. Dalton Transactions, 45, 11145–11149.

50. S. Guo, T. Zhao, Z. Jin, X. Wan, P. Wang, J. Shang, S. Han. (2015). Self-assembly synthesis of precious-metal-free 3D ZnO nano/microspheres with excellent photocatalytic hydrogen production from solar water splitting. *Journal of Power Sources*, 293, 17–22.

51. M. Reli, M. Edelmannová, M. Šihor, P. Praus, L. Svoboda, K.K. Mamulová, H. Otoupalíková, L. Cˇapek, A. Hospodková, L. Obalová, K. Kcˇí. (2015). Photocatalytic hydrogen generation from aqueous ammonia solution using ZnO photocatalysts prepared by different methods. *International Journal of Hydrogen Energy*, 40, 8530–8538.

52. Khan, S., Je, M., Ton, N. N., Lei, W., Taniike, T., Yanagida, S., … Katsumata, K. (2021). C-doped zns-zno/rh nanosheets as multijunctioned photocatalysts for effective H2 generation from pure water under solar simulating light. *Applied Catalysis B: Environmental*, *297*, 120473.

53. Quanjun Xiang, Jiaguo Yu. (2013). Graphene-Based Photocatalysts for Hydrogen Generation. *Journal of Physical Chemistry Letters*, 4, 753−759.

54. Mina Ghorbani, Hossein Abdizadeh, Mahtab Taheri, Mohammad Reza Golobostanfard. (2018). Enhanced photoelectrochemical water splitting in hierarchical porous ZnO/Reduced graphene oxide nanocomposite synthesized by sol-gel method. *International Journal of Hydrogen Energy*, 43, 7754–7763.

55. SMIDSROD, O., & SKJAKBRK, G. (1990). Alginate as immobilization matrix for cells. *Trends in Biotechnology*, 8, 71–78.

56. Rinaudo, M. (2008). Main properties and current applications of some polysaccharides as biomaterials. *Polymer International*, 57(3), 397–430.

57. Vauchel, P.; Kaas, R.; Arhaliass, A.; Baron, R.; Legrand, J. (2008). A new process for extracting alginates from Laminaria digitata: Reactive extrusion. *Food and Bioprocess Technology*, 1(3), 297-300.

58. Kaplan, D.L. (1998). Introduction to Biopolymers from Renewable Resources. In: Kaplan, D.L. (Eds.) Biopolymers from Renewable Resources. *Macromolecular Systems — Materials Approach*. Springer, Berlin, Heidelberg.

59. Qin, Y. (2007). Alginate fibers: An overview of the production processes and applications in wound management. *Polymer International*, 57(2), 171–180.

60. LeRoux, M. A., Guilak, F., & Setton, L. A. (1999). Compressive and shear properties of alginate gel: Effects of sodium ions and alginate concentration. *Journal of Biomedical Materials Research*, 47(1), 46–53.

61. Sundarrajan, P.; Eswaran, P.; Marimuthu, A.; Subhadra, L.; Kannaiyan, P. (2012). One pot synthesis and characterization of alginate stabilized semiconductor nanoparticles. *Bulletin of the Korean Chemical Society*, 33(10), 3218-3224.

62. Brayner, R.; Vaulay, M.; Fiévet, F.; Coradin, T. (2007). Alginate-mediated growth of Co, Ni, and CoNi nanoparticles: Influence of the biopolymer structure. *Chemistry of Materials*, 19(5), 1190-1198.

63. Ma, H.; Qi, X.; Maitani, Y.; Nagai, T. (2007). Preparation and characterization of superparamagnetic iron oxide nanoparticles stabilized by alginate. *International Journal of Pharmaceutics*, 333(1-2), 177-186.

64. Trandafilović, L.; Božanić, D.; Dimitrijević-Branković, S.; Luyt, A.; Djoković, V. (2012). Fabrication and antibacterial properties of ZnO–alginate nanocomposites. *Carbohydrate Polymers*, 88(1), 263-269.

65. Trandafilović, L.; Whiffen, R.; Dimitrijević-Branković, S.; Stoiljković, M.; Luyt, A.; Djoković, V. (2014). ZnO/Ag hybrid nanocubes in alginate biopolymer: Synthesis and properties. *Chemical Engineering Journal*, 253, 341-349.

66. Varghese, S., & Elisseeff, J. H. (2006). Hydrogels for musculoskeletal tissue engineering. In Polymers for Regenerative Medicine (pp. 95–144). Springer.

67. Grant, G. T., Morris, E. R., Rees, D. A., Smith, P. J. C., & Thom, D. (1973). Biological interactions between polysaccharides and divalent cations: The egg-box model. *FEBS Letters*, 32(1), 195–198.

68. Drury, J. L., Dennis, R. G., & Mooney, D. J. (2004). The tensile properties of alginate hydrogels. *Biomaterials*, 25(16), 3187–3199.

69. Al-Shamkhani, A., & Duncan, R. (1995). Radioiodination of alginate via covalently-bound tyrosinamide allows monitoring of its fate in vivo. Journal of Bioactive and Compatible *Polymers*, 10(1), 4–13.

70. Kuo, C.; Ma, P. (2001). Ionically crosslinked alginate hydrogels as scaffolds for tissue engineering: Part 1. Structure, gelation rate and mechanical properties. *Biomaterials*, 22(6), 511-521.

71. Dhamecha, D.; Movsas, R.; Sano, U.; Menon, J. (2019). Applications of alginate microspheres in therapeutics delivery and cell culture: Past, present and future. *International Journal of Pharmaceutics*, 569, 118627.

72. Ching, S.; Bansal, N.; Bhandari, B. (2015). Alginate gel particles–A review of production techniques and physical properties. *Critical Reviews in Food Science and Nutrition*, 57(6), 1133-1152.

73. Algothmi, W.; Bandaru, N.; Yu, Y.; Shapter, J.; Ellis, A. (2013). Alginate–graphene oxide hybrid gel beads: An efficient copper adsorbent material. *Journal of Colloid and Interface Science,* 397, 32-38.

74. Guo, H.-L. et al. (2016). Artificial photosynthetic Z-scheme photocatalyst for hydrogen evolution with high quantum efficiency. *The Journal of Physical Chemistry C*, 121(1), 107–114.

75. Desai, K.; Pathan, A.; Bhasin, C. (2017). Synthesis, characterization of cadmium sulphide nanoparticles and its application as photocatalytic degradation of Congo red. International *Journal of Nanomaterials and Chemistry,* 3(2), 39-43.

76. Xian-Yang Sun, Feng-Jun Zhang, Cui Kong. (2020). Porous g-C3N4/WO_3 photocatalyst prepared by simple calcination for efficient hydrogen generation under visible light. *Colloids and Surfaces A: Physicochemical and Engineering Aspects*, 594, 124653.

77. Juan Wang, Guohong Wang, Jie Jiang, Zhen Wan, Yaorong Su, Hua Tang. (2020). Insight into charge carrier separation and solar-light utilization: rGO decorated 3D ZnO hollow microspheres for enhanced photocatalytic hydrogen evolution. *Journal of Colloid and Interface Science,* 564, 322–332.

78. Fei He, Aiyun Meng, Bei Cheng, Wingkei Ho, Jiaguo Yu. (2020). Enhanced photocatalytic H2-production activity of WO_3/TiO_2 step-scheme heterojunction by graphene modification. *Chinese Journal of Catalysis,* 41(1), 9-20.

79. Raja, A. et al. (2021). Facile synthesis of sphere-like structured ZnIn2S4-RGO-CuInS2 ternary heterojunction catalyst for efficient visible-active photocatalytic hydrogen evolution. *Journal of Colloid and Interface Science*, 602, 669–679.

80. Abd-Rabboh, H.S.M. et al. (2021). Synthesis of an efficient, and recyclable mesoporous BIVO4/TiO2 direct Z-scheme heterojunction by sonochemical route for photocatalytic hydrogen production and photodegradation of rhodamine B dye in the visible region. *Optical Materials*, 114, 110761.

81. Revathi, M., Pricilla jeyakumari, A., & Saravanan, S. P. (2021). Design and fabrication of zno/cds heterostructured nanocomposites for enhanced hydrogen evolution from solar water splitting. *Inorganic Chemistry Communications*, 134, 109056.

82. Zhao, X.; Zhang, Q.; Chen, D.; Lu, P. (2011). Enhanced Mechanical Properties of Graphene-Based Poly (Vinyl Alcohol) Composites. *Macromolecules*, 44(7), 2392-2392.

83. Yanze Wang, Da Chen, Yiqian Hu, Laishun Qin, Junhui Liang, Xingguo Sun, Yuexiang Huang. (2020). An artificially constructed direct Z-scheme heterojunction: WO_3 nanoparticles decorated ZnIn2S4 for efficient photocatalytic hydrogen production. *Sustainable Energy Fuels*, 4, 1681-1692.

84. Algothmi, W.; Bandaru, N.; Yu, Y.; Shapter, J.; Ellis, A. (2013). Alginate–graphene oxide hybrid gel beads: An efficient copper adsorbent material. *Journal of Colloid and Interface Science*, 397, 32-38.

85. Xie, X. et al. (2019). Fabrication of a CU2-xse/RGO heterojunction photocatalyst to achieve efficient photocatalytic H2 generation. *International Journal of Hydrogen Energy*, 44(60), 32042–32053.

86. Junli Xu, Ya Cui, Yide Han, Men Hao, Xia Zhang. (2016). ZnO–graphene composites with high photocatalytic activities under visible light. *RSC Advances*, 6, 96778-96784..

87. Jie Jiang, Guohong Wang, Yanchi Shao, Juan Wang, Shuang Zhou, Yaorong Su. (2022). Step-scheme ZnO@ZnS hollow microspheres for improved photocatalytic H2 production performance. *Chinese Journal of Catalysis*, 43(2), 329-338

88. Al-Betar, A. (2021). Enhanced electrocatalytic water oxidation using cobalt-based polyaniline hybrid assembly. *Synthetic Metals*, 275, 116738.

89. Zhang, L.; Niu, C.; Liang, C.; Wen, X.; Huang, D.; Guo, H.; Zhao, X.; Zeng, G. (2018). One-step in situ synthesis of CdS/SnO2 heterostructure with excellent photocatalytic performance for Cr(VI) reduction and tetracycline degradation. *Chemical Engineering Journal*, 352, 863-875.

90. Lin, H. et al. (2022). Robust visible-light photocatalytic H2 evolution on 2D RGO/$Cd_{0.15}Zn_{0.85}In_2S_4$–Ni2P hierarchitectures. *Catalysis Science & Technology*, 12(13), 4181–4192

91. Hu, T., Li, P., Zhang, J., Liang, C., & Dai, K. (2018). Highly efficient direct Z-scheme WO_3/CDS-diethylenetriamine photocatalyst and its enhanced photocatalytic H2 Evolution under visible light irradiation. *Applied Surface Science*, 442, 20–29.

92. Abd-Rabboh, H.S.M. et al. (2021). Synthesis of an efficient, and recyclable mesoporous BiVO4/TiO2 direct Z-scheme heterojunction by sonochemical route for photocatalytic hydrogen production and photodegradation of rhodamine B dye in the visible region. *Optical Materials*, 114

93. Xie, X. et al. (2019). Fabrication of a CU2-xse/RGO heterojunction photocatalyst to achieve efficient photocatalytic H2 generation. *International Journal of Hydrogen Energy*, 44(60), 32042–32053.

94. Sarkar, A., Chaule, S., Mandal, S., Saha, S., Ganguly, S., Banerjee, D., & Kargupta, K. (2023). Enhanced photocatalytic hydrogen generation by splitting water using sodium alginate decorated RGO-cds hybrid photo-catalyst. *Materials Today: Proceedings*.

95. Balali-Mood, M., Naseri, K., Tahergorabi, Z., Khazdair, M. R., & Sadeghi, M. (2021). Toxic mechanisms of five heavy metals: Mercury, lead, chromium, Cadmium, and arsenic. *Frontiers in Pharmacology*, *12*.

96. Sun, J. and Tan, H. (2013). Alginate-based biomaterials for regenerative medicine applications. *Materials*, 6(4), 1285–1309.

97. Senturk Parreidt T, Müller K, Schmid M. (2018). Alginate-Based Edible Films and Coatings for Food Packaging Applications. *Foods*, 7(10), 170.

Chapter 5

Summary and Future Scopes

Highlights

- **Outcome of the Research**
- **Future Scopes**

5.1 Outcome of the Research

Photocatalytic water splitting is a promising way to produce Green Hydrogen. In this research work, attempt has been made to address some of the process bottlenecks namely fast recombination of hole-electron pair, slow kinetics and low yield of hydrogen, low water retention capacity of the photocatalyst, low quantum efficiency those restrict the commercialization of Photocatalytic water splitting.

The major outcome of the research is the development of three dimensional milli spherical bead like environment friendly, recyclable, relatively low-cost organic-alginate encapsulated rGO based heterojunction photocatalysts exhibiting remarkably high activity (more than 80 mmol $g_{photocatalyst}^{-1}$ h^{-1}, refer to Table 5.1)) and apparent quantum efficiency. Each such bead like hydrated photocatalyst acts as a miniaturized photoreactor and produces constant rate of continuous hydrogen generation.

Here a systematic approach is adopted in this research work. Several nano hybrid powder photocatalysts (as listed in Table 5.1) namely rGO-CdS, rGO-ZnO, ZnO-WO_3, type II heterojunction rGO-ZnO (1:3) -WO_3 and Z scheme heterojunction (CdS-rGO-WO_3) are synthesized, characterized and tested for hydrogen generation and compared with pristine ZnO, CdS, WO_3. Among these, rGO-ZnO- WO_3 type II heterojunction and CdS-rGO-WO_3

Table 5.1 Comparative analysis of Activity of different synthesized photocatalyst

Photocatalyst	Activity (mmole g^{-1} h^{-1})
WO_3	2
ZnO	2.57
ZnO-WO_3	4.43
CdS	4.9
rGO-CdS	6.9
rGO-ZnO	10.46
rGO-CdS-WO_3	11.69
rGO-ZnO(1:3)-WO_3	13.29
rGO-CdS-WO_3-Alginate	81.8
ZnO-rGO-WO3-Alginate	90.63

Z scheme comprising of HEP as well as OEP, exhibiting photocatalytic activity 13.29 and 11.69 mmol $g_{photocatalyst}^{-1}$ h-1, respectively under full spectrum of solar irradiation, are further encapsulated with alginate to develop 3D spherical catalysts.

Incorporation of rGO enhances the activity (mmol $gmcat^{-1}$ h^{-1}) of pristine ZnO from 2.5 to 10.4 (at an optimized ratio of 1:3)) and of pristine CdS from 4.9 to 6.9 under full spectrum of solar irradiation. Incorporation of WO_3 with rGO-ZnO(1:3) formation of heterojunction further enhances the activity to 13.29 and utilization of Z scheme further improve the activity of CdS-rGO-WO_3 to 11.6. The strategies of two component heterojunction and solid state mediator, rGO based Z scheme allow tuning of the band gap for better absorptivity in visible spectrum, lowering of recombination of photogenerated electron-hole pairs, utilization of higher redox potential (in Z scheme), minimize photo-corrosion, the aggregation of photocatalyst and enhance the photocatalytic activity and apparent quantum efficiency of the synthesized powder like nano-hybrid photocatalyst with respect to pristine photocatalyst. The mechanism of photocatalysis in presence of type II heterojunction rGO-ZnO-WO_3 and solid-state mediator rGO based Z scheme photocatalytic system CdS-rGO-WO_3 are also studied.

Further rGO-ZnO-WO_3 type II heterojunction as well as CdS-rGO-WO_3 are successfully encapsulated with organic alginate hydrogel and 3D mili-spherical beads like catalyst having very high- water adsorption capacity. The study on water uptake over time of such encapsulated photocatalyst reveals 97% and 96% equilibrium water uptake at around 12 hrs time. The encapsulated bead like-photocatalysts are hydrated for 6 hrs prior to the irradiation and dynamic adsorption of water continues over the 6 hrs period of irradiation. The encapsulated photocatalyst rGO-ZnO-WO_3-alginate and CdS-rGO-WO_3-alginate exhibits remarkable photocatalytic activity (mmol hydrogen $g_{photocatalyst}^{-1}$ h^{-1}) of 90.63 and 81.8, respectively under full spectrum solar irradiation. The AQE (under irradiation through 420 nm band pass filter) of rGO-CdS-WO_3-alginate is 21.9%. It may be summarized that among all the synthesized photocatalyst, alginate encapsulated rGO-ZnO-WO_3 type II heterojunction exhibits the maximum phot-catalytic activity under full spectrum of solar irradiation.

Study on continuous hydrogen generation using encapsulated rGO-ZnO-WO_3-alginate reveals sustainable almost constant rate of generation (35-40 mmol hydrogen $g_{photocatalyst}^{-1}$ h^{-1} over 10 hrs of irradiation) which is nearly invariant of inlet flow rate of water. It can be inferred that each 3D milli spherical bead like encapsulated photocatalyst acts as a miniaturized photoreactor. The recyclability study further reveals ~ 6% loss in activity after 4 cycles (over 30 days). Thus, metal loss is almost insignificant for encapsulated photocatalyst. Further, toxicity of powder catalyst especially comprising of CdS is also reduced (as confirmed by cell viability test). Thus, alginate hydrogel encapsulated photocatalysts are environment friendly and recyclable.

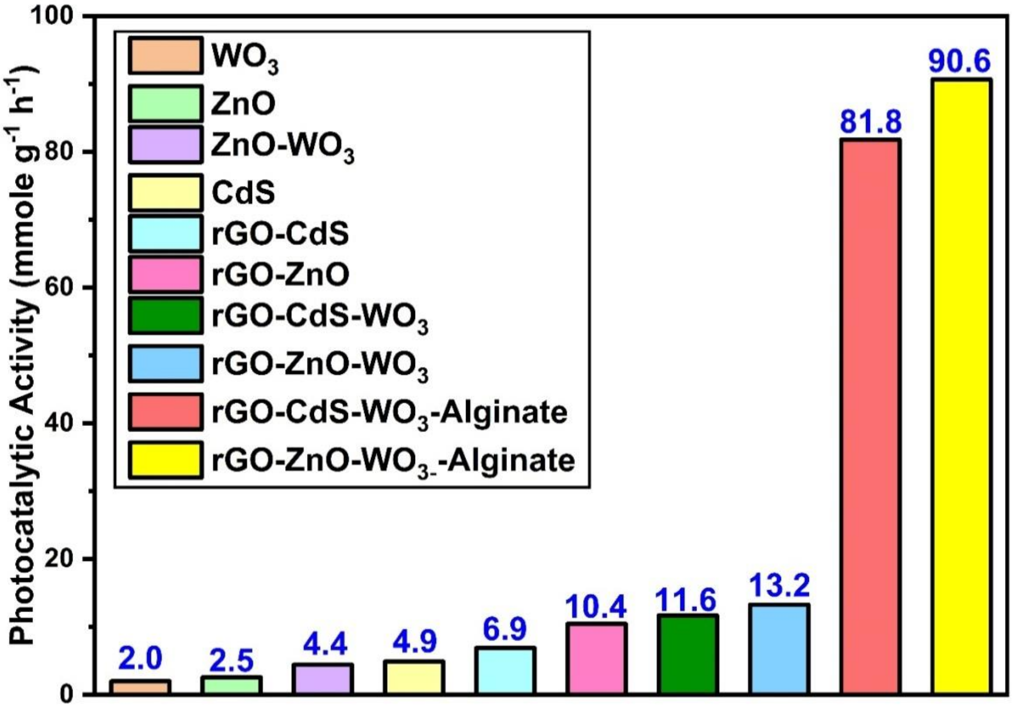

Figure 5.1 Photocatalytic activity of different synthesized photocatalysts

Table 5.2 Cost of catalyst for 1 mole per hour Hydrogen production

Photocatalyst	**Catalyst Type**	**Photocatalytic activity Mmol g-1h-1**	**Cost(in dollar) of catalyst for 1 mole of Hydrogen generation per hr (Including 4 times recyclability)**
rGO-CdS-WO_3	Powder type	11.69	575
rGO-ZnO-WO_3 (1:3)	Powder type	13.29	652.5
rGO-CdS-WO_3-Alginate	3D MOF based catalyst	81.8	85
rGO-CdS-ZnO-Alginate	3D MOF based catalyst	90.63	97.5

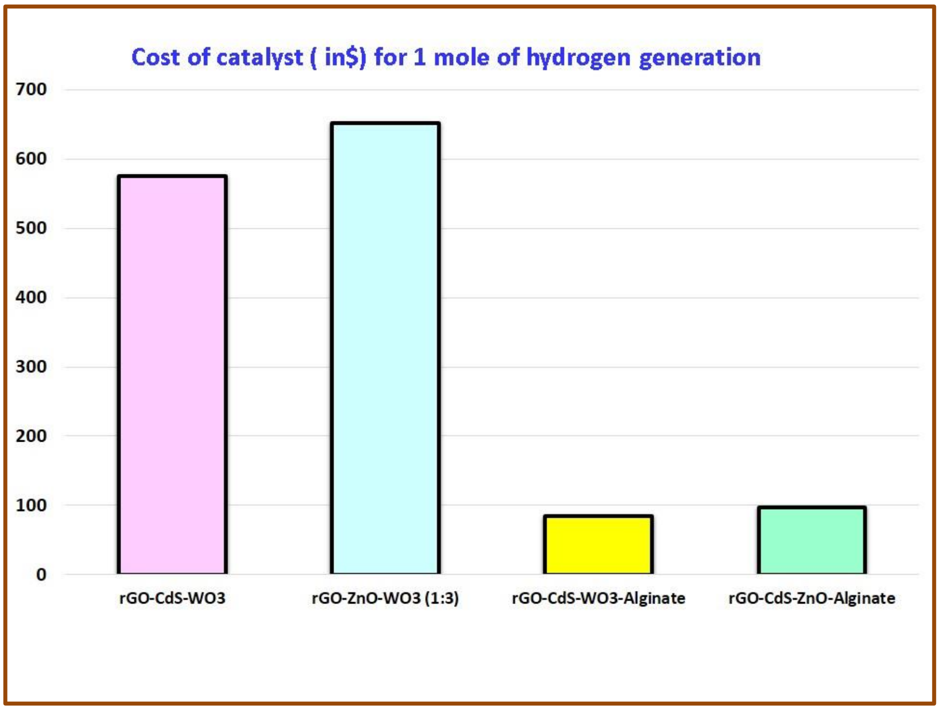

Figure 5.2 Catalyst Cost for different Photocatalyst

Cost Analysis Comparison:

The cost of each photocatalyst shows the expenditure of each catalyst for 1 mole of Hydrogen production per hour including 4 times recyclability cycles. The results of comparative cost analysis based on catalyst cost are displayed in Fig 5.2. and Table 5.2. In case of organic 3D polysaccharide- based catalyst, 1 moles of hydrogen generation cost of rGO-CdS-WO_3-Alginate and rGO-CdS-ZnO-Alginate will be \$85 and \$97.5, respectively. Similarly for the powder type catalyst, 1 moles of hydrogen generation cost of rGO-CdS-WO_3-Alginate and rGO-CdS-ZnO-Alginate will be \$ 575 and \$ 652.5 respectively. Both the powder and alginate- based catalyst has high reusability and may be used for 4 runs with minimum loss in activity. Scale up of laboratory scale continuous hydrogen generation set up with alginate encapsulated heterojunction photocatalyst may lead to commercialization of the process.

5.2 Future Scopes

The research presented in this thesis aids to synthesize highly efficient recyclable, environment-friendly hydrogel encapsulated heterojunction photocatalyst exhibiting high activity and AQE, for continuous hydrogen generation through photocatalytic water splitting.

Future scopes of this work are

(i) Study on continuous hydrogen generation using 3D encapsulated photocatalyst and optimization of size and number of catalyst beads and operating variables

(ii) Modelling, simulation and optimization of hydration/pre-adsorption of water into photocatalyst and photocatalytic hydrogen generation

(iii) Scale up of the laboratory scale set up and commercialization of Photocatalytic water splitting based green hydrogen generation process

(iv) Study of surface area effect regarding photocatalysts employing Brunauer-Emmett-Teller (BET) analysis

Chapter 6

Annexure I

Synthesis, characterization and photocatalytic performance study of rGO-$SnFe_2O_4$ photocatalyst for solar hydrogen generation

Highlights:

- **Synthesis and characterization of $SnFe_2O_4$ photocatalyst**
- **Modification of $SnFe_2O_4$ photocatalyst by incorporating rGO to obtain the photoactive rGO-$SnFe_2O_4$ photocatalyst for increasing the yield of hydrogen production.**
- **The rGO-$SnFe_2O_4$ photocatalyst shows the hydrogen production rate of 2.1428 mmol/g.h under visible light irradiation.**

6.1 Introduction

The overutilization of natural resources by an increasing global human population has given rise to a huge energy demand, globally, leading to global energy crisis. World economy is currently dependent on fossil fuels as a source of energy [1]. Emission of greenhouse gases occurs during the burning of fossil fuels, causing pollution. The necessity for an alternative form of energy to replace the fossil fuels is of prime concern, in this context. Due to the higher value of energy per unit mass of hydrogen compared to other fuels [140 MJ/kg], emergence of hydrogen as an alternative clean source of energy can be seen [2]. Hydrogen can be produced from both renewable and non-renewable sources. Presently, hydrogen is derived commercially, mainly by steam reforming of non-renewable sources like fossil fuels [3]. Pollution occurs during these processes, which has a slow impact on the climate of the Earth [4]. Water, an abundant natural resource can be used to obtain hydrogen, by photocatalytic splitting of water. Photocatalytic water splitting is a simple and cost-effective process. Researches have been conducted on developing oxide semiconductor photocatalysts for hydrogen production by photocatalytic splitting of water [5]. Amongst these photocatalysts, TiO_2 has been quite commonly used as a photocatalyst for photocatalytic water splitting due to the low cost, photostability and high photocatalytic activity [6].

In recent years, spinel ferrite based nanomaterials (empirical formula $M_xFe_{3-x}O_4$), formed up of divalent and trivalent metals, like $NiFe_2O_4$, $CoFe_2O_4$, $SnFe_2O_4$ etc., have drawn attention of the researchers. This is because of the ability of these ferrites to absorb the visible spectrum of light and the ease of recyclability due to the magnetic properties, exhibited during photocatalytic water splitting [7–10]. $SnFe_2O_4$ is one such spinel ferrite belonging to the group of inverse spinels, displaying face-centered cubic (FCC) lattice system [11]. Sn 2p ions occupy the octahedral sites and Fe 3p ions cover evenly tetrahedron and octahedron sites, in $SnFe_2O_4$ [11]. However, the efficiency of these ferrites is low due to the rapid rate of recombination of phootogenerated electrons and holes [12].Doping with impurities like heteroatoms can be possible solutions to the problem.

Graphene is sp^2 bonded uniatomic layer of carbon atoms, having exceptional properties like a very large specific surface area (2630 m^2 g^{-1}) and a superb electronic mobility (200,000 cm^2 V^{-1} s^{-1}). [13] The band structure of graphene is aligned in such a way that the bonding π and antibonding π^* orbitals in graphene touch each other at the Dirac point with the Fermi level positioned between the valence and conduction bands, making it a zero band gap semiconductor. The Fermi level in graphene can be shifted by doping of heteroatoms. [14-16]. Moreover, the functionalization of graphene can effectively promote the synthesis of graphene based nanocomposites. As a result, graphene can be employed both as a photocatalyst and a cocatalyst. Multiple oxidation states can be found in the spinel ferrites (empirical formula $M_xFe_{3-x}O_4$), constituting of various transition metals (M). Due to this reason, different metal ions can be integrated into spinel crystal lattice, thereby modifying the structural and catalytic properties. Spinel ferrites can function as photocatalysts, as the optical band gaps are usually low, absorbing visible range of light. Additionally, the inexpensive ferrites can be used to replace the expensive noble metal based photocatalysts. [17] The synergistic effect of reduced graphene oxide on being used as a dopant along with a photocatalyst can be found in literatures. Previous reports on synthesizing reduced graphene oxide based spinel ferrite composites exhibited a high photocatalytic activity when compared to single component MFe_2O_4 (M=Ni, Co, Sn). [18]

In this work, reduced graphene oxide based ferritic nanocomposite (rGO-$SnFe_2O_4$) photocatalyst is proposed for hydrogen generation from water. The synthesised nanocomposites are characterized by using FESEM, EDS, XRD, FTIR, UV-vis absorbance spectroscopy, PL and XPS. The comparative performance analysis of generation of hydrogen by water splitting has been performed, between ferritic photocatalyst ($SnFe_2O_4$) and graphene loaded ferritic nano-catalysts (rGO-$SnFe_2O_4$).

Problem Statement: Synthesis and characterization of rGO based $SnFe_2O_4$ photocatalyst to study the enhanced H_2 production for rGO incorporating.

6.2 Experimental

6.2.1 Materials and Methods

Graphite flakes, Sulphuric Acid (H_2SO_4), Ortho Phosphoric Acid (H_3PO_4), Potassium Permanganate ($KMnO_4$), Hydrogen Peroxide (H_2O_2) (30% concentration), Hydrochloric Acid (HCl), Tetrahydrofuran have been obtained from MERCK, Mumbai, India. Tin Chloride ($SnCl_2$) Ferric Chloride, hexahydrate ($FeCl_{3,}$ $6H_2O$) have been obtained from SIGMA Aldrich.

6.2.2 Synthesis of graphene oxide (GO)

Graphene oxide has been synthesized employing Improved method [7]. 3 g of graphite flakes (1 wt. equiv.) and 18 g of $KMnO_4$ (6 wt. equiv.) have been added to a mixture of concentrated H_2SO_4/H_3PO_4 (360 ml: 40 ml) and stirred for 8 hour, at 50^0 C. The reaction has been terminated by adding 3 ml of 30% H_2O_2. A yellowish coloured solution has been obtained. Thus obtained material has been then successively mixed with 200 mL of water, 200 ml of 30% HCl, and 200 ml of ethanol. The resulting suspension has been filtered and vacuum-dried overnight at room temperature and labelled as GO (Graphene Oxide).

6.2.3 Synthesis of $SnFe_2O_4$

Synthesis of has been done by employing solution based technique that is by hydrothermally. During synthesis, $SnCl_2\cdot 2H_2O$ (1 mmol) and $FeCl_3\cdot 6H_2O$ (2 mmol) considering a stoichiometric ratio of Sn/Fe =1:2 have been added and stirred for 2.5 h to form a suspension. NH_4OH has been added dropwise to adjust the pH. The solution has been stirred for about 2 h and then the solution is transferred in a 50 ml Teflon lined autoclave at 150°C for 24 h.

6.2.4 Synthesis of rGO-$SnFe_2O_4$

Stoichiometric amount of iron based precursor salt has been added to ethanol and stirred at room temperature. Suitable amount of graphene oxide has been dispersed in ethanol with the aid of an ultrasonicator. Then, these two systems have been added together and stirred. NaOH solution has been used to modify the pH of the mixture. The mixture has been then stirred for few more minutes. Then the mixture has been transferred to a Teflon lined autoclave and kept at 180^oC for about 20 hours. After that the mixture has been cooled, filtered and has beenhed with distilled water. Then it has been dried in a vacuum oven for about 10 hours.

6.2.5 Characterization

The morphologies of the samples are characterized using a Field Emission Scanning Electron Microscope (FESEM, Carl Zeiss, EVO 18). The image has been taken at an accelerating voltage of 20 kV. The crystalline structure of the synthesized material has been studied with X-Ray diffractometer (PAN alytical *X'Pert PRO)* with Cu Kα radiation. The UV-vis absorbance spectra of synthesised visible light-active nanocomposite are examined using a PerkinElmer Lambda 35 UV-Vis spectrophotometer to determine the absorption edge and band gap energy. To assess the lifetime of the photogenerated charges, photoluminescence (PL) spectra are performed using a TRIAX 320 detector (excitation wavelength: 380 nm). X-ray photoelectron spectroscopy (XPS: AXIS Supra Model with Al K - 1486.6 eV Dual Al K / Mg K achromatic X-ray source) is used to examine the defect type, concentration, chemical state composition, and variation in band structure in the sample. The Fourier transformed infrared spectra (FTIR) of the synthesised samples to know the chemical structure are investigated in the range of 400–4000 cm^{-1} by Perkin Elmer

6.2.6 Photocatalytic hydrogen generation

The photocatalytic hydrogen generation has been carried out in a batch type photoreactor. Tungsten lamp (100 W) has been utilised as the source of light. At first, the system has been purged with N_2 for 30 min to remove O_2 (air). Synthesized photo catalyst then has been added in the water, inside the photoreactor and the solution has been continuously stirred. The photocatalytic activity (mmol hydrogen g^{-1} h^{-1}) of the different photocatalysts is evaluated from the cumulative hydrogen production versus time data. The evolved hydrogen gas has been collected by the downward displacement of water, whereas the oxygen has been trapped using alkaline pyrogallate solution.

6.3 Results and Discussion

6.3.1 Morphological characterization: Field Emission Scanning Electron Microscopy (FESEM)

Irregular sized particles of spinel ferrite can be seen from Figure 6.1-a. Formation of some agglomerates can also be seen.

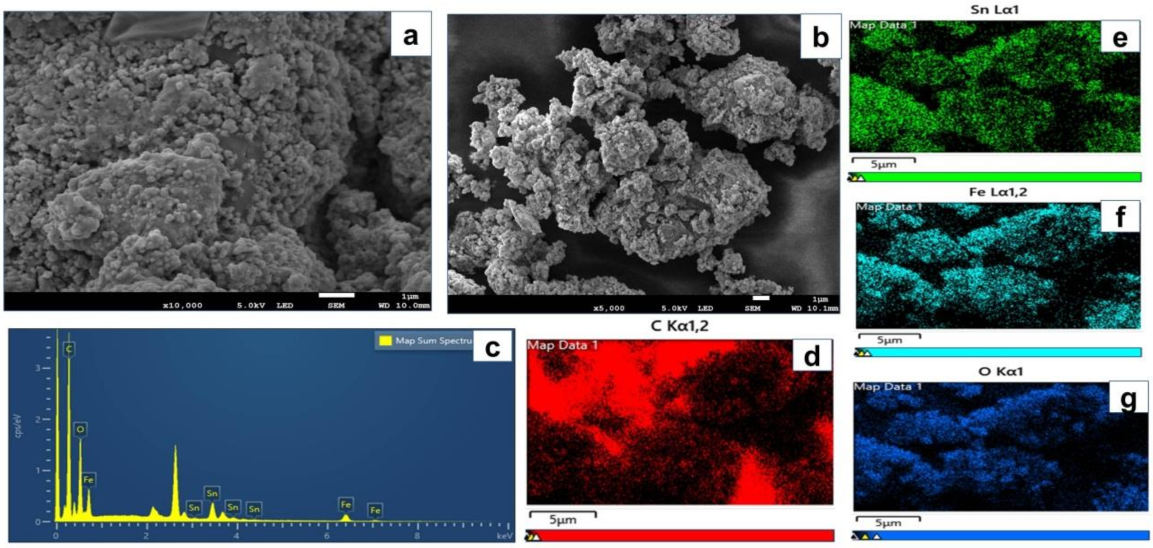

Figure 6.1 (a) FESEM images of $SnFe_2O_4$ and (b) rGO-$SnFe_2O_4$, (c) EDS of rGO-$SnFe_2O_4$ and (d-g) elemental analysis of rGO-$SnFe_2O_4$

The clusters of cabbage like nano-sized particles scattered on layer of rGO can be seen in the Figure 6.1 b. These clusters might have been formed due to the forces of attraction between the metal oxide nanoparticles. The elemental analysis in Figure 6.1-c and elemental mapping in Figure 6.1-d to 6.1-g confirms the presence of different element like C, Sn, Fe, O respectively in the synthesised rGO-$SnFe_2O_4$ photocatalyst.

6.3.2 Crystallinity Study: X-Ray Diffraction (XRD)

The Figure 6.2a shows the XRD pattern of ferritic nano-hybrid material. Sharpened diffraction peaks indicating the growth of the crystalline material can be observed in the Figure 6.2a.

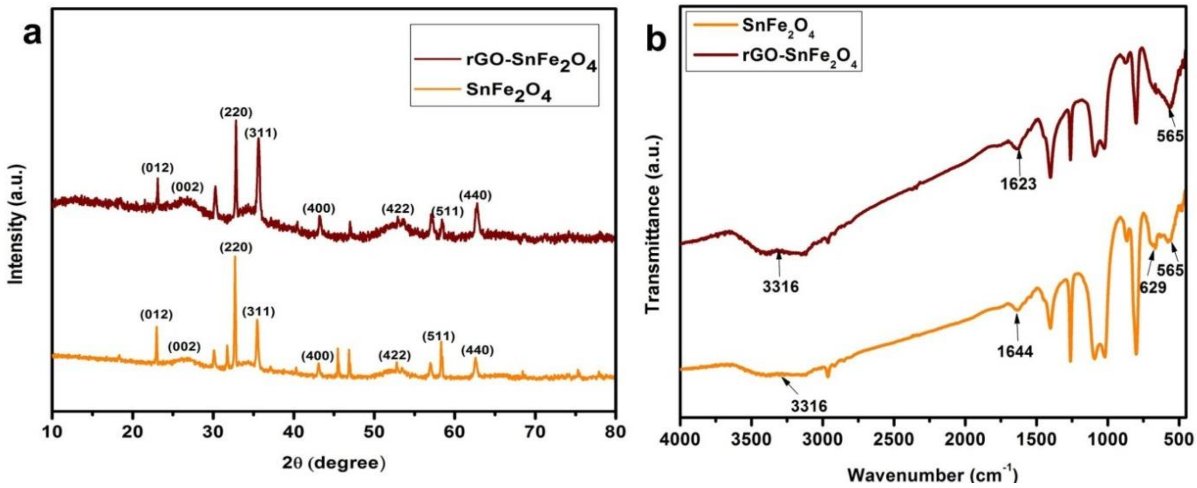

Figure 6.2 (a) XRD of $SnFe_2O_4$ and rGO-$SnFe_2O_4$, (b) FTIR of $SnFe_2O_4$ and rGO-$SnFe_2O_4$

In the figure 6.2-a the XRD spectra of synthesized rGO-$SnFe_2O_4$ show several reflections at $2\theta = 23.02°, 26.79°, 32.76°, 35.56°, 43.30°, 53.42°,58.3°, 62.75°$ with crystallographic planes of (012), (220), (311),(400), (422), (511), (440) respectively (JCPDS card No.11-0614)[14-16]. The diffraction peak at $2\theta = 25.8°$ indicating the presence of (002) plane in rGO-$SnFe_2O_4$ photocatalysts reveal the presence of reductive graphene oxide and also indicates a complete reduction of GO by hydrothermal process during the growth of $SnFe_2O_4$.

6.3.3 Identification of bonds: FTIR

Figure 6.2-b shows the FTIR spectra of $SnFe_2O_4$ and rGO-$SnFe_2O_4$ nanocomposites. The peak at 3616 cm^{-1} is attributed to the O–H stretching vibration, which corresponds to the

internal water molecules of the samples. The stretching at 1644 cm^{-1} and 1623 cm^{-1} is due to the presence of graphitic element. The vibrations at 565 cm^{-1} and 629 cm^{-1} are assigned to the Sn-O and Fe-O stretchings respectively. [18]

6.3.4 UV-vis spectra and Band gap energy analysis

Figure 6.3-b & Figure 6.3-c to d displays the UV-vis absorbance spectra and Tauc plot $[(\alpha h\upsilon)^2$ vs. $(h\upsilon)]$ of $SnFe_2O_4$ and rGO-$SnFe_2O_4$ photocatalysts, respectively. In contrast to $SnFe_2O_4$, rGO-$SnFe_2O_4$ displays a red shift in the absorption edge in the visible light range, allowing photo-generated electrons and holes to move more easily. According to studies, $SnFe_2O_4$ and rGO-$SnFe_2O_4$ photocatalysts have small band gaps of 2.38 eV and 1.92 eV, respectively. The increased absorption edge of the rGO-$SnFe_2O_4$ photocatalyst in figure 5.3-b is 600 nm, due to the addition of rGO, which changes the forbidden band width of the nanocomposite and enhances optical absorption performance in the visible light region. Tauc plots may be used to calculate the band gap (E_g) of photocatalysts using the equation (6.1):

$$(\alpha h\upsilon)^2 = A(h\upsilon - E_g) \qquad (6.1)$$

In this equation, the photon energy is indicated by ‘h’, the absorption coefficient by ‘α’, and the proportionality constant by ‘A’. According to Tauc plots in figure 6.3-d, the optical band gap value of rGO-$SnFe_2O_4$ photocatalysts is decreasing. The band gap of rGO-$SnFe_2O_4$ energy has shrunk as a result of the formation of oxygen vacancies, which has accelerated photo electron transfer under visible light irradiation and improved photocatalytic hydrogen generation.

6.3.5. Photoluminescence study

The photoluminescence (PL) spectrum may be used to investigate the photo-recombination rate of electron-hole pairs. At an excitation wavelength of 390 nm, figure 6.3-a shows the composite PL spectrum of $SnFe_2O_4$ and rGO-$SnFe_2O_4$ photocatalysts. The intensity changes in the order of rGO-$SnFe_2O_4$ < $SnFe_2O_4$, accordingly. The suppression of the electron-hole recombination rate is directly related to the decrease in intensity. The lower recombination rate demonstrates effective charge transfer inside the rGO-$SnFe_2O_4$ photocatalysts, implying that rGO primarily accelerates electron transfer from $SnFe_2O_4$ to rGO, increasing the rate of hydrogen evolution owing to the photocatalytic performance of rGO-$SnFe_2O_4$ photocatalysts

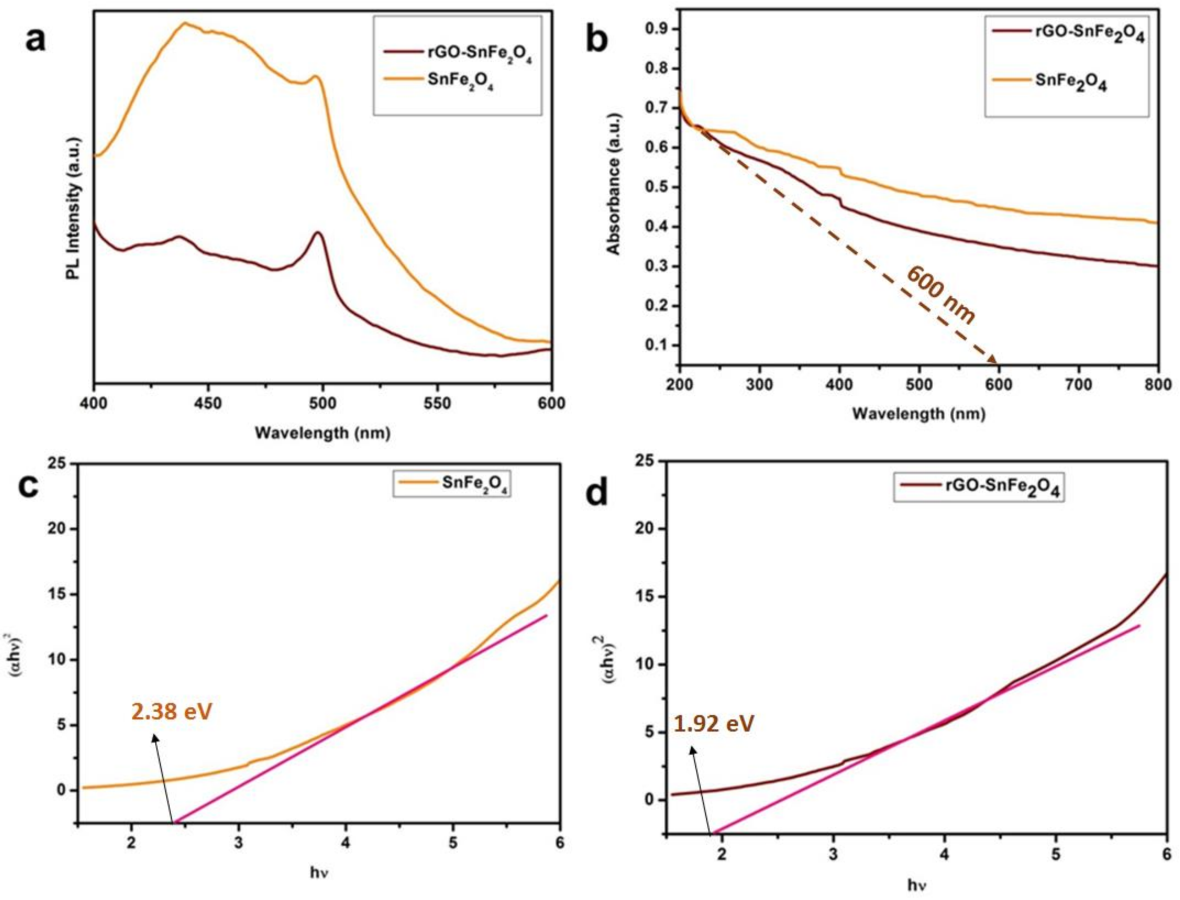

Figure 6.3 (a) PL of $SnFe_2O_4$ and rGO-$SnFe_2O_4$, (b) UV-vis spectroscopy of $SnFe_2O_4$ and rGO-$SnFe_2O_4$ (c) and (d) Band gaps of $SnFe_2O_4$ and rGO-$SnFe_2O_4$

.

6.3.6 XPS study

XPS has been implemented to investigate the surface chemical states of the rGO-$SnFe_2O_4$ photocatalyst. Figure 6.4-a shows the high-resolution Fe 2p spectra of rGO-$SnFe_2O_4$ photocatalyst under visible light irradiation that reveals five symmetrical peaks. The corresponding main peaks at 710.48 eV (Fe 2p3/2) and 722.71 eV (Fe 2p1/2) correspond to + 2 valence state of Fe ions and other two main peaks at 712.36 eV (Fe 2p3/2) and 724.33 eV (Fe 2p1/2) correspond to + 3 valence state of Fe ions. The satellite peak at 716.06 eV indicates the confirmation of oxide form of Fe^{2+} and Fe^{3+} may be present in the rGO-$SnFe_2O_4$ composite. In figure 6.4-b the peaks centered at 486.27 eV and 494.66 eV are assigned to Sn $3d_{5/2}$ and Sn $3d_{3/2}$, respectively, implying that Sn exists primarily as Sn^{2+} In figure 6.4-c the XPS of C 1s pattern of the rGO-$SnFe_2O_4$ composite can be deconvoluted into three peaks at 284.28, 284.77 and 289.66 eV, which can be assigned to the interaction between Fe-C and Sn-C, hydroxyl (C–O), and carboxyl (O–C=O) groups, respectively.

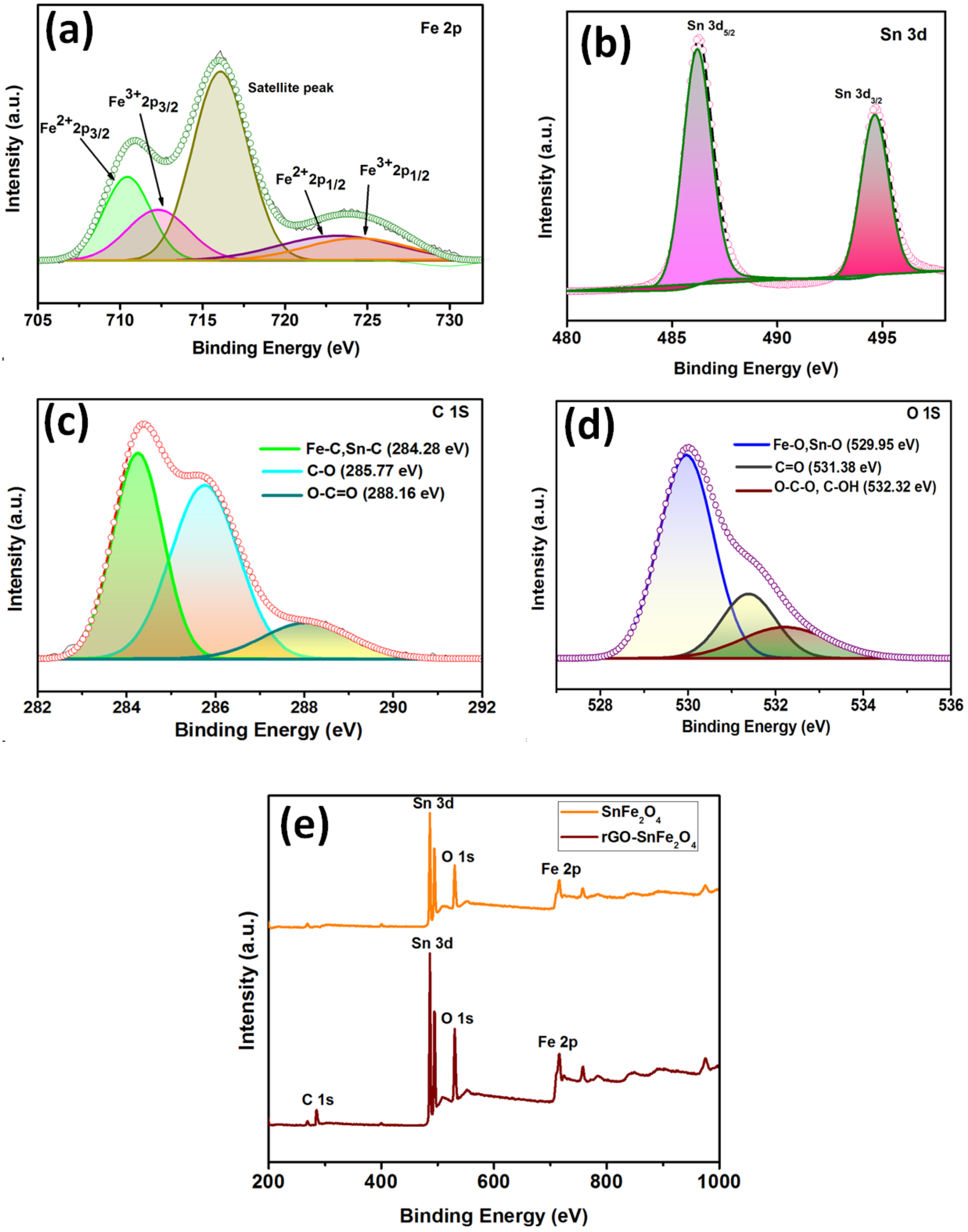

Figure 6.4 Core level XPS scan of (a) Fe 2p, (b) Sn 3d, (c) C 1s, and (d) O 1s, (e) survey scan of X-ray photoelectron spectra (XPS) of the rGO-SnFe$_2$O$_4$ photocatalyst.

The results confirmed the existence of rGO. The O 1s XPS pattern in figure 6.4-d displayed three peaks at 529.95, 531.38 and 532.32 eV, corresponding to lattice O (Fe–O, Sn–O), C=O, and O-C-O/C-OH bonds, respectively. Figure 6.4-e shows the survey scan of X-ray photoelectron spectra (XPS) of the rGO-$SnFe_2O_4$ photocatalyst. The XPS patterns of rGO-$SnFe_2O_4$ suggests that electrons transferred from $SnFe_2O_4$ to rGO or at the interfaces. Therefore, $SnFe_2O_4$ has been successfully anchored on the rGO nanosheets.

6.3.7 Photocatalytic activity

The photocatalytic activity of the as prepared sample has been studied under visible light irradiation. The enhancement of the photocatalytic activity of the graphene-ferritic photocatalyst (2.1428 mmol/g.h) has been observed while compared to the ferritic photocatalyst (1.784 mmol/g.h).

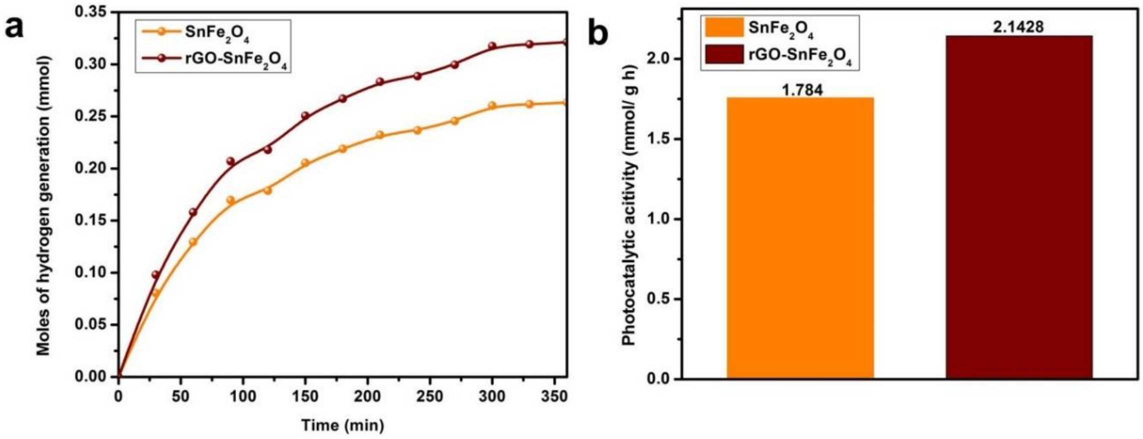

Figure 6.5 (a) Moles of hydrogen evolved for $SnFe_2O_4$ and rGO-$SnFe_2O_4$ (b) Photocatalytic activities of $SnFe_2O_4$ and rGO-$SnFe_2O_4$

The result suggests that the incorporation of rGO in rGO-$SnFe_2O_4$ enhance the visible light absorption and suppress the recombination of electron hole pairs to enhance the charge separation, which is demonstrated in the photoluminescence (PL) study. Further incorporation of rGO, results also in an enhancement of H_2 production of about 20% which can be seen from figure 6.5 (a & b).

6.4 Conclusion

- The functionalized rGO-$SnFe_2O_4$ composite photocatalyst displayed a rise in the photocatalytic activity when compared with the $SnFe_2O_4$ photocatalyst.

- The rate of recombination of photogenerated electron-hole pairs is reduced upon inclusion of an excellent electron transporter like reduced grapheme oxide (rGO).

- This work demonstrated the role of rGO in the enhancement of the generation of hydrogen.

6.5 References

1. Veziroğlu, T. N. and Şahi˙n, S., 2008, 21st century's energy: Hydrogen Energy System, *Energy Conversion* and *Management*, 49(7), 1820–1831.

2. Geim, A. K. and Novoselov, K. S., 2007, The rise of graphene, Nat. Mater., 6(3), 183–191.

3. Kudo, A. and Miseki, Y., 2009, Heterogeneous photocatalyst materials for water splitting, *Chemical Society Reviews*, 38(1), 253–278.

4. Xie, G., Zhang, K., Guo, B., Liu, Q., Fang, L. and Gong, J. R., 2013, Graphene-based materials for hydrogen generation from light-driven water splitting, *Advanced Materials*, 25(28), 3820–3839.

5. Fujishima, A.and Honda, K., 1972, Electrochemical photolysis of water at a semiconductor electrode, *Nature*, 238(5358), 37–38.

6. Casbeer, E., Sharma, V. K. and Li, X.-Z., 2012, Synthesis and photocatalytic activity of Ferrites under Visible light: A review, *Separation and Purification Technology*, 87, 1–14.

7. Marcano, D. C., Kosynkin, D. V., Berlin, J. M., Sinitskii, A., Sun, Z., Slesarev, A., Alemany, L. B., Lu, W. and Tour, J. M., 2010, Improved synthesis of graphene oxide, *ACS Nano,* 4(8), 4806–4814.

8. Hongru Han, Yi Luo, Yuefa Jia, N. Hasan, Chunli Liu, 2022, A review on $SnFe_2O_4$ and their composites: Synthesis, properties, and emerging applications, *Progress in Natural Science: Materials International*, Volume 32, Issue 5, Pages 517-527

9. Wei Jing-Lan, Wang Zi-Yu, Sun Yan-Hui, Zhang Guang-Li, Guan Dong-Cai, Nan Jun-Min, 2021, The kinetics investigation of nitrogen/sulfur co-doped reduced graphene oxide@spinel $SnFe_2O_4/Sn_{0.205}Fe_{1.727}O_3$ as high performance anode for lithium-ion batteries and its application in full cells, *Electrochimica Acta*, Volume 375, 138026.

10. Vignesh Sahadevan, Dineshkumar Loganathan, Ying Chuang, Chien Feng Lo, Chia-Yun Chen, Chia-Yuan Chen, 2023, Synergetic benefits of microfluidics using artificial cilia and ZnO/$SnFe_2O_4$ for the degradation of pollutants, *Materials Chemistry and Physics*, Volume 307, 128068.

11. Lavanya Rathi P, Deepa Seetharaman, 2022, Investigation of thermal stability, structure, magnetic and dielectric properties of solvothermally synthesised $SnFe_2O_4$, *Open Ceramics*, Volume 9, 100222 .

12. Yuefa Jia, Qizhao Wang, Weibin Zhang, Misook Kang, Jong-Seong Bae , Chunli Liu, 2021, Octahedron-shaped $SnFe_2O_4$ for boosting photocatalytic degradation and CO_2 reduction, *Journal of Alloys and Compounds*, Volume 889, 161737.

13. Yan-Hui Sun, Dong-Cai Guan, Jing-Lan Wei, Guang-Li Zhang, Jun-Min Nan, Yue-Peng Cai, 2020, The lithium ions storage property of a novel polyhedral SnFe2O4 and Core-shell composite $SnFe_2O_4$@carbon or carbon@$SnFe_2O_4$ for lithium ion batteries, *Applied Surface Science*, Volume 532, 147396.

14. Dong-Cai Guan, Sheng Tian, Yan-Hui Sun, Fen Deng, Jun-Min Nan, Guo-Zheng Ma, Yue-Peng Cai, 2019, Investigation of the electrochemical properties and kinetics of a novel $SnFe_2O_4$@nitrogen-doped carbon composite anode for lithium-ion batteries, *Electrochimica Acta*, Volume 322, 134722.

15. Chao-Feng Pan, Yan-Hui Sun, Chen-Hao Sun, Zi-Yu Wang, and Jun-Min Nan, 2022, A Spinel Tin Ferrite with High Lattice-Oxygen Anchored on Graphene-like Porous Carbon Networks for Lithium-Ion Batteries with Super Cycle Stability and Ultra-fast Rate Performances, *ACS Applied Materials* & *Interfaces*, 14, 18393−18408

16. Wan-Kuen Jo, Satyanarayana Moru, Surendar Tonda, 2019, Magnetically responsive $SnFe_2O_4$/g-C_3N_4 hybrid photocatalysts with remarkable visible-light-induced performance for degradation of environmentally hazardous substances and sustainable hydrogen production, *Applied Surface Science*, S0169-4332(19)33756-0.

17. Yuefa Jia, Haoxuan Ma, Weibin Zhang, Gangqiang Zhu, Woochul Yang, Namgyu Son, Misook Kang, Chunli Liu, 2019, Z-scheme $SnFe_2O_4$-graphitic carbon nitride: reusable,

magnetic catalysts for enhanced photocatalytic CO2 reduction, *Chemical Engineering Journal*, S1385-8947(19)32584-7.

18. Yan-Hui Sun, Man-Xia Huang, Dong-Cai Guan, Guang-Li Zhang, Jing-Lan Wei, Jun-Min Nan, Fen-Yun Yi, 2021, Influence of the Sn(Fe)-C bonds content in $SnFe_2O_4$@ reduced graphene oxide composites on the electrochemical behavior of lithium-ion batteries, *Journal of Alloys and Compounds*, 854,157297.

LIST OF FIGURES

Figure Number

LIST OF TABLES

Table number

LIST OF SCHEMES

Arundhati Sarkar
16.08.2023

Kajari Kargupta
16/08/2023

Professor
CHEMICAL ENGINEERING DEPARTMENT
JADAVPUR UNIVERSITY
Kolkata-700 032

Ganguly
16/8/2023

Prof. Saibal Ganguly
Consultant
(Retired)
Ex Head and Ch[illegible]nan GRC, BITS Goa
Ex Professor, C[illegible] UTP Malaysia
Ex Advisor, DF[illegible] of Defense
Ex faculty, Ch[illegible] IIT Kharagpur
Email: ganguly[illegible]011@gmail.com

Materials Today: Proceedings xxx (xxxx) xxx

Contents lists available at ScienceDirect

Materials Today: Proceedings

journal homepage: www.elsevier.com/locate/matpr

Enhanced photocatalytic Hydrogen generation by splitting water using Sodium Alginate decorated rGO-CdS hybrid photo-catalyst

Arundhati Sarkar [a], Sourav Chaule [a], Sayantanu Mandal [a], Suparna Saha [a], Saibal Ganguly [b], Dipali Banerjee [c], Kajari Kargupta [a,*]

[a] *Chemical Engineering Department, Jadavpur University, Kolkata 700032, India*
[b] *Department of Chemical Engineering, BITS Pilani, Goa 403726, India*
[c] *Department of Physics, I.I.E.S.T, Shibpur, Howrah 711103, India*

ARTICLE INFO

Article history:
Available online xxxx

Keywords:
Photo catalyst
Visible spectra
Graphene
Biopolymer
Moisture-adsorbent
Hydrogen

ABSTRACT

A Spherical bead like hybrid photo-catalyst rGO-CdS-Sodium Alginate, comprising of water adsorbent Sodium Alginate, a visible light active semiconductor Cadmium Sulphide and an excellent electron transporter reduced graphene oxide, is hydrothermally synthesized, characterised and tested for hydrogen generation from water in presence of visible light (45 W LED). Sodium Alginate, a biopolymer, with very good moisture adsorbing capacity due to the presence of functional groups like hydroxyl and carboxyl, was used to fabricate spherical beads, which adsorbed and stored the water molecule by intermolecular hydrogen bonding with the functional groups. Instead of the conventionally used powder photo-catalyst, spherical beads make the continuous operation of the photo-reactor easier. The toxic and photo-corrosive effects of CdS were minimized in this process through the encapsulation by rGO-Sodium Alginate. Reduced Graphene Oxide (rGO), an electron transporter, aided in decreasing the recombination rate of photo-generated electron-hole pairs. SEM analysis confirms nano-fibrils of Sodium Alginate interspersed with nano-flowers of CdS on the crumpled up sheets of Graphene. The hybrid photocatalyst exhibits a lower band gap (2.33 eV) compared to pristine CdS (2.4 eV). The maximum value of the photocatalytic activity of 6 mmol h^{-1} g^{-1} is achieved using the hybrid photo-catalyst with the optimum loading, in absence of any co-catalyst. This rationally designed composite photo-catalyst will bring new insight into the field of photocatalytic water splitting.

Selection and peer-review under responsibility of scientific committee of the International Conference on Advances in Chemical and Material Science.

1. Introduction

With the advent of rapid mechanisation since the 19th century, the global consumption of fossil fuels has gradually increased [1]. The overutilization of the three primary fossil fuel sources namely coal, oil and natural gas by an exponentially increasing human population, leading to the energy crisis and environmental pollution, is a matter of serious concern. In recent years, Hydrogen energy has evolved as an alternative source of energy. Photocatalytic water splitting is a simple, cost-effective way to the generation of hydrogen by splitting the most abundant natural resource, water [2].There are several roadblocks in the way to the process of photocatalytic water splitting being commercially viable. These are slow reaction kinetics, rapid recombination of photogenerated electrons and holes and low yield of hydrogen [3]. Thermodynamically, the water-splitting reaction is not favorable ($\Delta\ G_f^{\circ}$ = +237.2 kJ/mol).

Honda and Fujishima in 1972 first demonstrated the generation of hydrogen under UV irradiation using TiO_2 electrode and Pt counter electrode in a PEC cell [2]. Since then, the attention of the global scientific community had been directed towards the development of a photocatalyst for efficient photocatalytic water splitting. However, most of the designed photocatalysts were developed using expensive metals like Platinum (Pt), which significantly increased the cost of the process [4–8]. In general, wide band gap semiconductors were studied mainly due to their photostability and bandgap energy [9]. Only a few of these photo-catalysts were able to absorb visible range of the solar spectrum (that constitutes of about 43 % of total light energy) for photocatalytic water splitting.

---

* Corresponding author.
E-mail address: kajari.kargupta@jadavpuruniversity.in (K. Kargupta).

https://doi.org/10.1016/j.matpr.2023.02.095

Selection and peer-review under responsibility of scientific committee of the International Conference on Advances in Chemical and Material Science.

Please cite this article as: A. Sarkar, S. Chaule, S. Mandal et al., Enhanced photocatalytic Hydrogen generation by splitting water using Sodium Alginate decorated rGO-CdS hybrid photo-catalyst, Materials Today: Proceedings, https://doi.org/10.1016/j.matpr.2023.02.095

MRS Advances © 2020 Materials Research Society
DOI: 10.1557/adv.2020.316

Cadmium Sulphide Sensitized Crystal Facet Tailored Nanostructured Nickel Ferrite @ Hematite Core-Shell Ternary Heterojunction Photoanode for Photoelectrochemical Water Splitting

[1]Soumyajit Maitra, [2]Arundhati Sarkar, [1]Toulik Maitra, [1]Somoprova Halder,
[1*]Subhasis Roy, [2]Kajari Kargupta

[1]Deparment of Chemical Engineering, University of Calcutta, 92, APC Road, Kolkata, West Bengal 700009, India.

[2]Deparment of Chemical Engineering, Jadavpur University, 88, Raja Subodh Chandra Mallick Rd, Jadavpur, Kolkata, West Bengal 700032, India.

ABSTRACT

Design of composite semiconductor nanostructures with proper band alignment for efficient charge separation and carrier transport has been at the center of research for photoelectrochemical water splitting. This work demonstrates the deposition of a $NiFe_2O_4$ *@*Fe_2O_3 *core-shell nanostructured film sensitized with CdS to form a ternary heterojunction for cascade type electron transfer. The hematite nanostructures were grown by hydrothermal approach through dipping into a solution of Nickel Nitrate yielded anchoring of* Ni^{2+} *ions on the outer surface. The films were then annealed at 650* ^{0}*C for the diffusion of* Ni^{2+} *ions into the hematite lattice which forms core-shell* $NiFe_2O_4$ *@*Fe_2O_3 *heterojunction. The films were further sensitized with CdS nanoparticles deposited by a hydrothermal approach to form the final ternary heterojunction photoanode. Several different nanostructures were grown and the effect of crystal facet tailoring was observed on Ni loading and photoelectrochemical performance. The photoelectrochemical measurements were carried out using a potentiostat under 100 mW/cm*^{2} *light source (150W Xenon Lamp) with Pt counter electrode and 0.5 M* Na_2S *and*

NJC

PAPER

View Article Online
View Journal | View Issue

Cite this: *New J. Chem.*, 2021, **45**, 12721

Solvothermal phase change induced morphology transformation in CdS/$CoFe_2O_4$@Fe_2O_3 hierarchical nanosphere arrays as ternary heterojunction photoanodes for solar water splitting†

Soumyajit Maitra,[a] Arundhati Sarkar,[b] Toulik Maitra,[a] Somoprova Halder,[a] Kajari Kargupta[b] and Subhasis Roy *[a]

The design of efficient heterojunction photoanodes with appropriate band alignment and ease of charge separation has been one of the most highly focused research areas in photoelectrodes. This work demonstrates the fabrication of a photoanode comprised of CdS sensitized $CoFe_2O_4$@Fe_2O_3 hierarchical nanosphere arrays on a FTO glass substrate and its application in photoelectrochemical water splitting. The hierarchical hematite nanosphere arrays were grown on FTO substrates by a solvothermal approach. Impregnation of Co^{2+} was achieved by surfactant-assisted low-temperature solvothermal phase transformation and a dipping process followed by annealing to form a $CoFe_2O_4$@Fe_2O_3 heterojunction. The effect of pre-annealing of substrates before the second hydrothermal step on Co^{2+} impregnation was studied along with the choice of the solvent. The fabricated electrodes were further sensitized with CdS nanoplate-like structures by a hydrothermal method to form a Z-scheme-Type II ternary heterojunction. The photoelectrochemical properties of the electrodes were analysed by potential linear sweep voltammetry under simulated solar irradiation (AM 1.5G, 100 mW cm^{-2}) with a 0.5 M Na_2S and 0.5 M Na_2SO_3 electrolyte. The highest ABPE% observed at 0.59 V (vs Ag/AgCl) was 0.86% for the photoanode comprised of CdS sensitized porous nanosphere arrays formed by solvothermal Co^{2+} impregnation along with pre-annealing. The fabricated electrodes showed low sheet and charge transfer resistance as observed from the EIS plot. The nanostructure morphology, crystal structure, and phase analysis were carried out using XRD, TEM, SEM and FESEM with EDAX. DFT calculations were carried out to unravel the underlying electronic structure and electron transport processes at the heterostructure interfaces. We hope to inspire more research on ordered heterostructures with superior charge transport properties, proper band alignment, enhanced light absorbance, and charge separation with this work. We also aim to focus on the effect of pre-annealing and solvent–surfactant pair selection on ion impregnation induced phase transformation in nanostructures.

Received 20th February 2021,
Accepted 9th June 2021

DOI: 10.1039/d1nj00864a

rsc.li/njc

1. Introduction

The rise in global temperature and the increase in air pollution caused due to decades of uncontrolled fossil fuel combustion have been poised as a severe environmental threat in recent years, resulting in a desperate need for new renewable energy sources to meet humanity's need for power.[1] Since the demonstration of the photocatalytic and photoelectrochemical performance of TiO_2 by Fujishima and Honda in 1972,[2] research on semiconductor nanostructures for efficient solar energy utilization to split water into H_2 and O_2 has received tremendous attention.[3–8] Hematite has so far emerged as one of the most promising contenders in this field due to its highly desirable properties like low cost, high abundance, small bandgap (1.9–2.2 eV), high light absorbance in the visible region, easily tunable properties, low toxicity, high stability in alkaline media and a high theoretical STH of 14–17%.[9–12] However, as good as

---

[a] Department of Chemical Engineering, University of Calcutta, 92, APC Road, Kolkata, West Bengal, 700009, India. E-mail: subhasis1093@gmail.com, srchemengg@caluniv.ac.in

[b] Department of Chemical Engineering, Jadavpur University, 88, Raja Subodh Chandra Mallick Rd, Jadavpur, Kolkata, West Bengal, 700032, India

† Electronic supplementary information (ESI) available. See DOI: 10.1039/d1nj00864a